THÈSE

En vue de l'obtention du

DOCTORAT DE L'UNIVERSITÉ DE TOULOUSE

Délivré par :

Institut National Polytechnique de Toulouse (Toulouse INP)

Discipline ou spécialité :

Génie des Procédés et de l'Environnement

Présentée et soutenue par :

Mme KONSTANTINA TOPKA

le mardi 30 mars 2021

Titre :

Experimental study and kinetic modelling of chemical vapor deposition process of silicon oxide and oxynitride thin films for aqueous corrosion barriers

Ecole doctorale :

Mécanique, Energétique, Génie civil, Procédés (MEGeP)

Unité de recherche :

Laboratoire de Génie Chimique (LGC)

Directeur(s) de Thèse :

MME BRIGITTE CAUSSAT
M. CONSTANTIN VAHLAS

Rapporteurs :

M. KHALED HASSOUNI, UNIVERSITE PARIS 13
Mme ANJANA DEVI, RUHR UNIVERSITAT BOCHUM

Membre(s) du jury :

M. SOTIRIS PRATSINIS, EIDGENOSSISCHE TECH HOCHSCHURE ZURICH, Président
M. CONSTANTIN VAHLAS, TOULOUSE INP, Membre
M. HUGUES VERGNES, TOULOUSE INP, Invité
Mme BRIGITTE CAUSSAT, TOULOUSE INP, Membre
M. NATHANAELLE SCHNEIDER, CNRS, Membre
M. PIERRE-LUC ETCHEPARE, SGD Pharma, Invité

To my sister Maria and my mother Dimitra,

who support me in every step.

Acknowledgements

A journey, be it professional or personal, educational or adventurous, is always more enjoyable when you share it.

I had the honor to work with and be supported by amazing people, who involved themselves with my thesis directly or indirectly. With the following words, I would like to thank them wholeheartedly, as this three-year journey would not have been possible without them.

To start, I would like to thank the reviewers of my thesis manuscript, Prof. Dr. Anjana Devi, Chair of Inorganic Chemistry II at Ruhr University Bochum, as well as Prof. Dr. Khaled Hassouni, Professor at Laboratoire des Sciences des Procédés et des Matériaux (LSPM), Université Paris 13, CNRS. I am grateful to them for showing interest in my work and accepting to review it, for the time they dedicated in reading my manuscript, and for their insightful comments that I received.

I would also like to extend my thanks to Dr. Nathanaelle Schneider, Researcher at Institut Photovoltaïque d'Île-de-France (IPVF), CNRS, for having accepted to be a member of the PhD thesis jury. I am grateful to her for examining my work, as well as for the comments and advice she shared with me. I am equally grateful to Prof. Sotiris Pratsinis, Professor in the Department of Mechanical and Process Engineering, ETH Zürich, and thank him profusely for accepting to chair the jury of my PhD defense and for contributing to the examination with his in-depth comments and insight.

Of course, the joyful conclusion of this PhD adventure would not have been possible without the sponsorship of the Agence Nationale de la Recherche (ANR), who I sincerely acknowledge for the financing of my thesis, and my supervisors. I thank deeply my thesis director, Brigitte Caussat, Laboratoire de Génie Chimique (LGC), Professor at ENSIACET, Toulouse, for her steadfast guidance, her constant encouragement and unwavering support, her knowledge and advice on CVD processes, her structural and organized approach and the warm welcome that she and LGC extended to me throughout all three years of my thesis. I am equally deeply grateful to the co-director of my thesis, Constantin Vahlas, Centre Interuniversitaire de Recherche et d'Ingénierie des Matériaux (CIRIMAT), Director of research, CNRS, for the motivation he gave me continuously, his broad, bold and creative thinking, as well as for the co-ordination of the overarching ANR HEALTHYGLASS project and the collaborations he enabled. My gratitude also goes to Hugues Vergnes, Director of Atelier Inter Universitaire de Génie des Procédés (AIGEP), who played an integral role to supervising my thesis. I thank him deeply for his invaluable help in all modeling aspects, his in-depth knowledge and constructive comments to all of my scientific productions. I would like to thank all of my supervisors for the trust they showed me in carrying out this

characterization methods. I also deeply thank Air Liquide and Christian Dussarrat, Scientific Director at Air Liquide, for providing their precursor product and for giving me the opportunity to test it. I sincerely thank him for the confidence he placed in my thesis, for his advice and his availability despite the difficult circumstances.

From a more personal side, I want to sincerely thank the people that I worked very closely with. The contributions of both Babacar Diallo, post doctoral researcher at CEMHTI, and Maxime Puyo, post doctoral researcher at CIRIMAT UPS, were integral to my thesis. I thank them extensively for their attentiveness, their expertise and the enthusiasm they brought to the project, but also for their humor, their encouragement and their good advice, especially during the final months prior to my defense. I also deeply thank Laura Decosterd, engineer in project HEALTHGLASS, for the extremely valuable work that she executed and the innovative methodology that she implemented to my deposition experiments. I thank her for her excellent collaboration, her availability, her thorough work and the lovely discussions we had. I also want to thank all master students involved in the project; Nicholas Marios Katritsis and George Alexander Chliavoras for their substantial work in simulations using Code_Saturne and FLUENT, as well as Charlotte Lebesgue, Paris Papavasileiou and Tryfon (Nakos) Tsiros, for their excellent work on nanoscratch characterization, SiO_xN_y thin film analysis and SiO_xN_y simulations respectively. I especially commend Charlotte, Paris and Nakos for their perseverance and the unwavering motivation they showed despite the extremely difficult circumstances and the major influence that the first lock-down had on their work.

I also want to thank my colleagues, and fellow PhD students at that time, Beatrice Kawas, Timothy (Deji) Oluwadero, Milad Mirabedin (now PhD) and Simon Ponton (now post doc). I deeply thank them for our discussions, the encouragement, the worries and hopes we shared, their support, and the things I learned from them. I feel especially indebted to Beatrice and Deji, whom I had the opportunity to share the office with for the majority of the three years of my PhD. I thank you both for your warm smiles, your kind words, your support, your help, the fun and thought-provoking discussions and the great atmosphere you created in our office. I also think very fondly of all people and friends from Alambic and the Uno team, in no particular order: Hassan, Robbie, Astrid, Emilien, Thomas, Alexandre, Claire, Florent, Michelle, Marco, Thibaut, Sid, Magno, Carlos, Yohann, Pierre,… Thank you all for your support, the fun times and the good laughs, and the community spirit you offered in the laboratory.

Naturally, I am deeply thankful to have been blessed with my best and closest friends, Sara Al-Menae, Melissa Chiu, Nadja Kreitschitz and Peter Hsieh. I thank them all for their endless support, their encouraging messages, the funny pictures they sent me, the daily updates on their pets and the handwritten letters we exchanged from different parts of the world. Our activities together, our common interests and our discussions about books, fiction, video games, space launches and astronomy among many other things

always helped me take my mind off whenever a break was needed. I thank them endlessly for making every day so enjoyable and exciting, for watching closely every single one of my steps, for reminding me to take care of myself and especially for supporting me, both during stressful and good times.

Finally, I would like to deeply and warmly thank all of my family and relatives, in particular my sister Maria and my mother Dimitra. From the bottom of my heart, thank you for always being there for me, for taking care of me, for you sacrifices, for giving and doing everything you could and for providing the best conditions so that my PhD endeavor could progress as smoothly as possible. Thank you for your endless, unwavering support, your comfort, for always being by my side and believing in me.

Thank you for your everlasting love.

Konstantina Christina Topka,

Toulouse, 2021.

Table of Contents

Nomenclature and Abbreviations

Symbols

a	Hyperfine coupling constant in ESR analysis
A_o	Pre-exponential factor
E_a	Activation energy
g	g factor of the free electron in ESR analysis
J^3_{HH}	Coupling pattern in 1H NMR analysis
k	Arrhenius rate constant
Mr	Molecular weight
[M]	Total gas mixture concentration
R	Universal gas constant
r	Rate of reaction
T	Temperature
T_g	Glass transition temperature
T_s	Local temperature of the solid surface

Abbreviations

ALD	Atomic Layer Deposition
ANR	Agence Nationale de la Recherche
APCVD	Atmospheric Pressure Chemical Vapor Deposition
BEMA	Bruggeman Effective Medium Approximation
BOE	Buffered Oxide Etchant
CFD	Computational Fluid Dynamics
CL3	Critical Load 3
CVD	Chemical Vapor Deposition

DR	Deposition rate
EP	European Pharmacopeia
ESR	Electron Spin Resonance spectrometry
FDA	Food and Drug Administration
FT-IR	Fourier Transform Infrared Spectroscopy
GC-MS	Gas Chromatography – Mass Spectrometry
HMDS	Hexamethyldisilane (Chapter I), Hexamethyldisilazane (all other chapters)
IBA	Ion Beam Analysis
INT	Fictive group of intermediate compounds containing the constituent element
L-J	Lennard Jones
NMR	Nuclear Magnetic Resonance
RI	Refractive Index
sccm	Standard cubic centimeters per minute, volumetric flow rate unit
SE	Spectroscopic Ellipsometry
SLS	Soda-lime-silica Glass
SPT	Set-point Temperature
TDMSA	Tris(dimethylsilyl)amine
TEOS	Tetraethylorthosilicate
TSAR	Trisilylamine derivative
UDF	User-Defined Function
UI	User Interface
USP	United States Pharmacopeia
WCA	Water Contact Angle

INTRODUCTION

Recent developments in the pharmaceutics industry have encountered challenges regarding sustainable packaging of novel medicinal molecules (NMEs) and delicate active pharmaceutical ingredients, particularly those with intended use in oncology. Due to their sensitivity towards their environment, such molecules are accompanied by excipient solutions that protect them from degradation induced from changes in pH, oxidation and other processes [1]. However, even though pharmaceutical glass vials, the primary packaging of choice, appear chemically inert vis-à-vis an aqueous phase, reactive excipient solutions can still lead to an aggressive interaction with the drug container. Such interactions can alter the glass surface and even produce glass flakes through delamination, reducing the integrity of the vial. In fact, this degradation of the functionality of the primary packaging is a longstanding problem and can result in product failure. Such failures force numerous recalls, especially in drug products with low-filling volumes [2, 3]. Between 2008 and 2012, 22 % of drug product recalls and withdrawals from the market were due to particles identified in the contained liquids [3], with one of their origins being the occurrence of advanced delamination on the internal glass surface of the pharmaceutic container.

Delamination and release of glass fragments in the stored drugs are causes for great sanitary concerns, especially in the case of substances administered intravenously. For that reason, procedures that assess the propensity for delamination have been established and preconized by the European (EP) and the United States (USP) Pharmacopeias. In that context, the U.S. Food and Drug Administration (FDA) emphasizes the significance of testing the compatibility between container and stored drug, as well as the selection of proper glass composition and quality control of the glass vials [2]. The recommendations described in the USP <660> and <1660> chapters suggest procedures for this evaluation by utilizing wet corrosion tests under extreme thermal and chemical conditions that aim to replicate the prolonged exposure of the glass surface to aggressive pharmaceutical substances [4, 5]. For safe product circulation in the market, the primary packaging medium, in the present case the vial, must demonstrate an excellent response to the recommended USP <660> and <1660> tests. Passing criteria are the low extraction of glass constituent elements and low hydrolysis of the silicate network. Both phenomena are initiated through ion exchange between the modifier cations of the glass and the water molecules of the aqueous solution and

alter the pH of the solution when left unaddressed. Prolonged exposure of the internal vial surface to an aqueous solution results in detachment of whole fragments, i.e. delamination.

Unfortunately, despite the various compositions of primary glass packaging that have been developed over the years, the challenge of protecting the container from the active molecule and excipient solution that is to be stored still remains. To combat this, the presence of a barrier coating on the internal surface of pharmaceutical vials has been explored as a potential solution that can help limit the interaction between the stored drug and the glass container, extending product shelf life and sustainability. Such coatings can aid in fulfilling targeted requirements, namely reduction of ion leaching from the glass or protein adsorption, but their deposition process must at the same time be integrated in industrially established glass vial production-lines.

Pharmaceutical vials based on the above concept are already circulating in the market. As a form of an example, the product SCHOTT Type I Plus® marketed by SCHOTT AG utilizes the application of a pure, 100-200 nm thick SiO_2 coating, deposited on the internal surface of Type I glass using plasma impulse chemical vapor deposition (PICVD). SCHOTT AG advertises a greatly reduced drug-to-container interaction, providing effective barrier performance and improved resistance against the recommended test described in the USP <660> chapter [6]. However, it fails to respond satisfactorily to the specifications of the more aggressive USP <1660> tests, under which the coating eventually dissolves in the solution [7]. This unsatisfactory response can be attributed to a nanoporous microstructure of the coating, often traced back to the deposition process, or even to the inherent limitation of silica as a barrier material. Alternative methods for SiO_2 production exist, such as sol gel or colloidal techniques, dip coating, atomic layer deposition (ALD), or plasma enhanced (PE) and thermal CVD. However, strict requirements tied to the glass manufacturing line must be respected if a barrier coating is to be implemented. The operation at atmospheric pressure combined with high throughput is desireable. Process temperatures lower than 570°C should also be favored, so that compatibility with the glass-transition temperature is ensured, are some of the limitations defined within this frame. In 2019, Ponton studied in his thesis the deposition of SiO_2 barrier coatings from tetraethylorthosilicate (TEOS) and O_2, using a thermal, atmospheric pressure CVD process [7]. This specific CVD technique is less complex than PICVD and can be directly implemented at the back end of the vial production lines of vial manufacturing. However, although the selected chemistry and process led to the deposition of high quality SiO_2 barrier coatings that passed the USP <660> assessment, the coating material did not manage to overcome the challenges of some of the more aggressive USP <1660> tests. Once again, the covalent bonds of the silica coating were eventually hydrolyzed. Ponton illustrated how a significant link exists between the densification of the silicate network and the chemical durability of the coating [8]. For that reason, denser network structures, either of pure silica or of alternative

silica-based coatings, need to be studied, if they are to stand the severe corrosion tests performed in acidic and basic solutions according to the general recommendations of the pharmacopeias.

In this context, the HEALTHYGLASS project funded by ANR was conceptualized, involving a consortium of four laboratories (LGC, CIRIMAT INPT, CIRIMAT UPS, CEMHTI) and an industrial partner [9]. The present thesis, carried out in the frame of this project, explores alternative barrier coating solutions by thermal CVD, based on the concept of improved densification of the amorphous ceramic network through an increase in its crosslinking as a result of different material compositions. In the case of amorphous SiO_2, this claim is put forth based on the different coordination levels between oxygen, nitrogen and carbon. It is proposed that a partial replacement of divalent O^{2-} anions in the silicate network by trivalent N^{3-} or tetravalent, carbidic C^{4-} anions can result in a denser lattice. As such, amorphous silicon oxynitride (SiO_xN_y) and silicon oxycarbide (SiO_xC_y) films are expected to perform better than amorphous SiO_2. The resulting SiO_xN_y and SiO_xC_y films can present improved diffusion-limiting properties, greater chemical and thermal durability and constitute more efficient corrosion barriers. However, very little information is available in the literature concerning the CVD of SiO_xN_y and SiO_xC_y thin films in accordance with the constraints dictated by the pharmaceutical application in question; these pertain namely to the production of chemically inert films in confined surfaces, deposited at atmospheric pressure and at moderate temperatures (<570°C), with high growth rates.

In light of all of the above, reactive and novel chemistries are tested with the aim to achieve material deposition within the frame of the desired specifications using a thermal CVD process. The deposition of amorphous SiO_2 is initially carried out via reactive O_3-based chemistries, serving as a starting point for the investigation of silica-based film deposition at low to moderate temperatures. Insertion of N and C in the silicate network, with some Si atoms of the $Si(O)_4$ tetrahedra being bonded to one or more N or C atoms substituting O, is explored while still maintaining the amorphous state. Via carefully selected reactive chemical pathways, the thermal CVD production of SiO_xN_y and SiO_xC_y films is attempted at temperatures lower than the conventional ones, aiming to render this deposition process compatible with the glass transition temperature of the pharmaceutical vials. Innovative deposition routes are explored, based on single or dual-precursor combinations of silicon-containing compounds such as the classical tetraethylorthosilicate (TEOS) and hexamethyldisilazane (HMDS) molecules, and the rarely reported tris(dimethylsilyl)amine (TDMSA) precursor. Deposition from a novel, proprietary trisilylamine derivative compound developed and provided by Air Liquide is also studied. A multidisciplinary approach is embraced, combining materials science and process engineering in a way that involves the simultaneous development of resistant barrier films through experiments, alongside simulation and numerical computation for process optimization.

Starting with Chapter I, the challenges faced currently by the pharmaceutics industry are recounted, explaining in more detail the delamination and glass alteration mechanisms in aqueous media. Following that, the chapter lists potential solutions for overcoming these challenges and emphasizes the effective network densification by the partial replacement of O anions by N and C ones. An extensive bibliographic analysis on the various chemistries used for the deposition of silica-based films is presented, illustrating the constraints of certain deposition routes and illuminating promising prospects of thermal CVD. Based on the collected information, a strategy on the selection of potential precursor molecules that can effectively lead to deposition of SiO_xN_y barrier coatings by thermal CVD is formulated. The principles governing the CVD process itself are further touched upon, presenting the usefulness of combining the experimental investigation with computational simulation studies for process optimization.

Progressive incorporation of nitrogen and carbon in the films, as well as the resulting evolution of the silica network and the influence of its composition on its performance, is at the core of the thesis. As such, Chapter II initially details the design and setup of the utilized CVD reactors, following which great focus is placed on the techniques implemented for the definition of the composition and structural characteristics of the produced materials. Elaborate physicochemical, structural and mechanical characterization protocols are established, involving microscopy, ellipsometry, nuclear and vibrational spectroscopies and nanomechanical tests. Upon definition of the characterization methods, both those used for the analysis of solid phase as well as for the gas phase, information regarding the simulation software and structure of the computational environment is provided.

After explanation of all utilized characterization and simulation tools, results on the deposition of silica-based films are presented in the chapters succeeding it. In more detail, Chapter III deals with the deposition of silica and carbonated-silica films from O_3 activated chemistries. SiO_2 films from TEOS-O_2/O_3 on flat Si substrates serve as a reference point for subsequent comparisons in this thesis. These comparisons are drawn in terms of material structure, composition, chemical bonding state and resistance to wet etching corrosion. The barrier properties of the SiO_2 films produced from TEOS-O_2/O_3 are then assessed based on the recommendations of the USP <660> chapter. Following deposition and material characterization, the experimental results are utilized in order to enrich previous literature models describing the deposition process via simulation. By combining experimental study and theoretical kinetic model development, a better understanding of the involved gas phase and surface phenomena is sought, in order to optimize the deposition process and efficiently adapt it to coat complex 3D substrates. In the same chapter, a dual-precursor chemistry based on HMDS is explored for the deposition of SiO_xC_y films at low temperature. Extensive focus is placed on the influence of carbon incorporation on the various properties of the films. A distinction between organic carbon and desired carbidic -Si-C-Si- incorporation is underlined. The

transition of the produced material from SiO_2 to SiO_xC_y is studied, with its effect on functionality and performance being a focal point.

Following the above, Chapters IV and V concern the deposition of SiO_xN_y films from novel precursor chemistries. Starting with Chapter IV, the thermal CVD of SiO_xN_y layers on flat Si substrates from TDMSA is described, studying in depth the effect of deposition temperature and inlet gas supply on the resulting material composition, structure and properties. In parallel to the deposition process, an innovative methodology coupling GC-MS, NMR and ESR is implemented, aiding in the study of the effluent gases during the deposition process. Through this methodology, radical species and stable by-products are identified, allowing for the proposal of a series of reactions that describe the scarcely reported deposition mechanism of SiO_xN_y films. The obtained information is subsequently used for the definition of an apparent chemical model proposed through an original approach that combines the aforementioned gas phase and solid phase results, alongside simulation.

Finally, Chapter V studies once again the deposition of SiO_xN_y films, produced however from a more reactive chemistry. This chemistry utilizes a novel, proprietary precursor developed by Air Liquide, selected specifically to overcome the previously faced challenges in regards to thermal limitations of the coating process and compatibility problems between the deposition temperature and the pharmaceutical container. Comparison between all developed films is done with the aim to illustrate the effects of the composition, material structure, silicate network environment and level of network densification on the barrier properties and protection efficiency. Through this, the improved corrosion resistance induced as a result of the partial replacement of the divalent O anions is illustrated tangibly by wet etching corrosion tests. Although assessment based on the USP <1660> recommendations is under progress, the compositional variety of the developed films can be adapted to the desired characteristics and could eventually allow for new, advanced pharmaceutic molecules to be commercialized. Lastly, given that functional silica-based materials are encountered numerous Key Enabling Technologies [10], the multitude of the studied chemical systems can additionally offer alternative CVD pathways for their implementation in microelectronics, spintronics, systems for energy harvesting, food packaging and gas sensor applications.

Chapter I. Silica-based CVD coatings for barrier applications: Motivations, processes and chemistries

In the present chapter, various subjects dealt with in this thesis are discussed based on a review of the literature. Initially, the multiple application domains in which silica-based materials can be encountered, are presented. Certain focus is placed on applications regarding pharmaceutical packaging and the challenges faced by the primary packaging of drug molecules. These challenges pertain to the phenomena glass hydrolysis and delamination. Protection of pharmaceutical glass containers from alteration mechanisms through the application of protective barrier coatings constitutes the motivation of this thesis. The alteration phenomena are explained in detail in order to understand the particular aspects that influence them, but also as a means to gain insight into which parameters can be touched upon to help improve the chemical durability of the primary glass packaging. Potential solutions for overcoming the challenges induced by alteration are listed and current technologies for the application of barrier coatings on heat-sensitive substrates are discussed. The constraints of certain deposition routes and their particularities are considered in view of the limitations dictated by the manufacturing process of pharmaceutical glass vials. Based on this information, the chosen thermal CVD process is defined. Emphasis is placed on the composition and effective network densification of silica-based coatings, and how this can be achieved by the partial replacement of O anions by N ones. A bibliographic analysis on the various chemistries used for the deposition of silica-based films is presented. Based on this information, a strategy for identifying and selecting the most promising precursor molecules for deposition of SiO_xN_y protective barrier coatings by thermal CVD is formulated. Lastly, the coupling of gas-phase analyses and computational fluid dynamics (CFD) calculations is discussed, two approaches that are used in this thesis alongside deposition experiments, as a means to elucidate the deposition process and to provide further insight into the selected chemistries.

I.1. The glass and the silicate network

I.1.1. Applications of silica-based materials

Materials from the silicon oxide, nitride and carbide family exhibit numerous functional properties. It is thus no surprise that thin films of such compounds are encountered in all Key Enabling Technologies including microelectronics, materials for energy harvesting, spintronics and biomedical applications [10]. Silicon oxynitride (SiO_xN_y) films specifically have attracted a lot of attention over the past decades due to their tunable properties [11], exhibiting characteristics in-between those of silica (SiO_2) and silicon nitride (Si_3N_4) films. Starting from silica layers, applications in the field of optics, optoelectronics and food or pharmaceutical packaging benefit from their optical properties, transparency and effective gas diffusion barrier [12]. Additionally, SiO_2 coatings are deposited on nanoparticles, membranes and structures for energy harvesting, hydrocarbon gas separation, wastewater treatment and oil-water separation among others [13, 14]. Combination of alternating silica and nitride multilayer films have also been studied for the protection of OLEDs from humidity and oxidation [15].

Going one step further, the partial replacement of O^{2-} anions by trivalent N^{3-} ones with higher coordination results in SiO_xN_y films exhibiting denser network structure compared to SiO_2, improved oxidation resistance [16] and higher thermal and chemical stability [17]. At the same time, a SiO_xN_y material presents reduced intrinsic mechanical stress, which commonly describes the more rigid Si_3N_4 material, avoiding thus the emergence of cracks that can be detrimental to product performance [18]. SiO_xN_y films are often encountered in semiconductor applications and flexible solar cells [19]. Moreover, their use in food packaging and gas barrier applications has attracted considerable interest in recent years thanks to their improved oxidation and corrosion resistance [16].

It is worth noting that all of the above applications deal either with heat-sensitive or complex-in-shape structures, if not both. In the case of pharmaceutical applications, both characteristics apply: when the coating of glass vials is desired, one must consider the 3D complexity and confined space of the glass container, while keeping in mind that the coating treatment needs to be compatible with the particularities of the glass itself (i.e. glass transition temperature) and the glass manufacturing process. In order to respond to the continuous advances of the drug industry and provide viable and sustainable drug containers, these aspects are used to define the margins of operating conditions under which a protective coating can be applied. This will be touched upon in more detail in the following sections.

I.1.2. *The glass network*

As a general description, silica-glass is comprised of an arrangement of Si and O atoms, in which each silicon atom is surrounded by four oxygen atoms [20]. Out of these four oxygen atoms, at least three of them are connected to a neighboring silicon atom. This results in network crosslinking via –Si–O–Si– bridges, while the difference in the angles and rotation of these bridges leads to a random network arrangement (i.e. amorphous silica). Oxygen atoms that are not connected to two silicon atoms are called non-bridging oxygens and an increase in their number decreases the degree of polymerization and stoichiometry of the material. Both of these characteristics greatly influence the physico-chemical properties of the glass. On this basis, modulation of the glass composition can help address specific properties for target applications.

Commonly, glasses are the product of various oxide mixtures, with each oxide serving a different function. They are usually categorized into five different groups: network formers (SiO_2, B_2O_3, etc.), network modifiers (primarily alkali and alkaline earth oxides such as Na_2O, MgO, CaO, etc.), intermediates (Al_2O_3, PbO, etc.), colorants (FeO/Fe_2O_3, CuO/Cu_2O, etc.) and filling agents [1]. The utilization of network modifying and intermediate elements is widely applied to induce a change in the properties of the vitreous material through alteration of its polymerization. This is achieved as follows: starting with the network modifying cations, their addition results in the formation of an ionic bond with oxygen. This causes the local rupture of the –O–Si–O–Si–O– sequence (polymerization chain) into two ionic –O–Si–O$^-$ groups and the appearance of non-bridging oxygens, as illustrated in Fig. I.1, using addition of Na_2O as an example [21]. Through this, a reduction in viscosity and melting temperature of the glass can be brought about, as is the case for addition of sodium carbonate (Na_2CO_3). A second utility of network modifiers involves the compensation of the electric charges of intermediate elements. As for the intermediate oxides, their function depends on the composition of the overall vitreous network. They can either play the role of network former or network modifier, depending on the concentration in alkali or alkaline-earth ions and the resulting charge compensation.
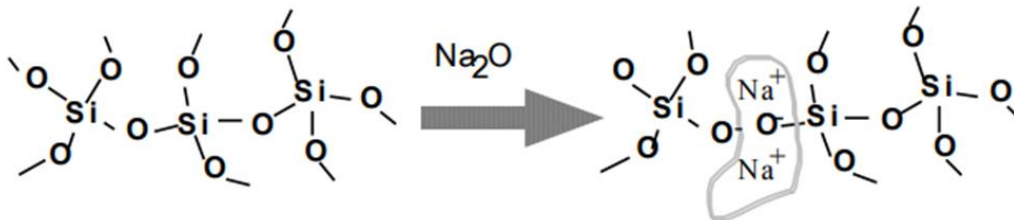
Fig. I.1. Forming of non-bridging oxygen in silicate glasses [21].

I.1.3. *Pharmaceutical glass*

Glass containers (vials, cartridges, ampoules, etc.) are widely encountered in medicine as they offer an advantageous packaging solution thanks to their chemical inertness and ease of sterilization with heat. Although transparency is oftentimes desired for easier content inspection, colored glass is also used in pharmaceutical storage, as it can protect the contents from ultraviolet light degradation. Glass as a packaging medium is impermeable to water and air, allowing for safe storage of medicinal substances. Glass containers intended for pharmaceutical use are categorized in different types, namely Type I to IV, distinguished by their composition and/or treatment. Table I.1 lists representative compositions of Type I and Type III vials. Type I vials are made from borosilicate glass, containing approximately 10 w.% boron oxide (B_2O_3) and ca. 70 w.% SiO_2, along with network modifiers such as sodium oxide (Na_2O) and potassium oxide (K_2O). Beginning at around the 1910s, borosilicate glasses started seeing use in packaging of parenteral solutions [1]. According to the European Pharmacopoeia (EP), Type I glass has a high hydrolytic resistance due to its chemical composition and is described as suitable for most uses, be they parenteral or not.

Table I.1. Composition ranges of Type I (in w.%) and Type III (in mol.%) glass vials intended for pharmaceutical use [22].

Oxide	Type I	Type III
SiO_2	65 – 69 %	70 – 74 %
B_2O_3	11 – 13 %	-
Na_2O	6 – 9 %	13 – 17 %
K_2O	1 – 3 %	0 – 0.6 %
CaO	0 – 1.5 %	8 – 11 %
Al_2O_3	2 – 7 %	0.05 – 2 %
ZnO	0 – 2 %	-
MgO	-	0 – 6 %
SO_3	-	0 – 0.4 %
Fe_2O_3	-	0 – 0.6 %
BaO	1.5 – 3 %	-

Type II and Type III pharmaceutical vials on the other hand do not contain B_2O_3 and are comprised of approximately 10 w.% CaO, 15 w.% Na_2O and 75 w.% SiO_2, thus characterized as soda-lime glasses.

They can also contain small amounts of potassium oxide (K_2O) and magnesium oxide (MgO) among others, with the latter reducing the required molding temperature compared to Type I glass. Type II glass is distinguished from Type III in that it involves the treatment of its surface with sulfur, which gifts it high hydrolytic resistance. According to the EP, Type II is suitable for most acidic and neutral aqueous preparations, whether or not for parenteral use. Type III glass on the other hand is recommended for non-parenteral preparations, or for some non-aqueous preparations or powders for parenteral use, excluding lyophilized products. Lastly, Type IV containers are made of soda-lime glass with low hydrolytic resistance, suited for storage of oral dosage forms, but not recommended for parenteral use.

Despite the varying types of pharmaceutical glass and compositions developed over the years, their resistance to alteration in aqueous media is being pushed to its limits. The necessity to extend glass container shelf life for storage of sensitive medicinal molecules has given rise to extensive research for potential solutions. In all cases however, to combat the problem of chemical alteration of the glass, one must first grasp the mechanisms that lead to its hydrolysis, and eventually, its delamination.

I.1.4. *Mechanisms of hydrolysis and ion exchange*

When storing aqueous solutions, the glass container is in constant and direct contact with the liquid content. Aggressive solutions and prolonged contact (in the order of several months) can lead to alteration of the glass surface exposed to the liquid environment. The overall glass alteration process in aqueous media involves multiple stages and has been the subject of numerous studies [23-25], even debates [26]. The general scientific consensus is that it is initiated once water enters and diffuses into the vitreous network. The rate at which this diffusion, and all following alteration steps, take place, is dependent on the glass composition and the atomic arrangement of the elements in the glass matrix.

Upon diffusing in the lattice, the water molecules are involved in two sorts of interactions: a reaction with the covalent bonds of the silicate network, which causes the hydrolysis of the latter, and a reaction with the ionic bonds, which causes an ion exchange between the hydrogenated species (H_2O, OH^-, H_3O^+) and the modifying elements (Na^+, etc.) of the glass. In turn, these two interactions cause irreversible modifications not only to the glass container, but also to the stored aqueous solution, as is described shortly.

In more detail, the ion exchange mechanism, also referred to as *leaching* [26, 27], can be described through Reaction I.1 [22]:

$$(-O-Si-O-I)_{glass} + H_2O \rightarrow (-O-Si-O-H)_{glass} + I^+ + OH^- \qquad \text{Reaction I.1}$$
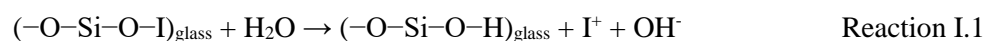
where *I* symbolizes the network modifying ion (mainly alkali or alkaline earth) in the silicate lattice. Reaction I.1 results in the release of the network modifying element and hydroxide anions (OH^-) in the solution. Departure of the modifier from the glass network towards the aqueous medium creates a SiO_2-rich alteration layer, the thickness of which increases over longer exposure times as a result of continuous network alteration (Fig. I.2). However, the rate of alteration is not linear. Cailleteau et al. [28] reported that the altered region can undergo structural reorganization, forming new –Si–O–Si– bridges through the condensation of silanol moieties and leading to pore closure. This decelerates the further diffusion of hydrated species and partially limits the rate of alteration.
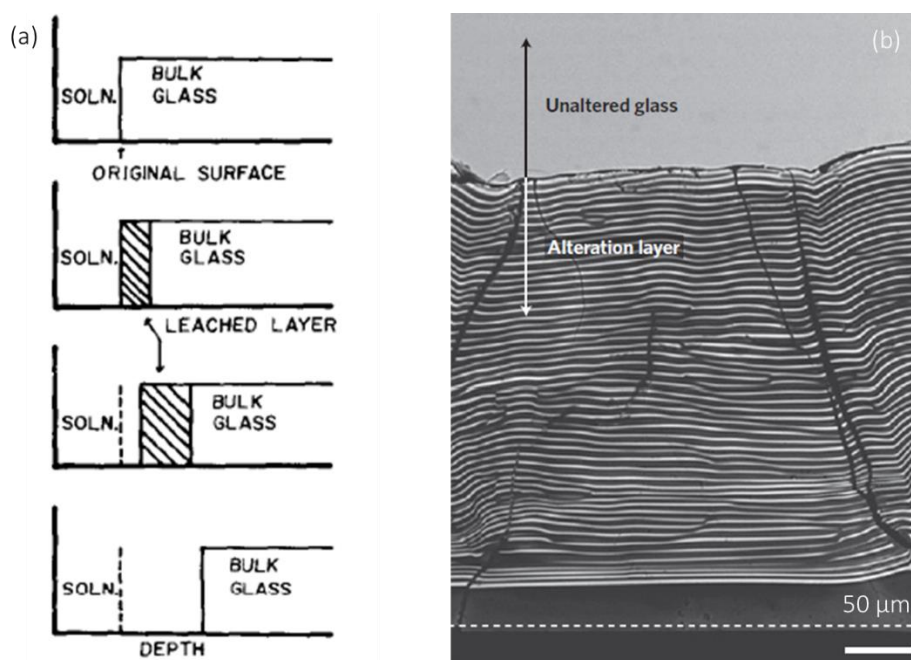
Fig. I.2. Schematic representation of the progression of glass alteration (a) [24]. Back-scattered electron image of the sharp interface between pristine borosilicate glass and silica-rich alteration zone (b) [29].

The OH^- and network modifying ions produced through ion exchange (Reaction I.1) cause an increase in the pH value of the stored solution. For pH sensitive-drugs, this can reduce or nullify the efficiency of the active drug molecule. Moreover, if pH values shift above 8-9, the glass network is hydrolyzed at higher rates by the now basic solution, according to Reaction I.2 and 3 [24, 30]:

$$(\equiv Si{-}O{-}Si(OH)_3)_{glass} + OH^- \rightarrow (\equiv Si{-}O^-)_{glass} + H_4SiO_{4\ solution} \qquad \text{Reaction I.2}$$

$$(\equiv Si-O^-)_{glass} + H_2O \rightarrow (\equiv Si-OH)_{glass} + OH^- \qquad \text{Reaction I.3}$$

$$H_4SiO_4 + OH^- \leftrightarrow H_3SiO_4^- + H_2O \qquad \text{Reaction I.4}$$
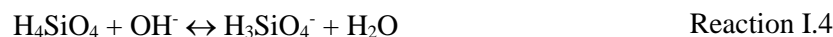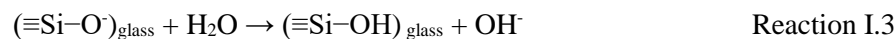
The rupture of the covalent bonds between the network forming Si atoms and oxygen results in the depolymerization of the lattice and formation of silanol (Si-OH) groups. The rupture of four –Si–O–Si– bridges extending from one silicon atom is required to release it from the glass network. This leads to the release of silicic acid (H_4SiO_4, Reaction I.2). For solutions that are not too basic, H_4SiO_4 can aid in balancing out the augmentation of the pH and slow down the dissolution rate [31]. For pH > 8 however, H_4SiO_4 is ionized and its solubility is increased (Reaction I.4), driving the silica dissolution reaction forward [32].

I.1.5. *Delamination and degradation of the glass container*

Hydrolysis of the glass can be observed directly at the extreme surface that is in direct contact with the aqueous solution. As additional water molecules diffuse and are incorporated in the network during prolonged exposure, the alteration progresses further inside the previously pristine glass and the thickness of the hydrated layer increases (Fig. I.2). Once thick enough, the corroded layer is detached from the extreme surface of the glass and released in the solution as flakes, called *lamellae* [33]. This phenomenon, referred to as *delamination*, produces insoluble, inorganic glass particulates that measure sizes from anything below 1 μm to >50 μm [34]. Bigger lamellae are visible to the naked eye, signaling sanitary risks (Fig. I.3). They are especially cause for great concern when the stored solution is destined for subcutaneous and parenteral administration, causing thrombotic, embolic or other vascular complications [2]. Additionally, the presence of lamellae can lead to the destabilization of the active ingredient contained in the pharmaceutical product, e.g. through aggregation of proteins on the surface of the glass flakes [35].

Delamination occurs more frequently when compositional inhomogeneities are present at the glass surface. These inhomogeneities are traced back to the glass manufacturing process. They are generally the result of evaporation and deposition of glass constituents with low melting temperature, or post-manufacturing thermal or chemical treatments. The repeated heating and cooling steps present in the glass tubing technology can accentuate their occurrence. Compositional inhomogeneities occurring from glass tubing are usually located at the heel region (i.e. the base of the vial) [34, 36, 37]. For borosilicate glass, a phase separation into a silica-enriched and a borate-enriched phase can take place, resulting in lower chemical durability and resistance to corrosion [37]. Borosilicate containers produced through the glass molding process on the other hand are somewhat less prone to this problem, because of the fewer heating

and cooling steps [34]. Details on the two glass manufacturing processes are given in upcoming sub-sections.
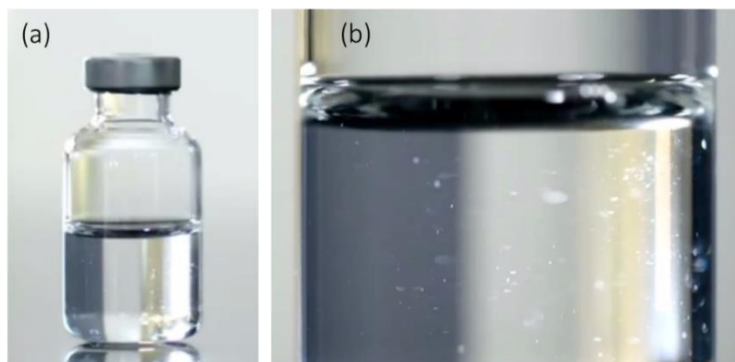
Fig. I.3. Pharmaceutical vial exhibiting progressed stage of alteration (a) and close up of the vial (b), showing the lamellae suspended in the stored solution as a result of delamination [38].

Multiple mechanisms for the formation of lamellae have been identified. Other than the above described delamination mechanism and lamellae detachment caused by progressed hydrolysis (Fig. I.4a), precipitation can also occur, observed when the leached components of the container react with the active drug molecule or the excipient solution towards the creation of a solid compound. If the solubility limit of the produced solid is exceeded, precipitation, often in the form of flakes or sheets, takes place [1, 39].

Another mechanism of corrosion has also been noted, described as alteration that occurs localy in the form of pits [32] and is the result of the previously explained inhomogeneity of the glass. This compositional inhomogeneity, such as areas rich in boron or sodium, can promote preferential interactions between the aqueous solution and these elements [40]. Pitting-style corrosion of glass can be especially accelerated when a surface treatment step is involved in the manufacturing process, such as exposure of the glass container to sulfuric acid [41]. Over time, the pits increase in size and can connect to other pits, facilitating as such the fracturing and detachment of glass fragments from the surface (Fig. I.4b).

Although alteration continues to be a persistent problem in the pharmaceutics industry, it also extends and affects multiple other sectors, from glass intended for food storage to glass used in the containment of nuclear waste. Assessing the propensity for delamination and the potential damage that could occur in the glass after prolonged exposure to an aqueous solution is therefore crucial. In the health sector, methods of assessment are recommended by the health authorities (EP, USP, FDA). One such recommendation used in the present thesis is the USP <660> chapter [4], which will be detailed in

Chapter II. However, merely assessing the probability and level of irreversible alteration is not sufficient. Manufacturers and the research sector are incentivized by the health authorities to explore solutions that retard the alteration process, increase resistance to corrosion, prolong product shelf life and ensure patient safety.
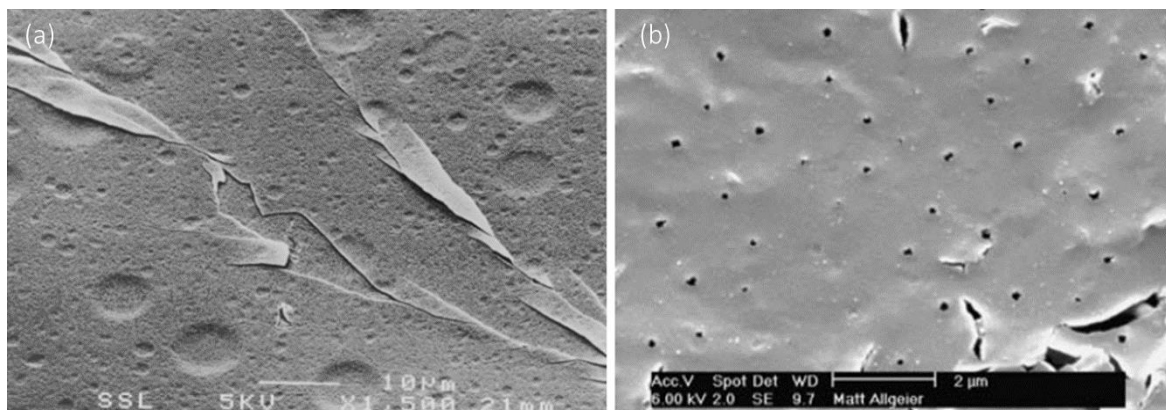
Fig. I.4. Scanning electron micrograph of delaminated region on the internal surface of a glass vial, after exposure to a drug solution (pH 8) and three sterilization cycles (a) [34]. Micrograph of an isolated lamella, showing intact pits (b) [32].

I.1.6. Current solutions to counter glass alteration

I.1.6.1. Glass composition and manufacturing process

Through the presentation of the alteration mechanisms, it becomes apparent that the intrinsic composition of the glass itself plays a key role in its resistance against hydrolysis. In section I.1.3, it was mentioned how borosilicate (Type I) glass demonstrates a higher hydrolytic resistance according to the European Pharmacopeia. This improved performance is in fact attributed to the difference in composition between it and soda-lime (Type III) glass. Borosilicate glass utilizes three network formers (SiO_2, Al_2O_3 and B_2O_3), exhibiting a vitreous network made up of SiO_4 and AlO_4 tetrahedra, and BO_3 triangles. Soda-lime glass on the other hand utilizes only two network forming elements (SiO_2 and Al_2O_3). Moreover, the total mass fraction of the network forming components in borosilicate glass is higher (~85 m.%) compared to their total mass fraction in soda-lime glass (~75 m.%). The higher contents in network modifying ions in the case of soda-lime glass results in more non-bridging oxygen atoms, which leads to an atomic arrangement that is more prone to ion exchange in an aqueous solution. Borosilicate glasses that contain an excess of either alkali cations or boron can exhibit similar behavior, i.e. become more susceptible to

hydrolysis, as was illustrated in Bunker et al.'s work [42]. Additionally, the authors showed that borosilicate glasses with a B:Na ratio over 2 tend to phase separate into silica-rich and boron-rich phases, with the borate phase being more vulnerable to water diffusion and hydrolysis. It is recalled however that B_2O_3 is added as a network former with the aim to rupture the –Si–O–Si– covalent bonds and facilitate the shaping and workability of the glass through reduction of its melting temperature. It becomes clear that simply improving the glass resistance to hydrolysis by changing its composition can lead to prohibitively high working temperatures. A trade-off exists therefore between durability and workability of the glass container.

In a recent review on glasses used for parenteral packaging, glass composition has been characterized as the "largest single influence on the chemical durability response" [1]. Evidently, other secondary factors also act upon the durability response, such as the manufacturing method, special treatments, annealing process, etc. However, they themselves affect the composition in their majority. In terms of composition, various proposals have been reported in the literature and industry to improved glass durability [43-46]. Corning Inc. has patented a boron-free glass composition [47], belonging formally to the family of aluminosilicate glasses. Instead of B_2O_3, increased amounts of alumina are used and workability of the glass is compensated by an increase of alkali, sodium and potassium oxides. Proprietary tests carried out on these vials showed low propensity for delamination [43]. Another example of increase in chemical durability through a change in composition was proposed for soda-lime-silica (SLS) glass, through exchange of Na_2O for K_2O, given that Na is prone to being preferentially leached [22]. The authors noted that an increase in Al_2O_3 content also significantly improves durability.

Certain improvements in terms of resistance to alteration can also be achieved through modification of the glass manufacturing process. In that context, SCHOTT AG is marketing the EVERIC™ glass vials, fabricated through a manufacturing process that aims to reduce delamination in delamination-critical areas, such as the vial shoulder and heel regions. The delamination-control is enabled through an improvement of the surface and compositional homogeneity of the internal glass vial surface (Fig. I.5).
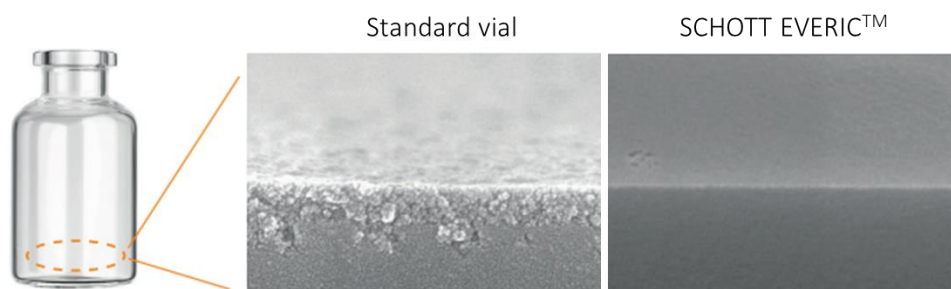
Fig. I.5. Scanning electron micrographs at the heel region of standard and SCHOTT EVERIC™ vials, after 4 h autoclaving. No scale information is provided by the company [48].

Although little information is shared, the company claims a chemical stability higher than in standard borosilicate glasses and advertises that their product complies with the USP <660> chapter, exhibiting high resistance to dissolution, low concentration of leached glass elements and prevention of a shift in the pH-value of the solution [38]. Similar technologies that aim to improve the resistance to delamination, either through modification of the glass composition, or through specialized manufacturing processes, are also encountered in a number of patents filed in recent years [49, 50].

I.1.6.2. Surface treatment

An alternative solution to reduce propensity for delamination is the surface treatment of glass containers. The previously described Type II pharmaceutical glass falls exactly in this category. Being made of soda-lime glass just like Type III glass, a surface treatment is applied on the internal surface of Type II vials, involving exposure to sulfate or fluoride containing compounds in the form of gas or powder [1]. In the case of gases, SO_2 and/or SO_3 gases are used to extract and deplete the internal glass surface of alkali and alkaline earth compounds. In the second case, ammonium sulfate $(NH_4)_2SO_4$ powder is added, serving the same purpose. Through this treatment, the extreme glass surface in contact with the aqueous solution is altered to contain lower concentrations of network modifiers, reducing the possibility of ion exchange reactions. For that reason, the resistance of Type II glass against aqueous alteration is generally assessed between that of soda-lime (Type III, lowest) and borosilicate glasses (Type I, highest).

I.1.6.3. Barrier coatings

As a matter of fact, the use of barrier coatings is attractive as it leaves room for using glass compositions that allow low melting temperatures and easier workability. In such cases, the burden of ensuring sustainable product performance falls on the barrier coating. Given that glass compositions with low concentrations in alkali and alkaline earth elements lead to lattices with improved hydrolytic resistance, various coatings based on oxides are being explored over the past years as alternatives for glass protection against delamination [51, 52]. Branching off to other sectors for a moment, AlO_x and SiO_x coatings have gathered attention as popular protective materials in the stainless steel, electronic devices and polymer industries, thanks to their low oxygen permeability and sodium diffusion [53, 54]. Their transparency also makes them attractive for pharmaceutical applications, since they enable the easy inspection of the contents. However, it must be underlined that, when intended for the packaging of pharmaceuticals, the barrier coating must fulfill certain functions. As a first rule, barrier coatings must exhibit a structure dense enough to withstand hydrolysis. Additionally, they must also demonstrate sufficient barrier properties, meaning

that the coating should reduce, or ideally block, the diffusion of elements from the glass towards the contained solution. Two recent theses have dealt with investigating this particular alternative by applying CVD coatings into glass vials. In 2015, Etchepare in his thesis studied the chemical durability of soda-lime glass vials after application of amorphous Al_2O_3 barrier coatings [55]. Following his work, Ponton investigated the chemical durability of soda-lime and borosilicate glass vials after application of amorphous SiO_2 barrier coatings [7]. The following sections will discuss these works briefly, before arriving at the barrier coatings proposed for the present thesis.

I.1.6.3.1. *Amorphous alumina coatings*

The work of Etchepare investigated the coating of the inner surface of soda-lime vials with amorphous Al_2O_3 (Fig. I.6), using direct liquid injection metal-organic chemical vapor deposition (DLI-MOCVD) [56]. The thermal and pressure ranges studied were 420-560°C and 5-730 Torr, respectively. The resistance to alteration of the produced Al_2O_3 barrier coatings was assessed in accordance with the USP <660> chapter [4]. The results showed a good barrier performance of the alumina layer, with only low concentrations of silicon, alkali and alkaline earth ions being released in the solution. However, a high amount of aluminum ions was probed. This indicated that, although the Al_2O_3 barrier coating was effective in reducing diffusion of network forming and modifying elements, it itself did not exhibit satisfactory hydrolytic resistance and eventually dissolved after contact with the aqueous solution. Therefore, merely presenting barrier properties is not sufficient. To ensure satisfactory performance, the barrier coating itself must also include covalent bonds strong enough to withstand aqueous hydrolysis. This translates to a requirement for denser structures.
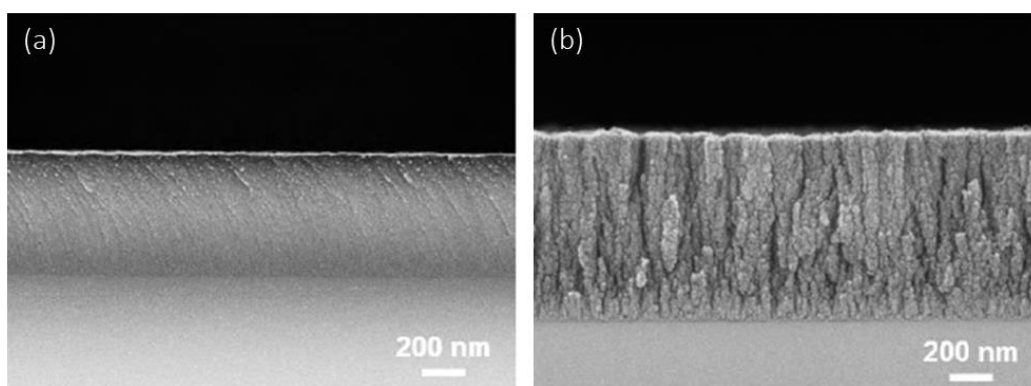
Fig. I.6. Cross-section SEM-FEG micrographs in backscattered electron mode of thin amorphous Al_2O_3 films, deposited at 520°C by MOCVD (a) and at 480°C by DLI-CVD (b) [55].

I.1.6.3.2. *Amorphous silica coatings*

Densification of the network in a barrier coating can be instigated through multiple methods. As a first example, Etchepare demonstrated how the deposition process can serve in that cause. In his thesis, alumina layers produced by classical MOCVD using a bubbler exhibited a denser and smoother microstructure compared to the more porous layers produced by DLI-MOCVD (Fig. I.6) [55]. Differences in composition were also noted, with the DLI-MOCVD coatings containing hydroxyl groups that impacted the hydrolytic resistance negatively. This brings us to the second point; namely the coating composition. Substitution of alumina by other oxides, such as amorphous silica, has been proposed as an alternative solution towards denser materials with lower alkali leaching.

In that context, Guanghui et al. [57] studied the diffusion of sodium through barrier layers of various oxides. The barrier coatings (SiO_2 and combinations of it with TiO_2, B_2O_3, ZrO_2 and/or P_2O_5) were produced via sol-gel method, utilizing a 1 h annealing post-treatment at 500°C. The lowest sodium diffusion was observed for the pure SiO_2 layer. In a similar study, Nagayama et al. [58] compared the barrier properties of pure, sol-gel deposited SiO_2 layers, with and without annealing at 500°C. After exposure of the coated SLS glass samples to an aqueous solution at 100°C for 24 h, the release of sodium ions from the underlying SLS glass was studied. It was found that the SiO_2 coated sample released approximately 4 times less sodium atoms compared to the uncoated glass sample. Moreover, when the SiO_2 coating was subjected to annealing, sodium release was reduced even further, measuring almost half that of the unannealed coating. The authors attributed this improvement in barrier property to a denser silica structure induced through the annealing step. The effect of the temperature was also reported by Yersak et al.[59], who studied the dissolution of atomic layer deposited (ALD) SiO_2 films intended as aqueous corrosion barriers. The authors measured an approximately 49 % reduction in dissolution rate by increasing the deposition temperatures from 150 to 300°C, attributing it to structural changes related to dehydrogenation and densification of the network.

The above-described densification was further confirmed through Ponton's work [7]. Using tetraethylorthosilicate (TEOS) and O_2 gas mixtures in a thermal CVD process, SiO_2 deposition at 350-570°C and 730 Torr was investigated, with and without annealing. The SiO_2 barrier coatings deposited at 550°C demonstrated an improvement factor of 72 % compared to uncoated vials after subjection to aging tests according to the USP <660> chapter, meaning that 72 % less extractables were probed in the corrosion solution for the coated vials. The respective improvement factor, in regards to uncoated vials, for coatings deposited at 400°C on the other hand measured only around 10 %. The improvement of the barrier performance at higher deposition temperatures, or after an annealing post-treatment, is attributed to the denser network of the coating as a result of the operating conditions. In their study, Klause et al. [60] underlined this link further. Through investigation of the hydrolytic resistance of SiO_2 barrier coatings

deposited by PICVD, the authors pointed out the strong correlation between operating conditions and film microstructure. SiO_2 films with more homogeneous, untextured microstructures and fewer nanoporosities exhibit stronger cross-linking, which maintains the functionality of the coating for longer durations.

It is noted that the thermal CVD SiO_2 coatings produced by Ponton et al., as well as the aforementioned PICVD SiO_2 coatings used in the Type I Plus® vial product marketed by SCHOTT AG, were subjected to the more aggressive tests recommended in the USP <1660> chapter [5, 7]. Unfortunately, both failed to respond satisfactorily to the citric acid test of USP <1660>. Although diffusion of elements such as sodium and boron was successfully reduced, amounts of silicon, proportional to the deposited mass of the SiO_2 coatings, were measured in the solution, signifying that the silica network itself cannot withstand this particular corrosion test. Again, a SiO_2 network densification induced through optimization of any of the operating conditions is, in this case, not sufficient.

I.1.6.4. Densification through compositional and structural changes

Inspired by the works of Etchepare and Ponton, the current project was conceptualized, exploring how a further densification of a SiO_2 barrier film can be induced through a change in composition. Nocun et al. [54] reported that the addition of 0.08 mol.% Al in a SiO_2-Al_2O_3 barrier coating effectively reduces sodium diffusion. More examples can be found in literature on microelectronic devices, where sodium diffusion is undesired since it can cause device degradation [61]. Barrier coatings from silicon nitride (Si_3N_4, oftentimes noted as *SiN$_x$* when sub-stoichiometric) and oxynitride (SiO_xN_y) are frequently used to combat this problem, deposited as alkali-barrier layers on top of soda-lime glass or other surfaces [62-66]. Palm et al. [62] illustrated that Si_3N_4 and SiO_xN_y barriers effectively prevent sodium diffusion from a glass substrate towards molybdenum (Mo) films. According to their study, both materials performed better than Al_2O_3, with the Si_3N_4 barrier exhibiting more effective diffusion reduction of Na than SiO_xN_y, as was revealed through inductively coupled plasma mass spectrometry (ICP-MS) measurements (Fig. I.7a). Aubry et al. [67] also noted the effective diffusion barrier properties of silicon nitride, measuring only traces of diffused alkali elements in a TiO_2/SiN_x/glass-substrate system. The authors also compared the results to a TiO_2/SiO_2/glass-substrate system, noting that the SiO_2 barrier layer in their study was relatively permeable to sodium diffusion and underperformed by a factor of 3 in comparison to the SiN_x barrier layer. Satisfactory oxidation resistance [68], etching resistance [69] and boron diffusion [70], Cu diffusion [71] or gas [72] barrier performance of SiN_x and SiO_xN_y films have also been documented. In regards to etching resistance, Gumpher et al. [73] noted that incorporation of around 10 at.% carbon in SiN_x films markedly improves etching response through an improved material network structure that they illustrasted as shown in Fig.

I.7b and c, while Lee and Choa [74] claimed that their PECVD silicon carbonitride (SiC_xN_y) films exhibited excellent water diffusion barrier.
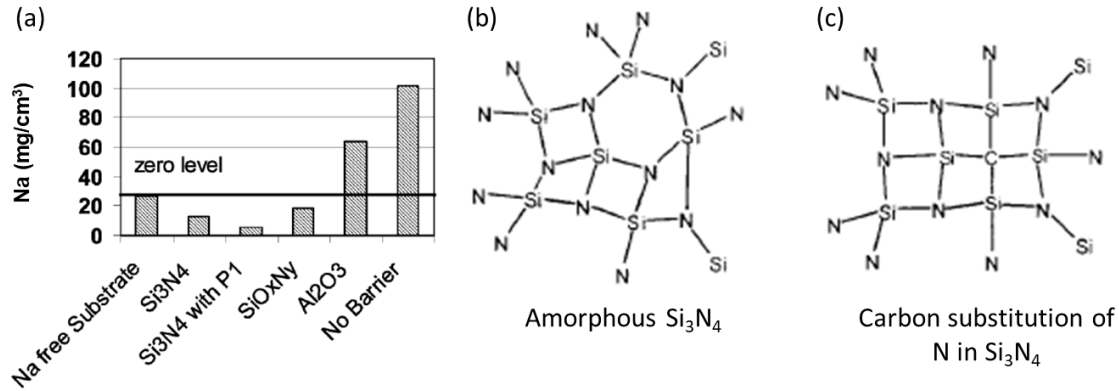
Fig. I.7. ICP-MS measurements of Na in Mo films deposited on different diffusion barriers in Mo-film/barrier/glass-substrate systems. ICP-MS was carried out after chemical dissolution of the deposited Mo film in nitric acid. Zero level refers to probing of Na as a result of handling and processing contamination. P1 refers to a patterning process of the Mo film using pulsed laser (a) [62]. Proposed densification of silicon nitride matrix (b) through nitrogen substitution by carbon (c) [73].

Based on the above, a partial replacement of the divalent O^{2-} anions in SiO_2 coatings by trivalent N^{3-}, or even tetravalent carbidic C^{4-} ones, is proposed. The resulting single-phase silicon oxynitride (SiO_xN_y) or silicon oxycarbide (SiO_xC_y) networks are characterized by the usual –Si–O–Si– bridges encountered in silica, this time however with some Si atoms of the tetrahedra being bonded to at least one nitrogen or carbon atoms, respectively. Through this, the short range disorder [75], cross-linking and density [76] of the network are increased compared to pure SiO_2, which can effectively lead to an improved diffusion barrier thanks to the enhanced coordination. Similarly, the carbon atoms in SiO_xC_y films are in turn tetrahedrally bonded to other silicon atoms [77, 78], exhibiting thus greater chemical durability in both alkaline and hydrofluoric solutions [79], as well as improved mechanical properties and thermal stability [80, 81]. However, if protective coatings inside pharmaceutical vials are to be produced under the context of eventual industrial implementation, certain constrictions need to be respected regarding the selection of the deposition method and process parameters. To identify these specifications, the fabrication process of vials intended for pharmaceutical use is explained briefly below.

The pharmaceutical industry utilizes mainly two routes for production of vials. The first one is based on converting a container from glass tubing. More specifically, a glass tube is repeatedly heated using

flames, as shown in Fig. I.8, while mechanical tools reshape it into the dimensions of the final product (vials, cartridges and ampoules, to name a few, Fig. I.8b). This particular technology established a significant advance in the manufacturing of pharmaceutical glass back at the start of the 19th century and is referred to as *glass converting technology* or *glass tubing*. The second and more traditional route, which is the primary focus for this thesis, involves the molding of vials from a drop of molten glass. As a matter of fact, molded containers are more popular for certain applications compared to glass tubing, because their thicker walls provide improved resistance against mechanical damage [1]. The absence of repeated heating and cooling steps also renders them less prone to delamination [1].
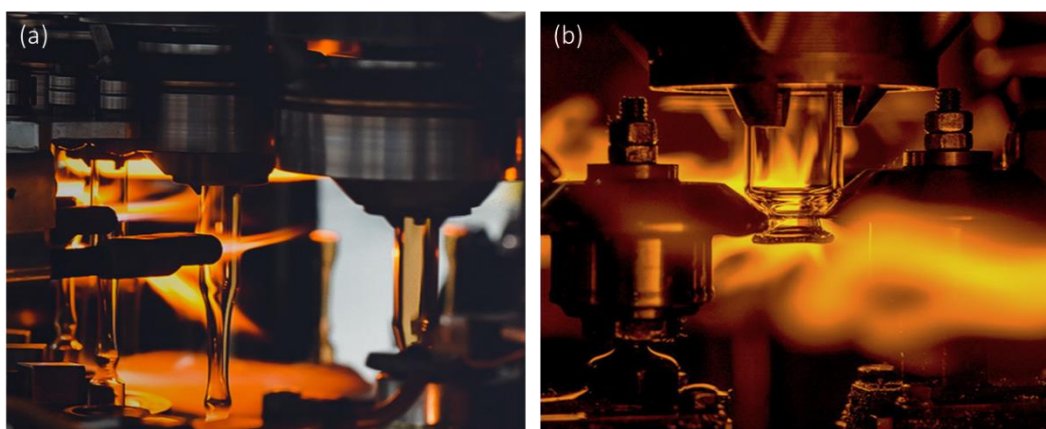
Fig. I.8. Heating of ampoules by flames (a) and shaping pharmaceutical vials (b) during glass tubing [82].

For the molding of glass containers, the molten glass drops are distributed to the forming machines at temperatures close to 1000°C. For pharmaceutical vials, the drop is shaped in two steps, the first one involving pressing or blowing with compressed air. At the second step, the shape of the container is finalized by blowing compressed air only. Both steps present a strong temperature gradient from 1000°C down to approximately 700°C, which leads to buildup of stress in the material. For this reason, after exiting the mold, the vial is transported on a conveyor belt towards an annealing arch, where it undergoes an annealing step aiming to release the accumulated stresses. Surface treatments, such as the application of barrier properties, can take place before and/or after this annealing step.

Based on the above, it becomes apparent that the application of a barrier coating must, ideally, respect two specific constraints dictated by this particular production line process. The first one is the deposition at atmospheric pressure, which is required in order to comply with the production line (i.e. open air conveyor belt). Due to this requirement, plasma enhanced CVD (PECVD) processes are excluded, as

they additionally lead to higher operational costs. Moreover, films deposited by plasma processes can exhibit increased hydrogen incorporation and potential film damage occurring from ion bombardment [83], which can be detrimental to the barrier performance. Silica-based films are also deposited using atomic layer deposition (ALD) [84-86]. However, ALD is non-compatible with an on-line coating process due to low deposition rates and the requirement for multiple deposition cycles. Vial manufacturing lines have high throughput, sometimes even in the order of a dozen vials per second. This makes high film deposition rates mandatory to ensure sufficient film thickness during a rapid vial-by-vial treatment. For the above reasons, the deposition of barrier coatings via an atmospheric pressure thermal CVD process is selected. Deposition rates observed by thermal CVD are more favorable in comparison to ALD. At the same time, thermal CVD is preferable over PECVD processes as more cost-effective and more easily implementable on a conveyor-based production line. Thermal CVD processes offer additional advantages in regards to more conformal films, with low hydrogen incorporation and denser structure.

The second constraint relates to the temperature window within which the barrier coating can be applied. Surface treatments need to be compatible with the operating margins of the annealing step, so as to avoid further accumulated stresses. More importantly though, the deposition temperature of a barrier coating shall not exceed the glass transition temperature, T_g, of the vial container, in order to not jeopardize its structural integrity. For Type I vials specifically, T_g is ca. 570°C. Addressing this second constraint, namely the specified temperature window, proves to be challenging. The majority of SiO_xN_y and SiO_xC_y films studied in the literature that fit these temperature margins are produced through plasma enhanced CVD (PECVD) processes under vacuum [87-89]. On the contrary, when no plasma activation is used, temperatures higher than 700°C, at low-to-atmospheric pressures, are reported [77, 90-92].

The deposition of SiO_xN_y and SiO_xC_y films at temperatures below <600°C by thermal CVD is rarely reported in the literature. Specifically, deposition of silicon carbide (SiC), and by extension SiO_xC_y films, by thermal CVD at low or atmospheric pressures is usually carried out at temperatures between 750°C and over 1000°C [93-95], well exceeding the upper temperature limit prescribed by the glass substrate and its manufacturing process. As a matter of fact, incorporation of carbon is possible at temperatures below 600°C, however it is mostly encountered in organic ($-CH_3$) form, compared to the desired $-Si-C-Si-$ carbidic arrangement. Incorporation of hydrocarbon terminal bonds ($Si-CH_3$) interferes with the formation of dense structures such as Si-C-Si and Si-N-Si, leading to increased porosity [74]. For these reasons, and given that the temperatures required for SiO_xC_y are prohibitive, the present thesis focuses mainly on the production of SiO_2 and SiO_xN_y films by thermal CVD. The lack of plasma activation leaves room for addressing the thermal limitation only through the reacting chemistry. In the sections that follow, a comprehensive literature review on the various precursors and gas mixtures utilized for the deposition of

SiO_2 and SiO_xN_y will be discussed, with occasional references to carbon-containing systems (SiO_xC_y, SiC_x, SiC_xN_y). Since the literature for their deposition at low temperatures by thermal CVD is scarce, chemistries used in other deposition processes are also examined. From the collected information, a strategy for the selection of the most suitable precursor molecules and gas chemistries is formulated.

I.2. Gas mixtures and precursors for silica-based materials by CVD processes

I.2.1. Conventional chemistries for SiO_x and SiO_xN_y films by CVD processes

The deposition of SiO_2 and SiO_xN_y logically requires the involvement of reactants that provide the elements of interest, namely Si, O and N. Starting from SiO_2 films, the conventional chemistry for its deposition back in the 1970s-1990s was based on gas mixtures utilizing silanes (SiH_4, Si_2H_6) or chlorosilanes (SiH_2Cl_2, Si_2Cl_6) as the silicon-providing precursor [96-98]. Beyond the 1990s however, tetraethylorthosilicate ($C_8H_{20}O_4Si$, TEOS) has substituted most other chemistries. The popularity of this precursor lies in its physico-chemical properties, ease of handling, cost-effectiveness and fewer safety concerns. In recent years, emergence of other precursors such as hexamethyldisiloxane ($C_6H_{18}OSi_2$, HMDSo) [99], hexamethyldisilazane ($C_6H_{19}NSi_2$, HMDSz) [100], 3-aminopropylmethyl diethoxysilane ($C_8H_{21}NO_2Si$, APMDES) [13], bis(tertiary-butylamino)silane ($C_8H_{22}N_2Si$, BTBAS) [101], and bis-dimethylaminosilane ($C_4H_{14}N_2Si$, BDMAS) or trisdimethylaminosilane ($C_6H_{19}N_3Si$, TDMAS) [102] has been reported. Despite the vast choice, TEOS still remains a popular silicon-provider for SiO_2 barrier or passivation films to this day [103, 104]. This preference shown for the TEOS precursor over silanes or methyl-containing silanes can be traced back to the presence of ethoxy ligands in the TEOS molecule, the oxidation of which is facile and results in films with lower hydrogen and carbon impurities. Many of the above listed precursors are also utilized as silicon-providers for the deposition of SiN_x, SiC_x SiO_xN_y, and SiC_xN_y films, alongside hexamethyldisilane ($C_6H_{18}Si_2$, HMDS) [94], (dimethylamino)dimethylsilane ($C_4H_{13}NSi$, DMADMS) [105], trisilylamine (H_9NSi_3, TSA) [106] and various derivatives.

Unlike the pyrolysis of such silicon precursors, executed for instance between 700 and 900°C for TEOS [107], the reduction in deposition temperature for thermal CVD processes and the incorporation of oxygen is carried out by adding an oxidant in the gas phase. The most commonly used oxidizing source gases are O_2 [108], ozone (O_3) [109], nitrous oxide (N_2O) [103, 110] and CO_2 [66, 96]. Among them, O_3 has been extensively used for the deposition of SiO_2 films in the microelectronics field [111-113]. It enables deposition at temperatures as low as 30°C [114], offering a significant decrease in thermal budget, elevated

deposition rates and conformal, smooth films [115]. It should be noted however, that a strong generation of particles through gas-phase nucleation can take place at temperatures below 300°C, as a result of the formation of short-lived radical species and predominant gas phase reactions [114]. This can be detrimental to the morphological homogeneity and quality of the films. At higher temperatures on the other hand (above 400°C), a strong inhibition of the deposition rate can occur, attributed to gas phase reactions between by-products from TEOS reaction with O_3 [116]. Operation with O_3 as the oxidant requires thus optimization of the process parameters, but its ability to significantly reduce the deposition temperature remains attractive. Due to this, O_3 was also considered as a candidate to aid in reducing the deposition temperature of SiO_xN_y and SiO_xC_y films below 600°C at the beginning of the ANR HEALTHYGLASS project and this thesis. However, by progressing in the understanding of the decomposition chemistry aspects of potential precursors, it became clear that O_3 would not be a solution. Its use as an oxidant in SiO_xN_y and SiO_xC_y deposition processes risks favoring the deposition of SiO_2, since Si-C and Si-N bonds are readily oxidized under sufficient monoatomic oxygen concentrations [113]. Monoatomic oxygen is naturally produced through the thermal decomposition of O_3 [117], ultimately meaning that this oxidant can have a negative, if not prohibitive, effect on nitrogen incorporation and distribution in the films [118]. For the above reasons, other oxidants should be preferred when deposition of SiO_xN_y is desired.

Incorporation of nitrogen and carbon is conventionally carried out by addition of ammonia (NH_3), and methane (CH_4) or ethylene (C_2H_4) gases, respectively [66, 119, 120]. However, the initiation of SiO_xN_y or SiO_xC_y deposition by thermal CVD depends strongly on the dissociation and decomposition potential of the silicon precursor. Therefore, the Si-providing molecule should be carefully selected if thermal limitations are to be respected. As a general rule, the reactivity (i.e. dissociation) of the precursor should be as high as possible. Based on information gathered from the literature (not limited to thermal CVD only), the next section will cover the strategy of selecting the appropriate precursor for SiO_xN_y (and potentially SiO_xC_y) deposition, able to comply with the thermal restrictions required in this thesis.

I.2.2. *Reactive SiO_xN_y chemistries*

Incorporation of N and C in silica-based films requires high energies to overcome the activation steps for deposition of the materials in question. Conventionally, plasma activation is used for that purpose. For example, Guruvenket et al. [121] performed SiC_xN_y deposition by atmospheric pressure PECVD (AP-PECVD) at 25-450°C. They used hexamethyldisilazane ((CH_3)$_3$Si)$_2$N, HMDSz) and tetramethyldisilazane ((CH_3)$_2$SiH)$_2$NH, TMDS) precursors as the silicon providers and N_2 plasma as the nitrogen source. The authors reported that film formation occurred if, and only if, nitrogen plasma was present in the deposition zone, arguing that, at this specific thermal range, their AP-PECVD process is dependent on radical-initiated

reactions. In absence of plasma, the two precursors failed to lead to deposition, even if the temperature was raised to 450°C. Similarly, Aoki et al. [122] performed deposition of SiN_x films from trisdimethylaminosilane (($Me_2N)_3SiH$, TDMAS) using remote plasma CVD (RP-CVD) at 30-600°C. The authors noted that no film formation by thermal activation occurred up to 500°C. It was concluded that, for temperatures below 500°C, hydrogen radicals produced by H_2 plasma activation were mandatory in order to initiate the decomposition of the monomer and lead to SiN_x production. Their results further illustrate the requirement for radical activation if deposition is to be performed at low temperatures.

However, for a thermal CVD process, which obviously does not deploy plasma, the activation of the deposition mechanism through radical reactions becomes a challenge. Dissociation and decomposition of the precursor in this case can be facilitated by increasing the supplied energy by increase of the temperature. However, the constraints of the project discourage elevated temperatures, since they will prohibit deposition on heat sensitive substrates. It becomes therefore mandatory to place great attention on the utilized Si-provider and O, N (and C) source gases. Table I.2 presents an overview of various precursors used for the deposition of nitrogen (and/or carbon) containing Si-based materials. The entries listed in Table I.2 are used as the basis for developing a checklist that will aid the above goal. It is recalled once again that the limited information found in the literature of thermal CVD made it mandatory to seek additional information on potential chemistries in literature dealing with plasma-activated processes.

Firstly, among the thermal CVD pathways (APCVD, LPCVD) listed in Table I.2, deposition temperatures spanning between 500 and over 900°C are noted. This variety is affected by various factors, but primarily by the choice of reagents. One of the most important elements is the chemical structure of the precursors, also noted in Table I.2. In their study, Wrobel et al. [123] used various silane-derivative precursors in RP-CVD and characterized the C–H, C–C, Si–C, Si–N, C–N and N–H bonds in the starting molecule as non-reactive. The authors claimed that only Si–H or Si–Si bonds play a vital role in the reactivity of the precursor. In their particular deposition system, initiation of film growth was dependent on elementary reactions between atomic hydrogen and the hydrosilyl (Si–H) or disilane (Si–Si) units in the precursors, according to Reaction I.5 and 6 [123]:

$$H^{\bullet} + HSi{-} \longrightarrow {-}Si^{\bullet} + H_2 \qquad\qquad \text{Reaction I.5}$$

$$H^{\bullet} + {-}Si{-}Si{-} \longrightarrow {-}Si^{\bullet} + HSi{-} \qquad\qquad \text{Reaction I.6}$$
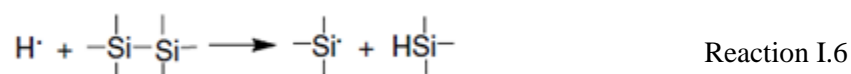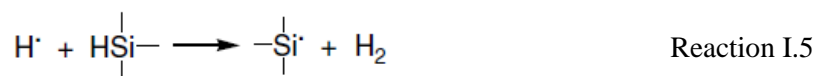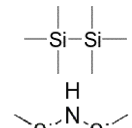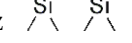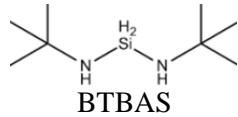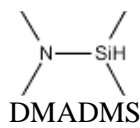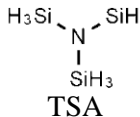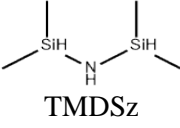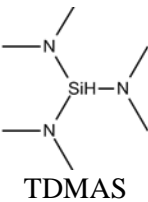
Table I.2. Overview of various precursors and source gases used for the deposition of nitrogen- (and/or carbon-) containing silica-based films from CVD processes.

Silane precursors	Film	Reagents	Process	Thermal range	Application domain	Ref.
HMDS HMDSz	SiC_x, SiC_xN_y	-	LPCVD	700-1000°C	N/S[a)]	[124]
HMDSz	SiO_xN_y	NH_3, O_2	APCVD	760-820°C	Photonic wave-guide devices	[119]
HMDSz	SiN_x	NH_3	APCVD	775-850°C	Photonics	[125]
BTBAS	SiN_x	NH_3	LPCVD	600-675 °C	Spacer and etch stop applications	[70]
Si_2H_6	SiN_x	NH_3	LPCVD	555-750°C	Electronics	[69]
DMADMS	SiC_xN_y	H_2 plasma	RP-CVD	30-400°C, 30°C	Coatings for tribological applications, N/S	[105], [123]
TSA	SiN_x	H_2 plasma	RP-ALD	150-350°C	Charge trap flash (CTF) memory applications	[126]
TMDSz	SiC_xN_y	H_2 plasma, He and N_2 plasma	RP-CVD, AP-PECVD	30°C, 25-400°C	N/S, antireflective coatings	[123], [121]
TDMAS	SiN_x, SiC_xN_y	H_2 and N_2 plasma, H_2 plasma	RP-CVD	25-600°C, 30°C	N/S	[122], [123]

[a)]N/S: "Not specified"

The dissociation of the Si–H and Si–Si bonds towards the production of Si-centered radicals plays an important role in rendering the precursor molecule more reactive according to the authors. Wrobel et al. also noted that the reactivity of the precursor increases markedly with an increasing number of Si–H units in the molecule and demonstrated that SiC_xN_y film growth rate from 1,1,3,3-tetramethyldisilazane $((Me_2HSi)_2NH$, TMDSz) was double compared to films grown from (dimethylamino)dimethylsilane $((Me_2N)SiHMe_2$, DMADMS) due to that exact reason. Similar to the above, Guruvenket et al. [121] showed that deposition from TMDSz leads to higher deposition rates compared to hexamethyldisilazane (HMDSz), attributed to the presence of Si–H bonds in the molecular structure of the former and absence in the latter. This increased reactivity can be the result of dissociation of the two Si–H bonds in TDMSz, which can convert it into a biradical product through Reaction I.7. This biradical intermediate can readily fragment to 1,1-dimethylsilanimine and dimethylsililene (Reaction I.8), facilitating nitride-related film formation [123].

$$2H^{\cdot} \ + \ Me_2HSiNHSiHMe_2 \ \longrightarrow \ Me_2\overset{\cdot}{Si}NHSi\overset{\cdot}{Me_2} \ + \ 2H_2 \qquad \text{Reaction I.7}$$

$$Me_2\overset{\cdot}{Si}NHSi\overset{\cdot}{Me_2} \ \longrightarrow \ Me_2Si{=}NH \ + \ Me_2Si{:} \qquad \text{Reaction I.8}$$
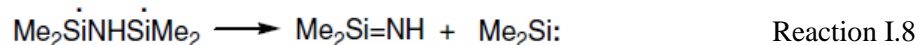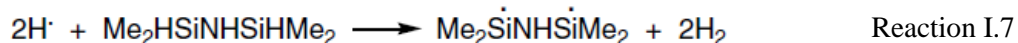
The claim on the importance of Si–H bonds was also previously confirmed by Blaszczyk-Lezak et al. [105], by performing RP-CVD deposition using (dimethylamino)dimethylsilane $(Me_2N)SiHMe_2$, DMADMS) and (dimethylamino)trimethylsilane $((Me_2N)SiMe_3$, DMATMS). The authors reported that DMATMS was unreactive and no film was formed at 30°C, in contrast to DMADMS, which features a hydrosilyl unit and could lead to deposition.

In light of the above, by inspecting Table I.2 once more, it is not surprising that HMDSz, a precursor lacking hydrosilyl units, is shown to form nitrogen-containing films (SiN_x, SiO_xN_y or SiC_xN_y) only at higher temperatures. In thermal CVD, the lowest temperatures reported for deposition of such films from this precursor have been around 750-770°C and oftentimes exceed 800°C [119, 124, 125, 127]. Compared to HMDSz, precursors featuring multiple Si-H units (e.g. disilane Si_2H_6, bis(t-butylamino)silane $[NH(C_4H_9)]_2SiH_2$, BTBAS) are reported to produce films at lower temperatures by thermal CVD processes [69, 70]. Interestingly, although silane (SiH_4) was reported to lead to deposition of silicon-rich SiN_x at around 570°C by thermal CVD [128], only temperatures above 700°C have been documented the literature for SiO_xN_y [129, 130]. Additionally, silane is a toxic explosive precursor and poses compatibility issues in regards to an implementation on the on-line vial production line. For that reason, the choice of different, and if possible less toxic or explosive, silicon-providing molecules is encouraged.

In the case of methylaminosilane precursors, other factors impacting the reactivity is the number of (di)methylamino substituents at the silicon atom. For instance, reactivity and growth rate is decreased for tris(dimethylamino)silane ($(Me_2N)_3SiH$, TDMAS) in comparison to DMADMS ($(Me_2N)SiHMe_2$). This has been explained as a result of the screening of the Si–H bond by the additional dimethylamino substituents [123]. In contrast, when the hydrosilyl unit is more easily accessible, conversion to radical intermediates can take place more easily, and thus precursor reactivity is increased. Regarding the size of alkyl substituents at the silicon atom, their increase from methyl to ethyl affects the reactivity of the precursors only negligibly. Preference could be given to ethyl substituents, as they have been reported to be more susceptible to thermal decomposition and facilitate the elimination of organic moieties from the films [131].

Another interesting aspect to consider is the presence of a second amine, either integrated in the molecule as an alkylamine substituent (though further away from the Si–H bond), or used in the source gas as an additional reactant. Multiple patents mention the use of methylamine, dimethylamine, trimethylamine, diethylamine and combinations thereof as a potential nitrogen sources [68, 132]. In some cases, addition of an amine gas was shown to promote film formation, increasing the deposition rate of SiN_x by thermal CVD up to 10 times [68]. According to Mittov et al. [118], amines are characterized as "carrier killers": upon decomposition, they recombine with organic radical species in the gas phase, thereby suppressing carbon contamination in the film. It is believed that their addition reduces the rate of decomposition of the source precursor and results in improved conformality [132]. However, the reason as to why film formation is promoted still remains unclear.

I.2.3. Selection of appropriate chemistries for SiO_xN_y deposition

I.2.3.1. Precursor selection

So far, it has been clearly demonstrated that the presence of multiple Si–H units is favorable for higher precursor reactivity, facilitating the deposition of nitride materials at lower temperatures compared to precursors lacking Si–H units. Another important point to keep in mind regarding the selection of a suitable precursor for SiO_xN_y by thermal CVD is the presence of Si–O bonds. Such bonds can impede the incorporation of nitrogen, as reported by Park et al. [13] who studied the deposition of SiO_2 from 3-aminopropylmethyldiethoxysilane ($CH_3Si(OC_2H_5)_2(CH_2)_3NH_2$, APMDES) at 650°C by thermal CVD. The authors noted that no nitrogen was detected in the films despite the high temperature, which is potentially attributed to the presence of Si–O bonds in the starting molecule. In the same sense, Vamvakas et al. [133] performed thermodynamic calculations for the thermal CVD of SiO_xN_y from TEOS mixtures, concluding

that incorporation of nitrogen is not possible at temperatures below 830°C or 930°C, in presence of NH_3 or N_2O gas, respectively, the biggest hindrance being the four oxygen atoms in the precursor molecule. It is therefore suggested that the inclusion of Si–O bonds should be avoided when the production of a nitrogen-containing silica-based film is desired at moderately low temperatures. By contrast, the innate presence of a Si–N bond in the starting precursor could prove more favorable.

I.2.3.2. Selection of reagents

The vast majority of thermal CVD processes utilizes NH_3 as the nitrogen source. Despite that, it is noteworthy to point out that many of the precursors used for the deposition of SiN_x, SiO_xN_y or SiC_xN_y materials contain Si-N bonds (Table I.2). This raises a question regarding the origin of the N atom in nitride-type films. Aoki et al. [122] performed deposition of SiN_x by RP-CVD at 25-600°C. Although the utilized tris(dimethylamino)silane (($Me_2N)_3SiH$), TDMAS) precursor included nitrogen atoms, the authors argued that N incorporation originated from the N_2 plasma instead. Ray at al. [134] on the other hand noted the incorporation of nitrogen in SiC_xN_y films from pure HMDSz by microwave plasma enhanced CVD, with and without the use of NH_3. At high enough temperatures (750-900°C), Kleps et al. [124] also reported the deposition of SiC_xN_y films by LPCVD without addition of NH_3. Due to the distinct gas phase reactions taking place in thermal and plasma process, it is difficult to arrive at concrete conclusions.

To elucidate the origin of the nitrogen in the films, Prybyla et al. [135] carried out isotopic labelling experiments. More specifically, the authors studied the deposition of titanium nitride (TiN_x) from tetrakis(dimethylamino)titanium ($Ti(NMe_2)_4$) in a CVD system using $^{15}NH_3$ and Rutherford backscattering spectrometry (RBS) to assay the incorporation of ^{14}N and ^{15}N in the produced solid film. The isotopic substitution experiments revealed that the nitrogen in the TiN_x films originated from ammonia and not from the $Ti(NMe_2)_4$ precursor. The authors described a transamination reaction that takes place between the precursor and ammonia, which produces a $Ti(NMe_2)_3^{15}NH_2$ intermediate and dimethylamine ($NHMe_2$) (Reaction I. 9). Under high NH_3 flows, multiple transamination reactions can occur, eventually cleaving all dimethylamino-ligands of the precursor, removing its innate nitrogen atoms and replacing them with those supplied by ammonia. For low ammonia flows the authors noted that ^{14}N, i.e. nitrogen originating from the precursor molecule, was still detected in the film. It was however accompanied by high levels of organic carbon, leading the authors to conclude that any nitrogen that originates from the dimethylamino-type precursor carries some carbon along with it. Isotopic labelling of the hydrogen atoms (deuterated ammonia, ND_3) on the other hand revealed that the nitrogen-bound hydrogen in the gaseous dimethylamine by-product

is derived exclusively from ammonia [136], further confirming the transamination reaction (Reaction I. 9). A similar reaction pathway is expected when titanium is replaced by silicon in the precursor molecule.

$$Ti(NMe_2)_4 + {}^{15}NH_3 \text{ (or } ND_3) \rightarrow Ti(NMe_2){}^{15}NH_2 + NHMe_2 \text{ (or } NDMe_2) \qquad \text{Reaction I. 9}$$

Based on the above information, one can conclude that the incorporated nitrogen can originate from precursor and NH_3 alike. Distribution across one origin over the other depends on the deposition process, the applied process parameters (temperature, NH_3:precursor ratio), as well as the structure of the precursor (centered around a Si atom with –N–Si–N– sequence, or centered around a N atom with –Si–N–Si– sequence). All things considered, the presence of nitrogen in the starting molecule could potentially favor the deposition of nitrogen-rich films, however at the expense of organic carbon contamination in cases where the nitrogen is included as a dimethylamino substituent in the precursor molecule.

I.2.3.3. Summarized strategy: checklist for selection of precursor and reacting chemistry

In summary, the information gathered from the literature suggests consideration of the following points when selecting precursors and chemistries for deposition of nitrogen containing films at moderate temperatures by thermal CVD:

- Presence of (ideally multiple) Si–H bonds in the precursor molecule enhances the reactivity of the precursor, decreasing the minimum temperature required for film formation as well as increasing the deposition rate;
- Presence of Si–O bond(s) in the precursor might impede the incorporation of nitrogen into the film;
- Presence of Si–C bond(s) should be avoided if carbon-free films are desired, since this bond is strong and cannot be effectively broken by hydrogen radicals. It can be however cleaved by NH_3;
- Presence of Si–N bond(s) in the precursor molecule can be favorable for nitride deposition, but might result in carbon contamination if organic ligands are linked to the nitrogen atom;
- When NH_3 is a co-reactant, carbon impurities can be reduced;
- Oxidants (O_3, N_2O) that result in the formation of monoatomic oxygen radicals should be avoided as they can impede nitrogen incorporation;
- Additional amine compounds, integrated in the precursor molecule or supplied as additional source gases could potentially augment nitrogen incorporation and/or deposition rate.

Given all that has been presented so far, deposition of SiO_2 is carried out in this work based on TEOS-O_2/O_3 chemical pathways. TEOS is selected as the Si-provider based on previously listed advantages such as ease of handling and low concerns regarding safety. Moreover, this precursor leads to deposition of high-quality films and the multiple Si–O bonds in its structure are favorable for SiO_2 deposition with low carbon impurities. The choice of an O_2/O_3 gas mixture as the oxidant is based on taking advantage of the high deposition rate and low temperatures that can be achieved thanks to the reactivity of O_3. Moreover, its dilution in O_2 could help minimize the occurrence of powdering phenomena. Experiments utilizing HMDSz, a precursor that contains one nitrogen atom and six Si–C bonds, is performed to investigate the potential for incorporation of C and/or N at moderate temperatures in presence of O_3. Lastly, the production of SiO_xN_y films is undertaken based on two different molecules; tris(dimethylsilyl)amine (N(SiHMe$_2$)$_3$, TDMSA) and a trisilylamine derivative (N(SiH$_x$)$_x$+alkylamine, TSAR). The latter of the two is a proprietary molecule developed and provided by Air Liquide. Both compounds have been chosen based on the presence of Si–N and multiple Si–H bonds, with the aim to carry out deposition at the lowest temperatures possible. Ozone-free O_2 gas at minimal flow rates is used as the oxidant for these experiments to facilitate incorporation of nitrogen. Lastly, NH_3 gas is also tested in selected cases as nitrogen source. The chemical structures and physico-chemical properties of the utilized precursors are detailed in Chapter II.

I.3. The CVD process: principles and simulation

Multiple processes for production of barrier coatings have been mentioned so far, with chemical vapor deposition (CVD) being at the forefront. Given the fact that the present work deals with this exact deposition method, proper understanding of the principles governing the CVD process is mandatory.

I.3.1. Basic principles of chemical vapor deposition

One can summarize the process of chemical vapor deposition as the conversion of reactive gases into a solid layer on the surface of a heated substrate. In more detail, the substrate can be heated directly (cold-wall CVD) or through thermal transfer from the heated walls of the reactor (hot-wall CVD). Fig. I.9 shows a schematic diagram illustrating the various stages and reactions taking place during CVD [137]. First, vapors of the precursor molecule, containing the constituent element(s) of the deposited material and found initially either in solid, liquid, or gaseous state, are transported in the reaction chamber by an inert carrier gas through convection and diffusion phenomena (1). Film formation is preceded by chemical

reactions that take place either via thermal activation (thermal CVD), plasma assistance (PECVD, PICVD, RP-CVD), radiation (Photo-CVD) or catalysts (Cat-CVD), to name a few. When being provided the required energy, the precursor can participate in homogeneous reactions in the gas phase towards the production of new species (2) or diffuse towards the surface of the substrate (3) and adsorb on available surface sites (4). The species produced previously in the gas phase from the precursor molecule can also partake in such steps. Moreover, when these species include the constituent element, they are named intermediate species or simply "intermediates". After adsorption on the solid surface, precursor and intermediates can diffuse on the surface before reacting towards film formation (5) in so-called heterogeneous reactions, based on nucleation and growth phenomena. During heterogeneous reactions, the formed gaseous by-products desorb from the surface (6) and diffuse towards the gas phase (7) [138].
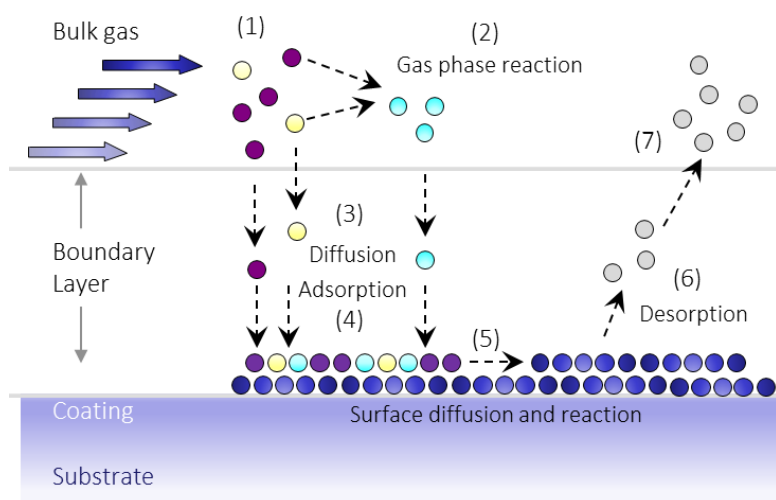
Fig. I.9. Schematic diagram of the various steps that can occur during a CVD process.

A competition exists between the homogeneous and heterogeneous reactions. This competition depends on multiple factors, such as the precursor molecule, the reactants used in the inlet gas composition, the operating conditions, the local temperature, the particular reaction kinetics, as well as the characteristics (i.e. geometry) of the solid surface on which deposition is taking place and the overall design of the reaction chamber. Competitive phenomena can lead to the consumption of the film-forming species in reactions other than the surface reactions that lead to film formation, influencing therefore the rate at which the film is produced. In the case of O_3 chemistries for the deposition of SiO_2, such reactions have occasionally been referred to as *parasitic type reactions*, since they favor the production of powder particulates in the gas phase instead of solid SiO_2 film [114, 139].

I.3.2. *The kinetic regimes*

In a CVD process, the deposition rate is generally controlled by the so-called rate-liming step, which can differ according to the kinetic regime, as is explained below. Fig. I.10 illustrates the logarithm of an arbitrary deposition rate as a function of the reciprocal of an arbitrary deposition temperature range. Three distinct operating regimes are identified. At low temperatures (Regime I), the rate-limiting step is tied to surface reactions. In this regime, noted *surface-limited regime*, the supply of material through diffusion towards the surface is greater than its consumption on the same. An increase in the local concentration of the film-forming species has therefore no impact on the rate of deposition of the thin film in this regime and the deposition rate is controlled only by the temperature of the surface. This is the only regime allowing uniform films over large surfaces, provided that the temperature profile remains constant. The overall deposition rate of the material can be expressed through an Arrhenius type formulation, i.e. the natural logarithm of the deposition rate as a function of the reciprocal temperature in degrees Kelvin. If only a singular surface reaction is taking place in the temperature range of this regime, its respective activation energy E_a can be calculated from the slope, equal to $-E_a/R$, where R is the gas constant.
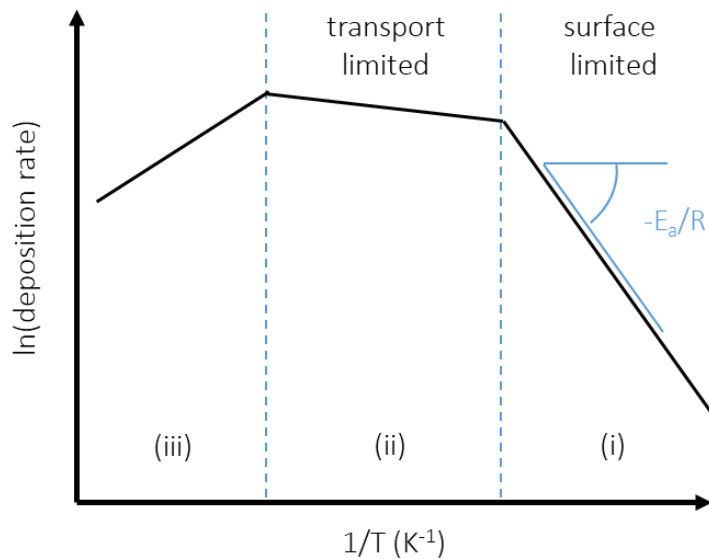
Fig. I.10. Schematic representation of the different regimes encountered in a CVD deposition process.

As the temperature increases, material deposition can reach rates high enough for the consumption of the film-forming species to be faster than their diffusion towards the surface. In this case, the supply, i.e. the transport of the material by diffusion through the boundary layer, becomes the rate-limiting step (Regime II). For that reason, this regime is also called *transport-limited regime*. An increase in temperature

has a secondary impact on the deposition rate for this regime, mainly facilitating the diffusion of gaseous species towards solid surfaces. An increase in precursor concentration on the other hand has a more pronounced influence and can increase the deposition rate more effectively.

At higher temperatures, a decrease in deposition rate is oftentimes observed despite the continuous increase in provided energy (Regime III). This behavior can originate from competitive phenomena that decelerate or inhibit the deposition rate, or through the depletion of a reactant that is essential for film formation by means of gas phase or surface reactions. Oftentimes, homogeneous reactions in the gas phase are the cause, consuming the precursor and leading to the production of species that do not participate in deposition, or that diffuse and adsorb on surface sites without reacting, occupying them and impeding the adsorption of film forming species. Reactions that cause the irreversible degradation of the precursor can also be at fault. Given the desired uniform coverage at low temperatures in the frame of this thesis, processes corresponding to Regime I would be ideal, as they tend to avoid side-reactions observed in the other regimes and additionally favor the deposition of uniform and conformal films, since they are not subject to local variations of gaseous reactant concentrations.

In general, CVD processes allow for non-directional, uniform coverage and are some of the most suitable for coating complex-in-shape substrates. Attention must be paid however when deposition is carried out within a confined volume such as a vial. A bottle is namely a hollow body, for which a single orifice is used for the entry and exit of the reactive gases and the produced by-products. This particular gas flow profile can lead to recirculation problems or preference for homogeneous reactions [56]. Depending on their nature and the specific deposition mechanisms, accentuation of homogeneous reactions can be beneficial or detrimental to the film growth rate. Thus, the areas of activity of particular reactions in the gas phase must be controlled through modulation of the temperature, pressure, flow rates or reactor geometry, in order to manipulate and shift operation in regimes where these reactions are favored or avoided, depending on the case. For this reason, the use of simulation and computational fluid dynamics (CFD) calculations is a powerful tool that can provide deeper understanding of the involved dominant gaseous and surface mechanisms. Process simulation can aid in the investigation of such modulations, enabling the fast screening of multiple operating conditions, geometry configurations and thermal profile distributions without the need for multiple, time-consuming, trial-and-error experiments [56].

I.3.3. *Simulation of the CVD process*

An in-depth understanding and control of the transport and reaction phenomena is an absolute prerequisite for establishing optimal operating parameters, reactor configurations and designs that lead to

the production of films with desired properties and performance, at the lowest possible consumption of resources. The simulation of the deposition process can be a great consultation tool during scaling-up towards an industrial implementation. However, utilization of simulation tools require the knowledge of the chemical and kinetic model describing the deposition mechanism. Generally, different scales exist when reproducing the interplay of phenomena that occur in a CVD setting. They are categorized in reactor-scale macroscopic simulations, simulations at the micrometer or nanometer scale, and multiscale models. The present work is focused on the reactor-scale, aiming to reproduce the transfer phenomena that occur in the gas phase. For that cause, CFD models are utilized, providing mathematical solutions of the conservation of mass, energy and momentum equations. Through these models, the velocity profile, pressure and temperature distribution in the CVD reactor are calculated, alongside information on the local concentration profiles and predicted deposition rates on the solid surfaces of the reaction chamber [140, 141].

To arrive at these predictions however, it is mandatory to define appropriate chemical reactions that lead to the formation of by-products and solid film, as well as their corresponding kinetic laws. The reactions and the associated kinetic constants describing the deposition mechanism can be determined by analyzing the chemical composition of the gas phase, either *in-situ* or at the reactor exhaust, and by measuring the local deposition and composition of the films. In reality, a CVD process involves multiple steps as was presented previously (diffusion, adsorption, etc.) and film formation is oftentimes carried out by species that have been produced through a cascade of reactions. For that reason, the consideration of an apparent mechanism, that is, a mechanism that "condenses" and presents a group of multiple, sometimes unknown, elementary reactions through a single representative fictitious reaction, is advised. The advantage of such a simplified approach is the relative rapidity of development, allowing for the simulation of complex chemical systems while still retaining a satisfactory level of accuracy regarding estimations of the film growth rate. The main drawback on the other hand is that the apparent mechanism is only valid for the operating range, in particular that of the deposition temperature, for which it has been developed.

I.3.4. *Characterization of the gas phase*

Multiple gas phase analysis methods have been implemented in CVD processes over the years. For example, *in-situ* UV spectroscopy or FTIR exhaust gas studies have been used to establish chemical reaction paths in the CVD of gallium nitride (GaN) films [142, 143]. Gas chromatography coupled with mass-spectrometry (GC-MS) has been by far one of the most popular methods, applied for the investigation of precursor decomposition and by-products generation in CVD of titanium nitride (TiN) [144] among many others. Regarding analogous studies involving silicon-containing precursors, the majority of the reported literature concerns the analysis of the gas phase in binary systems like SiC, SiO_2 or Si_3N_4 from

chlorosilanes, silanes or TEOS [145]. Among them, Arno et al. [146] used online FTIR analysis, detecting primarily carboxylic acids and water, among other compounds, during the SiO_2 deposition from TEOS and O_3. Multiple other studies have analyzed the gas phase in chemical routes involving TEOS, the results of which are summarized in Table I.3. As for Si_3N_4 films, the gas phase characterization and deposition mechanisms from SiH_4 and NH_3 by photo-assisted CVD, or from SiH_2Cl_2 and NH_3 by low-pressure CVD, have been investigated by transient mass spectroscopy [147, 148]. To the best of our knowledge, the gas phase characterization of a ternary SiO_xN_y system still remains unexplored.

Table I.3. Examples of gas phase characterizations and identified species in the gas phase of TEOS and TEOS-O_2/O_3 chemical pathways by thermal CVD.

Chemistry	Method	Identified species	Ref.
TEOS-O_2/O_3	Online FT-IR	CO, CO_2, H_2O, HCOOH, CH_3COOH, TEOS	[146]
TEOS decomposition	GC-MS	Ethylene, acetaldehyde, EtOH, TEOS, $(EtO)_3SiOCH=CH_2$	[149]
TEOS-O_2/O_3	*In-situ* FT-IR	CO_2, H_2O, CH_3CHO, HCHO	[150]
TEOS, TEOS-O_2/O_3	Molecular beam sampling (MBS)	H_2, H_2O, C_2H_5, $Si(OH)_3^\bullet$, $Si(OC_2H_5)OH_2^\bullet$, among others	[151]

Moreover, the generation of short-lived radical species and unstable intermediates is a common occurrence in CVD processes. Their identification is an important step towards the accurate characterization of the gas phase. For that reason, the combination of multiple classical physico-chemical methods is advised for the analysis of stable and radical species alike. *In-situ* FT-IR, molecular beam sampling (MBS) and electron spin resonance (ESR) have been utilized in the literature for the identification of radical species [151, 152]. In this context, combination of various analytical techniques can help identify stable by-products and radical intermediates and used to formulate an apparent chemical mechanism for the simulation of the deposition process using macroscopic CFD models. More details on how various gas phase characterization methods are implemented in the present work for this purpose are given in Chapter II.

I.3.5. *Literature models for silica deposition from TEOS-O₂/O₃*

The most relevant studies regarding the simulation of SiO_2 deposition from TEOS-O_2/O_3 have been conducted in cold-wall, low or atmospheric pressure CVD reactors using showerhead injectors [153, 154].

Such reactors, like the industrial Watkins Johnson reactor, were the main configurations of interest for the microelectronics industry back in the nineties. Kim and Gill [139] were among the first authors to propose mechanisms for the deposition of SiO_2 from TEOS-O_3. Working in a cold-wall reactor operating at 4-12 kPa and 280-405°C, the authors developed two global apparent mechanisms, in one of which TEOS decomposes in the gas phase in the fictitious intermediate molecule, denoted *INT,* and in acetaldehyde, through an excited O_3^*-centered mechanism. This INT molecule represents the various unknown chemical species produced by the homogeneous decomposition of TEOS in the gas phase and is formed through the substitution of the ethoxy ligands in TEOS by hydroxyl groups $(Si(OH)_{n-1}(OC_2H_5)_{5-n}$, where n=1-4). INT can also encompass oligomers, such as siloxanes, formed through a condensation reaction between two intermediates [149]. A cascade of reactions resulting in the stepwise cleaving of the ethoxy ligands has also been described in the literature [155]. Once formed, the INT species can either contribute to SiO_2 deposition or decompose into parasitic gaseous by-products. As was mentioned previously, the term "parasitic" has been proposed to describe any silicon-containing intermediates in the gas phase that do not contribute to film formation, and as a result decrease the deposition yield of the process [139].

Dobkin et al. [156] modified this model by assuming that deposition occurs due to the presence of oxygen radicals and described that both TEOS and the INT species contribute to film formation. However, their model was proposed for small ranges of pressure and temperature (103-105 Pa, 400-425°C). Following their work, Zhou et al. [157] developed a new model for a Watkins Johnson reactor operating at atmospheric pressure and 500-550°C. The main differences from their predecessors concern the assumption that TEOS must react with O_3 to form the INT species on one hand and the SiO_2 film on the other. Nieto et al. [158] adapted some kinetic constants of this particular model, illustrated schematically in Fig. I.11, to their specific chamber configuration and operating conditions.
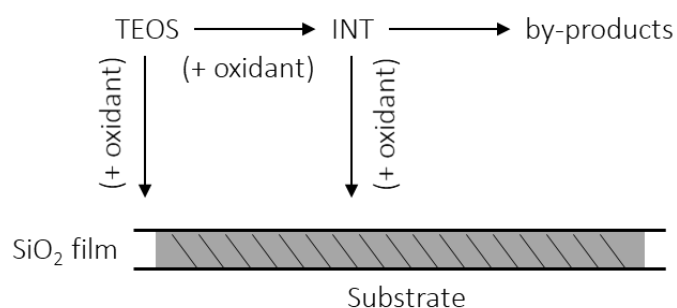
Fig. I.11. Schematic simplified representation of TEOS-O_2/O_3 models described in the literature.

It is worth pointing out that none of the above studies consider a thermal activation for heterogeneous reactions from TEOS, while some studies fail to achieve a good agreement between experimental and simulated data for temperatures above 400°C at low TEOS flow rates [155]. For the present thesis, an effort is made to simulate the deposition process over a larger temperature range (150-520°C) and propose temperature-dependent kinetics for all reactions. Given that the residence times and reactor configuration of Watkins Johnson type reactors are different in comparison to what is used in the present work, already developed kinetic laws are recalibrated and new ones are added. Based on the above literature data, a new kinetic model for the deposition of SiO_2 is developed.

In the case of SiO_xN_y however, the literature is still lacking severely. No computational analysis on the deposition of silicon oxynitrides has been proposed to this date. Certain information can be collected from gas phase and modeling studies on Si_3N_4 deposition from SiH_4 and NH_3 [159, 160]. In spite of that, the use of precursors with higher complexity (Si–H, Si–N, Si–C bonds), in addition to the involvement of O_2, obviously cannot conform to a model describing the binary Si_3N_4 system from SiH_4. Since the SiO_xN_y chemistries investigated in this thesis have not been previously documented in the literature, utilization of gas phase characterization results are mandatory for the definition of a chemical model. Through a novel approach combining multiple gas phase and solid phase analyses, an apparent mechanism for the deposition of SiO_xN_y is proposed. The experimental and computational details are touched upon in Chapter II.

I.4.   Conclusions

With this Chapter, the vast utility of silicon- and silica-based films has been presented, encompasing applications spanning from microelectronics to packaging of pharmaceuticals. As the main motivation for this thesis, the case of pharmaceutical glass containers (vials) is studied. When used as primary packaging media for drugs, glass vials can suffer from an alteration and delamination of their internal surface when in prolonged contact with the stored pharmaceutical solution, exposing patients to great sanity risks. To ensure patient safety, avoid product recalls, improve sustainability and extend product shelf life, the treatment of glass vials by SiO_2 coatings has been explored as a means to reduce container-to-drug interaction. Such coatings have in fact already found their way in commercial products. However, there is still room for improvement. This is especially evident in light of the eventual hydrolysis of the protective SiO_2 barrier coating itself.

For satisfactory barrier performance, a conformal and dense network, able to withstand hydrolysis and reduce diffusion of the glass constituent elements, is an absolute prerequisite. Based on numerous studies, it has been shown that the partial substitution of O anions in the silicate network by N or C ones can lead to higher network densification and improved barrier properties, effectively reducing B, Na or H_2O diffusion. However, the deposition of nitride or carbide silica-based coatings within the constraints defined by the glass manufacturing process (thermal deposition at atmospheric pressure and at moderate temperatures <600°C) is rarely reported in the literature, if not at all. Thermal atmospheric pressure processes for the production of SiO_xN_y for example require temperatures exceeding 750°C. Plasma activated processes on the other hand do indeed allow their deposition at acceptable temperatures, however they oftentimes lead to porous films with high hydrogen or carbon impurities, which can affect performance. In contrast, a thermal CVD process is promising in that regard, as it can enable the deposition of high quality, homogeneous and conformal films, while also being easily implementable in the on-line vial production. At the same time however, it faces a drawback – the lack of plasma activation demands activation by thermal means. This can create compatibility problems with heat sensitive substrates like glass.

To overcome this challenge, solutions for the deposition of such materials are sought in reactive chemistries. An extensive survey of the literature provided key information on the selection of appropriate chemistries and precursors for the deposition of SiO_2 and SiO_xN_y films at moderate temperatures. In that context, the most beneficial precursor structures are defined and novel molecules are selected. The strategy formulated for the selection of SiO_xN_y-forming precursors and chemistries can also be extended to SiO_xC_y materials. In that which follows, deposition of SiO_2 from reactive O_3-based chemistries is carried out, placing great attention on parameters that induce higher network densification. SiO_xN_y deposition follows right after, investigating the potential for further densification through insertion of nitrogen in the silica-based films. Alongside an extensive experimental investigation, computational fluid dynamics (CFD) calculations are applied, offering additional study of the deposition process through simulations. The obtained information is used to gain in-depth understanding of the mechanisms and reactive phenomena that define each particular deposition process. The eventual goal for the developed SiO_2 and SiO_xN_y models is to be transposed in reactor configurations treating vials or other complex 3D substrates and use optimization studies to identify optimal parameters for the production of homogeneous and uniform coatings.

Chapter II. Materials and Methods: Experimental setup and CFD calculations

Chapter II presents in detail the two CVD reactors used for the processing of silica-based films on the surface of planar substrates, as well as on the inner surface of pharmaceutical vials. Detailed descriptions of the reactors are given, along with a presentation of the substrates used and their placement in the respective reactors. Specifications of each experimental setup are addressed and the purpose of each reactor is explained in the frame of the project.

The second part of Chapter II deals with the various characterization techniques that are utilized in order to gain compositional, structural and functional insight on the produced materials. This information is used to ascertain the link between the utilized chemistries, the process conditions and the eventual structure-composition-performance correlation. Additionally, gas-phase characterizations that are executed in parallel to the deposition experiments are detailed. Their utility as key-information giving sources for the development of a silicon oxynitride chemical model and the subsequent CFD simulations is underlined.

In the last part of Chapter II, the simulation of the CVD process of SiO_2 and SiO_xN_y is addressed. The simulation environment is described step-by-step, starting from the creation of the reactor geometry, the meshing, then moving towards the implementation of a chemical model through kinetic constants and chemical reactions. The overall methodology, used for the development of deposition mechanisms that will be applied to simulate the experimental solid-phase results, is presented.

II.1. The CVD process

II.1.1. CVD Reactors and setup

The coatings studied in this thesis concern depositions of films with a thickness in the range of a few dozen to a few hundred nanometers. The present section deals with the presentation of the two reactors used for this purpose. The first reactor is a tubular horizontal CVD reactor designed and built at the start of the thesis, as a larger version of the tubular reactor used in Ponton's work [7]. This reactor is used for the initial testing of the various chemistries, as well as for establishing the optimal experimental conditions that lead to the desired film properties in terms of composition, structure, and barrier performance. Its second function is the treatment of multiple samples on the row, placed deliberately in regions with distinct local temperatures, as a means to extract kinetic information for the eventual development of the SiO_2 and SiO_xN_y deposition mechanisms.

The second reactor is a vertical CVD reactor utilized for the treatment of pharmaceutical vials. This reactor has been previously used in the theses of Ponton, following that of Etchepare [55]. The deposition of barrier coatings on the inner surface of Type I vials is carried out in this specific set-up. For this purpose, only the best-performing chemistries that have been tested in the tubular CVD reactor are utilized.

Training on the operation of both reactors was provided by Diane Samelor and Daniel Sadowski.

II.1.1.1. Tubular reactor for treatment of planar substrates

The horizontal atmospheric pressure CVD reactor used for the treatment of planar substrates, as well as for the investigation of potential chemistries and the development of the kinetic models, is shown in Fig. II.1. The reaction chamber is composed of a horizontal quartz tube with an internal and external diameter of 46 and 50 mm, respectively, and a length of 700 mm. It is heated by a semitransparent furnace (Trans Temp, Thermcraft Inc.), with two thermocouples installed on the outer walls to regulate the temperature. The exact evolution of temperature profile at the wall is measured manually by using an external type-K thermocouple. Measurements are taken every 20 mm along the tube under a N_2 gas flow of 4036 standard cubic centimeters per minute (sccm). Deposition experiments are performed at a total of seven different set point temperatures (SPT), namely 360, 400, 450, 500, 550, 625, and 650°C, defined as the temperature measured at 360 mm from the inlet. After it, i.e. moving towards the exhaust of the reactor, a 140 mm long isothermal region exists.
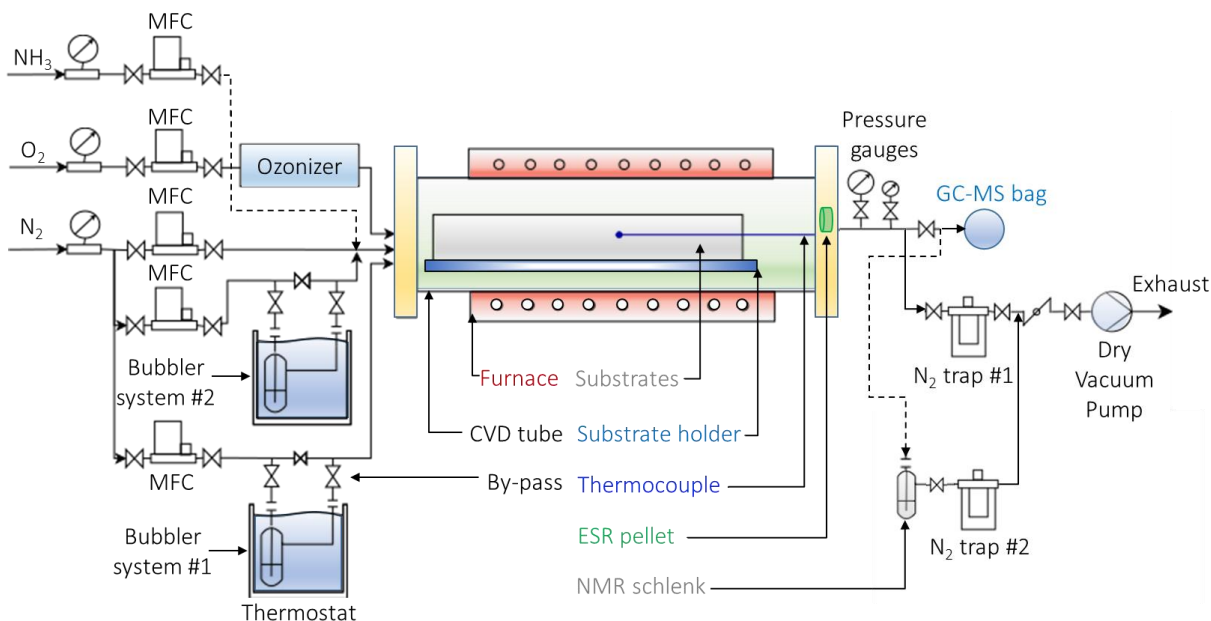
Fig. II.1. Schematical representation of the tubular CVD reactor used for the treatment of flat substrates.

The CVD reactor inlet is connected to three gas lines, the flow of which is controlled using mass flow controllers (MFCs) (Brooks 5850TR). The ranges are 0-100, 0-5000 and 0-10000 sccm for the MFCs of the NH_3 (99.999 %, Linde), O_2 (99.9995 %, Messer) and N_2 dilution (99.9999 %, Messer) lines, respectively. For the deposition of SiO_xN_y specifically, the O_2 line is controlled by a MFC with smaller range (0-10 sccm). The two MFCs regulating the N_2 lines passing through the bubbler systems have a range of 0-500 sccm. The N_2 dilution line with variable flow allows fixing the total gas flow at 4036 sccm for all TEOS runs, at 4040.7 sccm for all HMDS and HMDS-TEOS runs, at 4030 sccm for all TMDSA runs, and at 4028 sccm for all TSAR runs. This N_2 line is heated at approximately 100°C. Additional lines bubble N_2 gas through the bubbler systems containing the precursors tested for each chemistry. TEOS (99.999 %, Sigma-Aldrich) and TDMSA (95 %, abcr) are inserted in separate bubblers, each mounted on bubbler system #1. Similarly, HMDS (99.9 %, Sigma-Aldrich) and TSAR (proprietary, Air Liquide) are mounted on bubbler system #2. The N_2 carrier gas lines (99.9999 %, Messer) bubble 89, 223 or 444 sccm of N_2 gas through TEOS and 49 or 148 sccm through TDMSA in bubbler system #1. For bubbler system #2, the carrier gas line flows 20 sccm of N_2 through it when the HMDS bubbler is mounted, and 39 sccm when the TSAR-containing bubbler is installed, eventually transporting the vapors of the precursors towards the reactor. The bubblers are heated at 65.3±0.1°C for TEOS, 50 or 62±0.1°C for HMDS, 80±0.1°C for TDMSA and 60±0.1°C for TSAR. The N_2 carrier gas lines are always kept at approximately 15 to 20°C above the respective bubbler temperatures to avoid recondensation of the precursor vapors.

The O_2 line passes 1960 sccm through an ozonizer (Lab2b Laboratory Ozone Generator, Triogen LTD) when deposition from the TEOS and HMDS chemistries is carried out. The ozonizer is operating at its maximum ozone production, providing an O_3 concentration of 60 mg.l^{-1} at standard temperature and pressure, and thus supplying the reactor with an O_2/O_3 mixture. For the TDMSA and TSAR chemistries, the same line provides 0.3, 0.6, 1.2 or 2 sccm of O_2, by-passing the ozonizer. The oxygen line is not heated in any of the experimental runs.

For the SiO_xN_y experiments utilizing ammonia, the NH_3 gas line introduces 20, 40 and 80 sccm of ammonia in the reactor, after merging it with the N_2 dilution line. The ammonia line is not heated either.

The three gas-lines, namely O_2 line, N_2 carrier gas line, and N_2 dilution line with ammonia, are kept separated and their contents mix only after reaching the inlet of the reactor. For the TEOS and HMDS chemistries used for the deposition of SiO_2, the system is always in excess of O_2. The base and operating pressures are monitored with a Pirani (MKS MicroPirani Transducer Series 925C, 10^{-5}-760 Torr) and a Baratron (MKS Baratron Type 627, 1-1000 Torr) gauge respectively, positioned downstream of the deposition zone, before the liquid nitrogen trap #1 and the dry pump (Edwards, soXu 20iC). The operating pressure is fixed at 97.3 kPa (730 Torr) for all runs.

II.1.1.2. Vertical reactor for treatment of pharmaceutical vials

The reactor used for the treatment of pharmaceutical vials, shortly referred to as *vial reactor* hereinafter, is presented in Fig. II.2. The main compartments of the vial reactor are the gas lines regulated by the MFCs, the bubbler systems, the reaction chamber, followed by the two pressure gauges (Baratron, MKS, 1 to 760 Torr; Pirani, Edwards, 5·10^{-3} to 1 Torr), the liquid nitrogen trap and the dry vacuum pump (Edwards XDS 10). In this particular reactor configuration, the reaction chamber is oriented vertically. A stainless steel metal piece is used as the support (i.e. substrate holder) for the pharmaceutical vial, which is also placed upright. The substrate holder is hollow and features a small opening in its center, in order to allow a K-type thermocouple to pass through. The thermocouple measures the temperature at the base of the vial by contact. An injection nozzle (also referred to as *injector*) is located at the top of the reaction chamber. Its tip serves as the inlet for all supplied gases and is centered on the same axis as the bottle and the substrate holder. The distance between nozzle tip and vial, as well as its diameter and opening, have all been optimized by numerical simulations executed as part of Etchepare's work [55]. The tip of the nozzle is hovering at a distance of 17 mm above the crown of the vial and has an opening of 1 mm in diameter. A cylindrical quartz tube with an internal diameter of 51 mm and a length of 335 mm separates the entire

reaction chamber from the environment. It is connected to the metal structure by rubber joints sealing the assembly.
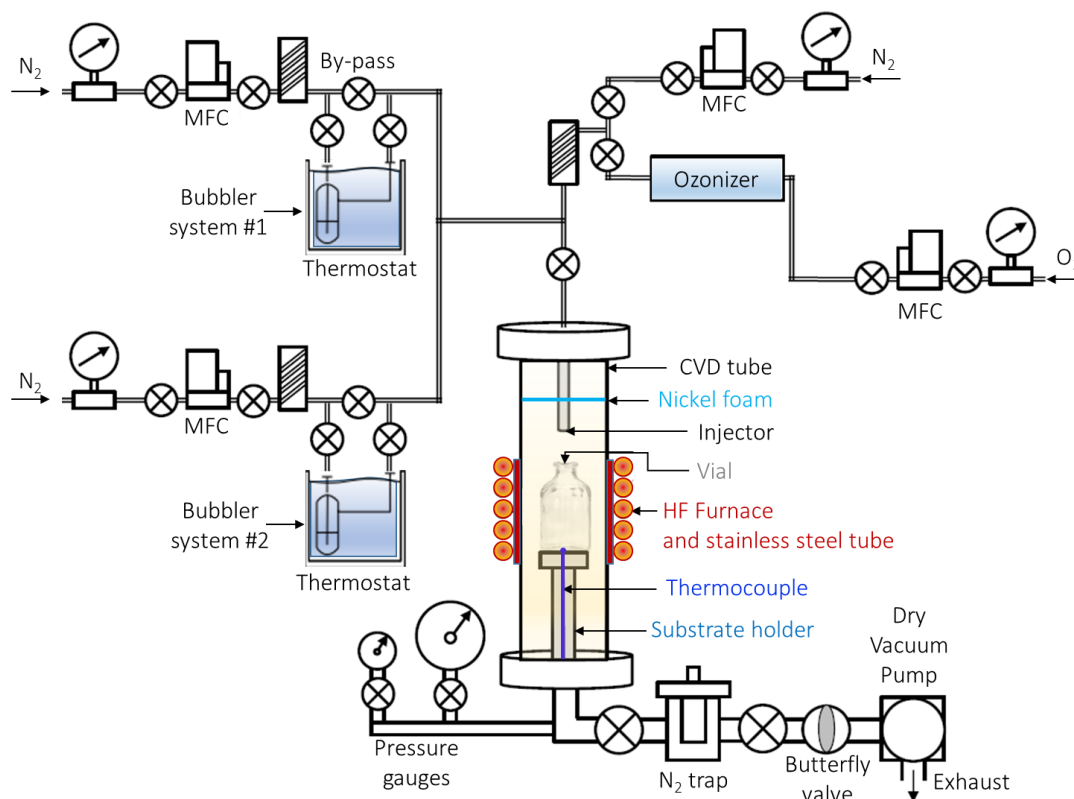
Fig. II.2. Schematical representation of the vertical CVD reactor used for the treatment of vials.

The reaction chamber is heated using an electromagnetic induction heating system. It consists of a coil powered by a high-frequency (HF) generator and a coaxial stainless steel tube located between the quartz tube and the coil. The HF generator is cooled by a cooling-water network. The system is thermo-regulated by a PID regulator connected to an external thermocouple in direct contact with the stainless steel tube. The studied deposition temperatures are 400 and 550°C for SiO_2 deposition, and 650°C for SiO_xN_y deposition, defined as the SPT applied at the base of the vial. The corresponding temperature profiles are measured every 10 mm along the vertical axis by utilizing the thermocouple of the substrate holder and a vial with a drilled hole at the bottom, which allows the thermocouple to pass through it. When a SPT is applied at the bottom of the vial, an approximately 50 mm long isothermal region exists above the base, spanning across the majority of the vial body. A working pressure of 97.3 kPa (730 Torr) is applied for all experiments.

Some modifications were made to the vial reactor compared to its previous iterations described in Etchepare's and Ponton's theses [7, 55]. First, an ozonizer connected to the O_2 line was installed. Ozonizer type and ozone output are the same as those described in the tubular reactor configuration. Additionally, a second bubbler system (#2) was added, to allow deposition from dual-precursor based chemistries. Lastly, a set of nickel foams were installed inside the reaction chamber, located 21 mm above the tip of the nozzle. Their purpose is to prevent gas from flowing towards the top region of the reactor, which tends to feature lower temperatures. Through this, gas recirculation upon exit of the gas from the vial is minimized, reducing gas residence time and avoiding potential formation of particulates caused by cooling of the gas.

The range of the two MFCs controlling the O_2 line and the N_2 dilution line in the vial reactor is 0-2000 sccm. For the deposition of SiO_xN_y, the O_2 line is regulated by a different MFC, featuring a smaller range (0-10 sccm). The two MFCs used to regulate the N_2 carrier gas passing through the bubbler systems have a range of 0-500 and 0-50 sccm for bubbler system #1 and bubbler system #2, respectively. System #1 houses the bubbler filled with TEOS, while the bubbler with TDMSA is mounted on bubbler system #2. All gases and chemicals have the same purity and provider company as those listed in the previous section.

For deposition of SiO_2 coatings in vials, the O_2 line transports 1079 sccm of O_2 through the ozonizer. For SiO_xN_y coatings, 0.3 sccm O_2 are used instead and the ozonizer is by-passed. The N_2 carrier gas lines pass 49 and 24 sccm through TEOS (bubbler system #1) and TDMSA (bubbler system #2), respectively. The N_2 dilution line passes 1094 or 1737 sccm N_2, depending on whether deposition of SiO_2 or SiO_xN_y is carried out. For SiO_xN_y deposition, the N_2 carrier gas line passing through bubbler system #1 also serves as a secondary dilution line, supplying 458 sccm N_2, with the by-pass valves closed. The total gas flow rate for all experiments is kept at ca. 2222 sccm for both SiO_2 and SiO_xN_y deposition. The N_2 lines are heated using heating cords, with the dilution line set at 100°C and the carrier gas lines set 15-20°C higher than the respective bubbler systems. The O_2 line is not heated. No NH_3 line is installed or used for this particular reactor.

II.1.2. Treated substrates

For the initial investigation of the various chemistries, 280 μm thick monocrystalline silicon (100) type N-wafers (Neyco) are utilized, cut in rectangles of 32×24 mm² with a diamond tip (Atelier Interuniversitaire de Micro-nano Electronique (AIME) at INSA Toulouse). The wafers are polished on both sides, with a surface roughness less than 1 nm. Before deposition the substrates are degreased in a succession of three ultrasound bath steps for 5 min each. The procedure included (1) an ultrasound bath using distilled water, then rinsed with acetone (>99%, VWR Chemicals), (2) an ultrasound bath using

acetone, then rinsed with ethanol (99.3%, VWR Chemicals), and lastly (3) an ultrasound bath using ethanol. The substrates are finally dried under Ar flow (99.9999%, Messer).

The above substrates are supported vertically by homemade, tubular, stainless steel substrate holders, with a 7 mm deep insertion slot, positioned on the row as illustrated in Fig. II.3. The total length of the substrate holders is 450 mm, supporting a maximum of 18 coupons for each run, arranged parallel to the gas flow. The first coupon is placed at a distance of 57 mm from the reactor inlet and is given the code "pA". Substrates placed after it are named according to the Roman alphabet up to the 12th sample, after which enumeration follows Arabic numbers. This change in naming is done to clearly distinguish between samples that are positioned outside (pA, pB, […], pL) and inside (p1, p2, […], p6) the isothermal region.
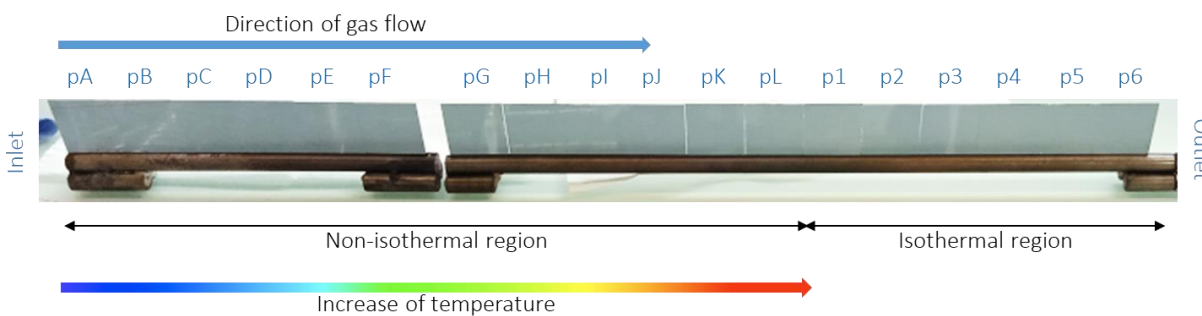
Fig. II.3. Standard samples placement and enumeration within the two stainless steel holders.

The aim of such a configuration is to process films deliberately in a 360 mm long non-isothermal zone existing before the ca. 140 mm long isothermal zone of the reactor, in order to obtain complementary compositional, mechanistic and kinetic information. Furthermore, the vertical configuration of the samples is chosen as a means to cover both sides of their surface, specifically adapted to facilitate potential leaching tests.

For experiments performed in the vial reactor, deposition of SiO_2 and SiO_xN_y coatings is carried out on Type I borosilicate glass vials, obtained from a European manufacturer of molded glass. One vial is treated per run. A photograph and a schema of the Type I vials used in the present thesis is shown in Fig. II.4. The structural features of the vial are the orifice at the top, also referred to as the *rim* or *crown*, followed by a rounded shoulder. The straight vertical part of the vial is characterized as the body, with the part beneath it being referred to as the *base* or *heel region* of the vial. The Type I pharmaceutical vials used as substrates for the present thesis have an internal and external surface of 87.05 cm^2 and 94.00 cm^2, respectively, without considering the external base surface. Its volume capacity at 100 %, i.e. to the rim,

measures 60 ml. Dimension-wise, the vial spans 7.3 cm in height and has an outer diameter of 4.25 cm, while the rim ring has an internal diameter of 1.25 cm. It must be noted however that 0.1 to 0.15 cm thickness variations can exist on the vials as a result of the glass molding manufacturing process.
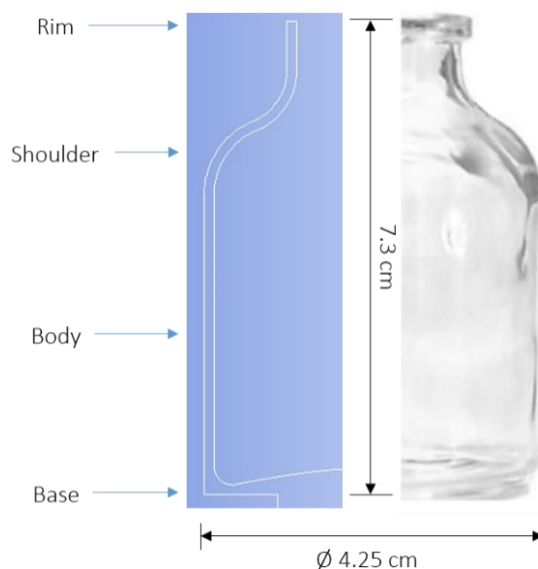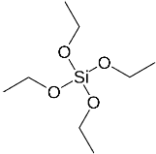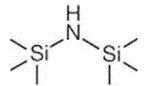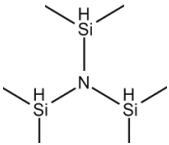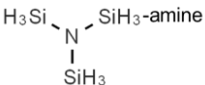
Fig. II.4. Two-dimensional representation (left) and photograph (right) of a Type I vial.

II.1.3. Chemistries for deposition of SiO_2 and SiO_xN_y films

Specific chemistries were identified at the end of Chapter I after the extensive literature review on the deposition of silica-based materials. All of the chosen precursor molecules are found in liquid form at room temperature and ambient pressure and have comparable physical properties. They are presented in Table II.1 alongside information on their physico-chemical properties, such as their boiling point, vapor pressure and hazard classification as specified in their respective safety data sheets (SDS).

All recommended health and safety instructions are carefully followed during handling of each precursor. For TEOS and HMDS, the bubbler-filling step is carried out under an extractor hood. For TDMSA and TSAR, this step is executed in a glovebox, under Ar atmosphere. The precursors are transferred into their respective bubblers, which are then mounted securely onto their corresponding by-pass structures. In the case of TDMSA and TSAR, all by-pass valves are sealed before exit of the bubbler+by-pass system out of the inert atmosphere of the glovebox. Protective personal equipment (laboratory coat, gloves and goggles) are also used.

Table II.1. List of silicon-containing precursors studied.

Precursor acronym	Compound name	Chemical formula	CAS number	Boiling point (°C)	Vapor pressure (mm Hg)	Hazard classification
TEOS	Tetraethyl orthosilicate		78-10-4	169°C	200 @ 108°C (1.5 @ 20°C)	
HMDS	Hexamethyl disilazane		999-97-3	126°C	50 @ 50˚C	
TDMSA	Tris (dimethylsilyl) amine		21331-86-2	153°C	< 10 @ 20˚C	
TSAR	Alkylamino-trisilylamine	H_3Si N SiH_3-amine / SiH_3 / *indicative structure*	Proprietary	189°C	-	

Through the utilization of three by-pass valves (Fig. II.1 and 2), the carrier gas flow can be diverted towards the bubbler. For all tested chemistries, the N_2 carrier gas bubbles through the respective precursor liquid found in the bubbler and transports part of it in the form of vapors. The liquid phase of the precursor is assumed to be in thermodynamic equilibrium with its gas phase at a pressure called the saturated vapor pressure, P_{sat} (in Torr). In order to calculate the highest possible transported volumetric flow rate of the vaporized precursor, $Q_{precursor}$ (in sccm), at the respective conditions where thermodynamic equilibrium is achieved in the bubbler, the equation by Hersee and Ballingal [161] is used:

$$Q_{precursor} = Q_{N_2\ carrier} \times \frac{P_{sat\ @\ T°C_{bubbler}}}{P_{reactor} - P_{sat\ @\ T°C_{bubbler}}} \qquad \text{Eq. (II-1)}$$

Where $Q_{N_2\ carrier}$ (in sccm) is the volumetric flow rate of the carrier gas and $P_{reactor}$ is the operating pressure of the reactor expressed in Torr.

The evolution of the saturated vapor pressure P_{sat} as a function of the temperature of the heating system can be expressed using an Antoine's law type equation. For the TEOS molecule, multiple such calculations are available in the literature [162-164]. For HMDS, data have been collected from multiple

safety data sheet sources (Sigma-Aldrich, ChemCon, VestaChem) and a $P_{sat} = f(T)$ function is extracted (Fig. II.5a). For TDMSA, a $P_{sat} = f(T)$ graph found in a patent [165] is utilized (Fig. II.5b). Lastly, for TSAR, the $P_{sat} = f(T)$ graph is supplied by the provider (Air Liquide, confidential).
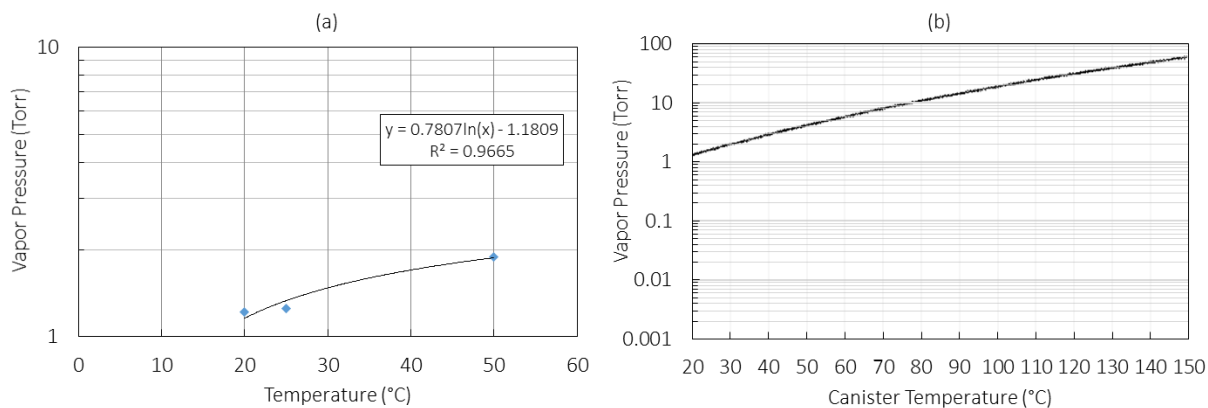
Fig. II.5. $P_{sat} = f(T)$ graphs for HMDS (a) and TDMSA (b) [165].

The precursor flow rate, as calculated by Eq. (II-1) has been cross-checked by measuring the weight of the bubbler before and after deposition, for a fixed deposition time. It is observed that the measured flow rate values for TEOS and HMDS are approximately 40 to 60 % lower than those calculated by Eq. (II-1). This discrepancy is attributed to an incomplete liquid exchange between the carrier-gas and the precursor liquid in the bubbler, as well as due to the conductance of the gas lines that connect the bubbler to the reactor volume, which cannot be considered infinite to maximize the liquid exchange. In contrast, in the case of TDMSA and TSAR, the measured flow rate values are 300 % higher than those calculated by Eq. (II-1). It is noted that both precursors are very volatile and rarely utilized in the literature. Very few sources exist on their vapor pressure and it is suspected that their respective $P_{sat} = f(T)$ graphs might not be accurate enough. Because of these differences, for the execution of the respective CFD simulations, it is deemed more suitable to consider the values that are deduced experimentally.

II.2. Solid and gas phase characterization techniques

A cross-linking of information from multiple characterizations is utilized in order to establish and understand the link between process parameters, material structure, composition and anti-corrosion

performance. A complete set of analyses of the gas phase composition at the exit of the tubular CVD reactor is also implemented in order to better understand the mechanisms involved in the deposition process. The extracted information is used to define deposition mechanisms and develop kinetic models, essential for the simulation and eventual optimization of the CVD process.

II.2.1. Gas phase characterization

A coupling of three different gas phase characterization methods has been implemented for the study of the stable by-products and radical species from the TDMSA chemistries. The three analyses in question are electron spin resonance (ESR) spectroscopy for the radical intermediates, and nuclear magnetic resonance (NMR) and gas chromatography coupled with mass spectrometry (GC-MS) for the stable by-products. This methodology was developed and implemented as part of Laura Decosterd's work, who worked as an engineer in the frame of the ANR HEALTHYGLASS project and was supervised by Prof. Marie-Joëlle Menu. To the best of our knowledge, the parallel use of all three methods is implemented for the first time in a CVD process. The simultaneous analysis of the stable by-products and radical gas species aims to elucidate the reaction mechanism with parallel consideration of the corresponding solid-phase results, allowing for the development of an original chemical model for the simulation of SiO_xN_y deposition.

II.2.1.1. Electron spin resonance (ESR)

Electron spin resonance or electron paramagnetic resonance spectroscopy is an analytical method that studies materials with unpaired electrons, allowing among others for the identification of radical intermediates. Any species with uncoupled electrons can be "trapped" by a so-called spin-trap (or spin label) molecule that possesses an unpaired electron, usually on a nitrogen atom. The spin-trap molecules can bind other molecules with unpaired electrons (such as radical species), creating an adduct that also features paramagnetic resonance (thus referred to as *spin-adduct*) and is detectable by ESR spectroscopy. As a result, the radical species is stabilized and its observation is possible, which enables obtaining information on its chemical structure.

In the present thesis, the spin-trap molecule used is α(4-Pyridyl *N*-oxide)-*N-tert*-butylnitrone (POBN), shown in Fig. II.6. The trapping reaction between the POBN molecule and the radical intermediate species R° occurs in beta position of the nitrone function, creating the spin-adduct. It is noted that the decomposition temperature of POBN is 185°C. This makes it obligatory to identify a region in the reactor that has a local temperature lower than the POBN decomposition temperature, but which is also allowing

for the trapping of radical species immediately after their production. Moreover, the POBN spin-trap molecule is acquired in powder form (Sigma-Aldrich). Therefore, it must be introduced in a way that does not contaminate the reaction chamber and the samples during the vacuum and purging stages. Considering the above limitations, POBN is compacted with KBr (dried at 80°C for 24 h) in pellet form. More specifically, 50 mg of POBN and 300 mg of KBr are mixed homogeneously and crushed together to form a pellet with 1 cm in diameter. The pellet is then placed inside the reactor at 78 cm from the inlet, technically at the outlet of the reaction chamber, which features a local temperature of 170°C. Additionally, the pellet is positioned in a vertical configuration, to maximize the available surface area for reaction (Fig. II.1).
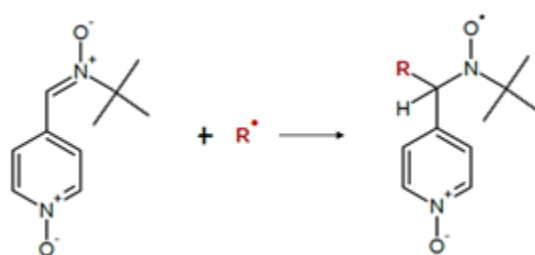
Fig. II.6. POBN spin trap molecule chemical structure before and after reaction with a radical species.

After each deposition experiment, the pellet is crushed into powder and transferred in two ESR tubes. One tube is sealed as-is and is referred to as "solid phase". For the second tube, 0.2 ml of toluene are added before sealing, referring to it as "liquid phase". The two ESR tubes are stored in a deep freezer until analysis. Analysis is performed at Laboratoire de Chimie de Coordination (LCC, Toulouse, France, operator: Lionel Rechignat) by conventional X-band ESR spectroscopy, using a Bruker Elexsys spectrometer equipped with a high-resolution cavity.

II.2.1.2. Gas chromatography – Mass spectrometry (GC-MS)

This analytical method was one of the two methods applied to identify stable gas phase by-products. It combines gas chromatography for separation and quantification of the constituents of a gas mixture, and mass spectrometry for their identification. The sampling of the gas mixture is done using an airtight, 1 L Tedlar plastic bag (Supelco), with a push-lock valve. The Tedlar bag is connected to the reactor through an adaptor placed at 93 cm from the inlet, located right after a valve (Fig. II.1). The sampling bags are purged three times with N_2 before use and are stored in a shaded place with no direct exposure to sunlight. Sampling is executed during the deposition process, first at variable timestamps to ascertain the steady state of the

CVD process. After establishing the time independence, the gas mixture is sampled at the midpoint of the total deposition duration.

The sampling bag is then transported to Institut de Chimie de Toulouse for GC-MS analysis (ICT, Toulouse, France, operator: Eric Leroy), performed using a Trace 1310 gas chromatograph coupled with a TSQ 900 mass spectrometer (Agilent Technologies), equipped with a TG-5SILMS separation column (Thermo Scientific, 30 m long, 0.25 mm id, 0.25μm film thickness). Helium is used as carrier gas. The carrier gas flow is programmed at 1 ml.min^{-1} for 12 min, then increased to 1.5-3 ml.min^{-1} and held for 8 min. The column temperature is programmed to stay at 25°C for 10 min, then is increased to 140°C with a step of 23°C.min^{-1}, and is lastly held at 140°C for 5 min. The molecules of the gas mixture exit the column at different times depending on their chemical affinity with the stationary phase of the column. Generally, the higher the chemical affinity, the higher the retention time. After exiting the column, the molecules are ionized and detected by the mass spectrometer according to the mass-to-electric charge ratio of each ion fragment. The mass spectrometer ion source is set to 250°C and the apparatus is used in scan mode with a range from 10 to 600 atomic mass units (amu). The identification of a molecule is simplified through the access to a database that regroups the mass spectra and suggests potential molecule structures and match percentage. However, the complexity of some molecules made their identification difficult. In those cases, matching information was collected from the literature.

Other than the deposition experiments themselves, additional gas phase samples were taken, serving specific purposes, such as:

- Creation of a calibration curve for the quantitative analysis of TDMSA,
- Measurement of TDMSA conversion rate and temperature of decomposition, aiding in extracting an activation energy of the respective decomposition reaction,
- Identification of gas phase by-products at 700°C,
- Duplicate experiments to compare results and reduce uncertainties.

During the above sampling procedures, "dummy" Si-coupons were inserted into the reactor in order to reproduce the deposition environment. The films produced from the above list of experiments were not characterized, since the focus was the gas phase analysis and not the solid phase results.

II.2.1.3. Nuclear magnetic resonance (NMR)

NMR is a quantitative analysis that can aid in identifying the main stable constituents of the gas phase and is used in the present thesis as a supplementary method to confirm the chemical structure of by-

products identified by GC-MS. This is done by making use of the chemical shift of each peak in NMR, which enables the characterization of functional groups and sheds more light on the overall chemical structure of the detected molecules.

In order to carry out NMR analysis, the outflow gases of the reactor are passed through a schlenk that is located between the outlet of the reaction chamber and the pump. The schlenk is filled with 0.8 ml of deuterated dimethyl sulfoxide (DMSO-d_6) that serves as the solvent. The effluents bubble through DMSO-d_6 for the whole duration of a deposition experiment, interrupted only for 40 s at the middle of the deposition process when GC-MS sampling is performed. The compounds transferred in the DMSO-d_6 solution after bubbling are not very stable and usually start decaying after 24 h. For that reason, 0.6 ml of the DMSO D_6 solution are extracted from the schlenk immediately after each experiment and transferred into an NMR tube, then stored in a deep freezer until analysis. It was confirmed that storage time did not affect NMR results, as long as the content of the NMR tube remained well frozen. Analysis is performed on a Bruker Avance III instrument operating at 500 MHz and equipped with a Prodigy cryoprobe. The analysis consisted of ^{1}H, ^{13}C Jmod, ^{29}Si echoing, HSQC ^{1}H-^{13}C, HSQC ^{1}H-^{29}Si, HMBC and COSY.

II.2.2. *Solid phase characterization*

A multitude of solid phase characterizations has been used to analyze the produced thin films. Analysis of the material structure by FT-IR and composition by ellipsometry for the identification of potential N and/or C incorporation are executed systematically after each experiment. After confirming that a material with desired composition has been produced, more accurate compositional data are acquired using Ion Beam Analyses (IBA). The environment of silicon, carbon, oxygen and nitrogen are investigated using XPS. Surface morphology studied by TEM and AFM. Lastly, the mechanical properties and the performance of the produced films is assessed through nanoindentation and resistance to aggressive, corrosive media. More specifically, two different wet etching solutions are utilized to screen the films, while the hydrolytic resistance and barrier performance is assessed in accordance to USP protocols. Unless otherwise precised, the majority of the characterizations are conducted on planar Si substrates.

II.2.2.1. *Deposition rates*

The average growth rate (kg.m^{-2}.min^{-1}) of SiO$_2$ films is calculated from the deposited mass by measuring the weight gain of each sample before and after deposition, using a Sartorius Genius Series ME215P analytical balance with 0.015 mg precision. It is assumed that deposition on each substrate surface

is uniform. To convert the deposited mass to thickness (or deposition rate), a density of 2200 kg.m^{-3} [158] is assumed for SiO_2 films. Since deposition of SiO_xN_y films results in minimal mass gain that is difficult to measure accurately by weighing, spectroscopic ellipsometry (SE) is utilized as explained below.

Local thickness profiles and deposition rates (nm.min^{-1}) are measured by SE using a Semilab SE-2000 ellipsometer operating in the 250−1000 nm wavelength range. All SE measurements are carried out in CIRIMAT (ENSIACET, Toulouse, France). Training on the operation of the SE apparatus and SE simulation software was provided by Olivier Debieu. The SE data are fitted in the 250−1000 nm wavelength range using the Semilab SEA software, through be application of different models. The incidence angle is kept constant at 70°. Each sample is probed on five locations along the vertical center, each 5 mm apart, starting 2 mm below the top edge of each sample as illustrated in Fig. II.7. The average thickness and average deposition rate per sample (referred to as "deposition rate (DR)" in Chapters III to V) is calculated from the average of these five points.
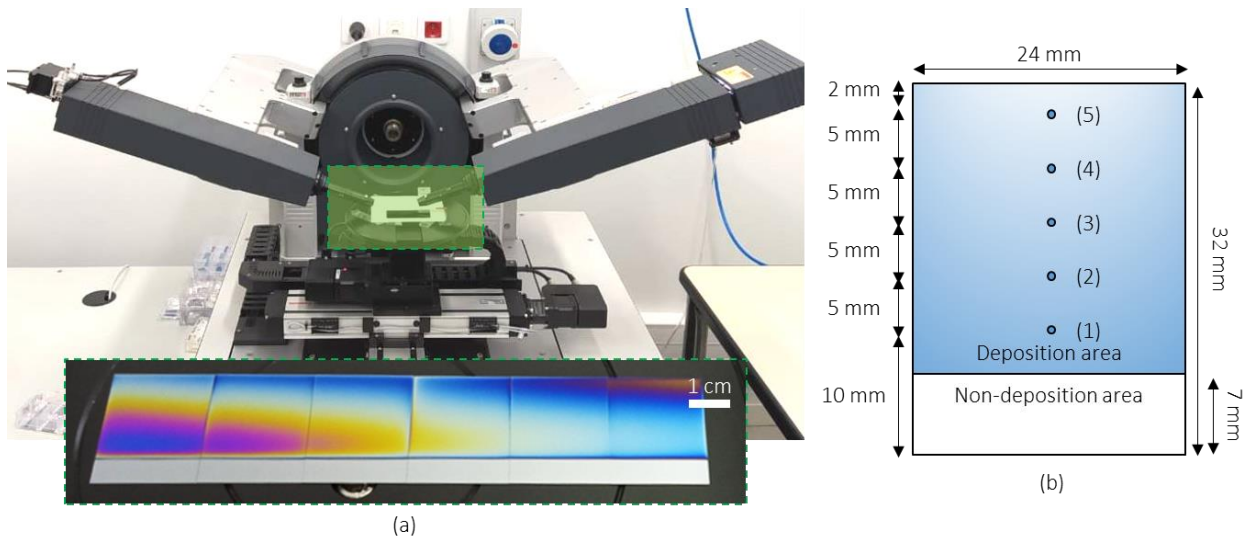
Fig. II.7. Spectroscopic ellipsometry (SE) instrument. Array of six samples placed on the stage for analysis (a). Position of locations (1) to (5) probed during SE analysis (b).

II.2.2.2. Film composition

Apart from local thickness information, SE also allows for the extraction of indirect information such as film density and composition, as well as optical properties of the films, for example the refractive index (RI) n and dielectric constant k. In order to extract such information from the raw values obtained by ellipsometry, the application of a model is required. This is executed by fitting the spectrum calculated by

a model to the measured spectrum acquired experimentally. When a good fit is achieved, the parameters chosen to define the model can give information on the macroscopic properties of the film.

A variety of models has been used throughout the present thesis, each specifically adapted for the various deposited materials. Failure of the simulated spectra to conform to the measured ones indicates that the model is not representing the material correctly and either requires to be adjusted (i.e. by modification of the various parameters of the model), enriched (i.e. by adding new parameters), or completely substituted by another model. It is noted that multiple models can be used to calculate the optical properties and thickness of a film. The calculated results are generally deemed acceptable for a R^2 goodness fit above 0.99. Lower goodness fits indicate a difference in material structure and/or composition and signify the requirement for modification or substitution of the applied model. A collection of the utilized models, as well as the respective chemistries they have been used in, is presented in Fig. II.8.
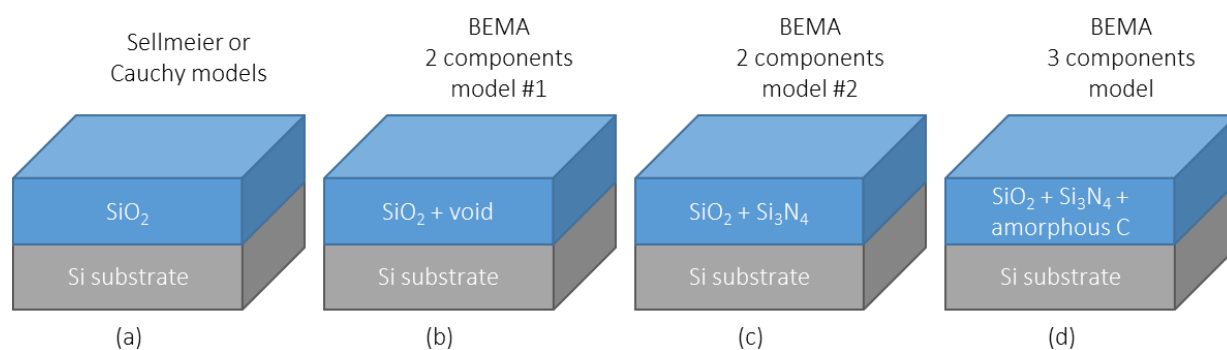
Fig. II.8. The different ellipsometric models used to fit the measured spectra. Models used for SiO_2 films from TEOS and HMDS chemistries (a), (b), and ellipsometric models used for SiO_xN_y films from TDMSA and TSAR chemistries (c), (d).

Throughout the thesis, local thickness and optical properties are calculated by application of a Bruggeman Effective Medium Approximation (BEMA) model, with different combinations of components, as illustrated in Fig. II.8. For SiO_2 films, the Sellmeier and Cauchy models [166] are also used to confirm the thicknesses calculated by the BEMA model (Fig. II.8b). Even though Sellmeier and Cauchy models are extensively used in the literature, they give information only on the thickness and refractive index, disconnected from the material composition. In contrast, the BEMA model makes use of components available in the SE database and assumes that the material is a globally homogeneous mixture of all the components used to describe it. As such, depending on the components applied and their volumetric fraction, additional information such as density or composition can be acquired.

More specifically, for analysis of SiO_2 films, the applied BEMA components were SiO_2 and void. Through this, an approximation of the film density is derived. For analysis of SiO_xN_y films, the applied BEMA components were SiO_2 and Si_3N_4 (Fig. II.8c), with an amorphous carbon component being added (Fig. II.8d) for films where the respective two-component BEMA model failed to conform to the measured spectra due to carbon incorporation. It is noted that the SE database does not include a component for organic carbon moieties and that the amorphous carbon component was used instead, as it gave the closest fit between simulated and measured spectra. In the case of SiO_xN_y films, the volumetric fraction of each component is used to extract information regarding the film composition. For a two-component model, this is done using the following equation:

$$f_1 = \frac{v_1}{(v_1+v_2)} \Leftrightarrow f_1 = \frac{x_1\frac{Mr_1}{\rho_1}}{(x_1\frac{Mr_1}{\rho_1} + x_2\frac{Mr_2}{\rho_2})} \qquad \text{Eq. (II-2)}$$

Where f_1 is the volumetric fraction (vol. %) of component 1 as given by ellipsometry, v_1 its volume, x_1 its molar fraction (mol. %), Mr_1 its molecular weight (g.mol^{-1}) and ρ_1 its density (g.cm^{-3}). The same apply for component 2. For a three-component model (n=3), Eq. (II-2) is further elaborated into Eq. (II-3) to calculate the molar fraction x_i of a component i (where i=1 to n) as follows:

$$x_i = \frac{f_i\frac{\rho_i}{Mr_i}}{\sum_{i=1}^{i=n}(f_i\frac{\rho_i}{Mr_i})} \qquad \text{Eq. (II-3)}$$

After using Eq. (II-3) to calculate the molar fraction of each component, the atomic percentage of each element is then calculated. However, in order to first arrive at the molar fractions through equation Eq. (II-3), the Mr and ρ of each component must be known. For SiO_2 and Si_3N_4, the density and molecular weight values are set equal to 2.65 g.cm^{-3} and 60.08 g.mol^{-1}, and 3.17 g.cm^{-3} and 140.28 g.mol^{-1}, respectively. For amorphous carbon, an atomic weight of 12 g.mol^{-1} is assigned. However, assignment of a density value is difficult. For this reason, accurate composition results by Ion Beam Analyses (IBA) are used as a calibration method in order to define a density value of the amorphous-C component, for which the composition given by SE is close to that measured by IBA. This value was calculated at 0.69 g.cm^{-3}. It is noted though that the composition calculated by SE is only approximate.

A more accurate chemical composition is provided by the use of IBA techniques, performed at the Pelletron facility of CEMHTI in Orléans, France (operator: HEALTHYGLASS post-doctoral researcher Babacar Diallo). The Ion Beam Analysis methods are a group of nuclear methods that allow for the

quantitative analysis and depth profiling (in the order of several nanometers) of the surface layer of films [167]. In the scope of this work, three different IBA methods are utilized, namely Rutherford Backscattering Spectroscopy (RBS), Nuclear Reaction Analysis (NRA) and Elastic Recoil Detection Analysis (ERDA). The contents in silicon are determined by RBS, which provides good sensitivity for the quantification of heavy elements, down to an order of parts per million. However, it cannot provide accurate information for lighter elements. For this reason, oxygen, carbon and nitrogen are measured by NRA, while hydrogen is analyzed by ERDA. Generally, films with a thickness range of 100-200 nm are used for this family of techniques. An overview of the basic principle of each technique is presented in Fig. II.9.
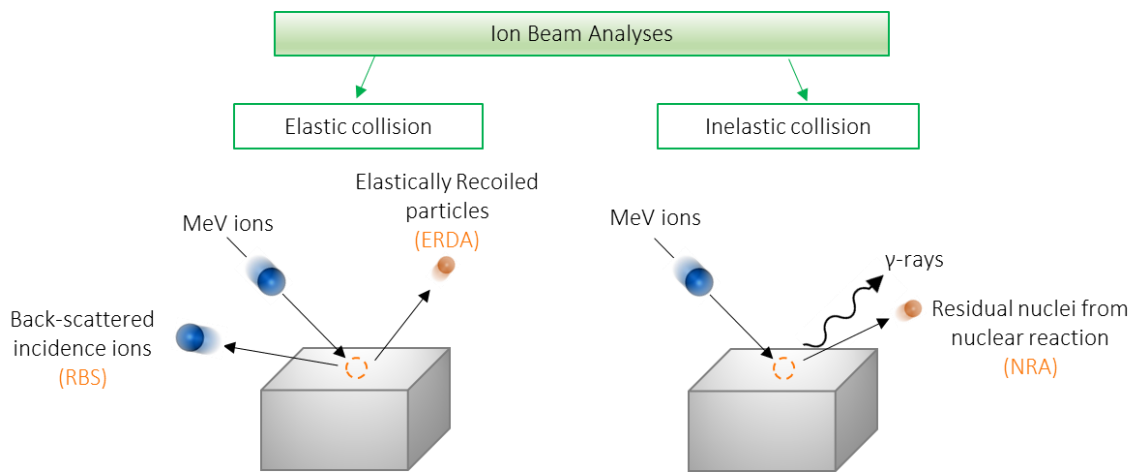
Fig. II.9. Visualization of the three IBA techniques.

RBS and NRA are performed at a 166° detection angle with 2 MeV α particles for the former. Oxygen, carbon and nitrogen concentrations are measured through the $^{16}O(d,\alpha_0)^{14}N$, $^{12}C(d, p_0)^{13}C$ and $^{14}N(d,p_5)^{15}N$ nuclear reactions, respectively, using incident deuterons of 0.9 MeV. ERDA measurements are performed using a 2.8 MeV alpha beam. For the measurement of hydrogen, the sample is positioned at a 15° grazing incidence angle and the recoiled hydrogen atoms are collected at a scattering angle of 30°. Ten spectra of 1μC charge are successively collected to get enough repeatability and intensity, and achieve a satisfactory signal-to-noise ratio. Detector energy calibration is addressed through the use of a polycrystalline silicon wafer with a top layer of 213 nm SiO_2, an a-Si(H^+) hydrogen standard at $2.19 \cdot 10^{17}$ $H.cm^{-2}$, a carbon and a SiC polycrystalline film. The overall composition of the films is obtained by simulating the RBS, NRA and ERDA acquired spectra in the SIMNRA software [168].

II.2.2.3. Chemical bonding state characterization

The chemical bonding in the films is studied using Fourier transform infrared (FT-IR) spectroscopy in transmission mode. A Perkin Elmer Frontier FT-IR MIR/NIR spectrometer located in CIRIMAT (ENSIACET, Toulouse, France) is used, equipped with a custom-made substrate holder that enables the analysis of flat samples at different angles. Training on the operation of the FT-IR equipment was provided by Olivier Marsan. The spectra are taken at the center of each sample, by applying a 0° and 60° angle between the sample and the incident beam (Brewster angle), to clearly observe the transverse and longitudinal optical (TO – LO) splitting, according to the Berreman effect [169, 170]. This effect is easily observable in oxygen rich silica-based films and is an indicator of a predominant silica character [8].

For all samples, the spectral range between 400-4000 cm^{-1} is probed with a resolution of 4 cm^{-1} and 8 cm^{-1} for SiO_2 and SiO_xN_y films, respectively. Up to sixty-four spectrum accumulations are taken after removal of the background signal. After acquisition, the obtained spectral data are further processed by removing the Si substrate signature and correcting the baseline within the Perkin Elmer Spectrograph Quantum software. For the removal of the substrate signal, the Si-Si absorption found at around 610 cm^{-1} is used as a guide and subtraction is executed until its intensity reaches zero.

Further data processing is then executed using Origin 2019 software. In a first step, the absorbance values are normalized by the thickness of each film, since the intensity of the main Si–O–Si absorptions are affected by the film thickness in FT-IR transmission mode, as noted by the Beer-Lambert law [171]. It is noted that probing location (3) indicated in Fig. II.7b has been systematically used for FT-IR analysis. As such, the thickness measured by SE at this specific probing location is the one utilized for absorbance normalization.

In a second step, spectra deconvolution is applied in certain key-areas of interest, such as large bands or shoulders, where multiple absorptions can overlap or even obscure each other. Deconvolution can help distinguish multiple overlapping peaks from each other and help ascertain their individual positions and intensities. The spectra are deconvoluted using the NLFit function in Origin 2019, based on Gaussian curves and with application of the Levenberg Marquardt iteration algorithm. It must be noted that Lorentzian [172] and Gaussian [110, 173] curves are both frequently applied in the literature for this purpose; however the authors do not specify the particular reasons for these choices. During the extent of this thesis, deconvolution conformed better to Gaussian curves and is thus systematically performed as such. A deconvolution is considered successful for a R^2 goodness fit higher than 0.98.

Another characterization technique applied for the study of chemical bonding state is X-ray photoelectron spectroscopy (XPS), performed in a Thermofisher K-alpha system. XPS analysis of films

from TDMSA was carried out in the IRPEM CNRS UMR 5254 laboratory (Université de Pau et des Pays de l'Adour, Pau, France, operators: Yann Tison, Hervé Martinez). Analysis of films from TSAR was performed at Tokyo Innovation Campus (Air Liquide, Tokyo, Japan, operator: Takashi Teramoto). XPS is carried out using an Al K-alpha source (1486.7 eV) with a 20 eV pass energy. Surface measurements are taken as is, after which a stripping step of 30 s is performed using Ar^+ (1000 eV). A low-energy flood gun delivering electrons and Ar^+ ions (<5 eV) to the sample surface is used in order to neutralize the surface charge during data acquisition. The environment of the elements is analyzed through deconvolution and curve fitting of the acquired XPS spectra using CasaXPS$^©$ (operator: Jerome Esvan). The deconvolution focuses primarily on the N1s, C1s and S2p spectra. Silicon carbide (SiC) and silicon nitride (Si_3N_4) references have been utilized to confirm the bond energies and valence of the Si–C and Si–N bonds.

II.2.2.4. Films surface morphology and depth profiling

The surface roughness of the films is measured using an Agilent Technologies 5500 atomic force microscope (AFM) housed in CIRIMAT (ENSIACET, Toulouse, France, operator: Claire Tendero). Analysis is executed in tapping mode. The utilized tip is an APPNANO ACT model, made of n-type silicon, with a <10 nm radius. A scan size of 1 µm² is used for all measurements.

High-resolution micrographs of the films and corresponding energy dispersive spectroscopy (EDS) elemental information are acquired using a JEOL ARM200CF (JEOL Ltd.) transmission electron microscope (TEM) instrument located in CEMHTI (Orleans, France, operator: Cécile Genevois). The TEM is operating at 80 kV. It is equipped with double spherical aberration correctors and fitted with a JEOL SDD CENTURIO EDS system. A 0.13 nm probe size is used for EDS analysis. Before analysis, the cross-section of the films is prepared by focused ion beam (FIB) technique using Ga^+ ions in a FEI HELIOS 600i instrument, located in Centre de Microcaractérisation Raimond Castaing (Toulouse, France, operator: Claudie Josse). After analysis, the samples are immediately sealed and put in a vacuum chamber for at least 24 hours. They are then packaged securely and sent out for TEM analysis. Analysis is performed as soon as possible after FIB preparation to minimize contamination.

II.2.2.5. Mechanical properties and wettability analysis

The hardness and elastic modulus of the films is assessed by nanoindentation tests carried out at CIRIMAT-UPS, Toulouse, as part of the work of Maxime Puyo, post doctoral researcher of the ANR project HEALTHYGLASS, who was supervised by Dr. Viviane Turq. An UltraNanoIndenter apparatus

from CSM Instrument (Anton Paar) equipped with a Berkovich diamond indenter is utilized for these measurements. The applied load is gradually increased until a maximum value of 0.5 mN is reached, at which point the load is maintained for 30 s. The loading and unloading rate is set to 60 mN.min^{-1}. Each sample was probed at 5 different locations. Average elastic modulus and hardness values are calculated from the load vs. depth curves according to the method proposed by Oliver & Pharr [174].

The adhesion of the coatings on Si-substrates is assessed through nanoscratch tests conducted using a Nanoscratch Tester from CSM Instrument (Anton Paar) housed at CIRIMAT-UPS, Toulouse, as part of the internship of Charlotte Lebesgue, master student of the ANR project HEALTHYGLASS, supervised by Dr Viviane Turq. The nanoscratch apparatus is equipped with a spherical diamond indenter (2 μm radius). Scratches were made under a linearly increasing load from 0.3 mN to 100 mN at a loading rate of 20 mN.min^{-1} and with a displacement speed of 1 mm.min^{-1}. Three measurements were taken at different locations on each sample to assess repeatability. Optical microscope (Nanoscratch CSM) and SEM (Vega 3 TESCAN) instruments were used to analyze the results and determine the critical normal loads corresponding to coating adhesivity failures.

The wettability of the films is investigated by measuring pure water contact angle with a GBX apparatus at CEMHTI, Orleans (operator: Babacar Diallo), using Young's equation [175], according to which the value of the contact angle depends only on the chemical composition of the material. Water droplets of 0.35±0.01 μl are placed carefully onto the sample surface at ambient. The equilibrium static contact angle is measured at five different locations. The water contact angle (WCA) value is then assessed by a CCD camera. To obtain the contact angle value affected by the surface roughness, the model described by Wenzel [176] is applied.

II.2.2.6. Assessment of anti-corrosion and barrier properties

The corrosion resistance of the films is evaluated with various methods. In a first step, films are screened by two different fluoride solutions, namely the P-etch solution test developed by Pliskin [177, 178] and the more aggressive Buffered Oxide Etchant (BOE) test. The P-etch solution is well established and widely used in the field of microelectronics for assessing the etching behavior of silica-based films, while the BOE solution is used for the etching of SiO_2, SiO_xN_y and Si_3N_4 films [179, 180]. Multiple other wet etching corrosion solutions can be found in the literature [181]. Such chemical abrasion solutions are used to indirectly assess the quality of a silica-based layer based on their etching rate, which according to Pliskin, is related to the density of the film. As a result, it can be said that the etching rate of a film is

implicitly linked to its porosity, composition and the structure of its network. A chemical abrasion test can thus help derive potential conclusions regarding these properties.

The etching tests are performed by immersion of coated samples at 25°C for 15 to 60 s as illustrated in Fig. II.10a, under continuous stirring of the respective solutions. More specifically, the P-etch solution consists of 3 parts hydrofluoric acid (HF, 49 % m.), 2 parts of nitric acid (HNO_3, 70 % m.) and 60 parts of distilled water. The BOE solution (Sigma Aldrich) consists of 6 parts NH_4F (40 % m.) and 1 part of HF (49 % m.). The etching rate for each sample is determined by measuring the thickness of the film before and after immersion using SE. Ten different locations are probed (Fig. II.10b) and the average thickness loss for a given etching time is then expressed as the etching rate in $Å.s^{-1}$. All etching tests were carried out in CIRIMAT INPT. Training on the handling of hydrofluoric solutions was provided by Alexandre Freulon.
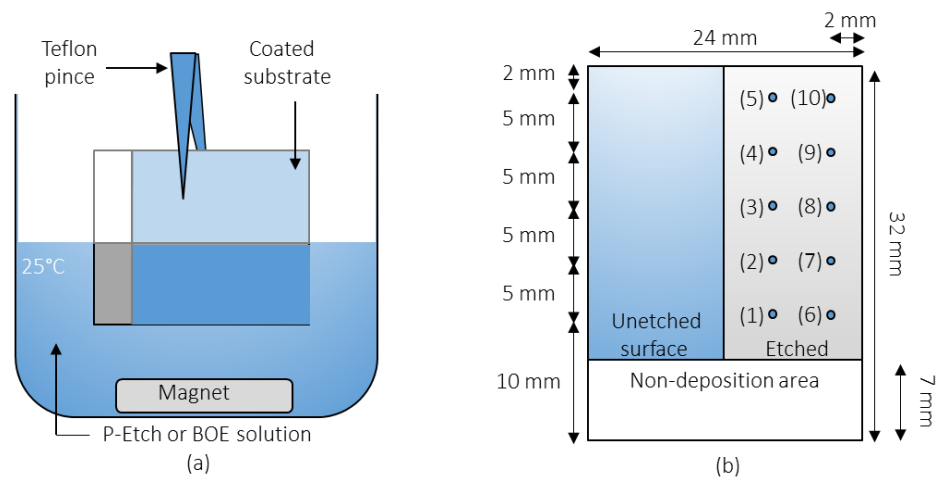
Fig. II.10. Schematic representation of wet etching corrosion test configuration (a) and locations probed by SE for calculation of the etching rate (b).

In a second step, the best performing films from the first screening tests are identified and the operating conditions that produced them are transposed to the vial reactor. The hydrolytic resistance and barrier performance of the produced Type I vials is then assessed according to the protocol suggested in the USP <660> [4] chapter, as recommended by the American and European Pharmacopoeias. The exposure of a coated vial to such solutions leads to the extraction and diffusion of elements from the glass structure, as was discussed in Chapter I. Induced Plasma Optical Emission Spectrometry (ICP-OES) is used to measure the different extractables. The ability of the protective barrier film to prohibit the various elements of the glass to pass to the aqueous solution is evaluated based on comparison of the amount of extractables

noted between it and an uncoated vial. This difference is expressed in a percentage and is referred to as *improvement factor*.

In more detail, the USP <660> test is carried out by first rinsing each vial 3 times using water for pharmaceutical use (WPU). Each vial is filled with WPU up to 90 % of its maximum volume and is then introduced into an autoclave. An isothermal sterilization cycle at 121°C is carried out for 60 min. During the test, the ions from the glass are released into the WPU, especially from regions where the surface of the vial is partially exposed due to non-uniform coating coverage, or if the quality of the coating is insufficient as barrier layer. At the end of the autoclave cycle, 2 vol.% of nitric acid (HNO_3, 65 % m.) (SUPRAPUR Merck) is added to the WPU solution, to limit the precipitation of certain elements. After the above preparation, 10 ml are injected in an Optima 7300 DV ICP-OES spectrometer (Perkin Elmer) located in the R&D laboratory of SGD Pharma (ANR HEALTHYGLASS project partner), by coupling a high frequency induced Ar plasma and a spectrometer. The liquid is injected as an aerosol into the Ar plasma (7000K). When ionized atoms of the solution return to their ground state, they emit a photon, whose energy is characteristic of the corresponding element. Calibration of each extractable allows to quantitatively measure their respective intensities, which is directly proportional to their concentration.

II.3. CFD calculation environment and simulations

The tubular and vial CVD reactors have been replicated in a 3D simulation environment using Computational Fluid Dynamics (CFD) calculations that consider gas phase and solid phase chemical reactions to realistically represent the reactive transport phenomena taking place during the CVD process [182]. The numerical simulations are run using the CFD code ANSYS® FLUENT®, version 18.2, with a cell-centered finite volume scheme and second-order spatial accuracy.

The first step to simulating a process is the replication of the reactor geometry and representation of the reaction chamber in a 3D spatial domain. After description and creation of the geometry, the spatial domain, namely the 3D fluid volume, is discretized in elementary cells within which the solver of the CFD software will execute the numerical calculations and solve the partial differential equations related to the mass, momentum and energy balance equations. In order to do that, the chemical model must be defined within the FLUENT® user interface by implementation of assumptions, reacting species, operating conditions and kinetic laws of the homogeneous and heterogeneous reactions that occur.

After calculation and convergence, post-processing actions are available, aiding the visualization of reaction rate profiles, thermal profiles and local distribution of species mass fractions or concentrations in the spatial domain. Plotting of the results can be performed on lines, surfaces or volumes specified by the user, with the software enabling additional calculations such as surface averages and volume integrals [183]. As such, the post-processing of any desired parameter defined during the implementation step, or after the calculations, is possible. Each of the above steps will be addressed in the following subsections.

II.3.1. *Representation of the reactor geometry*

In order to simulate a CVD process, the volume of the experimental setup, where the reaction process is taking place, must be reproduced in a 2D or 3D domain, depending on the reactor symmetry. This involves the reaction chamber, where the main reactions of interest, such as gas phase reactions and surface reactions leading to film formation, are taking place. As such, parts of the reactor upstream and downstream of the chamber (like supply and exhaust lines) are not simulated. Regarding the reaction chamber itself, all or parts of its volume can be taken into account, depending on the lack or presence of symmetry. In this thesis, the geometry is created using the DesignModeler module of FLUENT®. The sketch of the reaction chamber is created in true-to-size scale with the aid of Computer Aided Design (CAD).

A three-dimensional geometry is considered for the tubular reactor presented in Fig. II.11. The substrate holder utilized in this reactor is simplified in its 3D representation in order to eliminate the sharp edges existing between the separate cylindrical parts composing the holder (Fig. II.11a). Additionally, the substrate holder is extruded until the exhaust of the reaction chamber and any flow underneath the holder is ignored, assuming a solid material instead. These modifications are done in order to reduce the total volume and computational load as much as possible and keep the complexity of the 3D geometry at a minimum, while still maintaining accuracy around the deposition surfaces of interest, i.e. the samples.

Even though the tubular CVD reactor does not present an axisymmetry due to the placement of the sample holder and the configuration of the samples, it does in fact have a mirroring symmetry along the YZ plane. Because of this, only half of the reactor volume is considered for simulation. Additionally, the fluid domain is divided into three segments as shown in Fig. II.11b:

- An inlet segment, starting from the inlet and reaching until 55 mm into the reactor, namely 2 mm before the edge of the first sample,
- An exhaust segment, starting at 58 mm from the inlet and reaching until the outlet,
- A transitional segment connecting the two previous segments, spanning between 55 and 58 mm.

The segmentation of the geometry is performed in order to give the user more control over the meshing parameters, as will be explained in the next subsection.
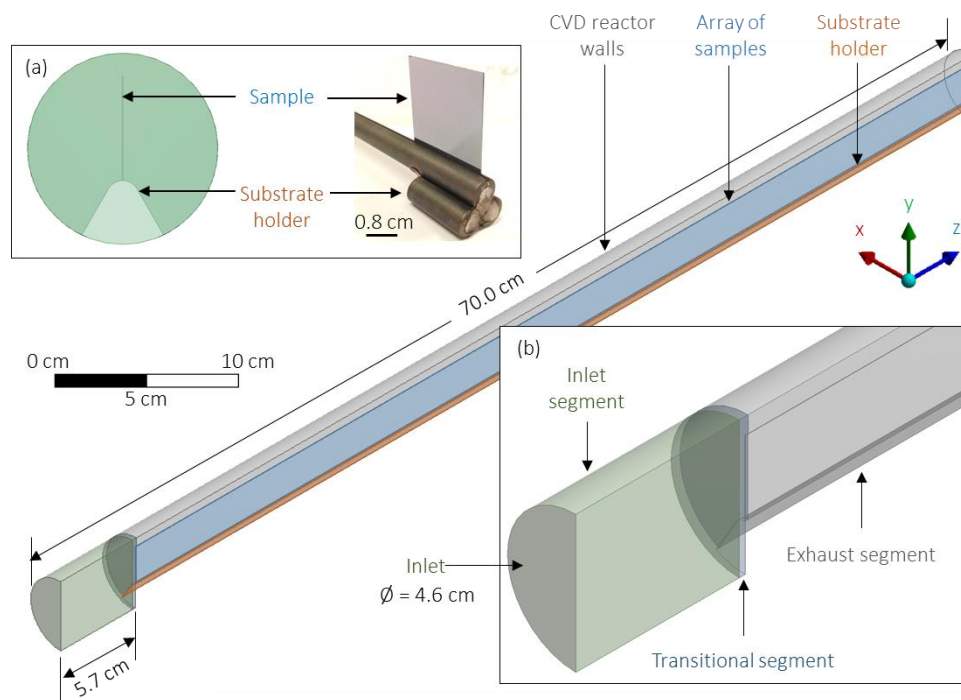
Fig. II.11. 3D geometry of the tubular CVD reactor. Inset figure (a) shows reactor cross-section along the XY plane and photograph of sample placed in the substrate holder, to illustrate the adopted simplifications. Inset figure (b) shows a zoom of the inlet region and the three segments of the geometry. Only half of the reactor is considered due to mirroring symmetry along the YZ plane.

In the case of the vial reactor, a two-dimensional geometry is considered, thanks to the axisymmetry allowing for revolution around it. As such, a 2D transverse cross-section of half of the reactor volume is sufficient to represent the various elements of this particular reaction chamber (quartz tube, injector nozzle, vial and sample holder), as shown in Fig. II.12. A simplification is applied at the region where the nickel foam is placed, with the volume existing above the nickel foam not being simulated. Lastly, the geometry of the vial reactor is segmented into two parts to separate the spatial domain within the nozzle and vial from the spatial domain outside the vial. Similar to the tubular CVD reactor, this segmentation is applied to allow better control of the meshing parameters.
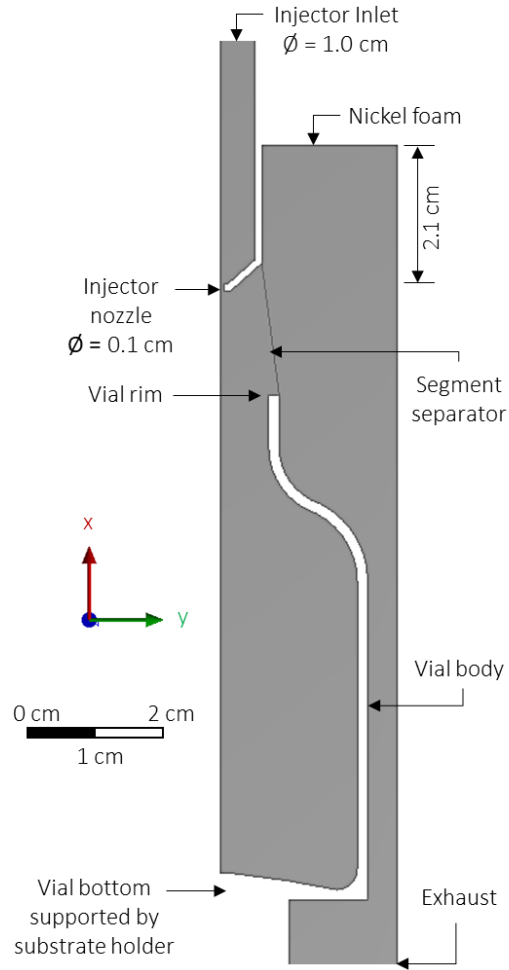
Fig. II.12. 2D geometry of the vertical CVD vial reactor. Only half of the reactor is considered due to axisymmetry.

II.3.2. *Meshing of the geometry and volume discretization*

After recreation of the reaction chamber in a 3D geometry, the spatial fluid domain needs to be discretized in elementary cells. The total sum of these discretized cells constitutes the mesh. Each cell represents a finite volume within which the partial differential equations are solved. Since FLUENT® uses a cell-centered finite element method, the partial differential equations are solved at the centers of each elementary cell and then extrapolated on the 8 nodes (for 3D domains with hexahedral cells). These node values are compared to the values calculated during the previous iteration and the difference between them is expressed as the residual value. The residual values are used as an indication regarding the progress of the simulation and the degree of convergence.

Hexahedral and quadrilateral cells are used for the tubular CVD reactor, while the vial reactor is meshed using 2D quadrilateral cells only. The maximum face sizes of the cells can be defined by the user and, alongside other parameters, allows controlling the size of the mesh and influences the total number of cells. Smaller maximum face sizes increase the total number of cells of the mesh, making it finer. However, this comes to the detriment of the computational time: the larger the total number of cells in a mesh, the longer it will take to solve the partial differential equations. As a result, a compromise must be made between the fineness of the mesh (i.e. total number of cells) and the average computational time. Obviously, the density of the mesh must be high enough in order to achieve good precision and obtain realistic values of local concentrations, reaction rates and so on. However, an overly fine mesh provides no additional value to the simulations precision and merely prolongs the calculation time. As a general rule of thumb, it is advised to refine regions of interest, while giving a lower mesh density to areas that are not critical to the studied system. To execute this, the mesh is oftentimes subdivided in sections, called segments hereinafter, each one adapted based on the particular needs that must be addressed. Such segments can involve regions near the walls and solid surfaces, where the presence of strong concentration gradients requires higher mesh density in order to represent the transfer phenomena and subsequent surface reactions with sufficient precision. Other concerned regions are areas with high velocities and velocity gradients, such as injector nozzles, tight spaces and impacting jets, or areas where the fluid follows a complicated flow profile.

The mesh of the tubular CVD reactor was developed in the frame of the Diploma thesis of George Chliavoras in LGC in 2019 [184] and is presented in Fig. II.13. Larger mesh densities are used in the proximity of all solid walls (quartz tube, sample holder and samples), by activating the "boundary layer gradient" option within the Meshing module of FLUENT®. Additionally, after the segmentation is applied to the geometry, the fluid domain is meshed as follows:

- The inlet and outlet (Fig. II.13a, b) segments are meshed with a hexahedral mapped cell type;
- The transitional segment is meshed with a tetrahedral cell type and a boundary layer gradient wrapped around the sample and substrate holder is applied. The boundary layer of the transitional segment is seamlessly continued throughout the outlet segment.

It is noted that the transitional segment is utilized to accurately resolve the complex flow produced when the fluid flow coming from the inlet segment impacts on the substrate holder and the first substrate.

Additionally, by adjusting the maximum cell size, three meshes of different refinements are created:

- A small mesh of 241,780 cells, with a maximum cell face area of 2.25 mm^2;
- A medium mesh of 980,786 cells, with a maximum cell face area of 1.1 mm^2;
- A big, very fine mesh of 1,927,954 cells, with a maximum cell face area of 0.85 mm^2.

Intermediate meshes are created as well. As such, meshes with different levels of fineness are produced and used to calculate the minimum mesh density for which simulation results become independent from the fineness of the mesh.
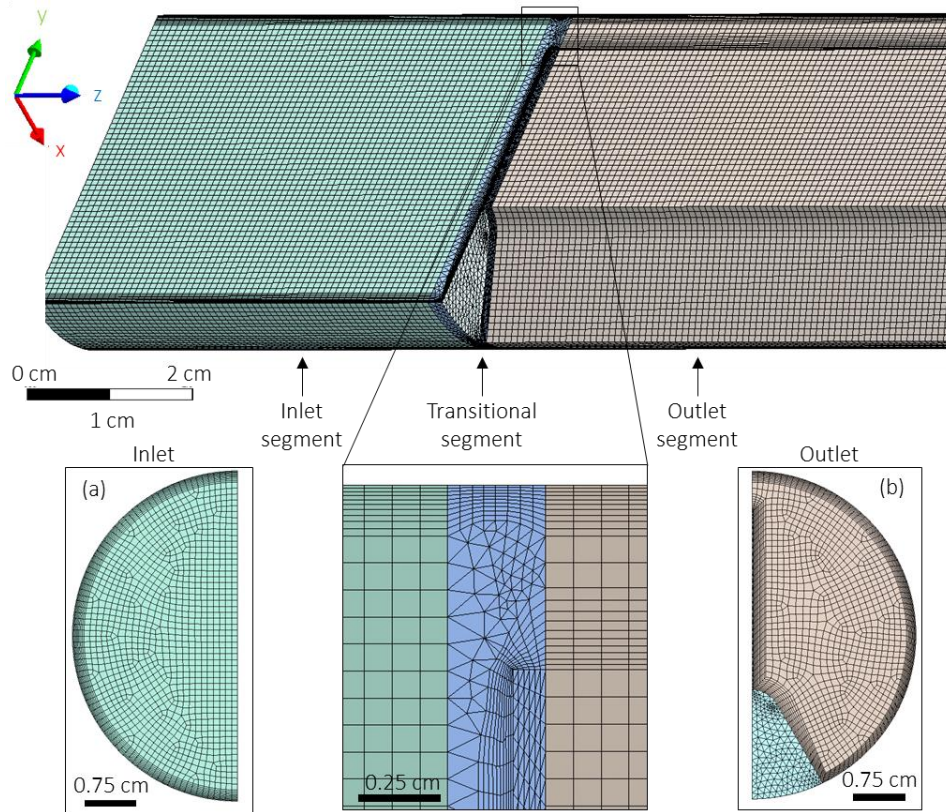
Fig. II.13. Mesh of the tubular reactor. Inlet mesh (a) and outlet mesh (b) are shown separately. Inset magnification illustrates the mesh transition between the three segments.

On the basis of the work of Pierre-Luc Etchepare and Simon Ponton, the discretization of the vial reactor fluid domain is executed as follows. First, a fine mesh is used for the volume contained within the nozzle. This fine discretization also is applied to the volume contained within the vial. A finer mesh is used along the axisymmetry, namely the main trajectory of the impinging jet. Lastly, a coarser mesh is applied to the regions outside the vial. This segmentation of the fluid domain allows the calculation and more accurate representation of the high velocity gradients created by the injector nozzle configuration, without creating additional computational load in regions of low interest.
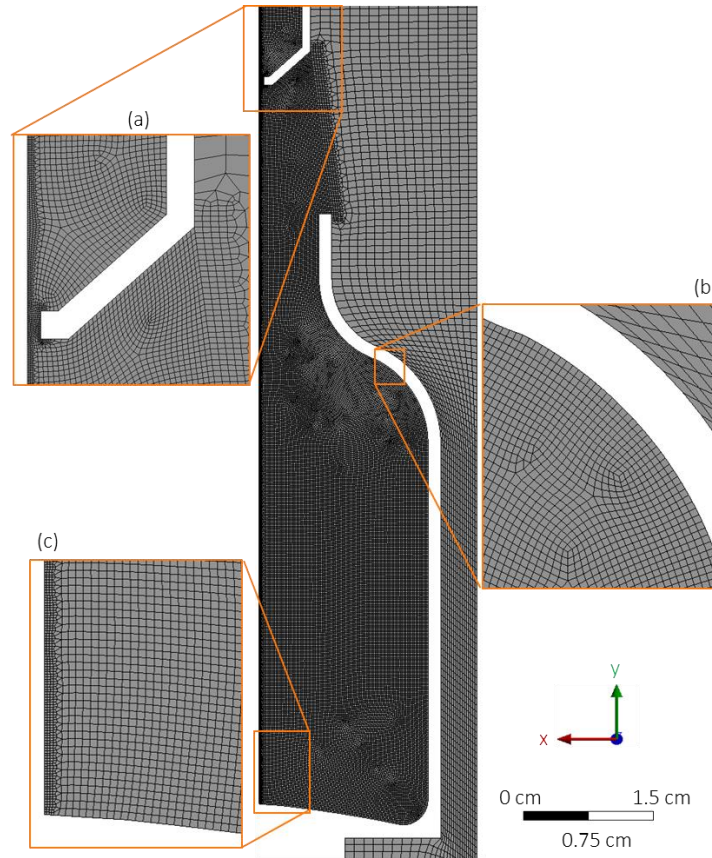
Fig. II.14. Mesh of the vial reactor. Inset figures show magnified regions of the mesh. Injector nozzle (a), vial shoulder (b) and vial base (c).

II.3.3. Considered assumptions

After the creation of the discretized spatial domain (mesh) and before the implementation of a chemical model (i.e. definition of species and reactions), it is imperative to define the hypotheses that will be considered to simplify the numerical complexity. The assumptions are the following:

- − Steady state regime,
- − Laminar gas flow, verified for Reynolds number *Re* lower than 2100;
- − Incompressible gas flow, due to the low value of the Mach number (<0.04) in the reactive zone;
- − Neglected heat of reactions, due to high N_2 dilution of the precursor;
- − Consideration of the gas mixture as an ideal gas.

More specifically, for the tubular CVD reactor a Reynolds number in the 300-400 range is calculated, depending on the operating conditions. The maximum velocity is taken at 40 cm from the inlet,

where the flow is fully developed. The diameter of the quartz tube (4.6 cm) is used as the characteristic dimension. Although the gas flow is clearly laminar in the tubular reactor, the situation becomes more complex for the vial reactor due to the presence of the nozzle. In the latter case, the maximum velocity of the gas phase is calculated at the tip of the injector and the opening diameter of the nozzle (0.1 cm) is taken as the characteristic dimension. A Reynolds number in the 1700-1900 range is calculated for the vial reactor, depending on the operating conditions.

The physico-chemical properties of the gas species, such as viscosity, specific heat and thermal conductivity, are calculated from the kinetic theory of gases in conjunction with the FLUENT® database. Through this, interactions between molecules, assumed to be of spherical shape with negligible diameter, are described. Intermolecular collisions, as well as molecule-solid surface collisions, are considered elastic. Since the kinetic theory is governed by statistical collision calculations, it involves the Lennard-Jones (L-J) parameter σ, which signifies the intramolecular length for which the forces of attraction and repulsion between two similar molecules are equal, and the energy parameter ε/k. These two L-J parameters are defined for each reacting species and are detailed in the respective sections of Chapters III and IV.

II.3.4. Application of boundary conditions

The final step of the pre-processing involves the definition of the boundary conditions, which are set as follows:

- − Inlet: Mass flow inlet boundary condition ($kg.s^{-1}$);
- − Outlet: Outflow boundary condition; zero diffusion flux for all flow variables;
- − Walls (and injector in the case of the vial reactor), samples, and substrate holder: No-slip boundary condition for gas velocity; mass flux density of each species is equated to the corresponding surface reaction rates;
- − Symmetry plane: Symmetry boundary condition at the YZ symmetry plane for the tubular; axisymmetry for the vial reactor; zero flux across the symmetry plane, which is required by the definition of symmetry.

The values of mass flow rate and mass fractions for the two utilized chemistries at the inlet are set in accordance with the respective experimental conditions and are detailed in the respective subsections of Chapters III and IV.

The temperature of all solid surfaces is fixed according to the thermal profiles measured experimentally on the wall of the reaction chamber before deposition. Definition of the temperature of the

solid surfaces allows for the calculation of local temperatures in the gas phase through solving of the energy balance equation. It is noted that due to the steep decrease of the temperature at the exhaust of the reactor, the thermal profile imposed in FLUENT® is modified in order to avoid backflow and delays in convergence. More specifically, a constant temperature is applied for the last 100 mm of the reactor, i.e. between 600 and 700 mm. This temperature is set equal to the one measured experimentally at z=600 mm. The modification of the temperature profile in this specific region does not affect the results, because the samples of interest are located only between 57 and 500 mm from the reactor inlet. Lastly, the temperature of the gas mixture at the inlet is set equal to the value of the thermal profile applied on the walls for z=0 mm.

II.3.5. Post-processing

After calculation, the visualization of the results is done within the FLUENT® user interface, by making use of the various post-processing possibilities that the software allows. As indicated in Fig. II.15, the gas temperature, gas flow velocity, homogeneous reactions and species concentration contours are plotted along the XZ plane that traverses the horizontal middle of the simulated half reactor. The heterogeneous reaction contours are visualized along the YZ plane, as shown in Fig. II.15.
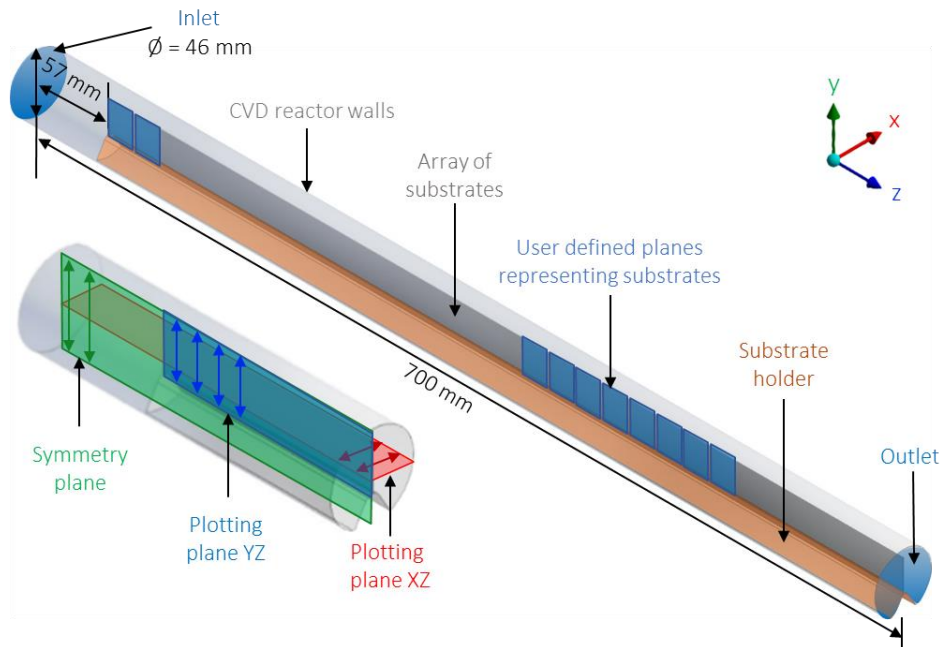
Fig. II.15. Plotting planes and user-defined planes for post-processing in the tubular reactor (not true-to-size representation).

Additionally, during the model development stages, local surface reaction rates and species concentrations are extracted from planes that have been specifically created to represent each one of the 18 samples mounted on the substrate holder (Fig. II.15). The results are taken as area weighted averages. The average calculated values of the surface reaction rates are then compared to the average values measured experimentally by weight (for SiO_2 films), or by ellipsometry (for SiO_xN_y films). As such, a sample-by-sample comparison of the average deposition rates is possible. Lastly, local distributions of temperature or concentration profiles are also plotted along user-defined lines in various regions of interest.

II.4. Conclusion

Chapter II demonstrates the various experimental and theoretical tools that have been implemented in order to produce and characterize SiO_2 and SiO_xN_y films on flat Si coupons, as well as assess their performance as barrier coatings on the internal surface of pharmaceutical Type I vials. The two CVD reactors that are used throughout the present work are showcased and described. The tubular reactor (in horizontal configuration) is used for the initial development of SiO_2 and SiO_xN_y films and constitutes the main reactor with which flat samples are produced to study the properties, composition and morphology of the deposited materials, and for some of them, to develop apparent kinetic models. The vial reactor (in vertical configuration) is dedicated to the development of coatings inside pharmaceutical vials. The selected precursors for SiO_2 and SiO_xN_y deposition are also presented and the operating windows of the various process parameters (gas flows, set point temperatures and pressure) are defined.

The deposition process is coupled with a number of characterization techniques, implemented either on line with the deposition experiments, or post-deposition. These pertain to both gas-phase as well as solid-phase analysis methods. The simultaneous implementation of GC-MS, ESR and NMR techniques is explained, showcasing the means for characterization of the gaseous by-products and radical intermediate species that can emerge during a deposition process. To the best of our knowledge, it is the first time these three analytical methods are coupled with a thermal CVD process. Post-deposition, the produced SiO_2 and SiO_xN_y films undergo a series of multiple solid-phase characterizations. Information on their composition, chemical bonding state and surface morphology is collected using SE, FT-IR, IBA and XPS, among others. Complementary characterizations allow for measuring the films surface wettability and mechanical properties. Assessment of the corrosion resistance of the films in relation to their final application as barrier layers is carried out through their subjection to wet etching corrosion tests involving hydrofluoric solutions. The barrier performance is then evaluated in accordance with the recommendations of the USP <660>

chapter. This extensive analysis of the deposition process and the produced films is made possible thanks to the involvement of all partners participating in HEALTHYGLASS project, funded by the ANR. Additionally, internship, engineering and post-doctoral contracts initiated in the frame of this project also provided indispensable results. Multiple external partners were involved as well, providing valuable information, alongside fruitful discussions and collaborations.

In the final part of Chapter II, the required steps for the simulation of the deposition process are explained. Simulations are carried out using the ANSYS® FLUENT® version 18.2 software. Initially, the geometry of each reactor is replicated in a 3D spatial domain. Steps undertaken to discretize this domain in finite cells are presented. The imposed assumptions and boundary conditions are detailed, as required for the definition of the simulation environment within the CFD code. After definition of the computational system using the above, calculation of the gas pressure, temperature, flow velocity and mass fraction profiles is made possible, the simulation of which will be used in an iterative process for the development of kinetic models in the chapters that follow.

Chapter III. Deposition of SiO_2 and SiO_x barrier coatings from O_3 based chemistries

The present chapter details the deposition experiments of silica films from O_3-based chemistries on flat substrates and pharmaceutical vials, as well as the development of a kinetic model for the simulation of the silica deposition process. Deposition of SiO_2 and SiO_x from TEOS-O_2/O_3 and HMDS-TEOS-O_2/O_3 chemical pathways is explored in a first step, serving as a basis for developing the methodology that will be applied throughout the present thesis as a means to establish the correlation between process, structure, properties and performance. Although reports on the APCVD of SiO_2 from TEOS-O_2/O_3 exist in the literature, they concern in their majority cold-wall reactors, with configurations, operating conditions and gas residence times different from those of interest for the present study. Thus, deposition of SiO_2 and SiO_x is initially carried out on planar substrates to facilitate characterization. The link between composition, properties and network densification is studied as a function of the deposition temperature and annealing post-treatment. The corrosion and hydrolytic resistance of the produced films are assessed by subjection to wet etching corrosion and USP <660> tests. Performance is evaluated and correlated back to structure-properties links.

In the frame of a multidisciplinary approach, the deposition rates (DR) of the films are used for the development of an apparent kinetic model for the deposition of silica using a thermal CVD process. The developed model is first validated in shape using visual comparison of the predicted and as-produced deposition profile patterns. Secondly, it is validated in value, through comparison of the calculated thickness profiles to the local thickness values probed at these areas by ellipsometry. After validation, the developed kinetic model is then transposed in the geometry of the vial reactor, as a means to investigate its suitability to be used in reactors operating on one hand within the probed process window, but featuring vastly different geometries and residence times on the other. Potential routes for optimization of the deposition process are also suggested.

All results extracted from the deposition of SiO_2 and SiO_x films by APCVD, carried out within the desired operating margins, are used as a reference point for the deposition of SiO_xN_y from original precursors.

III.1. Deposition of SiO₂ from TEOS-O₂/O₃

Deposition of silica films on planar substrates was performed in the tubular CVD reactor described in Chapter II. Four set-point temperatures (SPT) were tested for the TEOS-O_2/O_3 chemistry, namely 400°C, 450°C, 500°C and 550°C, under a constant pressure of 730 Torr. Applying a SPT creates a thermal profile in the tubular reactor, which consists of four zones as shown in Fig. III.1. First, a small isothermal zone (A) is present very close to the inlet of the reaction chamber. After it, a non-isothermal region (B) is encountered, within which the temperature increases steeply to reach the SPT. Once the SPT is reached, a third zone, namely the isothermal region (C), is defined, spanning from 36 to 50 cm. After the isothermal region, a fourth and final region (D) is encountered at the outlet of the reaction chamber, with the thermal profile decreasing abruptly back to temperatures close to those of zone A. These four zones characterize the thermal profile regardless of the SPT applied.
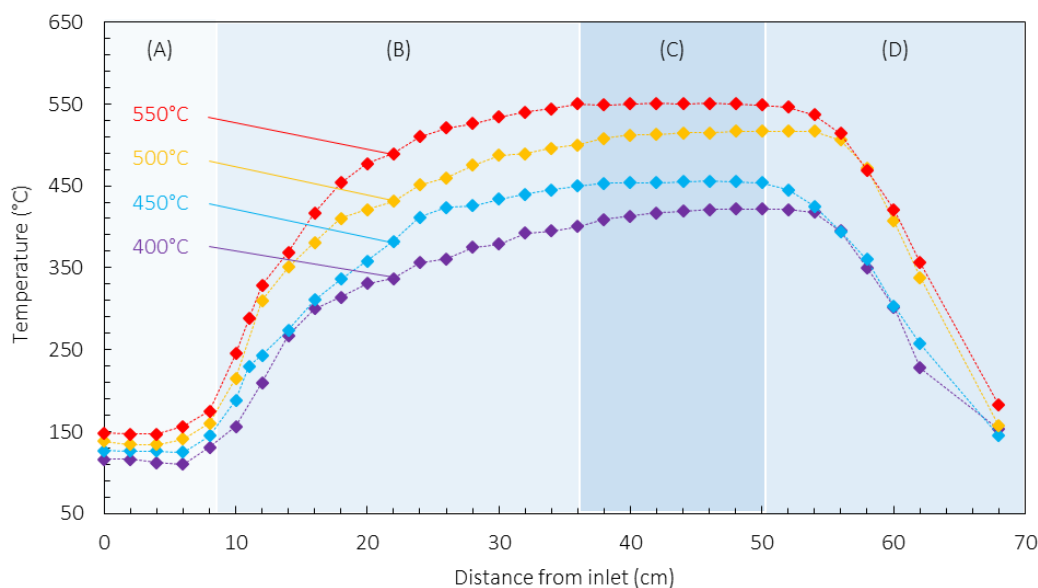
Fig. III.1. Thermal profiles for the four SPT 400, 450, 500, and 550°C. Regions (A), (B), (C) and (D) indicate the inlet region, the steep gradient-increase region, the isothermal region, and the outlet gradient region, respectively.

The presence of such thermal gradients was used deliberately: it allows for the simultaneous deposition of films with varying combinations of local gas phase composition and local temperature, increasing as such the information that can be obtained with one single experiment. For example, O_3-based

chemistries are highly active at low temperatures, thus samples located in regions A and B are essential for the investigation of reactions in which O_3 has a direct contribution. Similarly, DRs observed in the isothermal region C are utilized to develop reactions that govern secondary stages of silica deposition. Such information facilitates the study of the potential chemical mechanisms that can take place in the reactor. For material characterization however, the evolution of the gas phase composition along the reactor length can complicate interpretation. For that reason, material characterization is carried out on samples that have been produced in the isothermal region C, unless stated otherwise. Additionally, in order to minimize locality effects, the same sample position is systematically probed across specific characterization methods.

As a closing remark, no samples are placed in the outlet gradient region D.

III.1.1. Deposition on planar Si-substrates

III.1.1.1.   Deposition rates

The main experimental parameters for SiO_2 depositions from the TEOS-O_2/O_3 chemistry are summarized in Table III.1.

Table III.1. Experimental conditions of the TEOS-O_2/O_3 chemistry tested in the tubular CVD reactor.

Run	SPT (°C)	N₂ flow rate through TEOS bubbler (sccm)	TEOS flow rate (sccm)	N₂ dilution flow rate (sccm)	Deposition time (min)
E1	400	444	10	1632	30
E2	400	223	5	1853	30
E3	400	89	2	1987	50
E4	450	89	2	1987	90
E5	500	89	2	1987	30
E6	550	89	2	1987	30

Through runs E1 to E3, the influence of the TEOS flow rate is evaluated for a SPT of 400°C. The total flow rate is fixed at 4036 sccm. Photographs of the sample holder loaded with five to six silicon samples produced under variable TEOS flow rates (runs E1 to E3) is presented in Fig. III.2. The films exhibit an evolving iridescence, as is expected from the interaction between the gradient thickness of the

films and the light. Generally, a quick alteration in iridescent colors is an indication of a non-homogeneous thickness that presents gradients larger than 100 nm within the observed zone [185]. As such, the "richer" the color palette, the higher the thickness variations.
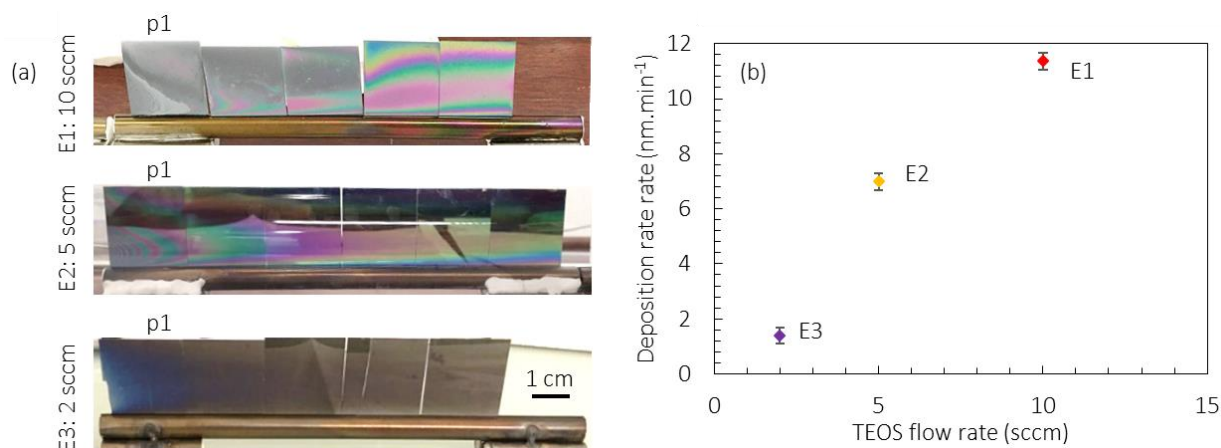
Fig. III.2. Photographs of samples after deposition experiments E1 to E3, using different TEOS flow rates (a). DR values measured through mass gain on sample p1 for runs E1 to E3 (b).

Globally, deposition is observed for all three tested TEOS flow rates (Fig. III.2a). It is noted that for 10 sccm of TEOS, the films have a very high thickness. Visually, this is confirmed by the following observation: once the thickness exceeds a certain threshold, the films lose their transparency and iridescence, appearing as greyish/white instead. This is a result of an elevated DR, which leads to an increase in surface roughness that consequently scatters the light. Additionally, it reveals the appearance of powdering phenomena due to particle generation, which is common for the reactive O₃ chemistry [114]. Measurement of the thickness by ellipsometry is not possible on such samples. In contrast, run E3 presents a milder iridescence, indicating more homogeneous deposition and lower variations in thickness, devoid of powder formation. The DR of sample p1 across the three experiments is presented in Fig. III.2b, indicating the influence of the precursor flow rate. It appears that for the tested range of flow rates, the DR of silica evolves almost linearly with the latter. From the results of runs E1 to E3 it was deduced that a TEOS flow rate of 2 sccm (run E3) can lead to satisfactory DRs, while avoiding the formation of powders noted in E1. Moreover, film thickness appears more uniform than in E2. For these reasons, a TEOS flow rate of 2 sccm has been used systematically for the rest of this thesis.

In a next step, after fixing the TEOS flow rate at 2 sccm, the DR of silica was investigated as function of the SPT. Fig. III.3 presents the DR of TEOS-O_2/O_3 films along the length of the tubular reactor (i.e. distance from the reactor inlet), processed under the four different SPTs (runs E3 to E6). For a SPT of 400°C (Fig. III.3a), the DR first increases in the inlet region A, measuring 9 nm.min^{-1} once the temperature reaches approximately 250°C. After this point, it decreases even though the thermal gradient shows an increase. The DR then settles down to an almost stable value within the isothermal region C.

A qualitatively similar behavior is observed for the other SPTs. For runs performed under a SPT of 450°C, 500°C and 550°C (Fig. III.3b-d), the DR reaches maximum values between 11 and 13 nm.min^{-1} at temperatures between 150 and 200°C. Another observation is that the maximum DR is shifting closer to the inlet when SPT is increased, e.g. the maximum DR is observed at 12 cm for SPT 400°C, but at 6 cm for SPT 550°C. Once the respective maximum DR values have been reached, the DR decreases and remains almost constant within the isothermal region.
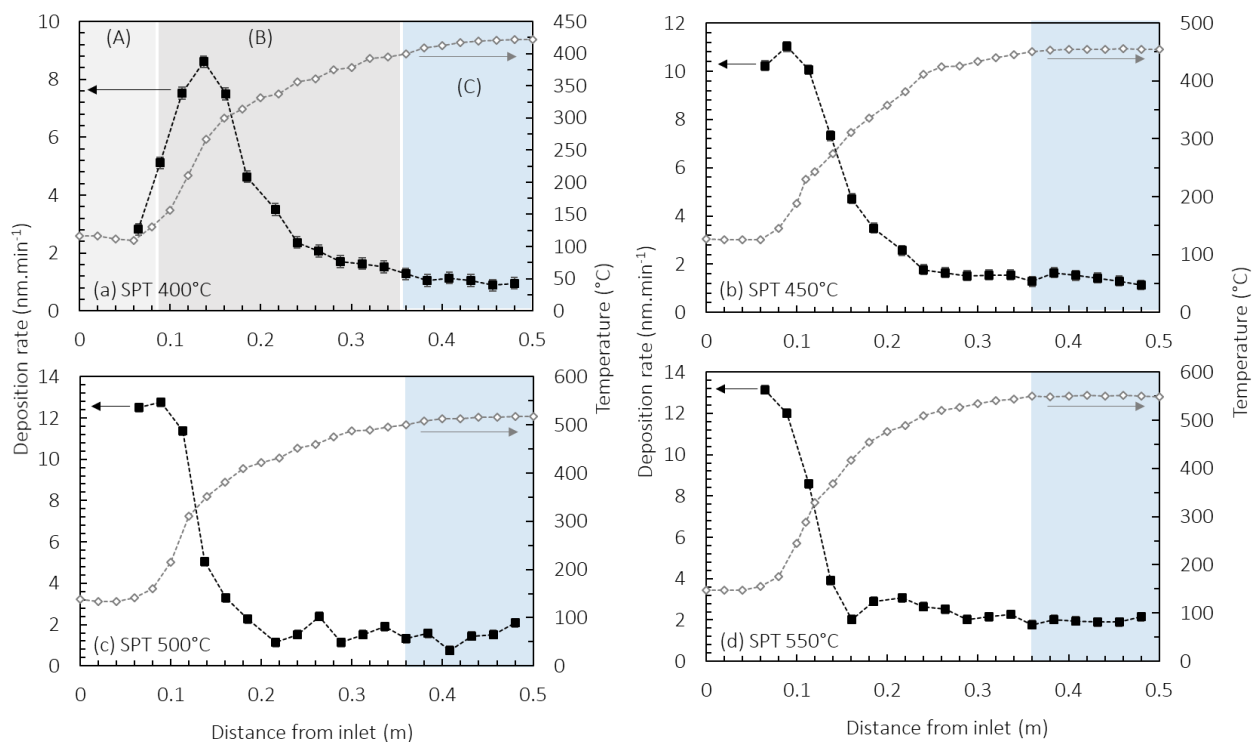
Fig. III.3. DR profiles (black squares) for TEOS-O_2/O_3 deposition at a SPT 400°C (a), 450°C (b), 500°C (c) and 550°C (d), along with the respective thermal profiles (grey diamonds).

Blue area signifies the isothermal region.

The above-described trends are explained as follows. First, the increased DRs in region A are attributed to the relatively high concentrations of O_3, resulting in deposition even at low temperatures. The latter is the result of the facile generation of monoatomic oxygen radicals through O_3 thermal decomposition [117]. In region B however, the DR decreases despite the increase of the temperature, reaching a constant value between 1.5 and 2 nm.min^{-1}, depending on the SPT. This behavior is due to the rapid consumption of O_3 in regions A and B, both due to reactions that lead to film formation and to the production of intermediate gas-phase by-products. As such, the quantity of O_3 that is available in region B is constantly diminishing. For the remainder of region B and then region C, the DR remains low and almost constant, with film formation possibly being dictated by the involvement of silicon-containing intermediate species, which have been produced uphill in the reactor. These species stem from the decomposition of the TEOS precursor after its reaction with O_3 and can lead to film formation once they overcome their respective activation steps. Multiple such intermediates can be produced through gas phase reactions that involve TEOS, O_2 and O_3 [151].

The above raises however the following question: if TEOS is transformed into a variety of silicon-containing intermediates, why is the DR not increasing between regions B and C, given that the increase in temperature from one region to the other should promote film formation? It has been proposed that at higher temperatures (>450°C), intermediates from TEOS participate in parasitic reactions, such as gas-phase polymerization, which lead to the production of large siloxane-chain molecules that do not participate in film formation [158, 186]. As a result, silica deposition is decelerated.

III.1.1.2.   Network structure and evolution

The evolution of the silica network with increasing temperature is shown in Fig. III.4a, as measured by FT-IR on sample p1. Various vibrational modes of the –Si–O–Si– bridge are active and can be easily observed in the 400-4000 cm^{-1} spectral range. More importantly, they are also directly linked to the structure, arrangement and level of densification of the silica network, as will be discussed in detail below.

The overall FT-IR survey spectrum is divided in two main sections: the fingerprint region between 400-1400 cm^{-1}, containing absorptions characteristic to the silica network [187], and the 2800-3800 cm^{-1} region, containing absorptions related to molecular water and Si-OH groups. The second region is referred to as the *hydrated network band* or *hydrated region* hereinafter.

First, the three main vibrational modes of the –Si–O–Si– bridge are identified in the fingerprint region of Fig. III.4a. More specifically, the transverse optical, out-of-plane rocking (TO1) and bending (TO2) modes of the –Si–O–Si– bridge are found at ca. 450 cm^{-1} and around 800-810 cm^{-1}, respectively

[187]. The strong absorption at 1074 cm^{-1} is attributed to the Si–O–Si transverse optical asymmetric stretching mode (TO3) [99, 187]. These three absorptions are characteristic of the silica network and relate to the displacement of atoms after a change in their dipole moment. The TO1 mode is usually minimally impacted by structural changes in the silica network. In contrast, the TO2 and TO3 modes are more sensitive to network modifications, as is discussed below. A fourth transverse optical absorption (TO4) can be observed at lower incidence angles (0°), appearing as a shoulder between 1100 cm^{-1} and 1250 cm^{-1}, and has been linked to various phenomena, among which strains in the network [188] or out of phase vibrations of the TO3 mode [189, 190]. However, when inspecting the spectrum at a 60° angle, the interaction of the electromagnetic field with the film changes and the TO4 peak is obscured under the resulting separation of the main Si–O–Si asymmetric stretching absorption into the transverse (TO3) and longitudinal (LO3) optical components at approximately 1074 cm^{-1} and 1234 cm^{-1} [169]. This split is also known as the Berreman effect [170, 191]. The non-Gaussian shape of the LO3 peak is noted, indicating that additional vibrations contribute at these frequencies. Such contributions found between the TO3 and LO3 peaks have been speculated to originate from the presence of the TO4 mode and its LO4 pair [169].

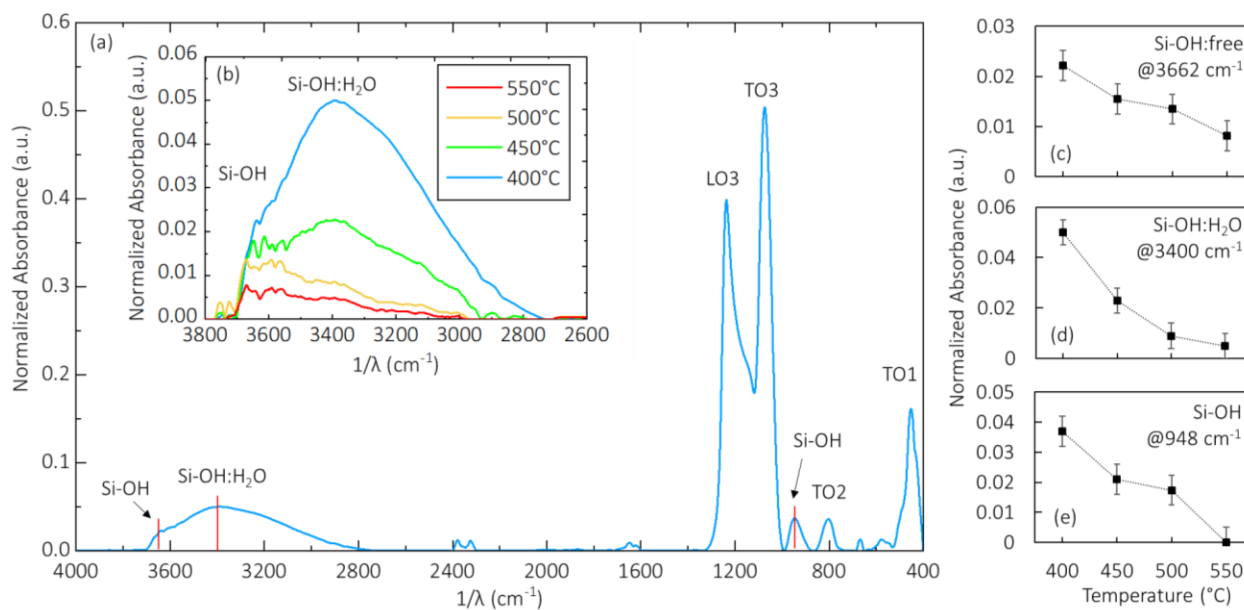Fig. III.4. FT-IR survey spectrum of a SiO₂ film deposited from TEOS-O₂/O₃ at 400°C, analyzed for an incidence angle of 60° (a). Inset diagram shows the evolution of hydrogen related bonds in the 2600-3800 cm^{-1} range (b). Supplementary diagrams track the change in intensity of the free silanol at ~3660 cm^{-1} (c), the water-bonded silanol (d) and free silanol at 948 cm^{-1} (e) as a function of the SPT.

As shown in Fig. III.4a, additional vibrational modes are also detected in the 400-4000 cm^{-1} spectral range. Starting from low wavenumbers, two weak absorptions are noted at 578 and 668 cm^{-1}, relating to impurities [192]. Another absorption is noticeable at 948 cm^{-1}, assigned to silanol (Si–OH) groups [188]. Moving towards higher wavenumbers, a weak absorption at around 1620 cm^{-1} is encountered, attributed to molecularly adsorbed water that can be removed by heating [193, 194]. Next, weak absorptions are observed at around 2400 cm^{-1}, pertaining to atmospheric CO$_2$ probed due to insufficiently removed background signal [195, 196]. It is worth noting that no Si–H absorption, normally appearing in the 1900-2200 cm^{-1} spectral range, was observed in any of the spectra [197, 198]. Lastly, the hydrated network band is observed at 2800-3800 cm^{-1}. It is known that Si–OH terminated silica films readily absorb water after exposure to air [156]. Thus, FT-IR absorptions at these frequencies for the produced SiO$_2$ films are not surprising. The large distribution of this band is explained by the presence of hydrogen bonds across water molecules and/or silanol groups [199]. Two types of silanol groups are distinguished: Si–OH bonded with water through hydrogen bonds is probed at ca. 3400 cm^{-1} [186, 200, 201], while the stretching OH vibration of hydrogen-bond free silanol groups are probed at ~3650 cm^{-1} [186, 202, 203]. The silica network can thus be described as cross-linked tetrahedral units interrupted by the additional presence of various hydrated species (i.e. Si–OH and water).

The evolution of the hydrated network band is presented in in Fig. III.4b. The broad absorption at around 3400 cm^{-1} (molecular water bonded to Si-OH) dominates the signal for low temperatures, but its intensity decreases markedly with increasing temperature. At the highest SPT tested (550°C), its intensity is significantly low, with the absorptions between 3550-3650 cm^{-1} becoming more apparent instead. The intensity of the various hydrated species is presented as a function of the SPT in Fig. III.4c-e. At higher temperatures, their concentrations decrease, with previous Si-OH bonds in the bulk of the film being transformed into new Si–O–Si bridges. Such cross-linking can be confirmed by tracking the evolution of the TO2, TO3 and TO4 absorptions. In order to include the TO4 mode in this particular discussion, the FT-IR spectra of the films were analyzed at a zero incidence (0°). A zoom on a part of the fingerprint region focusing on the TO2, TO3 and TO4 modes is presented in Fig. III.5.

Four different types of vibration modes are encountered in the spectral range 750-1300 cm^{-1} (Fig. III.5). The most intense absorption peak at 0° is the TO3 mode of the amorphous SiO$_2$ network, centered at ~1070 cm^{-1}. The neighboring TO2 vibrational mode at 800-810 cm^{-1} evidences the chemical bonding between the SiO$_4$ tetrahedra [204]. The intensity of this specific vibrational mode increases with the temperature, indicating the formation of additional SiO$_4$ tetrahedra. Simultaneously, the evolution of the Si-OH groups probed at 948 cm^{-1} is opposite to that of the TO2 absorption and decreases with increasing temperature. It can be concluded that for higher temperatures, the concentration of Si–OH groups in the

films decreases, with parallel increase of the chemical bonding between the SiO_4 tetrahedra, confirming our previous conclusion, which stated that the Si–OH groups are dissociated in favor of new Si–O–Si cross-linking. Consequently, the network becomes less hydrated and denser.
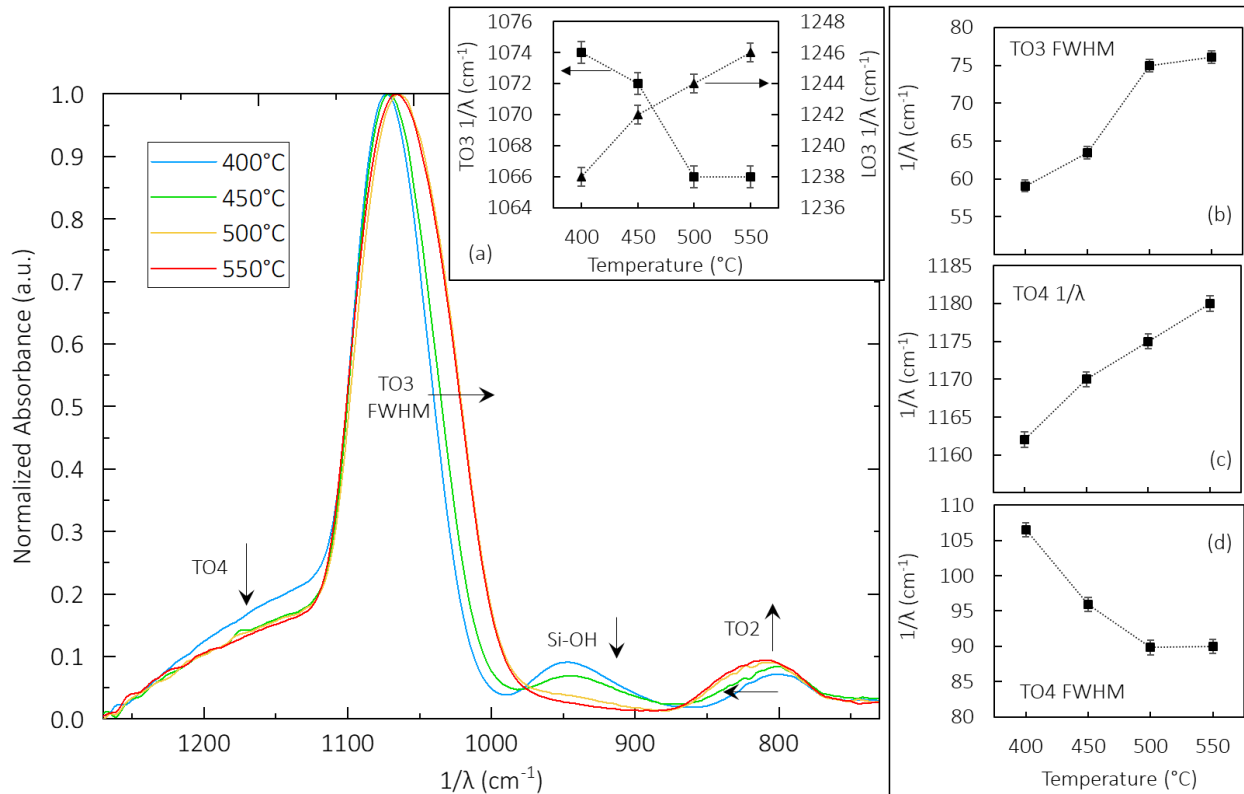
Fig. III.5. Evolution of the FT-IR spectrum of TEOS-O₂/O₃ films deposited at various SPTs, analyzed for an incidence angle of 0°. Inset diagram (a) shows the evolution of the TO3 and LO3 components, as observed for an incidence angle of 60°. Right hand-side inset diagrams show 0° angle evolution of the TO3 full width half maximum (b), the TO4 position (c), and the TO4 full width half maximum (d) as a function of the SPT, after deconvolution.

Further confirmation for the densification of the network can be established through inspection of the TO3, LO3 and TO4 vibrational modes. We will start with discussing the TO4 mode, which is only visible at 0°, noted as a shoulder between 1100 and 1250 cm⁻¹ [189, 190, 205]. It is suggested that the TO4 vibration is linked to the presence of nanoporosity [189, 206-208], or to impurities found in the atomic environment of the Si–O–Si bonds, related to residual TEOS precursor, water or silanol [172]. Their presence leads the affected Si–O–Si bonds to vibrate at the TO4 frequency instead of the typical TO3 one,

and globally signifies the deviation from a perfectly pure, stoichiometric and dense silica. It is noted that multiple factors contribute to the TO4 absorption, making it difficult to link it to one single, specific origin. However, it can be used as a way to define the general structural disorder of the network [209]. As is observed in Fig. III.5, the intensity of the TO4 mode decreases with increase of the temperature, suggesting that the organization of the silica network improves, leading to a redistribution of the Si–O–Si bonds in favor of the TO3 vibration. Consequently, this redistribution affects the position and broadening of the TO3 mode, as will be discussed below.

The evolution of the TO3 position is illustrated in Fig. III.5a, presenting a shift towards lower wavenumbers for increasing temperatures. Normally this would translate to lower levels of densification of the silica network, explained based on the higher bond-length. However, for films processed or annealed below 600°C, this trend is commonly reported in the literature and has been linked to a densification of the network despite the above [8, 172, 177, 189, 210-212]. It is generally proposed that below 600°C, this unorthodox behavior of the TO3 absorption is strongly impacted by film defects (impurities, sub-stoichiometry, etc.) and is biased by the TO4 shoulder. For temperatures above 600°C, the influence of all these factors is lower, to an extent that they do not interfere with the position and intensity of the TO3 peak.

It stands to reason that an ambiguity could be argued regarding the meaning of this reverse evolution of the TO3 position. As such, the position of its LO3 pair is also tracked in Fig. III.5a, given the fact that it is less impacted by film defects and the various other factors that influence the TO3 mode [8]. The LO3 absorption presents a monotonous shift towards higher frequencies as the temperature increases, clearly indicating the densification of the network.

As a final argumentation in favor of the proposed network densification at higher temperatures, the full width at half maximum (FWHM) of the TO3 and TO4 modes is also plotted in Fig. III.5b and d, respectively. It is revealed that a broadening of the TO3 peak is accompanied by a simultaneous shrinking of the TO4. The decrease in TO4 FWHM is readily associated with the further organization of the network [213], which is in good agreement with the results discussed so far.

As a closing remark to the FT-IR analysis, it is underlined that vibrations linked to carbon functions such as –CH₂ [89, 214], –CH₃ [215, 216] or Si–C [206, 214] found at around 2900, 1260 and 800 cm⁻¹ respectively, were never identified in any of the samples produced by the TEOS-O₂/O₃ chemistry.

III.1.1.3. Film composition

Nuclear analyses were carried out to determine the atomic composition of the films. The evolution of their hydrogen content as a function of the SPT is shown in Fig. III.6, along with the respective O/Si

atomic ratio. The hydrogen content decreases with increasing temperature from 7.8 at.% at 400°C, to 4.5 at.% at 550°C. The O/Si total atomic ratio remains at approximately 1.9 between 400°C and 450°C, above which it slightly increases to reach around 2.2 at 550°C. Values above 2 could originate from the presence of non-bridging oxygen or excess oxygen concentration originating from impurities vibrating at the TO4 frequency or surface pollution (C=O groups). The observed increase in stoichiometry can be explained in light of the previously discussed FT-IR spectra. First off, the incorporation of the hydrogen-involving species Si–OH and H_2O were observed to decrease with the temperature (Fig. III.4c-e). It is therefore logical to encounter a decreasing at.% H content in parallel to the increase in stoichiometry.
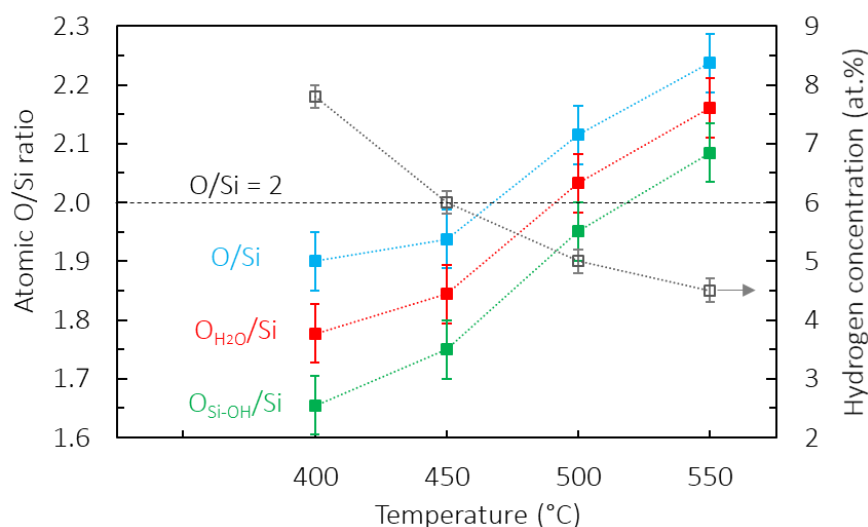
Fig. III.6. Silica film stoichiometry and hydrogen concentration (empty squares) as a function of the SPT. The O/Si ratio is presented as measured (blue squares) and after correction of the O concentration by considering its involvement in water (red squares) or silanol groups (green squares).

In a purely exploratory manner, the evolution of the O/Si atomic ratio is corrected by subtracting from the total oxygen content the atomic percentage of hydrogen that is found in the identified hydrogen involving groups. Two extreme cases are considered. In the first case, all hydrogen is assumed to be involved as molecular H_2O, in which case an atomic concentration of ½ at.% H is subtracted from the concentration of oxygen to recalculate the O/Si atomic ratio (named O_{H2O}/Si hereinafter). In the second extreme case, all hydrogen is considered as being found only in silanol groups, Si–OH. As such, the atomic concentration of H is assumed to occupy an equal atomic concentration of O. Thus, the total at.% H is

subtracted from the total oxygen concentration to recalculate the O/Si atomic ratio (named O_{Si-OH}/Si hereinafter).

The corrected atomic ratios of these two cases are also presented in Fig. III.6. An increasing trend continues to exist, however the calculated O_{H2O}/Si and O_{Si-OH}/Si values are lower than the original O/Si ratio, as expected. It is noted that for the case where all hydrogen is considered as Si–OH, the O_{Si-OH}/Si ratio is as low as 1.65 at 400°C. This value increases to almost 1.80 for O_{H2O}/Si, which seems more realistic when taking into consideration that the FT-IR data reveal a considerable amount of water in the films for this temperature (Fig. III.4b). As such, it is possible that at low temperatures, the network hydration is mostly due to incorporation of water, which is known to be a common by-product of SiO_2 production from TEOS and O_2 or O_3 [155]. At higher temperatures, a ratio of 2.16 and 2.08 is noted for O_{H2O}/Si and O_{Si-OH}/Si, respectively. Recalling the FT-IR spectra of Fig. III.4b, we see that the water absorption decreases drastically with the increase of the temperature. Additionally, the Si–OH stretching vibration at 948 cm^{-1} (Si–OH bonds in the bulk of the film) becomes null at 550°C, while surface free Si–OH are only weakly probed in the large 2800-3800 cm^{-1} band. Considering the above points, it is assumed that hydrogen is encountered mostly as surface Si–OH at higher temperatures, and as such the 2.08 value of the O_{Si-OH}/Si is considered more reliable. A similar conclusion was drawn by Hirashita et al. [217], who studied the gas desorption during heating of silica films produced by PECVD. According to the authors, at low temperatures (100-300°C in their case), gas desorption was attributed to water adsorbed in the macropores after an exposure to air, while at higher temperatures (350-650°C), gas desorption originated mainly from the presence of silanol groups in macro- and micropores.

The above assumption is also supported by the evolution of the refractive index (RI) as calculated by two different ellipsometry models (Cauchy and BEMA models) shown in Fig. III.7. The RI at 400°C measures ca. 1.453, decreasing to 1.447 at 500°C, after which it increases again to 1.450 for 550°C. This behavior is explained by considering the previously raised points. First, it is recalled that the produced silica films can present nanoporosity, as evidenced by the TO4 mode. In the literature, such nanoporosities have been defined to be as large as 4 to 6 Si–O–Si units [188, 189, 208]. These nanopores can be readily filled with water. Second, higher temperatures favor the desorption of H_2O and reduce the overall Si–OH concentration in the films, leading to new –Si–O–Si– bridges and increasing network cross-linking, as was presented by FT-IR.

Based on the above, the following explanation is suggested: As a basis, any sub-stoichiometric SiO_2 film, meaning a film in which part of the oxygen concentration is involved in hydrated species such as H_2O and Si–OH, has a RI below 1.458 (i.e. the RI of stoichiometric silica). Values below 1.458 are observed for all the produced films, which correlates well with the identification of hydrated species. The

decrease of the RI between 400°C and 500°C is then attributed to the desorption of water (either surface adsorbed or trapped in the nanoporosities) [218]. In the case of nanoporosities, such a desorption leads to the replacement of water by vacuum in the nanopores. Taking into account that the RI of vacuum is 1 and of water 1.332, desorption of water from the nanopores would result in lower RI values. Since a decreasing RI is indeed observed between 400 and 500°C, this hypothesis stands correct. Further confirmation is given by the decreasing trend of the H_2O and the increasing trend of the void components applied in the BEMA model, which further underline a desorption of water and subsequent increase of vacuum in the pores. At the highest temperature, the void component decreases again with continuous parallel desorption of H_2O. The RI on the other hand increases. This behavior can be explained by a change in the film structure induced through reorganization of the SiO_4 tetrahedra. The simultaneous decrease of the void and H_2O components indicate that the material becomes denser and more stoichiometric, resulting in the increase of the RI [219].
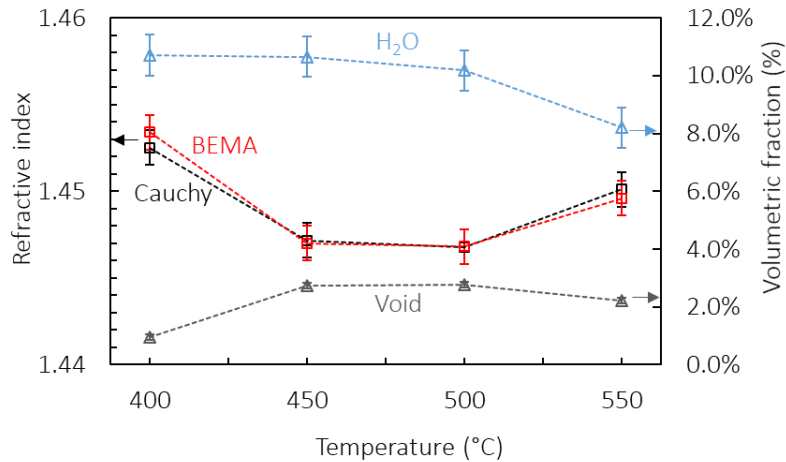
Fig. III.7. Refractive index of silica films as a function of the SPT, as calculated after simulations using the Cauchy model (black squares) and the BEMA model (red squares), along with the evolution of the volumetric fraction of the H_2O (blue triangles) and void (grey triangles) components used in the BEMA model.

To summarize, two regimes are observed when considering the FT-IR, IBA and ellipsometry results. Firstly a regime between 400 and 500°C is noted, where the desorption of water increases the O/Si ratio and decreases the RI, because nanopores previously filled with H_2O are emptied out. A second regime is then observed between 500 and 550°C, in which a reorganization of the network is induced through decrease of the nanopores and Si–OH species concentration, and increase in cross-linking. As a result, the films become denser and shift towards stoichiometry. Considering all the above, it is clear that, in order to

arrive at a more accurate correction of the O/Si atomic ratio, more precise information on the distribution of hydrogen between H_2O and Si–OH groups would be necessary to properly correct the oxygen concentration. Despite that, the current results suggest that a stoichiometric silica is produced at 500°C and above.

III.1.1.4. Mechanical properties

The effect of the temperature on the mechanical behavior of the films in terms of resistance to penetration (Hardness, H) and deformation (Elastic modulus, E) is also studied as presented in Fig. III.8. The hardness appears constant, with an average value of 7.4±0.3 GPa. A slight decrease is noted for H at 450°C. A notable difference for the film produced at 450°C is its lower DR, which resulted in its thickness not exceeding the required 500 nm for this characterization method. Consequently, nanoindentation analysis for this sample possibly integrated some interference from the substrate. However, it must also be noted that temperatures around 450°C have been described as transitional temperatures for the deposition mechanism from TEOS-O_2/O_3. More specifically, multiple authors [115, 139, 186, 220] explain the participation of distinct reactive species in SiO_2 deposition depending on the temperature. Mechanical properties of silica films have been reported to strongly depend on the starting chemistry of the precursor molecule. As a result, it is not surprising that a difference in the film-forming species, i.e. TEOS precursor versus its intermediates, can result in a silica film with different mechanical properties.

Fig. III.8. Evolution of the elastic modulus E (diamonds), hardness H (black squares) and critical load 3 (grey squares) of SiO_2 films from TEOS-O_2/O_3 as a function of the SPT.

The above argument is strongly reflected in the nanoscratch results included in Fig. III.8. More specifically, a low force value of 10.8±0.1 mN is noted at 400°C for the Critical Load 3 (CL3), w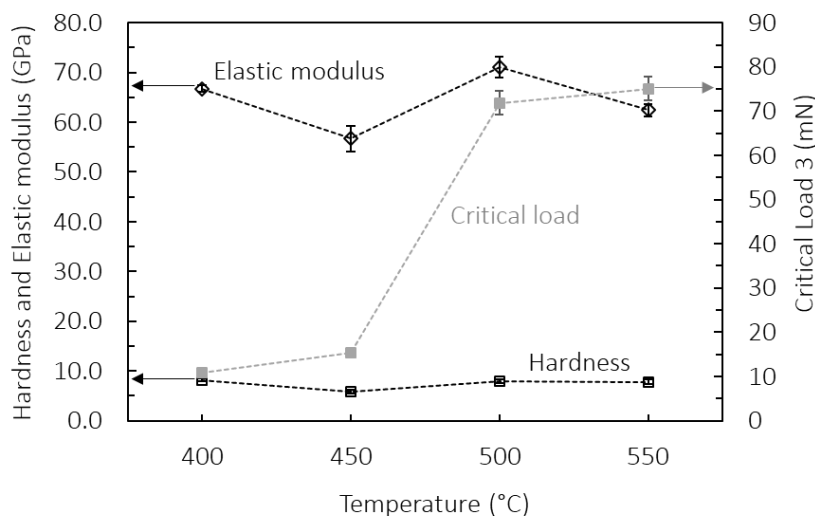hich describes the applied force after which a film undergoing the nanoscratch test starts to delaminate from the substrate. At 550°C, the CL3 load increases to 75.1±2.2 mN, meaning that higher force is required to peel off the film from the substrate surface, signifying that it presents better adhesion when produced at higher temperatures. Even though a general increasing trend of the CL3 is observed with the temperature, two distinct regions are identified; a region of low CL3 load for temperatures equal to and below 450°C, and a region of high CL3 load for temperatures higher than 450°C. This behavior further supports the previous suggestion that the mechanical properties are tightly linked to the nature of the film-forming species.

The influence of the temperature on the elastic modulus seems non-monotonous, showing an average value of 64.2±1.7 GPa. The elastic modulus is an intrinsic material property that is intimately linked to the types of bonds existing in the material. As such, it is safe to discuss this property as a function of the film composition, the microstructure and the stiffness of the network [79, 81, 221]. In view of all previous results however, no clear connection can be made to any of them. The simultaneous contribution of all these factors renders it difficult to propose concrete explanations for the observed non-monotonous behavior of the elastic modulus. As such, we discuss only the average value. The commonly accepted value of elastic modulus for stoichiometric SiO₂ glass in the literature is in the range of 69-73 GPa [174, 222, 223]. The measured average value of 64.2 GPa would in that case translate into a slightly sub-stoichiometric film, which is in good correlation with IBA, FT-IR and ellipsometry results. Globally, the mechanical properties of the SiO₂ films evolve mostly independently from each other and seem depend on combinations of distinct factors.

III.1.1.5. Surface wettability

The water wettability of the silica films is presented in Fig. III.9, illustrating its evolution with the SPT. The water contact angle (WCA) measures 51.5° at 400°C, increasing up to 62.6° at 500°C, before decreasing to 56.8° at 550°C. The order of magnitude is coherent with water contact angles (58°) reported for SiO₂ films synthesized from TEOS by dip coating [224]. In general, the films are hydrophilic, a character which decreases for higher temperatures. This decrease originates from the reduction of the hydrated species identified by FT-IR. According to Hair and Hertl [225], hydrogen bonded hydroxyl groups increase the hydrophilicity of a film, since water can readily physisorb on them, as opposed to free OH groups at the surface that reduce the affinity to water. This is in coherence with the high 81°±8 contact angle measured

for fused silica (SQ-1 SCHOTT) with high infrared absorption at ~3650 cm⁻¹, assigned to free OH groups) [226, 227].

In light of the above, the RI results of Fig. III.7 are recalled, which hinted that a strong water desorption is taking place between 400 and 500°C. This is coherent with the decrease in wettability at these temperatures. Additionally, between 500°C and 550°C, an increase in RI was noted, indicating a higher level of network cross-linking, i.e. decrease of Si–OH groups. The WCA decreases between these two temperatures. Considering all of the above information, it is proposed that the concentration of free OH groups is lower at 550°C, thanks to an increase in the formation of Si–O–Si bridges. This results in a renewed increase of the water affinity and a lower water contact angle.
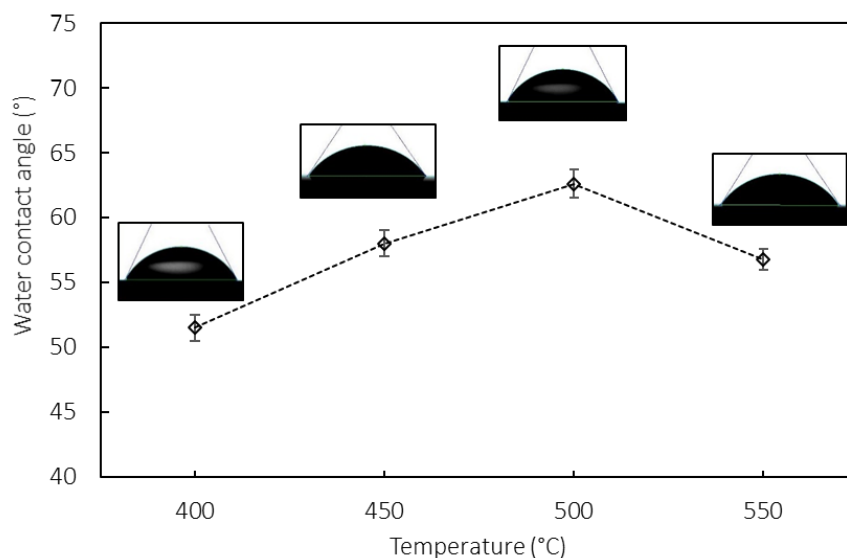
Fig. III.9. Water contact angle values for silica films produced at different SPTs.

III.1.1.6. Corrosion resistance of planar substrates: wet etching corrosion

The P-etch rate of SiO₂ films produced from the TEOS-O₂/O₃ chemistry are shown in Fig. III.10a. A photograph of a sample right after immersion in the P-etch solution for 30 s is also included (Fig. III.10b). The change in iridescence is noted, indicating the change in thickness between the etched and non-etched regions. The results reveal a moderate corrosion resistance of 19 Å.s⁻¹ for films deposited at 400°C, a value close to that of SiO₂ films produced by PECVD [228-230], but also similar to the etching rates observed from TEOS-O₂ produced at the same temperature in Ponton's thesis [7]. Such films are prone to contain nanoporosities and potential impurities, while also being sub-stoichiometric. These factors render them less

resistant to a corrosive attack. Their corrosion resistance is strongly improved with increasing temperature, reaching 9 Å.s^{-1} for films deposited at 550°C, a value that is within the range reported for SiO_2 films produced by thermal CVD [109, 231, 232]. The lower P-etch rate at higher temperatures supports the previous results well, underlining how an increase in SPT leads to a densification of the silica network. For reference, a P-etch rate equal to 2 Å.s^{-1} has been reported for stoichiometric silica produced by pyrolysis of TEOS at temperatures around 1000°C, with very low porosity (ρ=2.3 g.cm^{-3}, RI=1.453) [177]. Even though the measured etching rate values of the SiO_2 films produced in this thesis do not reach the "record" of 2 Å.s^{-1}, their decrease from 19 to 9 Å.s^{-1} still indicates that the SiO_2 films have become more stoichiometric and compact, with improved corrosion resistance.
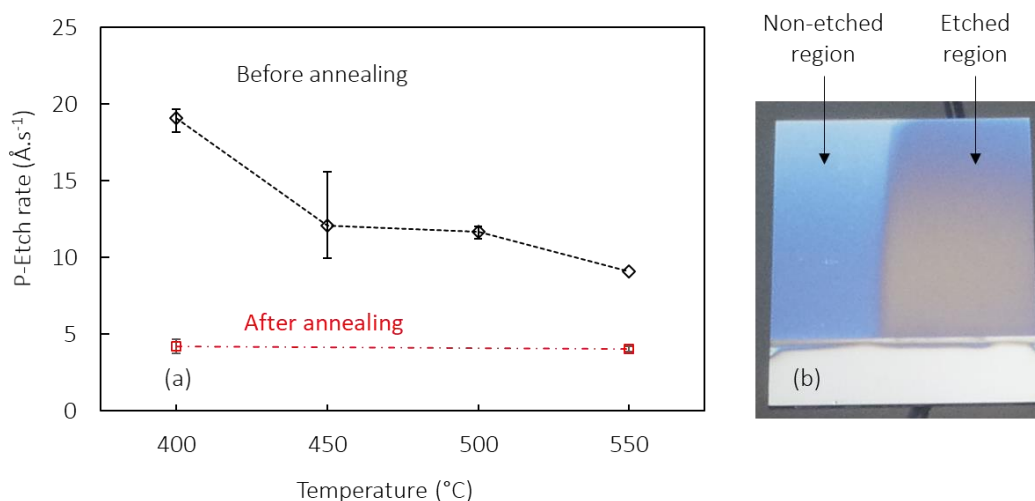
Fig. III.10. P-etch rate of silica films as a function of the SPT, before (black diamonds) and after annealing at 550°C (red squares) (a). Photograph of a sample after etching, showing the area of the sample (etched region) that was immersed in the P-etch solution (b).

Additionally, it is of interest to assess the films after taking into consideration the specific details of the acidic attack. More specifically, the P-etch test involves the interaction between the silica network and the polymeric HF aqueous species H_nF_{n+1}, which originate from the solvation of F^- from molecular HF in the aqueous solution [233]. Moreover, the dissolution of silica requires, in a first step, the breaking of all four siloxane bonds of each SiO_4 tetrahedral unit in order to release the silicon atom from the network, and, in a second step, the creation of a Si-F bond. The rate of this substitution reaction is pH dependent. Additionally, the literature indicates that the etching rate of SiO_2 is not dependent only on the HF concentration (noted a_{HF}) [181, 234-236], but may also depend on the adsorption mechanism of HF and/or

HF^{2-} on surface silanol groups and silicon atoms, with a catalytic effect by the H$_2$O or H$^+$ concentrations (noted a_{H+}) [237, 238]. Mitra and Rimstidt [233] proposed an empirical dissolution rate law equation for amorphous silica (Eq. (III-1)) deduced from a compilation of literature data. They concluded that the rate-limiting step for silica dissolution in fluoride solutions involves a coordinated attack of a Lewis acid on the bridging O atom, and a Lewis base on the Si atom, potentially H$^+$ and HF^{2-}, with the main step for the breaking of the Si–O bonds being the adsorption of the reacting species onto the silica surface.

$$r(mol/m^2\ s) = 10^{0.48}e^{\frac{-34243}{RT}}a_{HF}^{1.50}a_{H+}^{-0.46} \qquad \text{Eq. (III-1)}$$

where $10^{-2.37} < a_{HF} < 10^{1.61}$, $-0.32 < pH < 4.76$ and $23°C < T < 70°C$.

As such, according to Eq. (III-1), the expected etching rate corresponding to our etching conditions is calculated to be around 4 Å.s^{-1}, instead of the 2 Å.s^{-1} reported previously. As is observed in Fig. III.10, all measured P-etch rates are higher than the calculated value of 4 Å.s^{-1}, something that, as discussed previously, is attributed to the sub-stoichiometry of the films, as a result of hydrated species, nanoporosity and impurities. Higher values than the calculated one are therefore expected, and in that regard, the value of 9 Å.s^{-1} measured for 550°C is rather consistent.

Interestingly though, when subjecting the films to an *ex-situ* annealing post-treatment performed at 550°C under N$_2$ flow for 2 h, the etching rate decreases further. More specifically, two films that were produced at different SPTs, namely 400°C and 550°C, and then annealed in the above conditions, had their P-etch value decrease to 4.2 and 4.0 Å.s^{-1}, respectively. Unanimously in the literature it is observed that a post-processing annealing treatment promotes the formation of films with high corrosion resistance and a low P-etch rate, translating into a denser silica material. These results reveal that, for the adopted P-etch conditions (pH, HF concentration and etching test temperature), the calculated value of 4.0 Å.s^{-1} should be considered as the reference point. Combining these two points, it can be derived that the annealing post-treatment successfully led to denser films and achieved the lowest limit of projected corrosion resistance.

In conclusion, the resistance of the films to chemical etching is directly related to their network structure, namely the nanoporosity, composition and stoichiometry, with film densification being playing a major role. It is recalled that the barrier films, envisioned for application as barrier coatings in the pharmaceutics industry, must present dense enough networks to withstand hydrolysis. Given that the results so far on the deposition of SiO$_2$ from TEOS-O$_2$/O$_3$ are slightly improved in relation to those obtained from

Ponton's work (~10 Å.s^{-1} at 550°C) [7], deposition experiments were carried out in Type I vials to test their hydrolytic resistance according to the standard USP <660> test.

III.1.2. Deposition in Type I vials

III.1.2.1.   Deposition rates

The main experimental parameters for the deposition of SiO$_2$ barrier coatings in Type I vials have been previously detailed in section II.1.1.2 of Chapter II. To recall them, the total flow rate is fixed at 2222 sccm, with O$_2$, N$_{2\text{-dilution}}$ and N$_{2\text{-bubbler}}$ supplies being 1079, 1094 and 49 sccm, respectively. Deposition at two SPTs is carried out, namely 400°C and 550°C. A third run at SPT 550°C is performed, after which an *in-situ* annealing step of 2 h at 550°C is executed under N$_2$ atmosphere. The transparency of the vials is retained after 30 min of deposition and no macroscopic powder formation is observed. An average DR of 4.4 and 5.9 nm.min^{-1} is measured for SPT 400°C and 550°C, respectively.

III.1.2.2.   Barrier properties and hydrolytic resistance in vials: USP <660> test

After deposition of SiO$_2$ barrier coatings on the inner surface of Type I vials, their hydrolytic resistance against an aqueous medium is studied according to the USP <660> protocol [4]. The concentration of all the elements released from the glass into the aqueous solution are probed by ICP-OES analysis. For each experimental condition, a set of three vials is subjected to the USP <660> test in an attempt to reduce the experimental error. Additionally, a set of three uncoated vials underwent the same test to compare the concentration of constituent element diffusion between coated and uncoated vials.

Up to 11 different elements are probed in the aqueous solution after subjection to the USP <660> test. The total concentration of extractables is thus the sum of the individual concentrations of all elements probed (Si, Na, K, Ca, Mg, etc.). For uncoated vials, the extracted elements with the highest concentrations are Si and Na. Slightly lower, although still significant, concentrations of B and K are also noted. Probing of these elements in the extraction solution are expected for borosilicate glasses like the Type I vials used in the present thesis. Ideally, such elements should not diffuse in the solution, for reasons addressed in Chapter I. Application of barrier coatings is expected to reduce diffusion of these elements; this reduction in total extractables is expressed as the *improvement factor* hereinafter, which is used as the main indicator of the efficiency of the barrier coating.

Fig. III.11a presents the total improvement factor after coating of the internal surface of Type I vials at various SPTs and an annealing post-treatment. It is observed that the global improvement factor

measures up to 92 % (Fig. III.11a), meaning that the applied SiO$_2$ coatings demonstrate an excellent barrier property and manage to effectively reduce the presence of extractable elements in the aqueous solution. When deposited at 400°C, the presence of the SiO$_2$ barrier coating leads to a reduction of the total extractables by 89 %. Increase of the deposition temperature to 550°C gives similar results. A slight improvement is noticed for SiO$_2$ coatings deposited at 550°C with an annealing post-treatment step. It must be noted however that all values are within the error bars, making it difficult to comment on clear trends. Regardless, the SiO$_2$ films deposited from TEOS-O$_2$/O$_3$ performed better than those produced from TEOS-O$_2$ in Ponton's thesis [7]. The corresponding improvement factors when SiO$_2$ barrier coatings were deposited using the TEOS-O$_2$ chemistry were approximately 22 % at 400°C and increased to 72 % at 550°C. The better performance of coatings from the TEOS-O$_2$/O$_3$ chemistry studied in the present thesis is attributed their lower network hydration and improved cross-linking, as is revealed by comparative FT-IR analysis of SiO$_2$ films from the two chemistries (Appendix 1).
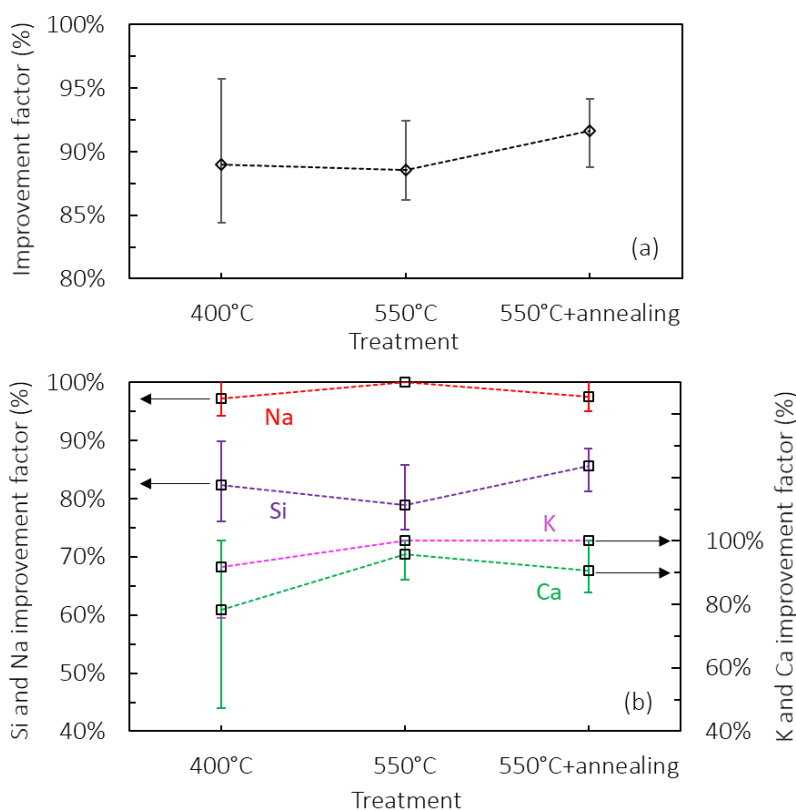

Fig. III.11. Total improvement factor for extractables measured for coated vials after application of a SiO$_2$ barrier coating at various conditions (a). Analysis of the individual improvement factors for Si, Na, K, and Ca extractables (b).

Fig. III.11b examines the individual improvement factors for specific extractable elements. As previously mentioned, up to 11 elements are probed in the solutions from uncoated vials after subjection to USP <660>. When a SiO$_2$ barrier coating is applied on the internal surface of the vial however, only four elements are probed, namely Si, Na, K and Ca. Their concentrations are drastically decreased in comparison to uncoated vials. More specifically, measured concentrations of Na are decreased by 97 up to 100 %. The concentrations of K and Ca also benefited from great reduction after application of the barrier coating, with 92 % and 78 % less K and Ca extractables being probed at 400°C, respectively. Reduction in their concentration reaches 100 % for SiO$_2$ coatings deposited at 550°C. When an additional annealing step is applied, barrier efficiency for K remains at 100 %, but drops slightly to 98 % and 91 % for Na and Ca, respectively, although both values remain within the error bars. Globally, the above results indicate that the SiO$_2$ barrier coatings are successful in retaining and obstructing the diffusion of the constituent elements of the glass.

On the other hand, Si is also probed in the solution. In contrast to the other elements, the Si extractables are most likely to be originating from hydrolysis of the silica coating itself, as was revealed in Ponton's work [7]. As such, even though the SiO$_2$ coatings successfully reduce the hydrolysis of the underlying glass, they themselves are affected and hydrolyzed.

Another important point to keep in mind is the potential presence of uncoated zones. In cases where the SiO$_2$ coating is not uniformly distributed on the internal surface of the vial, the uncoated regions of the glass are directly exposed to the solution and hydrolysis can proceed uninhibited. For this reason, it is of great interest to assure a uniform coverage of the vial. However, thin SiO$_2$ films are visually transparent and an assessment of the film distribution would require extensive analysis of multiple vial cross-sections. For that reason, the utilization of computational fluid dynamics (CFD) calculations is proposed. The simulation of the deposition process in a representative 3D domain and the use CFD calculations can be implemented to better understand and master the physical and chemical phenomena involved during the deposition process. This in turn offers potentials for visualization of the local film thickness and optimization of the process parameters for more uniform film coverage. However, in order to do that, knowledge of the various reactions taking place during the deposition process is required.

The following section details the development of a kinetic model that describes the deposition process of SiO$_2$ from TEOS-O$_2$/O$_3$. In a first step, the model is developed based on results obtained from the tubular reactor, by considering apparent gas phase and surface reactions, which describe in a simplified manner the multiple reactions that can take place during the CVD process. In a second step, validation of this proposed model is executed, to allow its transfer into reactors with different geometries and offer exploration for optimization of the deposition process.

III.2. Development of a kinetic model for the simulation of the SiO₂ deposition process from TEOS-O₂/O₃

Process optimization is dependent on understanding the interplay between the applied process conditions and the governing transport phenomena, i.e. the local gas velocity, temperature and reactive species concentrations, as well as the homogeneous and heterogeneous chemical reactions leading to the formation of the film. As this interplay is difficult to establish experimentally, a valuable and timesaving approach is to associate the experimental investigation with reactor modelling. In particular, CFD codes can be used for the implementation of chemical reactions and kinetic laws, with the aim to replicate the experimental process in a 2D or 3D environment. Since a wealth of homogeneous and heterogeneous reactions can occur simultaneously in a CVD process, their identification and calculation of their respective kinetics is the bottleneck of the simulation process. In a classical way, overcoming this difficulty is done by considering only apparent chemical reactions, meaning that each reaction represents, in a simplified way, many real chemical reactions that are otherwise difficult to determine one by one in detail.

Existing models in the literature that describe the SiO₂ deposition mechanism from the TEOS-O₂/O₃ chemistry have been previously discussed in Chapter I. Among them, the model of Nieto et al. [158] is used as the basis for formulating and adapting the chemical reactions and kinetic laws of the process, to best represent the deposition results obtained from the particular reactor configuration and deposition conditions used in the present thesis. The following simulation study of the TEOS-O₂/O₃ process was carried out in collaboration with George A. Chliavoras from the National Technical University of Athens (NTUA), supervised by Hugues Vergnes and Brigitte Caussat, in the frame of his Diploma thesis [184].

III.2.1. Implementation of chemical species and reactions

The definition of reactor geometry, mesh, working assumptions and boundary conditions has previously been described in Chapter II. Beyond that, simulation of the chemical model requires definition and implementation of the reacting and produced species, the reactions that are taking place and the kinetic laws that describe them.

Based on the literature data collected in section I.3.5 of Chapter I, a total of 10 species and up to 7 chemical reactions are considered to describe the SiO₂ deposition process from TEOS-O₂/O₃. The physical properties of O_2, O_3, H_2O, CO, CH_3CHO and N_2 are taken from the FLUENT® database. The L-J parameters of the oxygen radical $O^{\bullet}$ ($\sigma = 2.75$ Å and $\varepsilon/k = 80$ K), and of TEOS ($\sigma = 7.03$ Å and $\varepsilon/k = 522.7$ K) are taken from the CHEMKIN database [239]. Due to lack of concrete values in the literature, the L-J parameters of

the intermediate (noted INT hereinafter) are set equal to those of TEOS, since the INT molecule is considered to be similar to the latter, allowing for the use of comparable L-J parameters. The molecular weight of INT was fixed at 180.27 g.mol^{-1} by matching it to triethoxysilanol, $(Si(OH)(OC_2H_5)_3)$, one of the most probable intermediate species from the reactor of TEOS and O_2, as reported by many authors [150, 155, 240]. All physical properties of the by-product (R) produced by the INT were set equal to the latter.

The chemical reaction rates are implemented into FLUENT® in the form of an Arrhenius type expression:

$$R_r = A_{0,r} \, exp^{(-\frac{E_a^r}{RT})} \prod_{i=1}^{i=n} p_i$$

Eq. (III-2)

For surface reaction rates, R_r (kmol.m^{-2}.s^{-1}) stands for the rate of the heterogeneous reaction r and A_0 (kmol.m^{-2}.s^{-1}.Pa^{-n}) is the pre-exponential factor of the reaction r. The activation energy of the reaction r is symbolized with E_a^r (kJ.mol^{-1}), T (K) stands for the temperature of the surface where reaction r occurs, n is the total number of involved species, and p_i (Pa) is the partial pressure of the species i. For homogeneous chemical reactions, R_r is expressed in kmol.m^{-3}.s^{-1} and $A_{0,r}$ in kmol.m^{-3}.s^{-1}.Pa^{-n}, whereas T (K) is the temperature of the gas phase. By implementing the kinetic laws and conservation equations of each species, the molar fraction of each gaseous reactant and product, as well as the deposition rate of the solid film material, can be determined. Gas phase reactions are implemented in the FLUENT® code via user-defined functions (UDFs), while surface reactions are inserted through the FLUENT® user interface (UI). The list of the reactions adopted from Nieto et al.'s model is included in Appendix 2.

III.2.2. Comparison to current literature model

The experimental runs E3 to E6 of Table III.1 are used for the formulation of the kinetic model. The total mass flow rate (9.19653·10^{-5} kg.s^{-1}) and the mass fractions of all species at the inlet (TEOS: 0.00181, O_2: 0. 50534, O_3: 0. 02414, N_2: 0. 46871) are fixed to the experimental values. Initially, Nieto et al.'s model and kinetic laws [158] (Appendix 2) are implemented into FLUENT®. Given that this specific model was developed in a different reactor configuration (cold-wall Watkins Johnson type reactor), with substantially different total flow rates (exceeding 20000 sccm) and very short residence times (< 0.5 s), it is important to assess its validity in relation to the utilized tubular reactor and the applied operating conditions. Runs E3-E6 were used for this purpose, however none were successfully represented by Nieto

et al.'s model. Fig. III.12 shows a comparison between the simulated and experimental DR of run E3, serving as an illustrative example. It is recalled that the simulated average DR values were calculated from planes that represent each Si coupon, as previously explained in section II.3.5 of Chapter II.
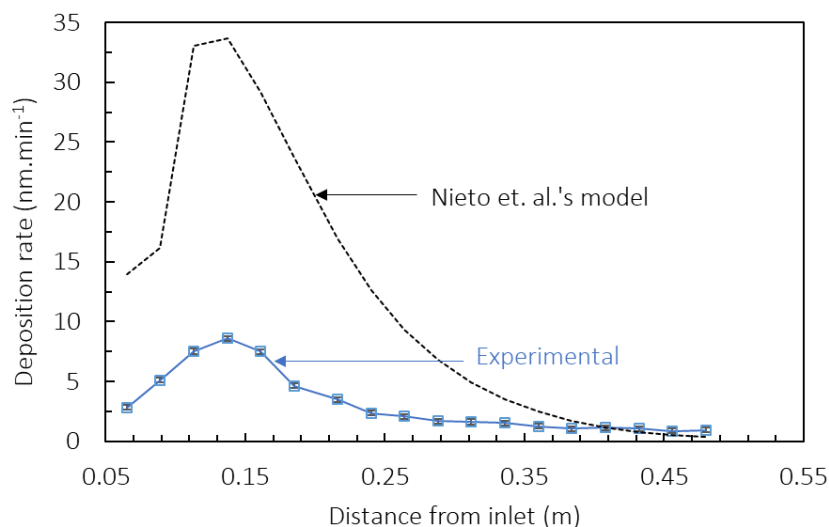
Fig. III.12. DR of run E3 (SPT 400°C) simulated using Nieto et al.'s model (black dashed line) and compared to the respective values per coupon obtained experimentally (blue squares).

A high simulated DR of around 33 nm.min^{-1} is observed in the first 0.15 m of the reactor, due to the intense surface reaction R6 (TEOS + 6O₃ → SiO₂ + O₂ + by-products). No such DR values were measured experimentally. This considerable discrepancy can be explained by the fact that Nieto et al. did not account for deposition on the reactor walls, due to their cold-wall CVD configuration, and only focused on simulating deposition on the Si wafer. Additionally, the average gas temperature of the single wafer treated in Nieto et al.'s reactor was always at around 400°C, a temperature at which the concentration of O₃ has decreased due to its thermal decomposition through reactions R1 (O₃ + M → O₂ + O$^{•}$ + M), R2 (O₃ + O$^{•}$ → 2O₂) and R3 (2O$^{•}$ + M → O₂ + M). In contrast, the local temperature of the first substrate at in run E3 is much lower and does not exceed 150°C. As has been pointed out in Chapter I, the kinetic constant k_6 of reaction R6 does not consider any temperature influence in Nieto et al.'s model. Therefore, for low temperatures such as 150°C, where O₃ concentration is still high and readily available to lead to SiO₂ deposition, the simulated DR values are overestimated. Moreover, the substantial consumption of O₃ through R6 influences as well all other reactions, in which this species participates.

As such, it is no surprise that Nieto et al.'s chemical model and the associated kinetic laws, in their current state, are unable to represent our experimental results. In the sections that will follow, an adapted

kinetic scheme will be developed, with an extended range of validity in terms of substrate temperature, rendering it more suitable for CVD reactor geometries that treat large and/or complex-in-shape substrates.

III.2.3. Exploitation of experimental data

Based on the preliminary observations of Fig. III.12, Nieto et al.'s model and kinetic laws were modified based on the following assumptions: (i) deposition in the vicinity of the inlet region is attributed to the reaction between TEOS and O_3 (R6), exclusively; (ii) deposition closer to the exhaust, where O_3 has been consumed, is attributed to INT (R7).

In a first step, the experimental results of runs E1 to E3 (Table III.1) were considered in order to calculate a new partial order exponent *a* for TEOS for reaction R6. This partial order exponent expresses, in essence, the impact of a change in TEOS concentration on the rate of reaction R6. From each run, a sample located 9 cm after the inlet was selected and its DR was calculated from the mass gain. Runs E1 to E3 are then coupled in pairs of two (three pairs in total). By using the kinetic law of reaction R6 (Appendix 2), the ratio of their reaction rates is expressed as:

$$\frac{R6_{E_i}}{R6_{E_j}} = \frac{k_6[TEOS]_i^a[O_3]_i^{0.25}}{k_6[TEOS]_j^a[O_3]_j^{0.25}}$$

Eq. (III-3)

where *R6* is the reaction rate of reaction R6, E_i and E_j are the experimental runs E1, E2, E3, with i = 1 or 2, j = 2 or 3, and $i \neq j$. Then, k_6 is the kinetic constant of reaction R6, *[TEOS]ᵢ* and *[TEOS]ⱼ* are the concentrations of TEOS at the inlet for runs E_i and E_j respectively, *[O₃]ᵢ* and *[O₃]ⱼ* are the concentrations of O_3 at the inlet for runs E_i and E_j respectively, and *a* is the partial order exponent of TEOS. With the kinetic constant k_6 remaining unchanged since all three runs were performed at the same temperature, and assuming that the concentration of O_3 at the inlet is approximately equal across all runs, Eq. (III-3) is simplified as:

$$\frac{R6_{E_i}}{R6_{E_j}} = \left(\frac{[TEOS]_i}{[TEOS]_j}\right)^a$$

Eq. (III-4)

Eq. (III-4) is then solved for *a*. The logarithm of $\frac{R6_{E_i}}{R6_{E_j}}$ is plotted versus the logarithm of $\frac{[TEOS]_i}{[TEOS]_j}$ as shown in Fig. III.13a.
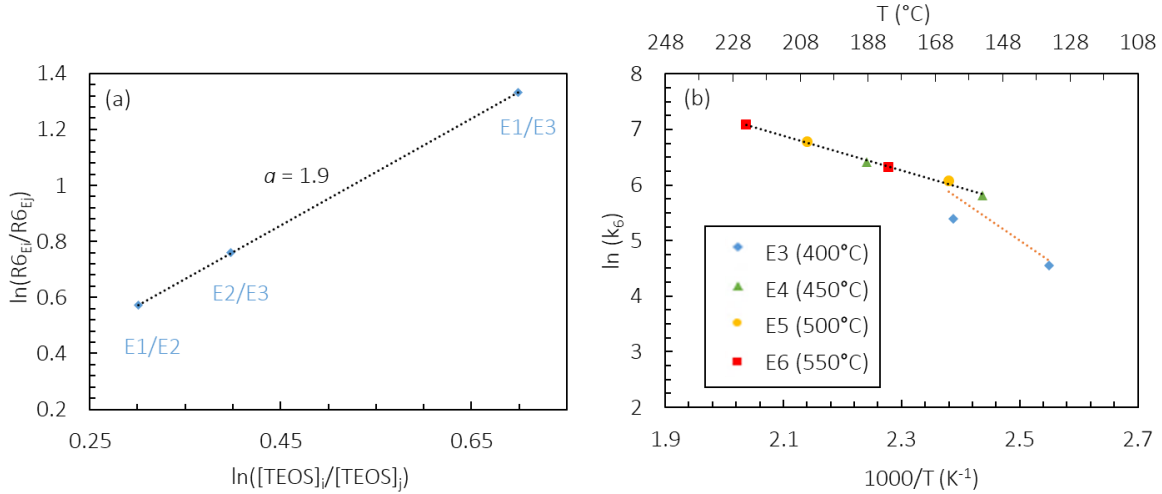
Fig. III.13. (a) Determination of partial order exponent a for TEOS in reaction R6. (b) Linear interpolation of k_6 logarithm versus the reciprocal temperature, plotted for selected samples of E3 to E6.

From the slope, a value of a equal to 1.9 is deduced, with the reaction law of R6 now becoming:

$$R6 = k_6[TEOS]^{1.9}[O_3]^{0.25} \qquad\qquad \text{Eq. (III-5)}$$

This calculated value for a is higher than the one used by Zhou et al. ($a = 1$) or Nieto et al. ($a = 0.4$). The difference may be due to the steep thermal gradient observed in their reactor configurations, which activates the conversion of TEOS to INT through reaction R4 more rapidly, downplaying the role of reaction R6 and subsequently the influence of the TEOS concentration on SiO₂ deposition.

As a second step, the first and second samples closest to the inlet were selected from runs E3 to E6, and their respective DR was divided by $[TEOS]_s^{1.9}[O_3]_s^{0.25}$ and plotted versus the reciprocal of their local temperature as shown in Fig. III.13b. It is worth noting that the two points relative to the lowest SPT (E3) are not aligned with those of the other runs. It is possible that the mechanisms involved at temperatures lower than 150°C are different from those prevailing between 150°C and 230°C. Thus, these two points were not considered when deducing the activation energy. This point is must be kept in mind, since it can affect the accuracy of the model for deposition temperatures lower than 150°C. From the remaining points, an activation energy of 21.8 kJ.mol⁻¹ is deduced, and R6 can be thus expressed with a temperature dependence. It is the first time that an activation energy has been calculated for this reaction, since all previous literature models considered this reaction to depend only on the TEOS and O₃ concentrations.
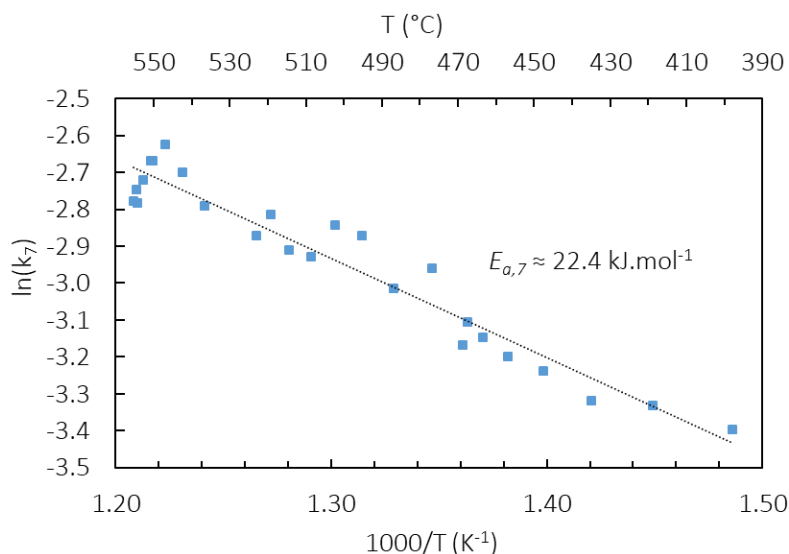
Fig. III.14. Linear interpolation of k_7 in an Arrhenius plot, calculated for selected samples within and close to the isothermal region of runs E3 to E6.

The kinetic constants of Nieto et al.'s reaction R7 (INT → SiO$_2$ + by-products) were then adjusted based on the experimental results of runs E3 to E6. Since reaction R7 requires the production of the INT species through reaction R4, it was supposed that reaction R7 takes place further downhill the reaction chamber, in contrast to R6. For that reason, samples within and close to the isothermal region (0.36-0.50 m) were chosen from all runs to extract DR values corresponding to this surface reaction. Before that however, reaction R7 was modified to include an oxidant species in the reactants. It is not out of the ordinary to make such an assumption, given that there is an excess in oxidant species (O$^•$, O$_2$, or O$_3$) and that the ethoxy ligands of INT need to be cleaved in order to form the SiO$_2$ film [155]. The two oxidant species that are present in this region (0.36-0.50 m) for our configuration and thermal profile are only O$_2$ and O$^•$, since O$_3$ has been consumed uphill in the reactor. Then, the experimental DR values of the selected samples were divided by the calculated concentrations of INT and the prospective oxidant, and were then plotted against the reciprocal of their local average temperature in an Arrhenius plot expression. Calculations using O$_2$ as the oxidant species yielded results with lower dispersion (Fig. III.14), out of which an activation energy of 22.4 kJ.mol^{-1} was deduced. As such, reaction R7 was reformulated to INT + O$_2$ → SiO$_2$ + by-products.

III.2.3.1. *Modification of the chemical model*

Inspecting Fig. III.3, no significant decline in the experimental DR is observed in the isothermal region (0.36-0.5 m). Deposition in this region is dictated by reaction R7 and INT serves as the silicon-

providing molecule. The models of Zhou et al. and Nieto et al. feature reaction R5, which serves to reduce the available concentration of INT in the gas phase and reduce deposition from reactions involving INT. Due to the lack of the aforementioned decline however, reaction R5 was removed in our model, like in Kim and Gill's work [139]. The modified model (i.e. adjusted R6 and R7, and exclusion of R5) was implemented into FLUENT® and the computed DR values were compared to the experimental ones (Fig. III.15).
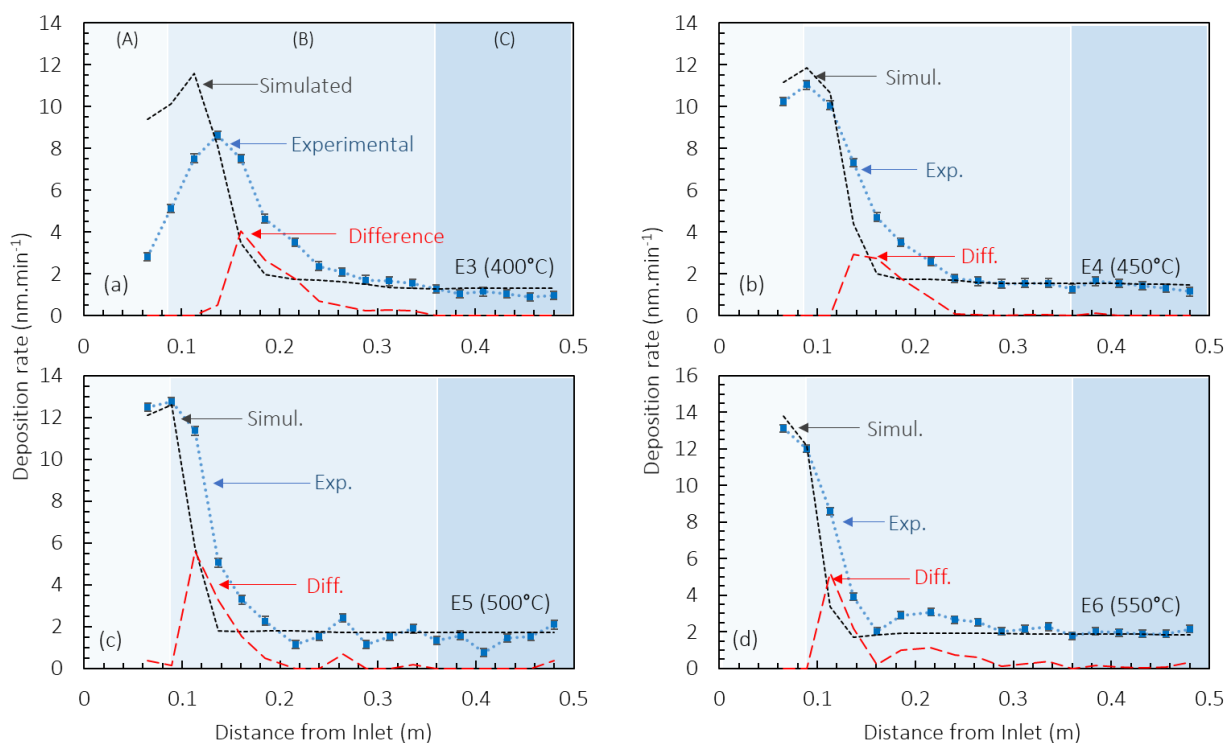
Fig. III.15. Evolution of the average experimental DR per sample (blue squares) and average simulated DR (black dashed line), after simulating reactions R1 to R7. Red dashed line shows the difference of experimental minus simulated DR, for the samples on which the simulation underestimates the experimental values. (a) Run E3, (b) E4, (c) E5, and (d) E6.

From Fig. III.15, it is observed that overestimation of the experimental DR is observed only close to the inlet of runs E3 and E4. Such deviations are expected given that the model loses its accuracy for temperatures below 150°C. In contrast, regions where the simulation underestimates the experimental results are noticeable across all runs, between approximately 0.07 and 0.25 m from the inlet. The respective difference between the experimental minus simulated results is also plotted for each run, for the points where the simulation underestimates the experimental DR. This difference appears across all runs and shifts

uphill the reactor with increasing SPT, which indicates that it is the result of a consistent behavior. It is assumed that it is related to the requirement for an additional heterogeneous reaction occurring at the intermediate temperatures of region B. After the testing of various scenarios involving TEOS and INT, it is proposed that this reaction involves the INT species as the silicon provider and an oxidant species as the oxygen provider. By observing the simulated local mass fractions in this specific region from previous simulations, O_3 and $O^{\bullet}$ were considered as the potential oxidants. The following methodology was followed: First, the calculated DR occurring from simulation of the as-defined R6 and R7 reactions is subtracted from the experimental DR, in order to find the DR values originating from this new reaction, noted R8. This difference was then expressed as either $k_8[INT][O_3]$ or $k_8[INT][O^{\bullet}]$, assuming first order exponents for both reactants. It was determined that a reaction of INT with O_3 better represents the experimental results (Fig. III.16) and an activation energy of 69.4 kJ.mol^{-1} was deduced for the new heterogeneous reaction R8.
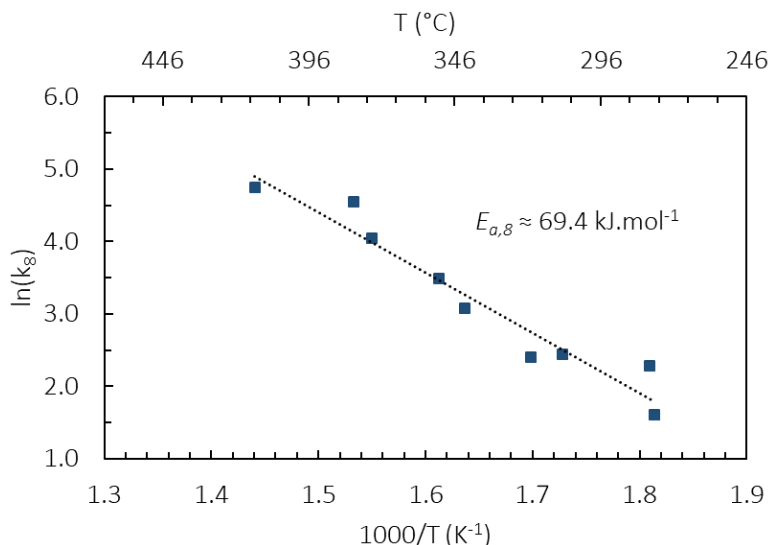
Fig. III.16. Linear interpolation of k_8 in an Arrhenius plot, calculated for selected samples within region B from runs E3 to E6.

It is noted that the addition of multiple surface reactions, in which INT participates as the silicon provider, seems plausible when taking into account the wide variety of molecules that INT represents. Romet et al. [155] mention that the inclusion of additional INT-centered surface reactions improves model accuracy and representation of experimental results, something that led them to remove deposition reactions involving TEOS altogether, and consider only INT as the film-forming species.

The final version of this adapted model and the respective kinetic constants are given in Table III.2. It is recalled that all chemical reactions considered in the model are apparent and stand for numerous elementary reactions and mechanisms. Phenomena such as reactive species adsorption, surface diffusion, chemical reaction and product desorption are accounted for in one single surface reaction.

Table III.2. Proposed apparent chemical model, after adjustment of reactions and their respective kinetic laws and constants.

Reaction stoichiometry		Reaction rate and kinetic constants	Kinetic constants units
		Volumetric Reactions $(kmol/m^3s)$	
(R1)	$O_3 + M \rightarrow O_2 + O^{\cdot} + M$	$k_1[O_3][M]$ $k_1 = 2.5 \times 10^{11} \times exp\left(-\dfrac{11430}{T(K)}\right)$	$m^3kmol^{-1}s^{-1}$
(R2)	$O_3 + O^{\cdot} \rightarrow 2O_2$	$k_2[O_3][O^{\cdot}]$ $k_2 = 10^{10} \times exp\left(-\dfrac{2090}{T(K)}\right)$	$m^3kmol^{-1}s^{-1}$
(R3)	$2O^{\cdot} + M \rightarrow O_2 + M$	$k_3[O^{\cdot}]^2[M]$ $k_3 = 4 \times 10^8 \times exp\left(+\dfrac{720}{T(K)}\right)$	$m^6kmol^{-2}s^{-1}$
(R4)	$O_3 + TEOS + M \rightarrow INT + R + M$	$k_4[O_3][TEOS][M]$ $k_4 = 4 \times 10^{17} \times exp\left(-\dfrac{14099}{T(K)}\right)$	$m^6kmol^{-2}s^{-1}$
		Surface Reactions $(kmol/m^2s)$	
(R6)	$TEOS + 6O_3 \rightarrow SiO_2 + O_2 + by-products$	$k_6[TEOS]_s^a[O_3]_s^b$ $k_6 = 2.2 \times 10^5 \times \exp\left(-\dfrac{2621.1}{Ts(K)}\right)$ $a = 1.9, b = 0.25$	$\dfrac{kmol_r m^{4.45}}{kmol_{TEOS}^{1.9}kmol_{O_3}^{0.25}s}$
(R7)	$INT + O_2 \rightarrow SiO_2 + by-products$	$k_7[INT]_s[O_2]_s$ $k_7 = 1.77 \times exp\left(-\dfrac{2695.2}{Ts(K)}\right)$	$\dfrac{kmol_r m^4}{kmol_{INT}kmol_{O_2}s}$
(R8)	$INT + O_3 \rightarrow SiO_2 + by-products$	$k_8[INT]_s[O_3]_s$ $k_8 = 2.24 \times 10^7 \times exp\left(-\dfrac{8345.1}{Ts(K)}\right)$	$\dfrac{kmol_r m^4}{kmol_{INT}kmol_{O_3}s}$

III.2.4. Simulation results using the adapted kinetic model

Fig. III.17 presents the calculated and experimental DR profiles along the reactor length for runs E3 to E6, after simulation using the adapted kinetic model of Table III.2. The respective contribution of TEOS and INT to SiO₂ film formation is also presented. It appears that the new kinetic model provides very

good agreement with the experimental data. The poorest agreement is observed at the inlet zone of run E3 (Fig. III.17a). This is not surprising, since experimental data for temperatures below 150°C were not considered and are as a result outside the range of validity of the model. The overestimation of the experimental results in this region further underlines that a different mechanism takes place for temperatures below 150°C.
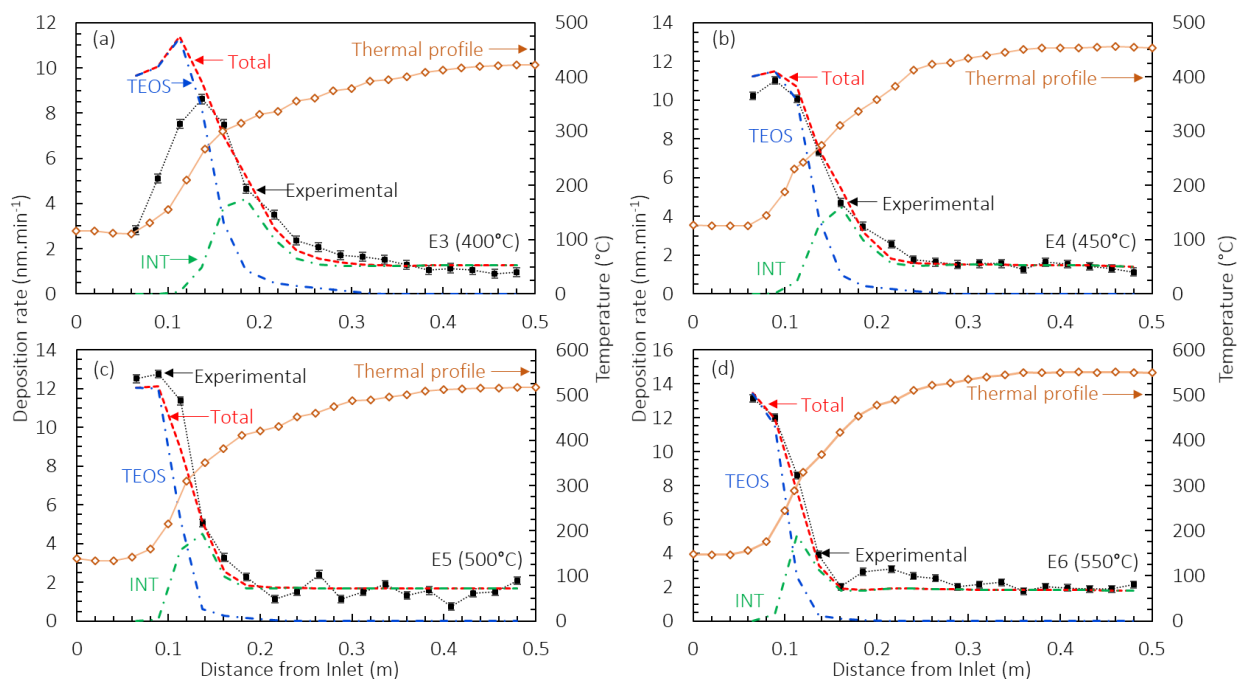
Fig. III.17. Comparison of average experimental DR (black squares) and simulated total DR (red dashed line) for runs E3 (a), E4 (b), E5 (c) and E6 (d). Calculated contributions of TEOS (through reaction R6) and INT (through reactions R7 and R8) to SiO$_2$ deposition are presented by dashed-dotted blue and green lines respectively. The thermal profile (orange diamonds) is included for each run.

For runs E4 to E6 (Fig. III.17b-d), the agreement at the inlet region is clearly improved with increasing SPT. It is also noted that for run E5 (Fig. III.17c), experimental errors appear close to and inside the isothermal region and are attributed to a slight vertical angular displacement of certain substrates within the substrate holder, which caused them to be out of vertical alignment. For run E6 (Fig. III.17d) a shoulder is observed on the experimental data between 0.15 and 0.27 m, corresponding to a zone where the temperature reaches and goes beyond 520°C. The model fails to conform to this specific deposition profile, underestimating the total DR in this region. This shoulder cannot be attributed to experimental error, like the previously mentioned vertical out-of-alignment displacement of the samples, as it is rather uniform in

shape and does not appear to be random. It is likely the result of another INT reaction contributing to deposition, activated at around 520°C.

Observing the respective contributions of TEOS and INT to SiO₂ deposition, the simulation results confirm that TEOS is responsible for film formation in the coldest zones close to the inlet of the reactor (the first 0.15 m from the inlet) through reaction R6. Deposition of SiO₂ from INT through reactions R7 and R8 occurs from around the first 0.10 cm and continues until the exhaust of the reaction chamber.

III.2.5. Validation of the proposed kinetic model

Beyond the average DR, further validation of the kinetic model is required. For this purpose, the calculated deposition profiles are plotted across the YZ plane, as was defined in Chapter II (Fig. II.15).
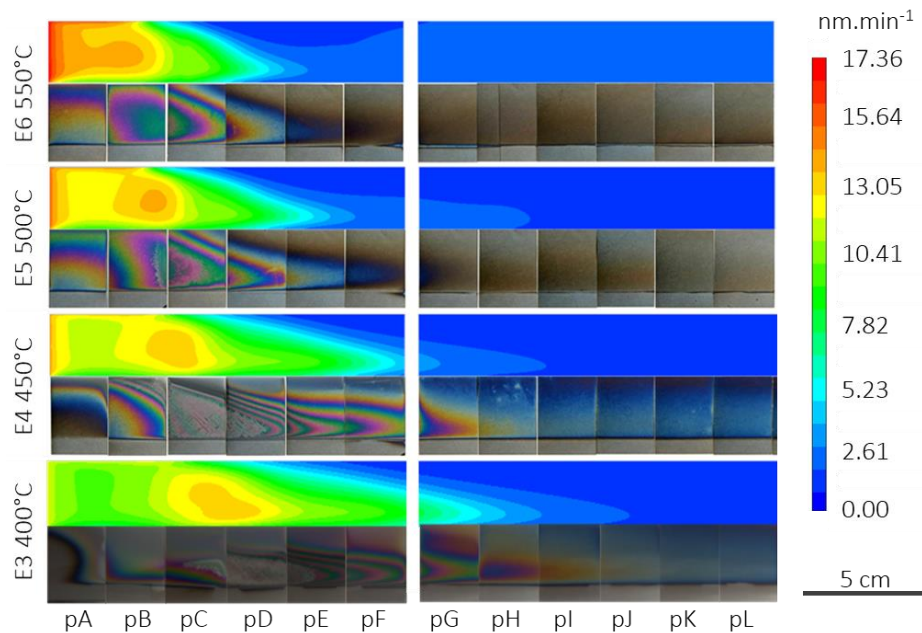
Fig. III.18. Photographs of the SiO₂ films along the substrate holder for runs E3 to E6 and corresponding contours of the simulated DR profiles along the YZ plane.

A visual comparison between the contours of the calculated DR profiles and photographs of the first 12 Si samples is shown in Fig. III.18. The DR of the samples beyond sample pL is similar to it. A remarkable agreement appears regarding the shape of the profiles, indicating that the main deposition mechanisms are well considered for this operating range.

Additional and quantitative validation is also carried out by considering local thickness profiles measured by ellipsometry and comparing them to local values calculated from the simulation. More specifically, the calculated thickness of run E4 was plotted across a horizontal line crossing the substrate surface (YZ plane), 2 mm below the top edge, corresponding to the ellipsometry probing point (5) (Fig. II.7b). Comparison between ellipsometry and values calculated by simulation is presented in Fig. III.19.
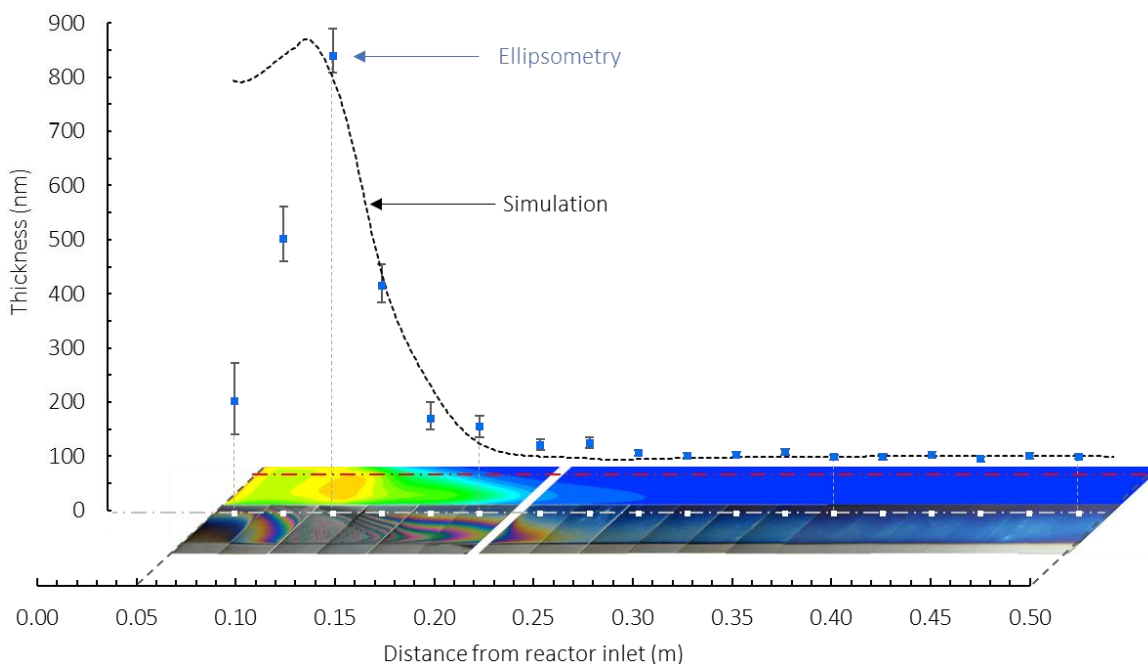
Fig. III.19. Comparison of calculated local thickness (dashed black line) from simulations and experimental local thickness (blue squares) measured by spectroscopic ellipsometry, for run E4. Photograph of array of samples and scale denoting distance from the reactor inlet are included for visual aid. Red dashed-dotted line represents the line along which the simulation results were extracted. White squares represent the points at which the samples were probed by ellipsometry.

A remarkable agreement is observed between the calculated and experimental results of Fig. III.19, confirming the ability of the model to predict local DR values. The local thickness is overestimated for the first two samples as expected, since deposition in this region is outside the validity range of the model. Despite that, Fig. III.19 illustrates that the model can give agreeable local thickness values, complementary to the average DR calculated by the mass gain in Fig. III.17. As such, the good agreement in both shape

and value validates the proposed chemical model and its adapted kinetic constants as an appropriate simplified representation of the involved chemical mechanisms, for the ranges of operating conditions tested.

III.2.6. Discussion of simulation results

The validated model provides valuable local hydrodynamic, thermal and mass transfer information for the studied TEOS-O_2/O_3 chemical system. Fig. III.20 shows the local velocity, thermal profiles and mass fraction profiles of various species in the gas phase, plotted across the XZ plane (Fig. II.15). The following discussion uses run E4 (450°C) as an example, given that the other runs exhibit similar behavior.
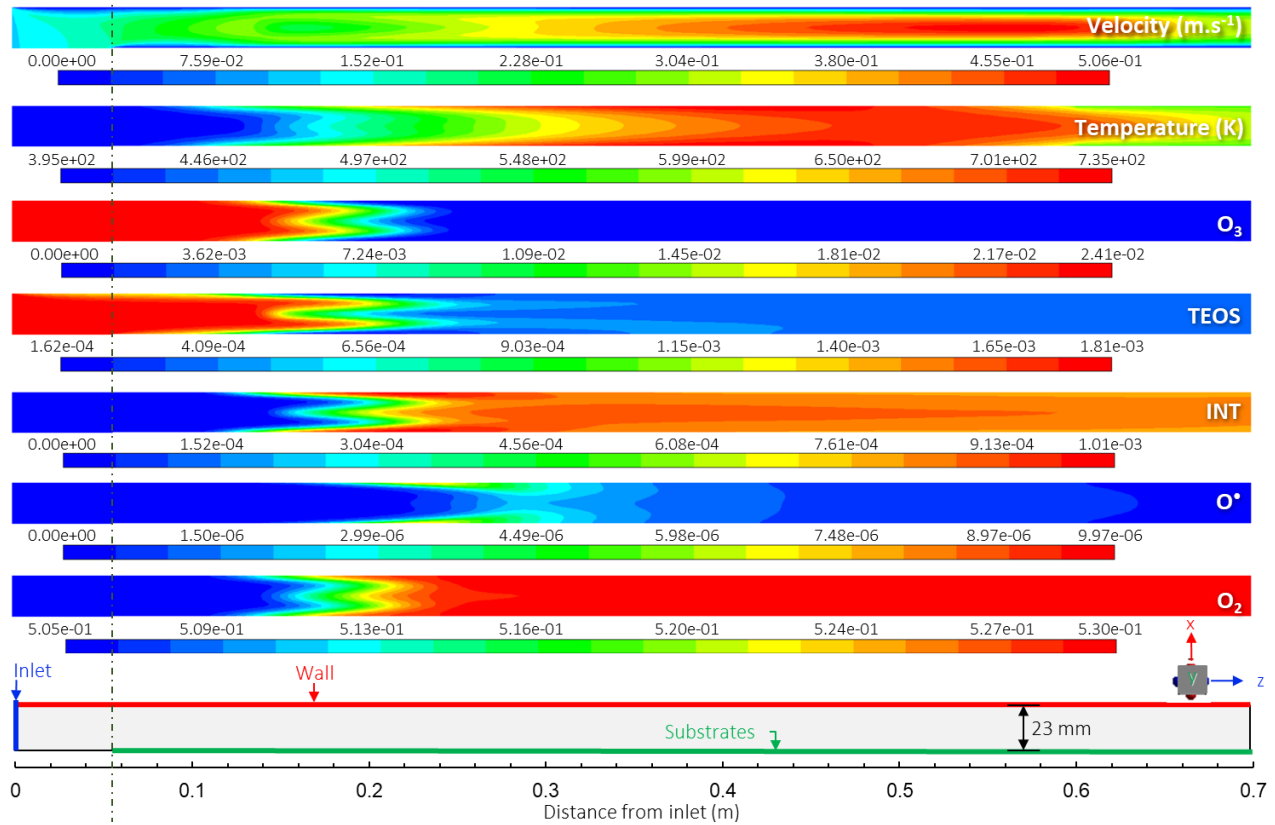
Fig. III.20. Local velocity, temperature and mass fraction profiles of TEOS, INT, O_3, $O^\bullet$ and O_2 plotted along the XZ plane for run E4 (450°C). Vertical black dash-dotted line signifies the start of the substrates.

Inspecting Fig. III.20, it is noted that the velocity profile presents a parabolic shape for the first 0.05 m, as classically observed for laminar gas flows. Beyond that, the gas impacts on the substrate holder and the supported Si substrates. This results in a shift of the flow profile, as will be discussed shortly. At

all solid surfaces, the velocity is zero. A maximum value of approximately 0.5 m.s⁻¹ is observed at the hottest zones of the reactor, i.e. between 0.36 and 0.60 m, which logically give rise to the maximum velocity. The corresponding minimum residence time of the gas into the reactor is about 1.4 s. This is a high residence time for a hot-wall CVD reactor and could favor homogeneous chemical reactions as previously explained. Moreover, it validates the motivation for this work, providing a model adjusted for deposition processes utilizing higher residence times.
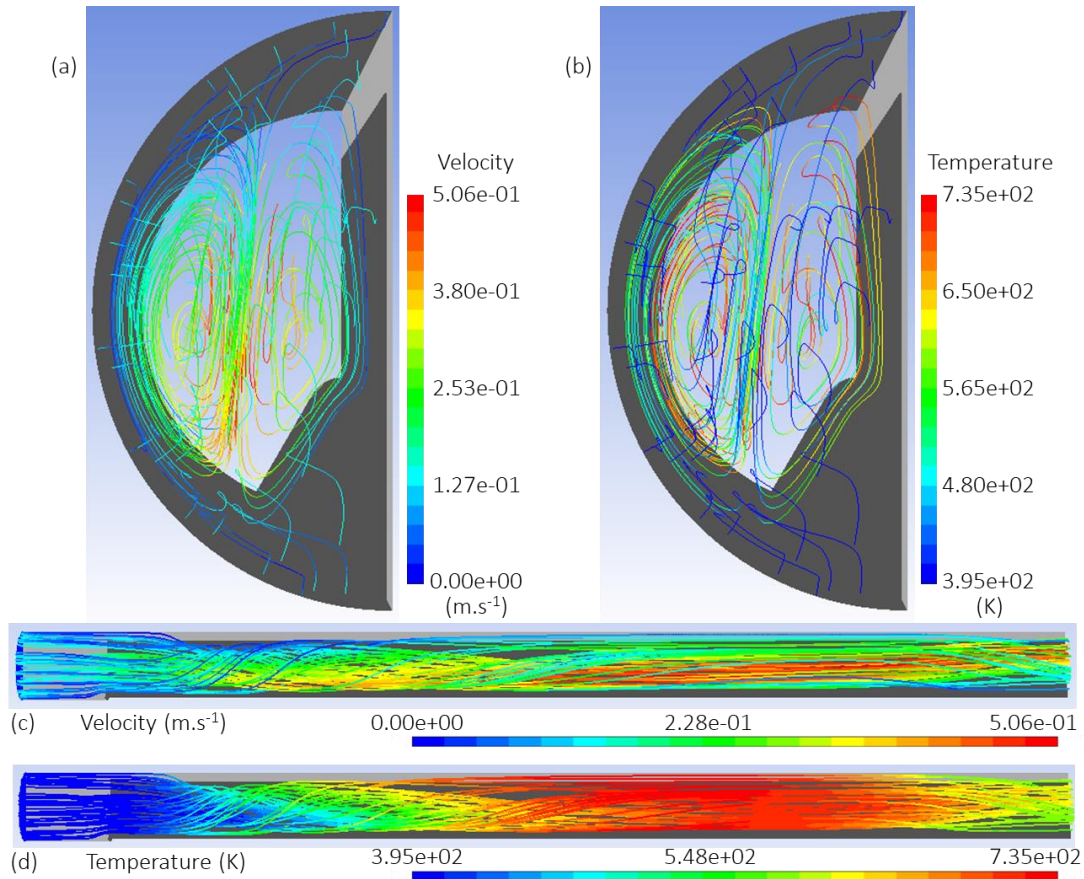
Fig. III.21. Static front view of velocity (a) and temperature (b) pathlines for run E4 (450°C). Results are plotted from the inlet facing towards the inside of the reactor. Only half of the reactor geometry is shown due to symmetry. Static side-view of velocity (c) and temperature pathlines (b). Solid surfaces (wall, substrates and substrate holder) are illustrated in dark grey. Symmetry plane is illustrated in light grey.

After impacting on the substrate holder and the substrates, the gas flow follows a double vortex-like trajectory in the inlet region and across the first substrates, as shown in Fig. III.21. This behavior is explained through the aforementioned impact, which forces the gas to change direction, and is additionally

accentuated by the concomitant heating of the gas by the heated surfaces of the wall and the substrates. As a result, the fluid flow is split in two portions when arriving near the substrates.

Going back to Fig. III.20, the thermal profile of the gas is also shown. The gas temperature remains below 150°C before the substrates. It then increases and presents a W-shape between 0.1 and 0.2 m, beyond which it follows a parabolic shape for the rest of the zone occupied by the substrates. The parabolic shape is expected, given that the solid surfaces are hotter than the bulk of the fluid and the thermal conductivity of the gas phase is low. The W-shape originates from the two-portion split of the gas as mentioned previously and is also encountered in the mass fraction profiles (Fig. III.20). At the inlet region, the O$_3$ and TEOS mass fractions remain constant in the bulk of the gas phase, with consumption happening only at the walls through reaction R6. From approximately 0.14 m from the inlet and onwards, the TEOS mass fraction decreases due to the homogeneous reaction R4 and the already active R6. O$_3$ is depleted slightly more rapidly in the same zone, until its mass fraction reaches zero. This depletion is attributed mainly to reaction R1 (Fig. III.22), whose rate is much higher than the other homogeneous reactions involving O$_3$ (R2, R4, R6 and R8).

Reaction R4 gives rise to the INT species formation in a localized region between approximately 0.12 and 0.24 m from the inlet, beyond which the reaction rate of R4 diminishes to very low values, given that O$_3$, one of the reactants participating in this reaction, has been consumed. For the same reason, reaction R8 is also active only in this region. Similarly, reaction R6 is unable to take place beyond this area.

In parallel, INT continues to be slowly depleted through reaction R7 (Fig. III.22), but still presents a remarkable 0.2 m long zone, between 0.25 and 0.45 m from the inlet, where its mass fraction stays relatively stable (Fig. III.20). Interestingly, despite the mass fractions of INT and O$_2$ remaining fairly constant beyond ~0.5 m, the reaction rate of R7 decreases, underlining its dependency on the temperature, which starts to decrease at the exhaust region.

Regarding the atomic oxygen, it is formed through reaction R1, between approximately 0.12 and 0.22 m. It appears in low concentrations before it drops to zero through its involvement in reactions R2 and R3. For O$_2$, it is present in excess and only participates as a reactant in reaction R7, which has the lowest reaction rate. Thus, its mass fraction is fairly stable inside the reactor, with a slight increase observed in the O$_3$ depletion zone and beyond as a result of the production of O$_2$ through reactions R1, R2 and R3.
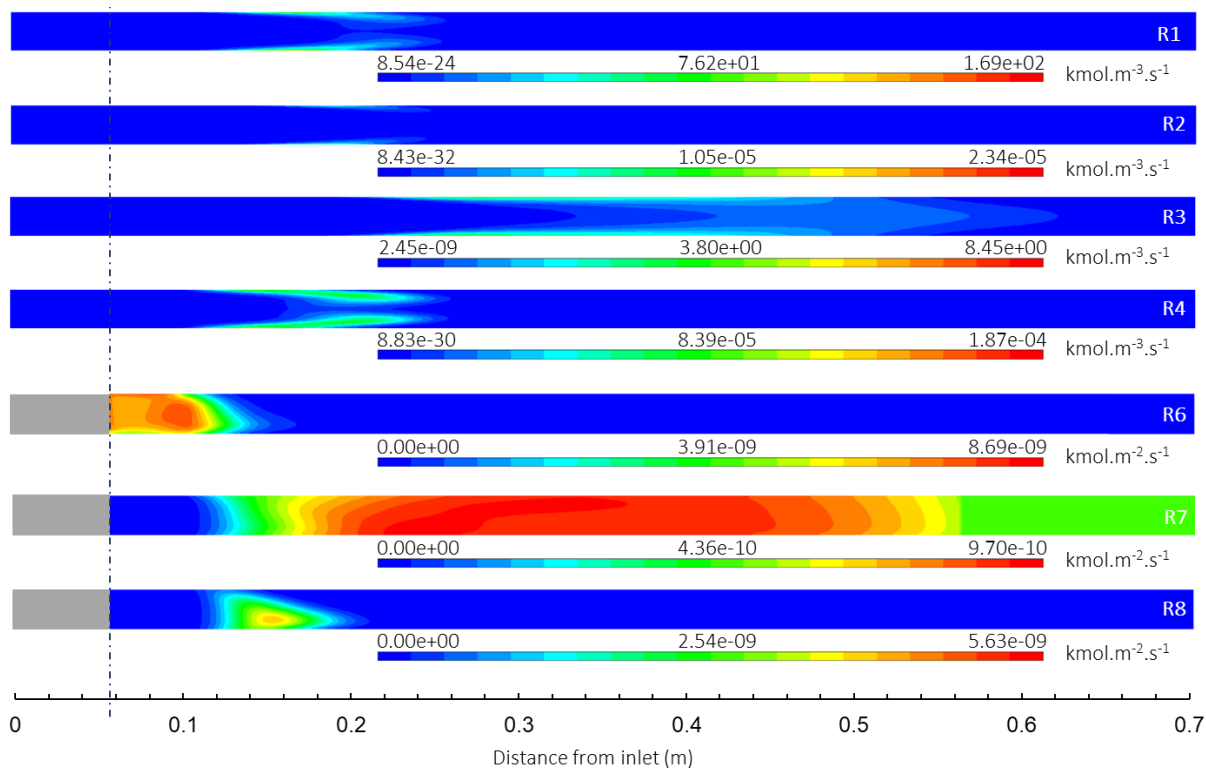
Fig. III.22. Reaction rate profiles for all reactions plotted along the XZ plane for the gas phase reactions (R1 to R4) and along the YZ plane for the surface reactions (R6 to R8) of run E4 (450°C). Vertical black dash-dotted line signifies the start of the substrates.

The overall consumption of TEOS to towards production of INT and SiO_2 for run E4 is approximately 79%, increasing for higher SPT. Despite that, the global TEOS-to-SiO_2 conversion rate on all solid surfaces remains low and does not exceed 5.2 % for all runs. This means that TEOS is predominantly involved in the production of INT through reaction R4, instead of the formation of SiO_2 through reaction R6. This is also evident when inspecting the maximum values of the respective reaction rates in Fig. III.22. Another key observation is that reaction R7 should be favored to uniformly coat complex-in-shape and/or large substrates, given that it has a large region within which its reaction rate remains stabilized and can lead to uniform deposition.

The rapid consumption of O_3, even at low temperatures, is also worth noting. As a result, quantities of TEOS and INT remain unreacted, with reactions R4, R6 and R8 ending prematurely. This leads subsequently to a low process yield. For these three reactions, O_3 depletion becomes the rate-limiting step, indicating that a higher O_3 flow all across the substrate zone would be preferable. However, increasing the O_3 concentration at the inlet would lead to higher deposition rates across the whole reactor length in general,

and especially at the inlet region where reaction R6 rapidly takes place. As such, big discrepancies in DR between the colder inlet zone and the hotter isothermal region would still exist. Another solution for increasing the deposition yield, while still retaining relatively flat DR profiles, would be a sequential introduction of O_3 at multiple parts along the length of the reactor. For better uniformity, it is proposed to insert O_3 in already heated zones, to favor reaction R4 over R6. As a result, higher quantities of INT would be produced, able to lead to uniform SiO_2 deposition through reaction R7, while also promoting reaction R8. The rapid depletion of O_3 is a known problem and similar solutions have been proposed in other works [158, 241]. A setup using multiple injection ports for O_3 cannot be easily implemented experimentally. Thus, the present model could be used to help finding the best combinations of geometry and operating conditions that can lead to the increase of precursor conversion and overall deposition yield.

III.2.7. Transfer of TEOS-O₂/O₃ model into vial reactor

The deposition experiments in Type I vials at SPT 400°C and 550°C were simulated using the above proposed and validated chemical model. The total mass flow rate and the mass fractions of all species at the inlet are fixed to the experimental values described in section II.1.1.2 of Chapter II. In Fig. III.23a the experimental and simulated DR values at both temperatures are compared. The experimental DR is deduced from weighing the vials before and after deposition. The simulated DR is the average value extracted from the DR values of the internal and external surfaces of the vial, excluding the external heel surface. A photograph of a vial after deposition is shown in Fig. III.23b.
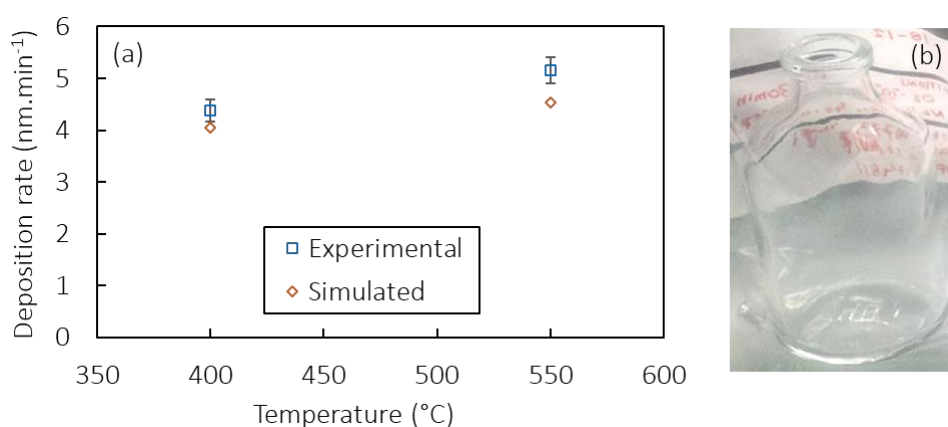
Fig. III.23. Experimental and simulated DR of SiO_2 barrier coatings deposited in pharmaceutical Type I vials at 400°C and 550°C (a). Photograph of a coated vial after deposition (b).

The simulated DR appears close to the experimental one, with a deviation of 7.3 % and 8.5 % at 400°C and 550°C, respectively. The increase in deposited SiO_2 material at higher SPT is also reproduced through simulation. Having verified the experimental data, the simulations are used to obtain predictions regarding hydrodynamic, thermal, and mass transfer properties of the gas phase and the involved species.
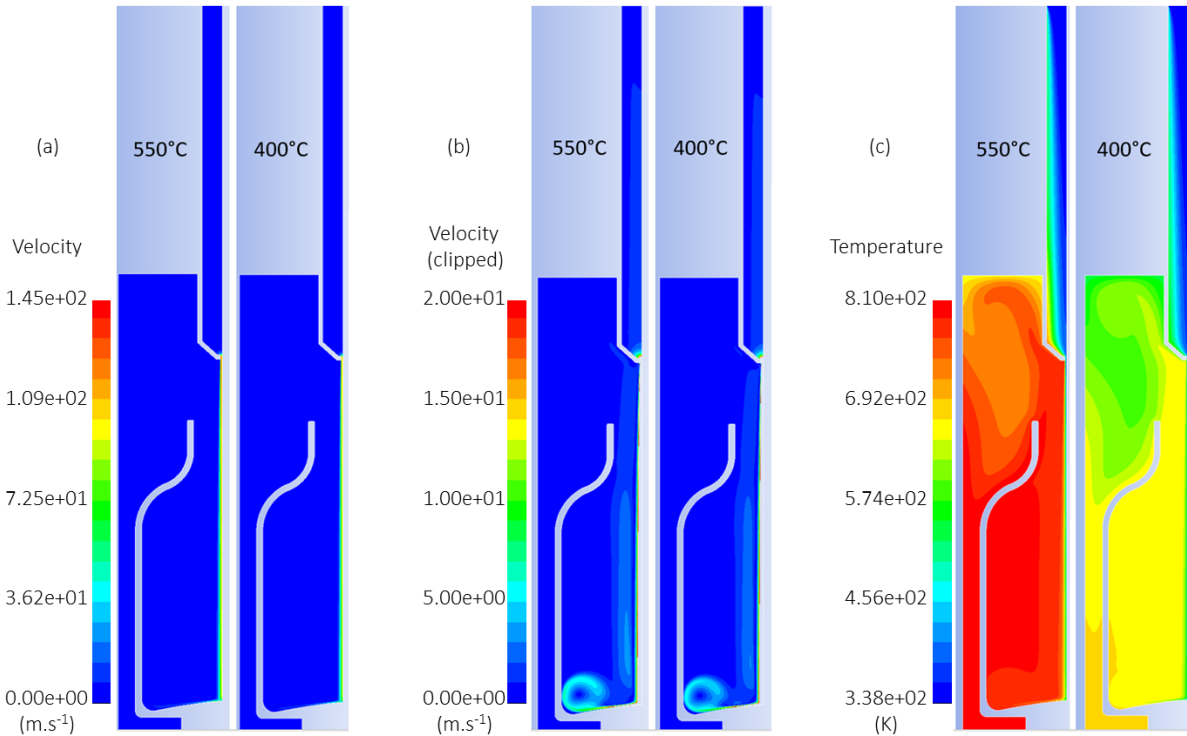
Fig. III.24. Gas velocity profile at full range (a) and clipped to a maximum value of 20 m.s^{-1} (b) for the two experiments. Temperature distribution profile (c).

First, the local gas velocity and temperature distribution profiles are presented in Fig. III.24. The full range of the velocity profile is shown in Fig. III.24a. The maximum velocity is noted at the exit of the injector nozzle, reaching values around 145 m.s^{-1}. Because this maximum value is high, it renders visualization of lower values more difficult. In order to aid in their presentation, the velocity range is clipped at a maximum of 20 m.s^{-1}. The corresponding velocity profile is shown in Fig. III.24b. Through this aided visualization, the impacting jet and its subsequent trajectory can be better observed. The vortex at the heel region also becomes visible, occurring through the aforementioned impact of the gas flow on the vial base. The velocity profile is similar to the ones obtained by Etchepare et al. [56] and in Ponton's thesis [7], who utilized simulations to represent Al_2O_3 and SiO_2 depositions in vials, respectively, utilizing the same reactor setup. Aside from the high velocities observed because of the jet, the average velocity in the reaction

chamber does not exceed 5 m.s^{-1}. This translates to a residence time of approximately 0.07 s, a value much lower than the 1.4 s noted in the tubular reactor and more comparable to that of Nieto et al.'s Watkins Johnson type reactor (<0.5 s).

The simulated thermal profiles are also shown in Fig. III.24c. Since the temperature of the gas at the inlet is much lower than the imposed temperatures at the quartz tube, it gives rise to a cooler impacting jet that gets heated and reaches the desired temperature only after entering the vial.
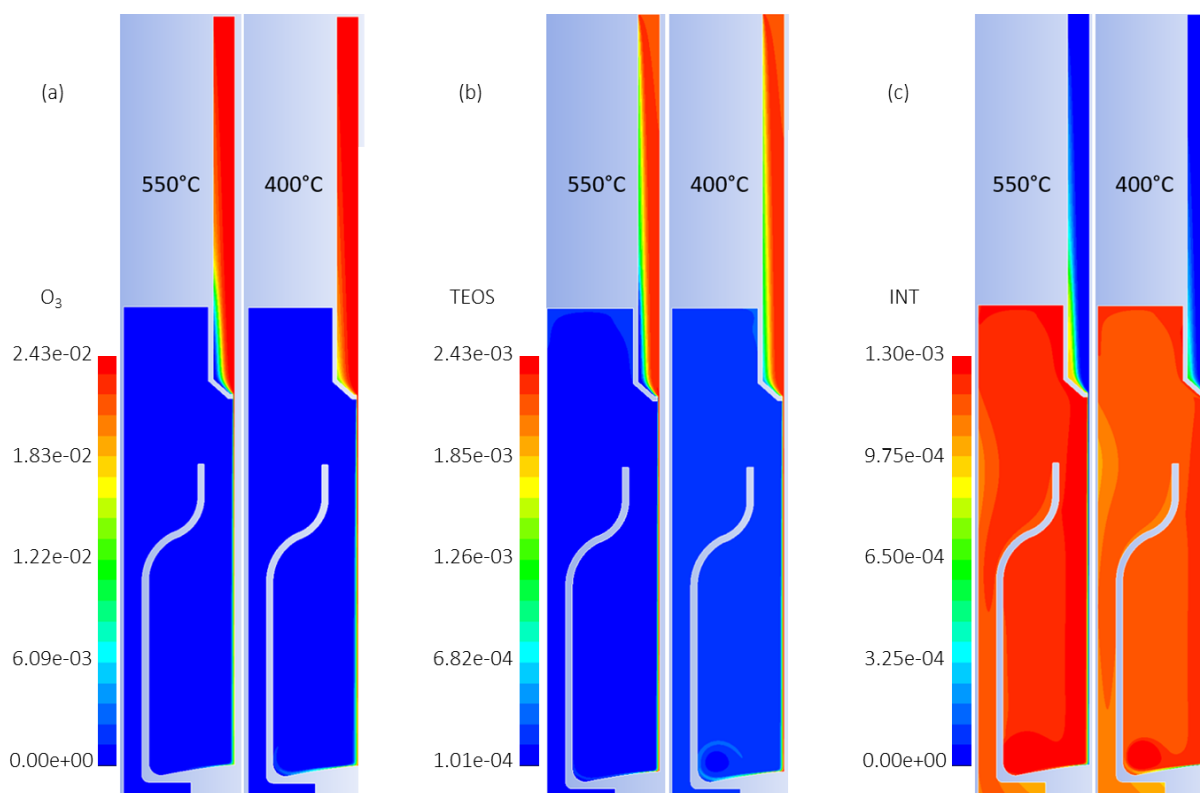
Fig. III.25. Local mass fraction profiles of O₃ (a), TEOS (b), and INT (c) for the two temperatures studied for the coating of pharmaceutical Type I vials.

Fig. III.25 shows the local mass fraction distributions of O₃, TEOS, and INT. Fig. III.25a illustrates how O₃ is immediately and completely consumed through reactions R1 to R3, which are activated once the gas mixture reaches the vial bottom and is heated. TEOS (Fig. III.25b) is also almost completely consumed, thanks to reactions R4 and R6. Fig. III.25c illustrates the production of INT, which takes place once the gas mixture is heated sufficiently. Its mass fraction appears to be distributed relatively homogeneously within the vial volume.

Table III.3. TEOS conversion and deposition yield for SiO₂ simulations performed in the vial reactor.

SPT	Overall TEOS conversion	Deposition yield (conversion into SiO₂)
550°C	91.7 %	12.04 %
400°C	87.3 %	9.23 %

The conversion of TEOS into INT and SiO₂, as well as the deposition yield for SiO₂ deposition on all solid walls are detailed in Table III.3. It is noted that both TEOS conversion and deposition yield are higher than the ones observed in the tubular reactor. These results show that the change in reactor configuration (use of injector nozzle) and substrate geometry (hollow body and deposition in a confined space) has led to a more efficient utilization of the supplied precursor quantity. This is especially reflected in the higher deposition yield, which is more than doubled in the case of the vial reactor, when deposition is performed at 550°C. The distribution of the deposited SiO₂ material is shown in Fig. III.26.
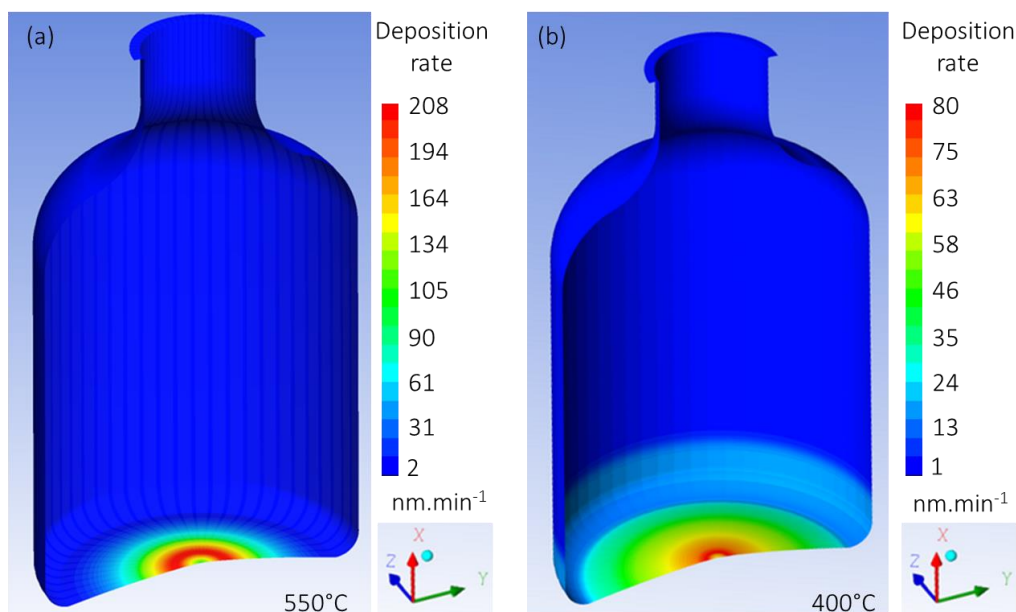
Fig. III.26. 3D representation of a pharmaceutical vial and simulated SiO₂ DR at 550°C (a) and 400°C (b).

The simulations indicate an uneven distribution of the DR. Higher values are observed at the region where the jet impacts on the vial bottom. Among the three deposition reactions, R6 is the major contributor to deposition in this region, while R7 and R8 are mostly active at the body and shoulder regions.

Considering the deposition duration (30 min), the maximum calculated DR values at the vial base translate to a local thickness of 6.2 μm and 2.4 μm at 550°C and 400°C, respectively. However, no such film thickness was observed macroscopically after the deposition experiments in vials. It is therefore concluded that the model can on one hand provide an average DR value for simulations in the vial reactor (Fig. III.23), but requires some refinements to represent the local phenomena occurring in this different reactor configuration, especially given the largely different gas residence times.

III.3. Deposition of SiO$_x$ from HMDS-TEOS-O$_2$/O$_3$

The results of Sections III.1 and III.2 illustrated clearly how the addition of O$_3$ in the starting TEOS-O$_2$ chemistry can help lower the minimum temperature required for the deposition of SiO$_2$. The lowest temperature for which SiO$_2$ deposition was formed in the present thesis was around 110°C. However, temperatures as low as 25°C have also been reported in the literature [114]. Through this, the role of O$_3$ and its potential to drastically activate film-forming reactions becomes clear. It is recalled that the aim of this thesis, and by extent of the ANR HEALTHYGLASS project, is to deposit SiO$_x$N$_y$ films at low temperatures. Moreover, in the frame of the ANR project, deposition of SiO$_x$C$_y$ is also a targeted goal. The objective to deposit at low temperatures naturally leads to the exploration of chemistries based on ozone. It must be kept in mind however that the generation of monoatomic oxygen radicals might impede the incorporation of nitrogen, as was previously presented in the literature review discussed in Chapter I. In a pure exploratory manner, the compound hexamethyldisilazane ((CH$_3$)$_3$SiNHSi(CH$_3$)$_3$, HMDS), a nitrogen and carbon containing organosilicon precursor molecule, was selected to investigate if incorporation of any of the two elements is possible at low temperatures facilitated by O$_3$-based chemistries.

The following sub-sections firstly deal with an initial investigation of the HMDS-O$_2$/O$_3$ chemistry, followed by an extensive analysis of the dual precursor HMDS-TEOS-O$_2$/O$_3$ chemistry. It is recalled that the latter atmospheric pressure chemical vapor deposition (APCVD) pathway is original in regards to the literature. The study is conducted on planar Si substrates and focuses primarily on the characterization of the material from a compositional and functional point-of-view. Deposition rate (DR), composition and film structure are studied for variable operating conditions. Similar investigation follows for the film mechanical and functional properties, concluding with its corrosion resistance. The overall study follows the methodologies previously adopted for the TEOS-O$_2$/O$_3$ chemistry.

III.3.1. Deposition rates

III.3.1.1. Deposition from HMDS-O$_2$/O$_3$ chemistry

Investigation using the HMDS precursor was first conducted through deposition experiments using the HMDS-O$_2$/O$_3$ chemistry (shortened to just *HMDS chemistry* hereinafter), to ascertain the ability of this molecule to lead to film formation under the desired operating conditions. Experiments were conducted for 30 min at 730 Torr, targeting thicknesses between 100 and 200 nm. The applied gas flow rates have been previously described in section II.1.1.1 of Chapter II. For the HMDS chemistry, the HMDS bubbler temperature was maintained at a constant 50°C, resulting in a HMDS flow rate of 2.7 sccm towards the reaction chamber. Four experiments were conducted in these conditions at four different SPTs, namely 360, 400, 500 and 550°C. The measured DR profiles are shown in Fig. III.27.

Fig. III.27. DR profiles (black squares) for HMDS deposition at SPT 360°C (a), 400°C (b), 500°C (c) and 550°C (d), along with the respective thermal profiles (grey triangles).
Darker blue area signifies the isothermal region C.

Globally, the deposition behavior is similar to that observed in section III.1.1.1 for TEOS-O$_2$/O$_3$. Region A is described by low local temperatures and initiation of film formation takes place at high DR

values on the first samples of this region, thanks to the presence of O_3 in high concentrations. For a SPT of 360°C (Fig. III.27a), the DR starts at around 4.5 nm.min^{-1} in the inlet region and increases to reach a maximum of approximately 7 nm.min^{-1} once the temperature reaches ca. 250°C. This increase is attributed to the increase of the temperature in region B, with O_3 still being present in the gas phase at sufficient concentrations. Once O_3 has been consumed, the DR presents a decrease after 0.2 m from the inlet despite the continuous increase of the temperature. Similar trends were noted for the TEOS-O_2/O_3 chemistry. An interesting and new observation however is that after O_3 consumption, there is no deposition noted for SPT 360°C and 400°C (Fig. III.27a and b). This means that HMDS itself, as well as any intermediates that were produced from its reaction with O_3 [242], do not have the required energy to overcome their respective activation steps and lead to film formation below 400°C, without the aid of O_3. That assumes of course that HMDS and its intermediates are still present in the gas phase and have not been depleted. This is confirmed by the resumption of film-formation for local temperatures around 450°C and beyond (Fig. III.27c and d). Once the gas phase is heated sufficiently, deposition starts anew and is especially promoted for temperatures above 500°C. The above deposition behavior is also visible when inspecting photographs of the samples presented in Fig. III.28.
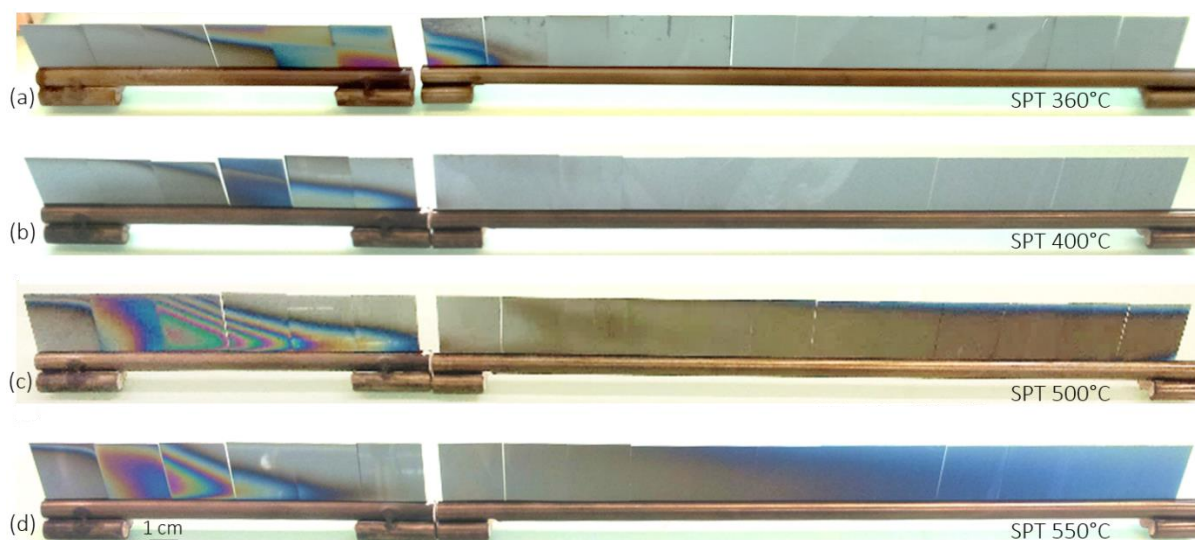
Fig. III.28. Photographs of array of Si samples within the substrate holders,
after deposition using HMDS chemistry at 360°C (a), 400°C (b), 500°C (c) and 550°C (d).

The lack of deposition on the last 10 to 12 samples of SPT 360°C and 400°C is visible by the silver color of the uncoated Si substrates (Fig. III.28a and b). On the contrary, visible deposition is observed for

SPT 500°C and 550°C (Fig. III.28c and d). Interestingly, deposition experiments utilizing the dual precursor HMDS-TEOS-O$_2$/O$_3$ chemistry resulted in a different behavior, as is presented below.

III.3.1.2. *Deposition from HMDS-TEOS-O$_2$/O$_3$ chemistry*

Deposition using HMDS appears to require O$_3$-activation, if film formation at temperatures below 450°C is desired (Fig. III.27a and b). On the contrary, the intermediates produced from TEOS are more reactive and can lead to deposition even after O$_3$ is consumed in the gas phase (Fig. III.3). To take advantage of the high reactivity of TEOS intermediates and the high carbon content of the HMDS molecule, vapors of both precursors are supplied in the reactor. The HMDS-TEOS-O$_2$/O$_3$ chemistry (abbreviated to *HMDS-TEOS* hereinafter) is investigated by varying two parameters. The first parameter is the deposition temperature. Five different SPTs are tested, namely 360, 400, 450, 500 and 550°C. The bubbler temperature is maintained at a constant 50°C across these five experiments, supplying 2.7 sccm of HMDS to the reaction chamber. The second parameter is the HMDS precursor flow rate, which is varied by increasing the HMDS-bubbler temperature to 62°C, which translates to a HMDS flow rate of 9.5 sccm. A SPT of 400°C is applied for this experiment. Deposition time is kept constant at 30 min for all runs. N$_2$ and O$_2$ flow rates, as well as O$_3$ output, have been previously described in section II.1.1.1 of Chapter II.

The DR profiles using the HMDS-TEOS chemistry are presented in Fig. III.29. Film formation appears to take place across the whole length of the reactor for all SPTs, in contrast to what was previously noted for the HMDS chemistry. In fact, the DR profiles are more similar to the TEOS-O$_2$/O$_3$ chemistry (abbreviated to just *TEOS* hereinafter).

Logically, the dual precursor HMDS-TEOS system has a deposition behavior that is dictated by the participation of both precursors to the formation of the film. Similarly to the previous O$_3$-based chemistries, HMDS-TEOS also follows DR profiles that reach a maximum in regions A or B, depending on the SPT, and which decrease in region B as a result of O$_3$ consumption. For comparison, at SPT 360°C (Fig. III.29a) the DR measures initially around 5 nm.min^{-1} and reaches a maximum ca. 12 nm.min^{-1} once the temperature reaches approximately 250°C. Both values are higher than those noted for HMDS (Fig. III.27a), which is expected, given that both HMDS and TEOS precursors contribute to deposition in the dual precursor chemistry. After this point, the DR decreases in region B due to lower O$_3$ concentrations in the gas phase. In region C however, a new behavior of the DR is noted. Firstly, DR values are not reduced to zero for SPT 360°C and 400°C, as was observed for HMDS. Instead, deposition continues to take place, but at a constantly decreasing rate (Fig. III.29a to c). For SPT 500°C (Fig. III.29d), the DR profile settles down to an almost stable value, similarly to what was observed for TEOS. However, for SPT 550°C (Fig.

III.29e), the DR of HMDS-TEOS shows a renewed increase, similarly to the DR profile observed previously for HMDS (Fig. III.27d).
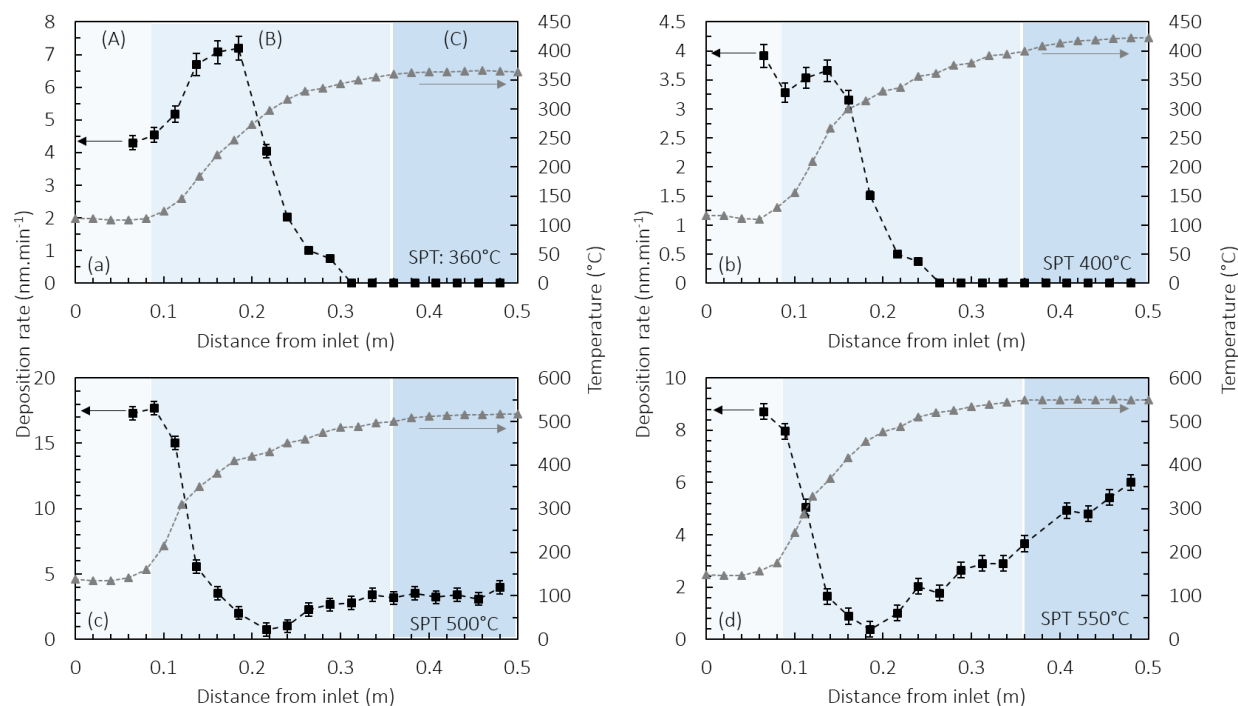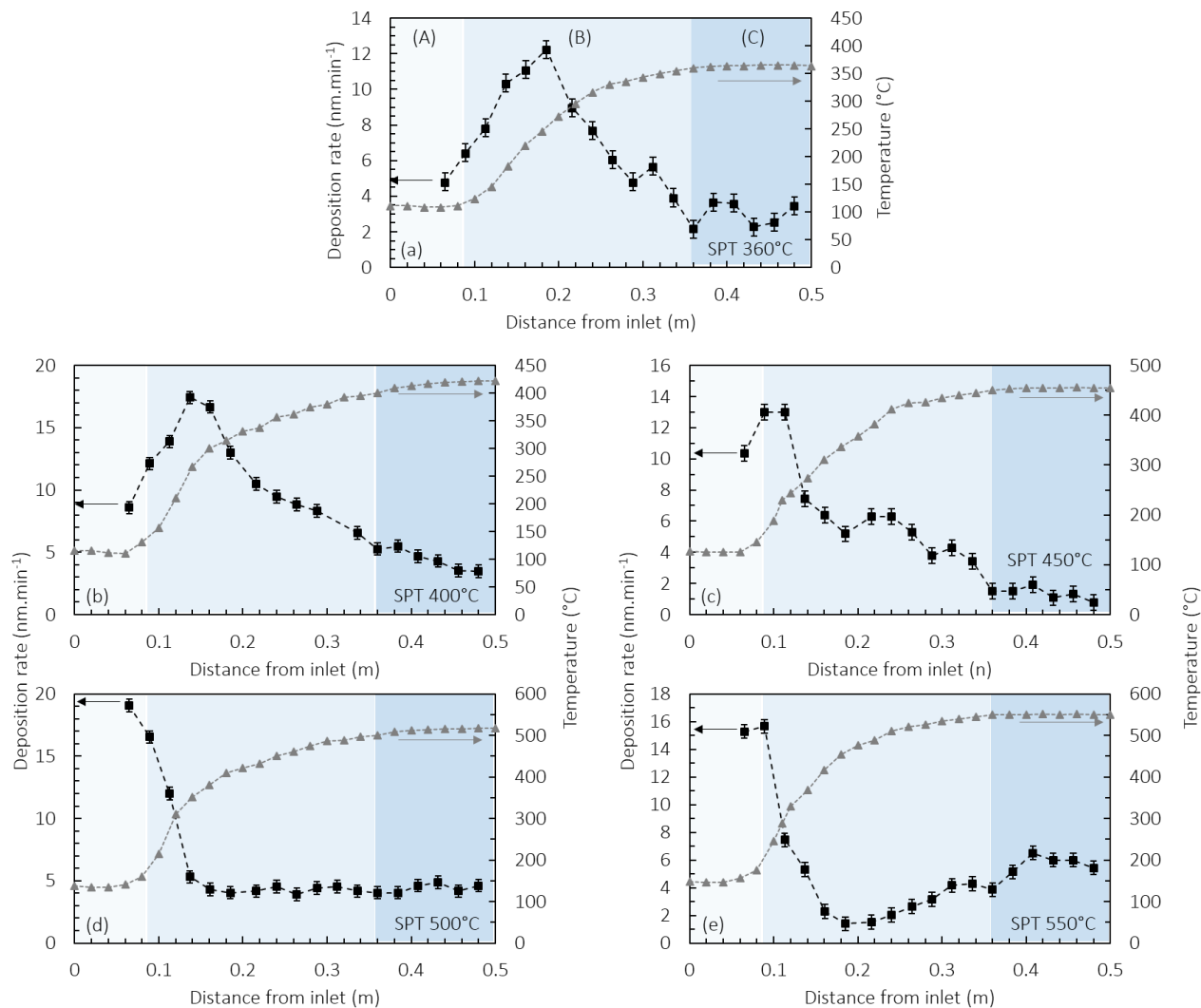

Fig. III.29. DR profiles (black squares) for HMDS-TEOS deposition for SPT 360°C (a), 400°C (b), 450°C (c), 500°C (d) and 550°C (e), along with the respective thermal profiles (grey triangles). Darker blue area signifies the isothermal region C.

The above is illustrated more clearly when directly comparing deposition from TEOS and HMDS for the highest SPT, i.e. 550°C, as shown in Fig. III.30a. For a temperature of 500°C and above, deposition from TEOS remains at a constant rate of approximately 2 nm.min^{-1}, while film formation from HMDS is continuously increasing up to values around 6 nm.min^{-1}. The lack of a renewed increase in the TEOS

chemistry beyond 0.2 m can be attributed to the potential polymerization reactions occurring in the gas phase. As was explained earlier in section III.1.1.1, at elevated temperatures (>450°C), the intermediates that are produced from the decomposition of TEOS are prone to be consumed in parasitic reactions such as gas-phase polymerization [158, 186]. As a result, their available concentration in the gas phase decreases, which subsequently partially decelerates further increase of SiO$_2$ deposition. In the case of HMDS chemistry however, this does not seem to be the case. A potential explanation could be that the intermediates originating from the decomposition of HMDS are less reactive than those from TEOS and do not participate in parasitic gas-phase reactions. As a result, they can actively contribute to film formation once they overcome their activation step for temperatures exceeding 450°C (Fig. III.30a).
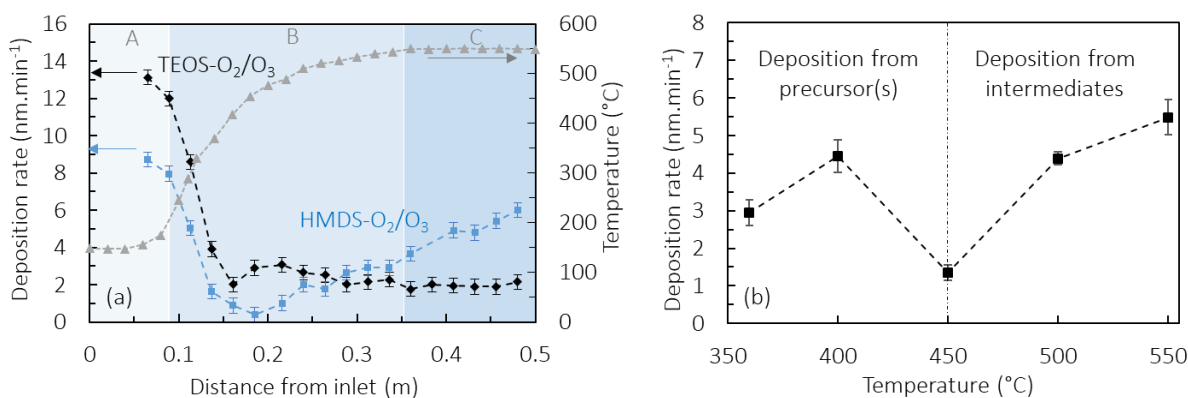
Fig. III.30. Individual deposition profiles from HMDS and TEOS at SPT 550°C (a). Corresponding thermal profile is shown by grey triangles. DR averaged across samples p1 to p6 of the isothermal region, taken from HMDS-TEOS runs performed at various SPTs (b).

The DR of HMDS-TEOS is averaged across the six samples (p1 to p6) located in the isothermal region C and its evolution with the SPT is shown in Fig. III.30b. It presents a wavy behavior with average DR values ranging between 1 and 6 nm.min^{-1}. More specifically, the DR increases from 360 to 400°C, then decreases at 450°C, after which it increases again from 450 to 550°C. This non-monotonous trend has also been observed for the thermal CVD of SiO$_2$ from TEOS [115, 139, 243] and is explained through the participation of distinct reactive species in SiO$_2$ film formation, depending on the temperature. For temperatures lower than 400°C, deposition depends primarily on the precursor molecule and the presence of O$_3$ in the gas phase. At higher temperatures, the precursor molecules are decomposed into Si-containing gaseous intermediate species. As a result, the deposition mechanism switches to an intermediates-centered mechanism. It is therefore assumed that when utilizing the dual precursor HMDS-TEOS chemistry, any

increase of the DR above 500°C is primarily due to the addition of the HMDS precursor. The dip at 450°C in Fig. III.30b is related to the overall transition of the deposition mechanism from precursor-governed to intermediates-governed. Potentially, a high contribution of carbon-rich species could also be involved in this deposition behavior, as is discussed in the following sections.

III.3.2. Film surface morphology

AFM surface micrographs for HMDS-TEOS films deposited at all five SPTs are presented in Fig. III.31a to e. The micrographs of the three lowest SPTs reveal rough surfaces, in contrast to the two highest ones, 500 and 550°C, which present a generally smoother surface. This trend is also confirmed when plotting the root mean square (RMS) roughness as a function of the SPT as shown in Fig. III.31f.
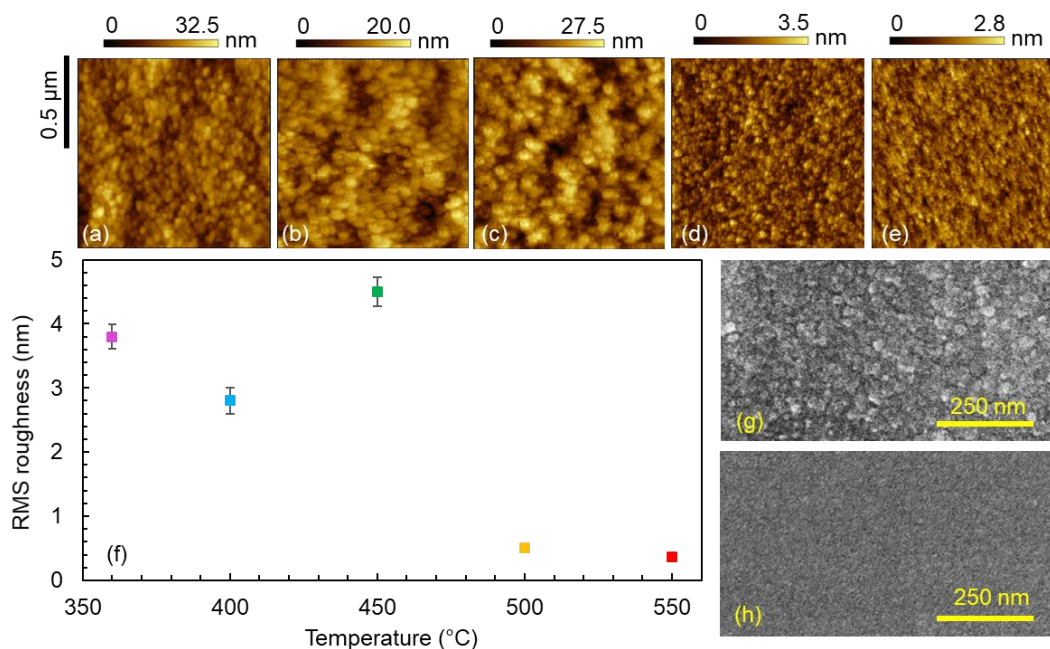
Fig. III.31. Surface topography and RMS roughness of HMDS-TEOS films at various SPTs. AFM 1 μm² surface topography at SPT 360°C (a), 400°C (b), 450°C (c), 500°C (d) and 550°C (e). RMS roughness of HMDS-TEOS films for different temperatures measured by AFM.
SEM surface micrographs for films deposited at SPT 360°C (f) and 500°C (g).

The RMS roughness of surfaces prepared at 360, 400 and 450°C is spanning between 3 and 4.5 nm, whereas it decreases to values around 0.5 nm for 500 and 550°C. SEM surface micrographs, representative

of the two observed surface morphologies, are also reported in Fig. III.31g and h, corresponding to samples processed at 360 and 500°C, respectively. In agreement with the AFM observations, the films morphology appears rough at the lowest temperature and becomes smoother at 500°C. Additionally, these results reveal a difference in the nucleation and growth mechanisms: an apparent 3D-dominated nucleation and growth behavior is observed at lower temperatures, attributed to the high DR, combined with the limited mobility of the adsorbed species. At elevated temperatures, the species participating in film formation have higher surface mobility due to the increased available energy. As such, they are able to diffuse more easily on the surface, following primarily a 2D growth behavior, and lead to the production of denser and smoother films.

Overall, the surface roughness decreases with increasing temperature, with the exception of 450°C. According to Gil et al. [216], who performed PECVD of SiO$_2$ films from HMDS and O$_2$, the surface roughness is influenced by the organic carbon content, incorporated in the films as CH$_3$ moieties. The authors reported that increasing oxygen flow aids in the decomposition and oxidation of HMDS, which leads to a decrease in the amount of Si–(CH$_3$)$_x$ bonds in the films and subsequently to the decrease of surface roughness. In the results of Fig. III.31 however, the O$_2$/O$_3$ flow rate remains unchanged across all runs, with the temperature being the only variable. Based on the authors' findings, the spike in roughness observed at 450°C could be connected to higher CH$_3$ incorporation. Connecting these results to those of Fig. III.30b, it is proposed that the transition of the deposition mechanism happening at this temperature introduces more CH$_3$ moieties in the films, increasing in turn the RMS roughness. In order to confirm this assumption, the films chemical bonding state and composition are analyzed by FT-IR and IBA.

III.3.3. Chemical bonding and network evolution

The infrared spectrum of a HMDS-TEOS film produced at 360°C is presented in Fig. III.32, as representative of the samples processed at low SPT. Acquisition was done at a Brewster incidence angle of 60°, with the aim to increase the signal-to-noise ratio and to reveal additional information related to the silica network [169]. The main peaks in the survey spectrum of Fig. III.32 are first identified and then the evolution of the various bonds is presented in respective inset graphs as a function of the temperature. Globally, the films are characterized as a silica-based material, evidenced by the strong absorption at 1064 cm^{-1} attributed to the transverse optical TO3 mode [99, 187], characteristically present in SiO$_2$ films prepared by TEOS-O$_2$/O$_3$ and HMDS-O$_2$ by thermal CVD [90]. Its longitudinal optical LO3 pair is encountered at 1216 cm^{-1}. The TO1 rocking and TO2 bending modes are also noted, found at 448 cm^{-1} and 806 cm^{-1}, respectively [187].

The presence of carbon is also identified in the films, mostly in the form of hydrocarbons. Methyl-related absorptions are observed at different wavenumbers, as indicated in Fig. III.32. Generally, weak absorptions within the 2800-3000 cm⁻¹ range are related to stretching vibrations of saturated C–H bonds [89, 214], with an increase in their intensity corresponding to an organo-rich structure and vice versa [244].
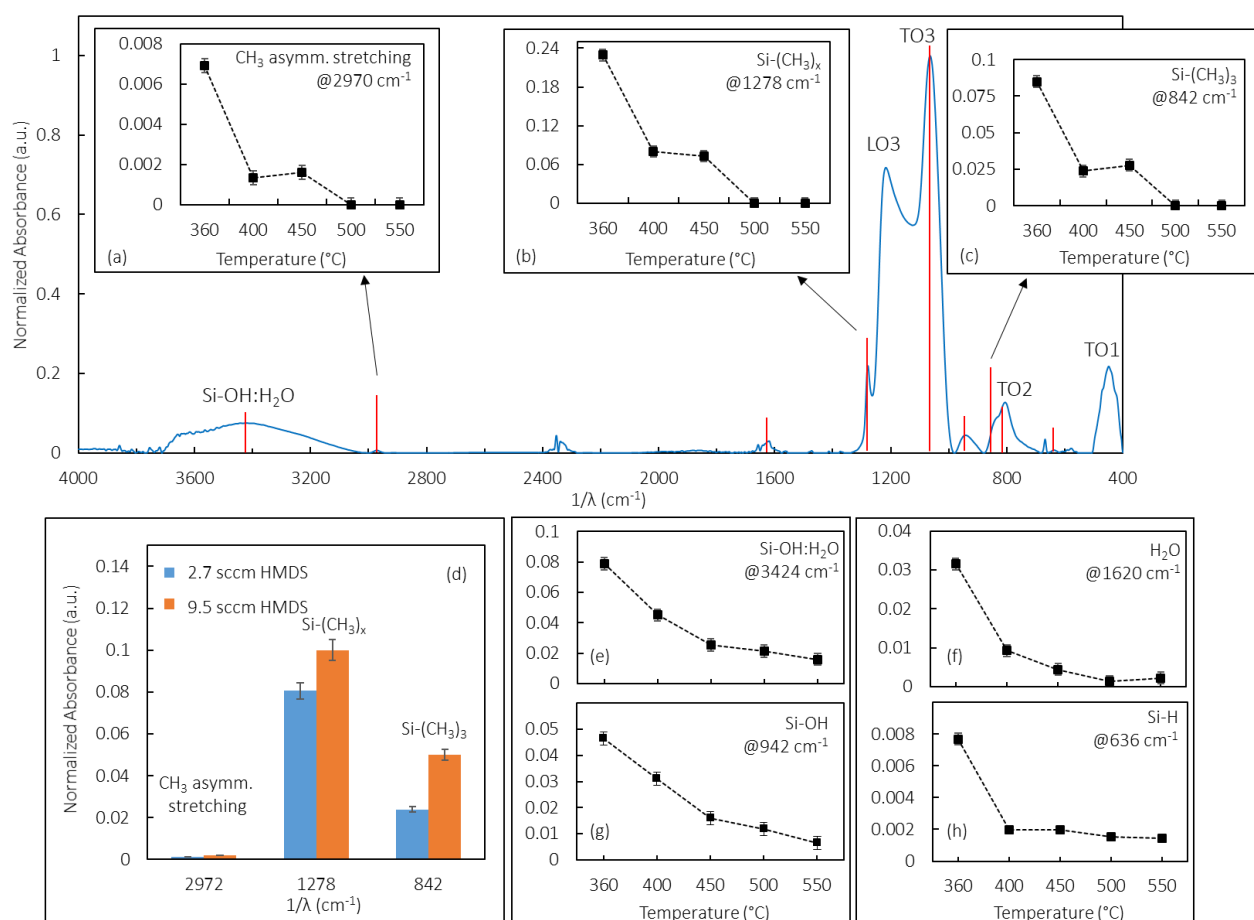
Fig. III.32. FTIR survey spectrum of a HMDS-TEOS film deposited at 360°C, analyzed for an incidence angle of 60°. Evolution of the CH_3 asym. stretching (a), CH_3 sym. bending in Si-$(CH_3)_x$ (b) and CH_3 rocking vibration in Si–$(CH_3)_3$ (c) as a function of the SPT. Inset histogram (d) shows these three absorptions for films produced at different HMDS flow rates at SPT 400°C. Evolution of water-bonded silanol (e), molecular physisorbed water (f), free Si–OH (g) and Si–H (h) absorptions with the SPT.

In the present case, one such absorption is found at 2970 cm⁻¹ and is assigned to the asymmetric stretching of CH_3 functional groups [242]. Secondly, the absorption at 1278 cm⁻¹ is related to the symmetric bending vibrations of CH_3 in Si-$(CH_3)_x$ groups [216, 245], while the small shoulder at ca. 845 cm⁻¹ is

attributed to the rocking CH$_3$ vibration in Si–(CH$_3$)$_3$ groups [242, 246]. The evolution of the intensity of these three absorptions is plotted versus the SPT in the inset figures Fig. III.32a to c. It is revealed that they all follow a similar behavior. Their intensities decrease at higher temperatures, with all three methyl absorptions reaching zero for temperatures equal to or higher than 500°C. This indicates that films deposited above 500°C do not contain carbon, as a result of the additional provided energy being high enough to break the Si–CH$_3$ bonds of the starting molecule (HMDS). A spike is observed for films processed at 450°C, correlating well with the RMS roughness results and confirming the previous proposal that the transition in the deposition mechanism at this specific temperature leads to an increase of the carbon content.

In the histogram of Fig. III.32d, the three CH$_3$ absorptions are probed for films processed under two different HMDS flow rates, with the SPT fixed at 400°C. Higher concentrations for all three CH$_3$ modes are found at the higher HMDS flow rate. This, combined with the fact that no methyl incorporation was observed in TEOS films, indicates that the methyl moieties originate from the HMDS molecule, as was observed by Gil et al. [216] and Lee et al. [247].

It is noted that for SiO$_x$C$_y$ films, a characteristic vibration is observed at 790-820 cm^{-1}, corresponding to the Si–C stretching bond [214]. It overlaps however with the TO2 bending mode of the Si–O–Si network, thus telling the two absorptions apart from each other is not as straightforward. Similarly, a rocking vibration of CH$_3$ in Si(CH$_3$)$_2$ groups is reported at 800 cm^{-1} in the literature [246], but is not easily discernable for the same reason. The non-Gaussian shape of the absorption at 800 cm^{-1} however is an indication of contribution of multiple peaks.

Additionally, a small absorption is found at 1410 cm^{-1} corresponding to the asymmetric CH$_3$ bending vibrations in Si–(CH$_3$)$_x$ [245], while a weak absorption at 1478 cm^{-1} could originate from the bending vibration of methylene (CH$_2$) groups [99]. Further absorptions related to CH$_2$ vibrational modes can be observed at 1372 cm^{-1}, related to scissoring and wagging CH$_2$ vibrations in Si–CH$_2$–Si [247, 248]. The signal for Si–CH$_2$–Si, normally found at 1350 cm^{-1}, is usually weak [99] and was not observed in any of the films. At the same time, a related absorption, namely the wagging vibrations of CH$_2$ in Si–CH$_2$–Si, can be typically found at around 1060 cm^{-1} [247], but is most likely overshadowed by the strong TO3 Si–O–Si asymmetric stretching absorption at 1064 cm^{-1}. Similarly, the main peaks related to Si–O–C and Si–CH$_2$–Si, normally reported at 1100 cm^{-1} and 1000 cm^{-1} respectively [249, 250], possibly overlap once again with the strong Si–O–Si network absorptions. As such, their presence cannot be confirmed with certainty.

Further inspecting Fig. III.32, the large band between 3000 and 3700 cm^{-1} is noted, which contains absorptions related to water and Si–OH bonds, as was mentioned in section III.1.1.2. Similarly to films from TEOS, HMDS-TEOS films present Si–OH bonded with water at ca. 3400 cm^{-1} [186], and physisorbed molecular water at 1620 cm^{-1} [193, 194]. An additional silanol fingerprint is found at 942 cm^{-1} [90, 216].

The intensity of these three absorptions is tracked as a function of the SPT in Fig. III.32e to g, revealing a decreasing absorption for films deposited at higher temperatures. This behavior suggests that the concentration of silanol bonds decreases when the temperature increases, with the Si–OH bonds forming new Si–O–Si bridges after dehydrogenation of the network.

It is worth noting that no Si–H absorption, normally appearing in the 1900-2200 cm^{-1} range [197, 198], is observed in any of the spectra. A weak absorption appears at 2353 cm^{-1}, which could correspond to a Si–H stretching mode according to Tomar and Gautam [90]. However, atmospheric CO_2 is probed at 2353 cm^{-1} as well [195, 196], originating from incomplete removal of the background signal. As such, absorption at this wavenumber cannot be entirely assigned to Si–H. Other absorptions relating to the Si–H bond, namely its bending and wagging/rocking vibrational modes, are normally found at 630 cm^{-1} [251] or ca. 640 cm^{-1} [197], respectively. For the produced HMDS-TEOS films, a weak absorption is observed at 636 cm^{-1}. However, when its intensity is traced as a function of the SPT (Fig. III.32h), the minimal Si–H absorption falls to insignificantly low values for T ≥ 400°C. In light of the above, we assume that films processed from HMDS-TEOS are devoid of Si–H bonds.

III.3.3.1.   Evolution of the silicate network

A similar investigation to the one conducted for the evolution of the network in TEOS films is also carried out for the produced HMDS-TEOS films. A zoom in the 750-1400 cm^{-1} region of the FT-IR spectra is presented in Fig. III.33. The evolution of three Si–O–Si vibrational modes (TO3, TO4 and TO2) and three carbon related ones (CH₃ symmetric bending in Si–(CH₃)ₓ groups, rocking CH₃ vibration in Si–(CH₃)₃ and Si–C) with the SPT is presented in Fig. III.33, at a 0° acquisition angle. The in-depth argumentation and the meaning behind the various evolutions was presented previously for TEOS films in section III.1.1.2. In light of the new carbon-related absorptions however, the results from the HMDS-TEOS films are discussed, albeit in a summarized manner, as follows.

First, the intensity of the CH₃ moieties decreases with the SPT, which is coherent with the overall decrease in carbon at the higher temperatures. Then, the position of TO3 moves towards lower wavenumbers, an inspection which is facilitated under an incidence angle of 60° (Fig. III.33a). In parallel, its LO3 pair shifts towards higher wavenumbers, similarly to the trends observed for TEOS films. As was discussed, the LO3 component is less biased by other types of vibrations compared to the TO3 component [169] and its shift towards higher wavenumbers can be correlated safely with a densification of the SiO₂ network as the SPT is increased. The broadening of the TO3 peak is also noted (Fig. III.33b) in parallel to the decreasing intensity of the TO4 shoulder with the SPT, which translates to lower nanoporosities [188],

hydrogenated impurities [172] and structural disorder of the SiO$_4$ tetrahedra [247]. The TO4 position shifts towards higher wavenumbers (Fig. III.33c), following a similar trend to the broadening of the TO3 vibrational mode, indicating the parallel and linked evolution of these two absorptions. The shrinking of the TO4 shoulder is also noted (Fig. III.33d), readily associated with the further organization of the network [213], and in good correlation with the results discussed so far. Lastly, the intensity of the Si–OH groups decreases with the temperature, indicating the breaking of silicon-hydroxyl bonds in favor of new Si–O–Si cross-linking.
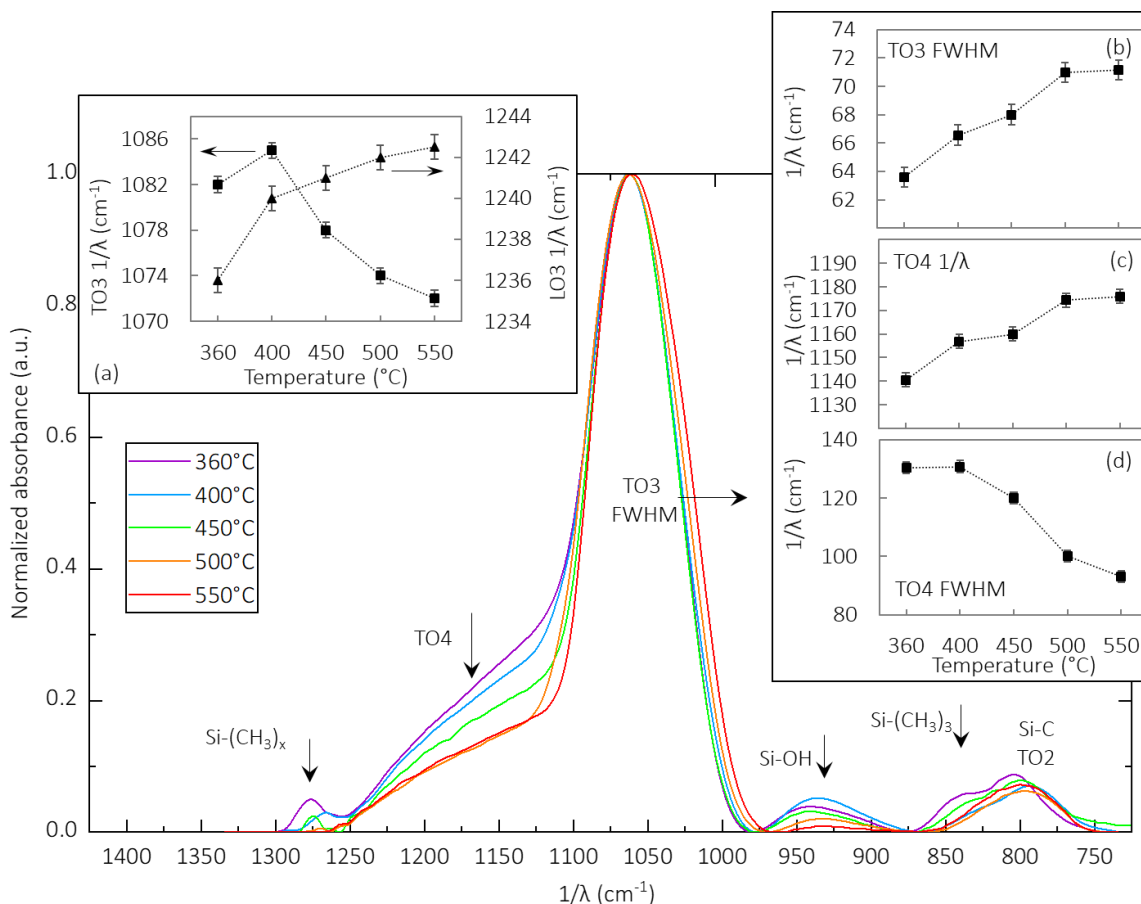
Fig. III.33. Evolution of the FT-IR spectra of HMDS-TEOS films deposited at various SPTs, analyzed for an incidence angle of 0°. Inset diagram (a) shows the evolution of the TO3 and LO3 components, as observed for an incidence angle of 60°. Right-hand side inset diagrams show evolution of the TO3 full width half maximum (b), the TO4 position (c), and the TO4 full width half maximum (d) at 0° incidence.

A key difference to the TEOS films is observed for the absorptions in the 750-850 cm^{-1} region. Multiple bonds are absorbing at these frequencies. First off, the rocking CH$_3$ vibration in Si–(CH$_3$)$_3$ groups is noted at ca. 850 cm^{-1}. Its intensity appears to be globally decreasing with the SPT, indicating the loss in

organic character. Neighboring this absorption, the overlapping bending Si–O–Si TO2 and stretching Si–C vibrational modes are found at ca. 800 cm^{-1}. For carbon-free films, i.e. TEOS films, a clear increase in the intensity of the TO2 mode was observed (Fig. III.5), which evidences higher chemical bonding between the SiO$_4$ tetrahedra and a densification of the network [204]. In contrast, this absorption in HMDS-TEOS films is not evolving as monotonously. This confirms that a Si–C absorption is overlapping with it. The intensity at ca. 800 cm^{-1} is first appearing to decrease between 360 and 500°C, then increases again between 500 and 550°C. Since all other Si–O–Si absorptions follow the same evolution as those presented for the TEOS films, the densification of the Si–O–Si network in HMDS-TEOS with an increase in temperature is undisputed. As such, the decrease of the 800 cm^{-1} absorption between 360 and 500°C is attributed to the loss of carbon and the consequent loss in Si–C absorption. Once no more carbon is probed in the films, the absorption at 800 cm^{-1} can be solely attributed to the TO2 mode. As expected, once the films are free of carbon (for T≥500°C), the TO2 absorption is noted to increase in intensity from 500 to 550°C, as expected for films that densify with the temperature.

III.3.4. Chemical composition by IBA techniques

The atomic concentrations in Si, O, C and H were determined by IBA techniques as a function of the SPT (Fig. III.34a). The content in C reaches ca. 5 at.% and is found in films deposited at 360, 400 and 450°C. No carbon is detected for films deposited at 500 and 550°C. Globally, the C content decreases with higher SPT, although a slight spike is observed at 450°C. It is recalled that a similar spike was noted in the intensity of the –CH$_3$ absorptions (Fig. III.32a to c) at 450°C, while at 500 and 550°C their intensities dropped to zero. The coherence between DR, AFM, FT-IR, and IBA results confirms the proposal that the transitional deposition mechanism at 450°C is linked to slightly higher incorporation of carbon.

No nitrogen was detected in any of the films, confirming the general conclusion of the literature review discussed in Chapter I stating that generation of monoatomic oxygen radicals may impede N incorporation. Despite that, carbon was successfully inserted in some of the films. Based on the compositional analysis and the infrared absorptions detailed in Fig. III.32, two different materials are identified hereinafter. The one material type is given a generic formula SiO$_x$C$_y$:CH$_3$, with carbon encountered as Si–C, but most predominantly found in the form of methyl moieties. This type of material is assigned to films processed at temperatures equal to or lower than 450°C, depicted by the grey area in Fig. III.34. The other material type is defined as a carbon-free, sub-stoichiometric silicon oxide, SiO$_x$ (off-white area in Fig. III.34) and is encountered for films deposited at 500 and 550°C. The stability domains of the two materials also coincide with the reported morphological evolution probed by AFM, namely rough and smooth surfaces for the SiO$_x$C$_y$:CH$_3$ and SiO$_x$ surfaces, respectively.
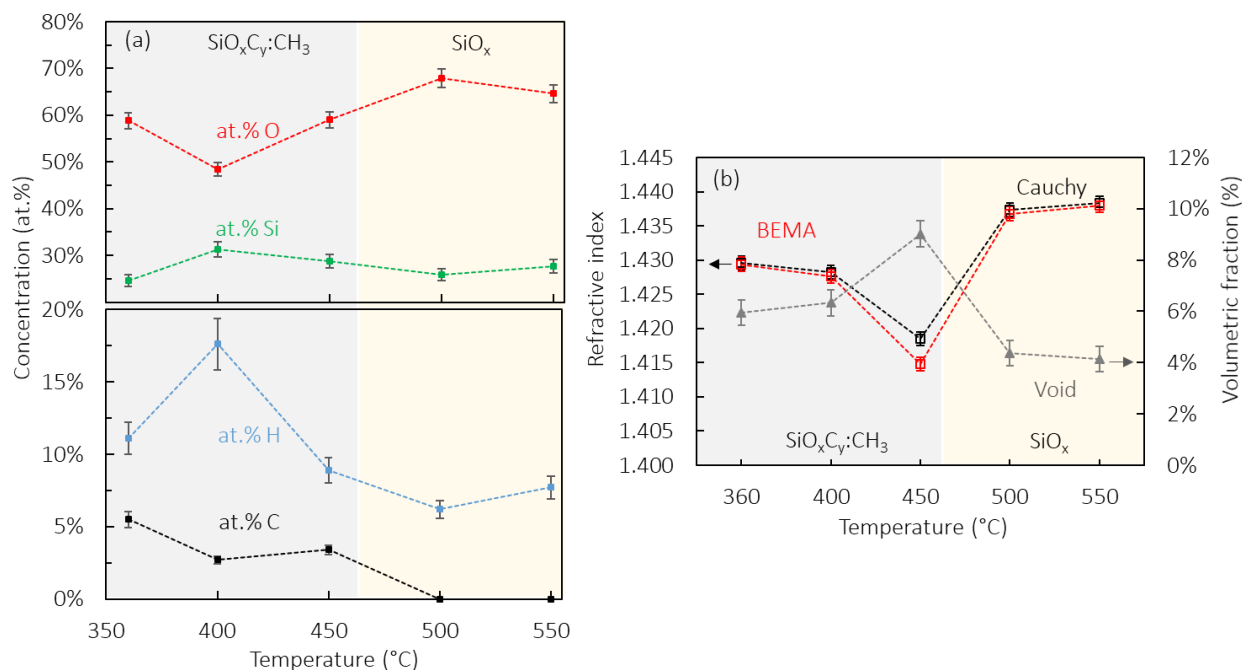
Fig. III.34. Evolution of HMDS-TEOS films composition as a function of SPT (a), obtained from the first spectral acquisition by IBA techniques. Evolution of the RI and void volumetric fraction, obtained by ellipsometry (b). Grey and off-white areas signify SiO$_x$C$_y$:CH$_3$ and SiO$_x$ material domains respectively.

Regarding the hydrogen content, it is noted that its evolution does not follow, in shape, that of carbon. This behavior is expected, considering that hydrogen is also involved in H$_2$O and Si–OH hydrated species, as revealed by the FT-IR spectra. The hydrogen content measured for SiO$_x$C$_y$:CH$_3$ films is high, measuring between 8 and 17 at.% depending on the process conditions, and decreases to ca. 7 at.% for SiO$_x$ type films. The opposite evolution is observed for oxygen. The measured O content is higher for SiO$_x$ compared to SiO$_x$C$_y$:CH$_3$ films. The determined silicon content remains almost constant, with a slight minimum atomic concentration observed at the lowest temperature (360 °C), for which the carbon content is the highest measured.

In terms of refractive index (Fig. III.34b), independent of the SPT, the films present values below 1.458, i.e. the RI of stoichiometric silica. As a result, they are considered to be overall sub-stoichiometric, correlating well with the identification of H and hydrated species. An evolution similar to that of the TEOS films is noted. First, a decrease of the RI between 360°C and 450°C is observed, with the lowest value measured for 450°C. As was previously discussed in section III.1.1.3, this behavior is linked to the desorption of water from the nanoporosities [218], freeing up the nanopores and replacing water by vacuum. Beyond this temperature, the RI increases again, progressing closer towards the stoichiometric value.

Indeed, the volumetric fraction of the void component, as calculated by the BEMA model, is increasing, which further underlines the desorption of water. The dip of the RI at 450°C is interesting when correlated to the spike in carbon content (Fig. III.34a), or to the lower DR (Fig. III.30b) observed at this temperature. Based on these results, it could be deduced that the transition of the deposition mechanism from precursor- to intermediates-governed not only decreases the DR and introduces more carbon in the films, but also leads to films with higher nanoporosities. As such, when dealing with radical chemistries and the production of intermediate species, it is potentially preferable to avoid deposition at temperatures where a transition in the deposition mechanism occurs, especially when dense films are targeted.

Beyond 450°C, the RI increases significantly, with a simultaneous decrease of the void component. This trend is explained by a change in the film structure, induced through reorganization of the SiO₄ tetrahedra, as was revealed by the increase of the TO2 intensity between 500 and 550°C (Fig. III.33), signifying the densification of the network [219]. However, it must be noted that, globally, the HMDS-TEOS films appear less dense than the TEOS film, having lower RI values and higher void vol.%.

III.3.5. Surface wettability

The water wettability of the HMDS-TEOS films was assessed and the measured contact angles are presented in Fig. III.35 as a function of the deposition temperature.
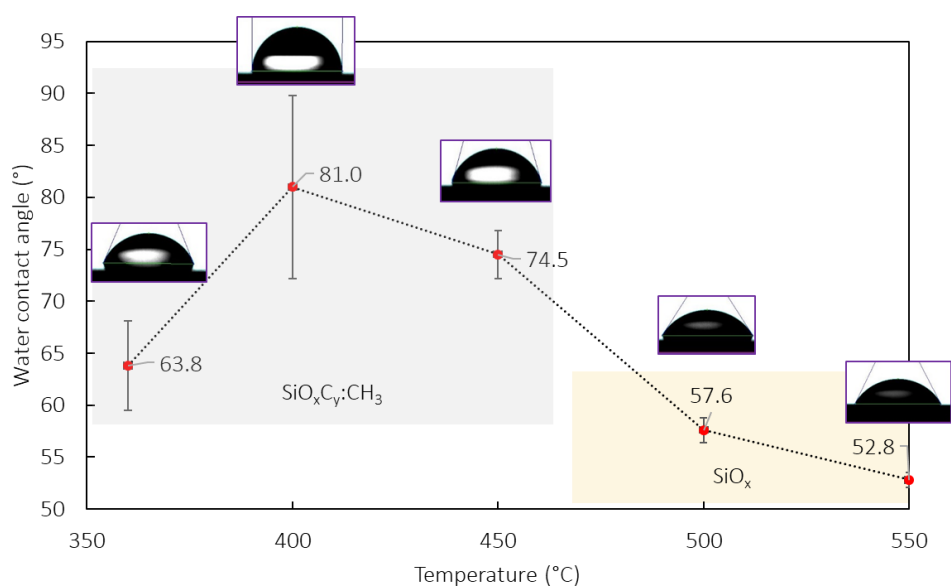

Fig. III.35. Water contact angles for HMDS-TEOS films and their evolutions as a function of the SPT. Grey and off-white regions signify SiO$_x$C$_y$:CH₃ and SiO$_x$ material domains respectively.

Overall, the films are hydrophilic. However, there are noticeable differences among them depending on the SPT. The hydrophilic character of films produced at the two highest temperatures is rather strong, with a WCA of 57.6° and 52.8° for 500 and 550°C, respectively. In contrast, a decrease of the deposition temperature results in a noticeable increase of the contact angle, which passes from 57.6° to a maximum of 81.0° at 400°C. The trend is inversed for the 360°C film, for which the contact angle decreases to 63.8°. This behavior reveals a distinction between the carbon-free SiO$_x$ and carbon-containing SiO$_x$C$_y$:CH$_3$ films. The reduced hydrophilic character of the latter, despite the increase in roughness that should normally enhance the hydrophilicity according to Wenzel [252], is attributed to the presence of carbon in the form of methyl moieties, as was observed by FT-IR (Fig. III.32). According to Gil et al. [216], the methyl-termination of surfaces increases the contact angle and renders the films less hydrophilic. This is not surprising, considering that HMDS is widely used as a silylation agent in hydrophobic coatings, removing Si–OH surface termination and replacing the silanol species by Si–CH$_3$ ones to increase film hydrophobicity [253, 254]. Indeed, the intensity of all methyl-containing bonds in Fig. III.32a to c is higher at lower deposition temperatures, explaining the less hydrophilic character of SiO$_x$C$_y$:CH$_3$ films.

Nonetheless, the above cannot explain the behavior of the 360°C sample, for which the contact angle is lower than that of 400°C. A possible explanation comes from the synergistic increase of the H and the decrease of the O contents from 400°C to 360°C, which could correspond to increased network hydration at the lowest deposition temperature. The results of Hair and Hertl [225] are recalled, stating how hydrogen bonded hydroxyl groups increase the hydrophilicity of a film, since water can readily physisorb on them. Indeed, as shown by the evolution of the hydrogen bonded Si–OH vibration at 3424 cm^{-1} (Fig. III.32), its intensity is higher for 360°C compared to 400°C, which can well explain the increased wettability at the lowest temperature. In contrast, free OH groups at the surface (evidenced through the absorption at ca. 3650 cm^{-1}) reduce the affinity to water.

At this point, the results of Wei et al. are also considered [255], who deposited films by HMDS via PECVD at low temperatures. Their films gave a contact angle of 87-90°, but this value decreased to <10° when O$_2$ plasma was utilized. The authors proposed that this change of wettability stems from the significant surface chemistry variation caused by the change in reactants used, and specifically the addition of oxygen (which reduces –CH$_3$ incorporation).

In light of all of the above, it is evident that wettability does not depend only on film surface methylation, but is a parameter affected by the synergy between global surface chemistry (–CH$_3$, –OH, water, etc.), roughness and surface energy.

III.3.6. Mechanical properties

Nanoindentation and nanoscratch analysis is carried out on films with >500 nm and ca. 100 nm in thickness, respectively. It is noted that thick films at 450°C and 550°C were not produced. The influence of the temperature on the mechanical properties of the films in terms of hardness H, elastic modulus E, and critical load *CL3* is presented in Fig. III.36. Similar to TEOS films, the hardness of HMDS-TEOS films appears constant at ca. 3 GPa and independent from the process temperature. Such a behavior was also reported by Merekov et al. [256], who performed laser-assisted CVD at 1210-1510°C using hexamethyldisilane, measuring a hardness value of 9±2 GPa that remained constant with the process temperature. It is possible that for small thermal ranges, H values do not vary much and are possibly more dependent on the process or the precursor chemistry used. This coincides well with the much higher H values obtained by the TEOS chemistry in section III.1.1.4 and the lower H values from HMDS chemistries in the literature. For example, double-discharge atmospheric pressure CVD of HMDS, plasma polymerized HMDS and PECVD of HMDS resulted in 1.47-3.15, 1.37 and 0.5-3.0 GPa, respectively [257-259]. In the present case, it can be assumed that the change in precursor chemistry, that is, the addition of HMDS to TEOS-O₂/O₃, globally degrades the mechanical properties of the film.
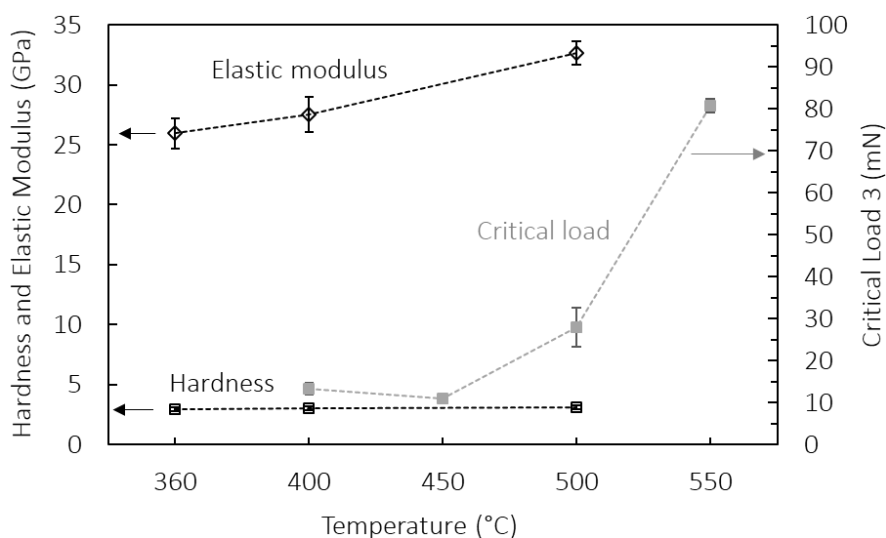

Fig. III.36. Evolution of the elastic modulus E (black diamonds), hardness H (black squares) and critical load CL3 (grey squares) of HMDS-TEOS films as a function of the temperature.

Decrease of the mechanical integrity of films from HMDS has also been correlated to the presence of –(CH₃)ₓ groups, potential C=C or Si–H bonds, and lower film density [257-259]. This does not seem to

be the case for the HMDS-TEOS films. It appears that the hardness of HMDS-TEOS films is not as sensitive to compositional changes and depends primarily on precursor chemistry.

The CL3 force values of HMDS-TEOS films are comparable to TEOS films, measuring 13.4±1.4 and 11.0±0.4 mN at 400°C and 450°C respectively. An increasing trend is observed with the temperature, translating to better adherence on the substrate for higher SPT. It is noted that the force value of 27.9±4.6 mN measure at 500°C is much lower than the one of TEOS films at the same temperature. At 550°C however, the required CL3 load increases to 80.6±1.6 mN, a value comparable with what was measured for TEOS.

The influence of the temperature on the elastic modulus seems fairly monotonous and increases with the temperature. A maximum value of 32.6±1.0 GPa is noted, half of the one observed for the TEOS films. The elastic modulus is an intrinsic material property that is intimately linked to the types of bonds existing in the material. As such, the influence of nanoporosities in the HMDS-TEOS films, the higher hydrogen content, as well as the presence of organic carbon, is well reflected in the elastic modulus values. In contrast to H, E appears thus to be more influenced by the transition of the material type from SiO$_x$C$_y$:CH$_3$ to SiO$_x$.

III.3.7. Wet etching corrosion resistance

The P-etch rate of HMDS-TEOS films is shown in Fig. III.37. The results reveal a relatively high etching rate of 51 and 60 Å.s^{-1} for films deposited at 360°C and 400°C, respectively. Such values are usually encountered for silica films with carbon and hydrogen impurities [229], which is indeed the case for HMDS-TEOS films at SPT ≤450°C. Improved corrosion resistance is noted at higher SPT, with the etching rate decreasing to 14.8 Å.s^{-1} at 550°C. Decrease of the etching rate with increasing temperature is also noted in the literature, for films deposited using HMDS and O$_2$ or N$_2$O [260]. This evolution is linked to the composition and the intrinsic nature of the material. Thus, it is no surprise that SiO$_x$C$_y$:CH$_3$ films exhibiting lower corrosion resistance compared to SiO$_x$ ones.

When subjecting films from the two extreme temperatures to an *ex-situ* post-deposition annealing treatment performed for 2 h at 550°C under N$_2$ flow, the etching rate decreases further. More specifically, two films produced at 360°C and 550°C had their P-etch value decrease to 7.9 and 5.5 Å.s^{-1}, respectively. It can be derived that the annealing post-treatment successfully led to the densification of the films through H$_2$O desorption and additional Si–O–Si cross-linking. Interestingly, FT-IR analysis of the annealed films shows significant decrease in H$_2$O and Si–OH absorption, but minimal changes to the absorptions of carbon related bonds (–CH$_3$, Si–(CH$_3$)$_x$) (Appendix 3). It is deduced that the presence of H$_2$O and Si–OH have a

higher detrimental effect to the corrosion resistance compared to the carbon related bonds, even if the latter are found in the form of organic moieties.
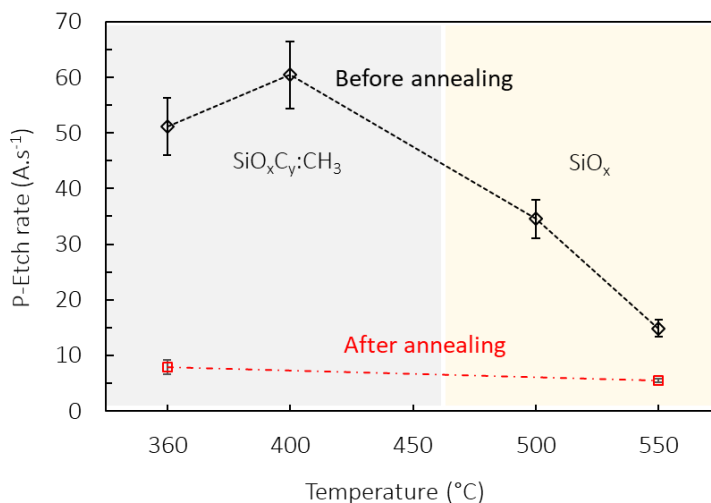
Fig. III.37. P-etch rate of HMDS-TEOS films produced at various SPTs,
before (black diamonds) and after (red squares) *ex-situ* annealing at 550°C.

Additionally, the P-etch rate appears to follow a trend similar to the hydrogen content (Fig. III.34a) and WCA of the films (Fig. III.35). This information could be used to reveal a potential link between P-etch rate, H and Si–OH concentration. This information is coherent with the etching mechanism of HF solutions, under which the silica network is dissolved primarily through a dissolution reaction initiated via the substitution of exposed –Si–OH by –Si–F groups, as the film is etched progressively [238].

However, the corrosion resistance of HMDS-TEOS films is globally much lower than that of TEOS films. It is recalled that the envisioned barrier films, aimed for application as barrier coatings in the pharmaceutics industry, must be dense enough to withstand hydrolysis. Although carbon incorporation did occur at low temperatures thanks to the utilization of O₃, its insertion in the form of mostly organic moieties did not benefit film densification. Based on the P-etch results, the resistance of HMDS-TEOS films was not deemed satisfactory enough to justify the transfer of the HMDS-TEOS-O₂/O₃ chemistry in vials.

III.4. Conclusions

The current chapter reported on results regarding the deposition of SiO_2 and SiO_x from O_3-based chemistries. The high reactivity of O_3 and its ability to enable deposition at low temperatures was illustrated. Deposition experiments from TEOS-O_2/O_3, HMDS-O_2/O_3 and HMDS-TEOS-O_2/O_3 chemistries were carried out. The results of the first chemistry were used in the development of an apparent kinetic model using process analysis by CFD simulation, allowing representation of the SiO_2 deposition process and providing suggestions for process optimization to achieve uniform coverage of complex and/or large substrates. The model presented a large range of validity in terms of temperature (150-520°C) and considered for the first time a thermal dependency of the direct formation of SiO_2 from TEOS and O_3. Attention should be paid however when it is transposed to reactor configurations with shorter residence times, since the model might fail to reproduce the local thickness distribution accurately.

Additionally, in-depth characterization of SiO_2 and SiO_xC_y:CH_3/SiO_x films produced from the TEOS-O_2/O_3 and HMDS-TEOS-O_2/O_3 chemistries respectively was carried out. A strong correlation between process temperature and film structure, composition, network hydration, functional properties and performance was built through the implementation of multiple characterization methods. It was found that increase of the process temperature up to 500°C is linked to strong desorption of water and hydrated species in TEOS films, with parallel reduction of carbon incorporation in HMDS-TEOS films. Beyond 500°C, concentration of Si–OH in the films decreases further, to the benefit of Si–O–Si cross-linking and network densification. The behavior of the films in terms of resistance against chemical etching was also assessed using the P-etch test. Etching rates ranged from 19 to 9 Å.s^{-1} for TEOS films and from 60 to 15 Å.s^{-1} for HMDS-TEOS films, when the process temperature increased from 400°C to 550°C, respectively. Annealing post-treatment applied to both chemistries underlined how the temperature-induced reorganization of the network can further decrease the etching rate down to 4-5.5 Å.s^{-1}.

Although carbon was successfully incorporated in the films from HMDS-TEOS-O_2/O_3, it was encountered mostly in the form of –CH_3 moieties, originating from the incomplete decomposition of the HMDS precursor. Although the tunability of the HMDS-TEOS films allows them to conform to various applications such as organo-silica membranes or sacrificial SiO_x films, they are unsuitable for application as dense barrier coatings. Only barrier coatings from TEOS-O_2/O_3 were tested in pharmaceutical vials. Their hydrolytic resistance was assessed using the USP <660> recommendation. The SiO_2 coatings demonstrated an excellent barrier performance, reducing the amount of extractables released in the solution by up to 92 %. Despite that, no particular breakthrough was noted in regards to their hydrolytic resistance, with Si being probed in the solution, indicating that the SiO_2 coating was hydrolyzed.

The results made it all the more clear that the SiO_2 material itself is already at its performing limit and that other chemistries and material types should be explored. Moreover, the HMDS-TEOS chemistry confirmed two key points. The first is that carbon integration in carbidic form, instead of organic, requires significantly higher temperatures than the ones probed in this work. Consequently, the oxycarbides research direction for inducing further network densification appears inefficient in regards to the defined specifications in this thesis. The second point is that the presence of O_3, and by extension the presence of monoatomic oxygen, impeded the incorporation of nitrogen in the films.

For the above reasons, the following chapters explore the deposition of SiO_xN_y films at moderate temperatures using novel, carefully selected precursor molecules and appropriate inlet gas compositions. The partial replacement of the divalent O anions by trivalent N ones is investigated, as a means to induce further network densification. The films produced by the chosen chemistries are analyzed thoroughly to establish their respective process-composition-structure-properties correlations and assess their consequent performance against corrosive attacks.

Chapter IV. Deposition of SiO$_x$N$_y$ barrier coatings from tris(dimethylsilyl)amine, TDMSA

The present chapter details our efforts to produce SiO$_x$N$_y$ films from a novel organosilicon precursor, tris(dimethylsilyl)amine (N(SiHMe$_2$)$_3$), TDMSA. Initial experiments involve the exploration of this precursor using NH$_3$ and O$_2$. An extensive parametric analysis is executed in order to analyze the impact of NH$_3$, O$_2$, and precursor flow rates on the deposition rate and the film composition. In a first step, the SiO$_x$N$_y$ films are deposited on planar Si substrates and are characterized following the previously developed methodologies. Links between the material properties and the level of nitrogen incorporation are established. The corrosion resistance of the films is analyzed by the previously presented P-etch test, as well as through an additional, more aggressive, hydrofluoric solution. Similarly to the TEOS-O$_2$/O$_3$ chemistry, initial screening of the SiO$_x$N$_y$ films corrosion resistance through the HF solutions is executed in order to establish operating conditions that lead to the best performing films, with the aim of future transfer in pharmaceutical vials.

In a second step, the gas phase of this novel chemistry is analyzed at the reactor exit by three different analytical techniques in an attempt to shed more light into the reactions that are taking place. GC-MS, NMR and ESR are executed in parallel to the CVD process, allowing the sampling and identification of stable gaseous by-products and radical species. The coupled consideration of gas phase and solid phase results allows proposing a series of reactions and formulate a deposition mechanism for the CVD of SiO$_x$N$_y$. To this date, it is the first time such a combined analysis has been implemented for a CVD process.

Lastly, the developed mechanism is used to propose a simplified, apparent chemical model for the simulation of SiO$_x$N$_y$ deposition using CFD calculations. The development of the model is executed with the vision to simulate local growth rates, while also giving accurate predictions of the film composition, for a better understanding of the phenomena involved and a possible process scale-up. The assumed homogeneous and heterogeneous reactions are justified through simultaneous consideration of gas phase products and solid phase data, respectively. The developed model is validated in shape and value through comparison with experimental results. The utilization of CFD calculations for the prediction of local film thickness and composition in a ternary SiO$_x$N$_y$ system has not been reported so far in the literature. Transfer of the developed model to the vial reactor is demonstrated in the final part of the chapter.

IV.1. SiO$_x$N$_y$ deposition from TDMSA chemistries on planar substrates

IV.1.1. SiO$_x$N$_y$ deposition from TDMSA-NH$_3$-O$_2$

TDMSA is initially introduced in the reactor as the silicon provider for the production of SiO$_x$N$_y$ films. O$_2$ is used as the oxidant and NH$_3$ as the external nitrogen source. The main experimental parameters for the SiO$_x$N$_y$ depositions from the TDMSA-O$_2$-NH$_3$ chemistry are summarized in Table IV.1.

Table IV.1. Experimental conditions of the TDMSA-O$_2$-NH$_3$ chemistry tested in the tubular CVD reactor.

Run	SPT (°C)	N$_2$ flow rate through TDMSA bubbler (sccm)	TDMSA flow rate (sccm)	O$_2$ flow rate (sccm)	NH$_3$ flow rate (sccm)	Deposition time (min)
TD1	550	147	6	2	20	30
TD2	580	147	6	2	20	30
TD3	650	147	6	2	20	150
TD4	650	48	2	2	20	150
TD5	650	48	2	-	20	150
TD6	650	48	2	0.6	20	150
TD7	650	48	2	0.6	-	150
TD8	650	48	2	0.6	40	150
TD9	650	48	2	-	-	150

Through experiments TD1 to TD3, the lowest possible temperature for deposition of SiO$_x$N$_y$ films from the TDMSA-O$_2$-NH$_3$ chemistry is investigated. It is noted that the first two experimental runs, namely TD1 at a set-point temperature (SPT) of 550°C and TD2 at SPT 580°C, did not result in any visible SiO$_x$N$_y$ deposition. No iridescence is noted on the Si substrates, with their color retaining its typical silver hue indicating that no film had been formed. Given that silicon nitride and oxynitride materials by thermal CVD are known to have low deposition rates in this thermal range [71, 73, 96, 261, 262], sometimes below 1 nm.min^{-1}, the deposition duration for run TD3 is extended from 30 to 150 min. Additionally, SPT is increased to 650°C. It is recalled that a thermal gradient exists within the reactor for a given SPT. This feature is used to faster ascertain the minimum temperature required for film formation, without losing time

exploring the process temperature in a stepwise manner. A photograph of the array of Si substrates after deposition at SPT 650°C (TD3) is presented in Fig. IV.1, alongside the local temperature.
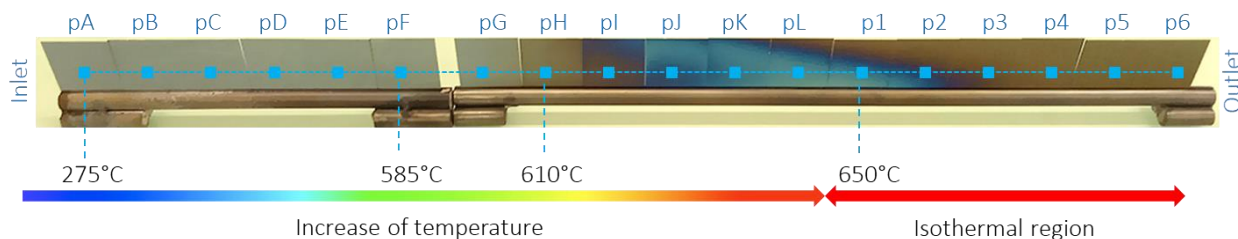

Fig. IV.1. Photograph of substrates after deposition for run TD3 (20 sccm NH$_3$ and 2 sccm O$_2$), with local temperature indicated for selected samples.

Inspecting Fig. IV.1, it is visible that successful deposition of a thin film is achieved for TD3 conditions. The iridescence reveals a change in thickness, as was discussed previously in Chapter III. The most important information is the definition of the minimum temperature required for film formation. Visual inspection of Fig. IV.1 reveals that at least 610°C are required to form a film, with a possible, but minimal, deposition between 585-610°C. There is no visible deposition below 585°C, in coherence with the failed attempts of runs TD1 and TD2. The results illustrate the higher temperature required for the activation of the TDMSA-O$_2$-NH$_3$ chemistry in comparison to the more reactive TEOS-O$_2$/O$_3$ one.

In order to verify if the deposited material contains nitrogen, the films are probed by ellipsometry. Application of models based on SiO$_2$ (Fig. II.8a and b) fails to give a satisfactory fit between the measured and simulated spectra. Moreover, application of the material-independent Cauchy and Sellmeier models reveals a refractive index (RI) of 1.58 for sample p6, well above the value of stoichiometric silica (1.458) and close to that of SiO$_x$N$_y$ material with 8-11 at.% of nitrogen [263]. These results reveal the incorporation of nitrogen, which is also confirmed by a successful fit of the ellipsometry spectra to a SiO$_2$+Si$_3$N$_4$ BEMA model (Fig. II.8c). However, an even better fit of the simulated ellipsometry spectra to the measured ones is achieved by considering an additional carbon containing component (Fig. II.8d). This hints at the potential inclusion of carbon in the films. The presence of nitrogen and carbon is further confirmed through FT-IR analysis, the results of which are discussed later in section IV.1.4. The evolution of the deposition rate (DR) and film atomic content in N and C along the reactor (calculated on five different point on each sample by ellipsometry and averaged per sample) for run TD3 is presented in parallel to the temperature profile in Fig. IV.2.
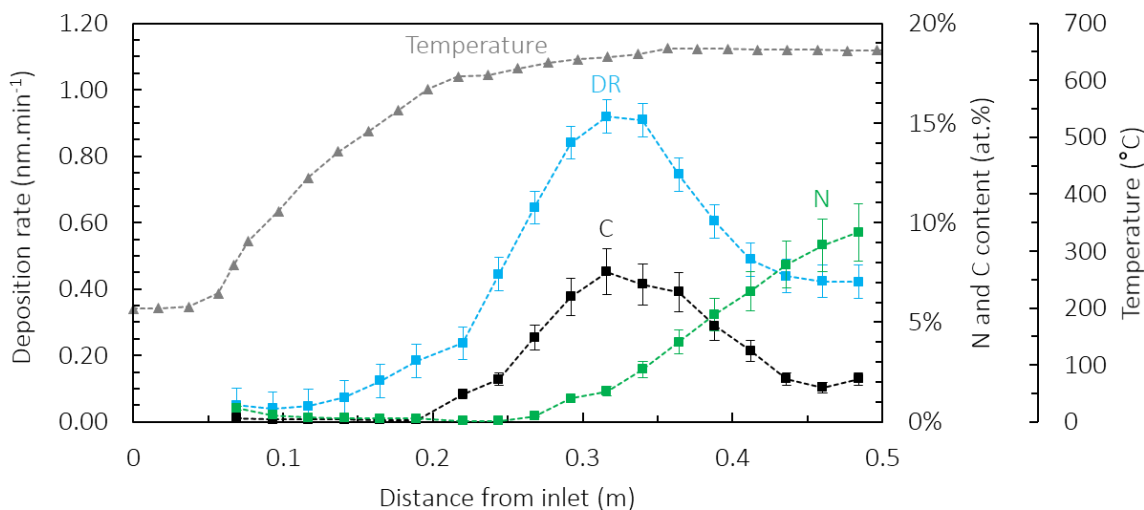
Fig. IV.2. DR, N and C contents per sample for run TD3, plotted versus the distance from the inlet.

From Fig. IV.2, it is noted that deposition is initiated at around 510°C, albeit with a significantly low DR of 0.12 nm.min^{-1}, which translates to a deposition of only 10 nm after 80 min. Such thickness values are indiscernible through mere visual inspection, explaining why no deposition could be noticed below 585°C in Fig. IV.1. A maximum DR of 0.92 nm.min^{-1} is reached at 641°C. A maximum carbon concentration of 7.5 at.% is noted at that point as well. Beyond 0.31 m from the inlet, both the carbon content and the DR decrease, with the DR stabilizing to around 0.42 nm.min^{-1}. The decrease of the DR is typical for deposition mechanisms dependent on more than one film-forming species. A different trend is observed for the nitrogen content. Nitrogen is first encountered at 0.27 m from the inlet, for samples whose local temperature exceeds ca. 631-637°C. This indicates that even though a film can be formed below this temperature, it is mostly a SiO_x material, with the production of SiO_xN_y taking place only after the temperature has reached (and exceeds) ca. 631°C.

Interestingly, even though the rate of film formation decelerates beyond the point of the maximum DR at 0.31 m, the nitrogen content of the material increases, reaching 9.5 at.% on the final sample. Since the temperature remains constant in the isothermal region (0.36-0.50 m), the DR decrease with the parallel N content increase is correlated back to the claim of multiple species contributing to deposition. It is known from the literature that N and O are competing in their incorporation and that O_2 promotes film formation [179, 180, 247, 264]. Combining all of the above information, it is concluded that the species responsible for the above-described behavior is most probably O_2: once oxygen has been consumed in the gas phase, deposition from oxygen-involving reactions is decelerated, while deposition from reactions involving NH_3 or nitrogen-containing intermediate species continues. As a result, the global DR decreases, but the molar

DR of nitrogen continues to take place and results in an increase of the N content in relation to O. As such, nitrogen and oxygen are inserted in the film through different reactions that are competitive to each other.

IV.1.1.1.   *Effect of the O$_2$ flow rate*

Referring back to Table IV.1, a parametric analysis is executed through experiments TD4, TD5 and TD6, studying the influence of the O$_2$ flow rate under constant SPT 650°C and 20 sccm NH$_3$ flow rate. The resulting DR and film composition profiles measure by ellipsometry are presented in Fig. IV.3.
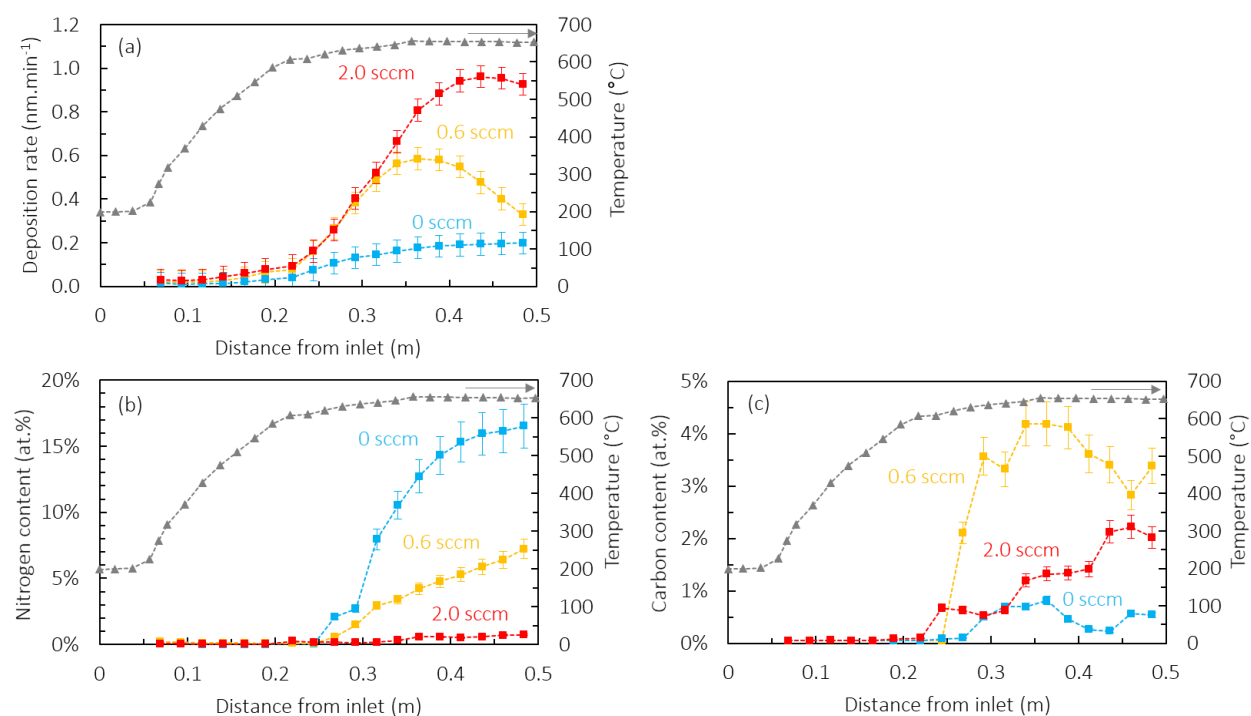
Fig. IV.3. Effect of the O$_2$ flow rate on the DR (a), nitrogen (b) and carbon content (c) for runs TD4 to TD6. Thermal profile for SPT 650°C is also included (grey triangles).

Inspecting Fig. IV.3a, deposition appears to start at about the same distance from the inlet (ca. 0.19 m) for all three experiments, corresponding to a local temperature of around 585°C. This result further confirms the clear thermal dependence of the SiO$_x$N$_y$ deposition process from the TDMSA-NH$_3$-O$_2$ chemistry. Additionally, it is revealed that the presence of O$_2$ in the gas phase has a promoting effect on the DR, in coherence with the literature. High DR values up to 0.96 nm.min^{-1} are noted for the highest O$_2$ flow rate (2 sccm), while the lowest DR is observed when no O$_2$ is added in the inlet gas composition. Moreover,

for higher O$_2$ flow rates, the maximum DR value shifts towards the end of the reactor, observed at around 0.36 m for 0.6 sccm O$_2$ and at around 0.44 m for 2 sccm O$_2$. In contrast, no maximum is observed for the experiment conducted without O$_2$. The decrease of the DR beyond the maximum value can be linked to the consumption of O$_2$. Since O$_2$ plays a major role in promoting film formation, the DR drops once it is consumed. In the same sense, when more O$_2$ is added in the inlet gas composition, it is indeed expected that the maximum DR value will be encountered downhill in the reactor. This happens because there is still sufficient concentration of O$_2$ in the gas phase to continue promoting deposition over an extended region.

Fig. IV.3b presents the effect of the O$_2$ flow rate on the nitrogen content. First, it is observed that nitrogen incorporation in the films starts at approximately 0.26 m from the inlet for all three experiments, translating to a local temperature of ca. 631°C. Similar results were observed previously for run TD3 (Fig. IV.2). This illustrates that incorporation of nitrogen is mostly a temperature-dependent process. Moreover, although film formation occurs below 631°C, N is inserted in the films only above that temperature. Thus, it is concluded that reactions that involve the incorporation of nitrogen have a higher activation energy than those involving oxygen. Additionally, it is observed that lower O$_2$ flow rates lead to higher N incorporation in the films, similar to what is reported in the literature [247]. Specifically, a maximum percentage of 0.7 at.% N is noted for 2 sccm O$_2$, with a tenfold increase to 7.2 at.% for a threefold decrease of O$_2$ flow rate to 0.6 sccm. The highest nitrogen content, 16.5 at.%, is observed for 0 sccm O$_2$, although the presence of O$_2$ through a small leak is not excluded, given that the films still contained some oxygen. These results illustrate well the competitive incorporation between the two elements. Moreover, the maximum nitrogen content for each run is always observed on the last sample on the array of Si coupons. Such behavior could be the effect of a globally lower oxygen concentration in the gas phase towards the exit of the reactor and slower activation kinetics of the species that lead to nitrogen incorporation.

Fig. IV.3c presents the effect of the O$_2$ flow rate on the carbon content. A slightly different behavior is noted here. First, carbon incorporation ranges from 0 to around 4.5 at.% and is not initiated always at the same position in the reactor. Moreover, the profiles are less monotonous, with spikes observed occasionally. Inspecting the evolution of C under variable O$_2$ flow, the highest carbon content (4.2 at.%) is observed for 0.6 sccm O$_2$. It then decreases to a maximum of ca. 2.2 at.% for 2 sccm O$_2$. Similar behavior is observed in the literature of SiO$_x$N$_y$ from organosilicon precursors, with an increase in O$_2$ flow rate decreasing the carbon incorporation [134, 247]. Interestingly, the lowest carbon content (maximum 0.8 at.%) is noted for 0 sccm O$_2$. This behavior is attributed to the effect of a NH$_3$ atmosphere. According to Weiller [265], the presence of NH$_3$ leads to lower incorporation of carbon in the films, by removing HN(Me)$_2$ groups from the precursor, presumably through the formation of an intermediate that, in absence of NH$_3$, decomposes

on solid surfaces. Although no methylamino-ligands are present in TDMSA, it seems that the –CH$_3$ cleaving effect of NH$_3$ is more efficient in an oxygen-free atmosphere, for the operating conditions tested.

IV.1.1.2.   *Effect of the NH$_3$ flow rate*

Further parametric analysis is carried out using runs TD6, TD7 and TD8 (Table IV.1), examining the influence of the NH$_3$ flow rate, varying from 0 to 20 and finally to 40 sccm, under a constant O$_2$ flow of 0.6 sccm at SPT 650°C. The average DR and film composition in N and C are presented in Fig. IV.4.
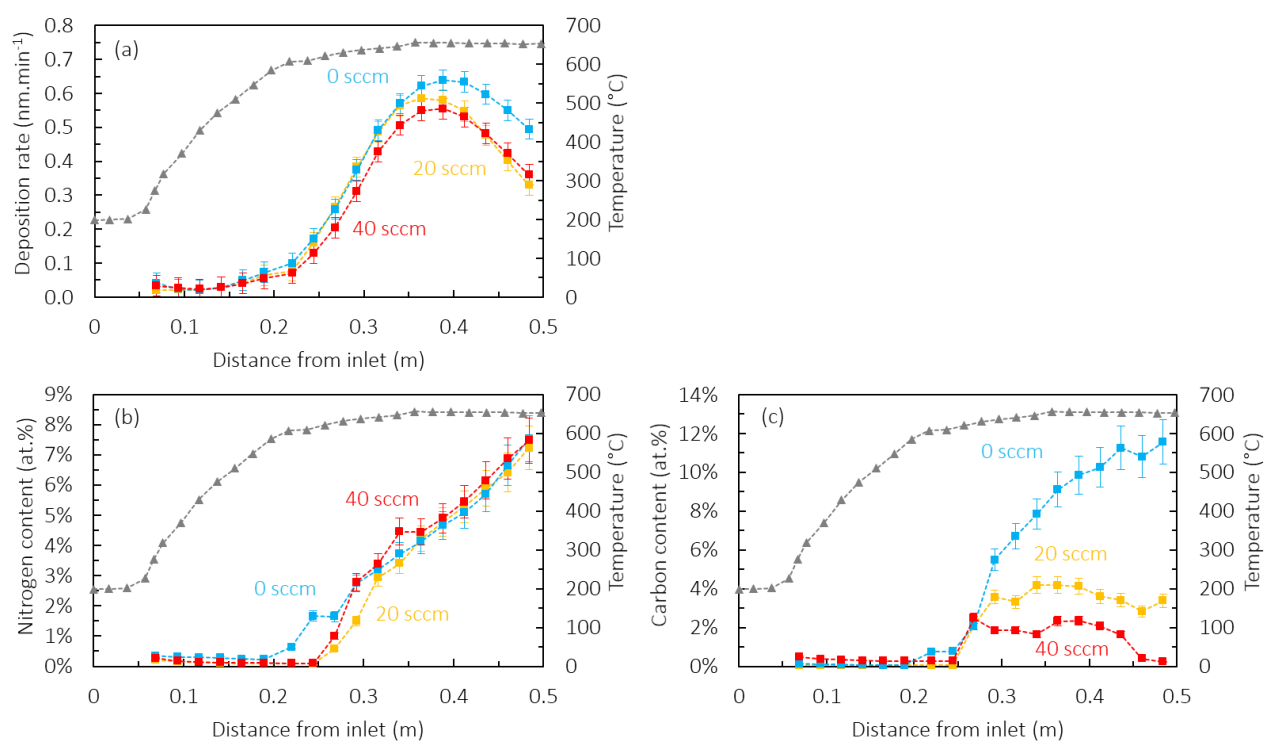
Fig. IV.4. Effect of the NH$_3$ flow rate on the DR (a), nitrogen (b) and carbon content (c) for runs TD6, TD7 and TD8. Thermal profile for SPT 650°C is also included (grey triangles).

Inspecting Fig. IV.4a, film formation appears to start at around 0.17 m for all runs, translating to a local temperature of 547°C. The NH$_3$ flow rate seems to have a low, if not negligible, influence on the DR, with the global values decreasing slightly at higher NH$_3$ flow rates. Similar behavior has been reported in the literature for SiN$_x$ films and is speculated to be the result of removal of the deposited material through etching by H• radicals generated during the deposition process through NH$_3$ dissociation [266-268]. This

effect, however, does not appear to be that strong for the conditions tested, with a maximum DR of 0.64 nm.min^{-1} at 0 sccm NH_3 decreasing to 0.55 nm.min^{-1} at 40 sccm NH_3. The maximum DR is observed at a similar position in the reactor for all three runs. Previously it was proposed that the position of the maximum DR is dependent on the O_2 flow rate. Since O_2 flow rate is constant across the three runs (Fig. IV.4a), the similar position of the maximum DR correlates well with this assumption.

No significant effect on the N content of the films is noted when NH_3 flow is varied, as shown in Fig. IV.4b. This result seems surprising, given that NH_3 was utilized as a nitrogen provider, yet failed to modulate the nitrogen content of the films. Similar results were reported by Lee et al. [247], who noted that NH_3 did not influence the N content in SiO_xN_y films deposited by PECVD. Even more surprising are the results of run TD7 (0 sccm NH_3). Despite the presence of only TDMSA and O_2 in the gas phase, nitrogen incorporation in the films still took place. Considering all of the above, it is apparent that the nitrogen originates, in fact, from the TDMSA precursor. This explains well the lack of influence of the NH_3 flow rate on the nitrogen incorporation. Lastly, similarly to previous results, the maximum nitrogen content for each experiment is observed at the sample closest to the reactor exhaust, at close values, namely 7.5 at.% N for 0 and 40 sccm, and 7.2 at.% N for 20 sccm.

Fig. IV.4c presents the effect of the NH_3 flow rate on the carbon content. The cleaving effect of NH_3 on the organic ligands of the TDMSA precursor is clearly illustrated here. With increasing NH_3 flow rate, the carbon content in the films decreases. Similar trends were observed in the literature [134, 265]. In absence of NH_3 (0 sccm), a maximum carbon content of 11.6 at.% is noted, dropping to around 4.2 at.% when 20 sccm NH_3 are supplied at the inlet. Further addition of NH_3 in the gas phase results in further decrease of the carbon content to values around 2.3 at.%. It is also noted that the evolution of the carbon content under high NH_3 flows presents a bell shape. This could be potentially linked to more efficient –CH_3 cleaving by NH_3 at higher temperatures and lower O_2 concentrations along the reactor, or to a decrease of the concentration of carbon-containing intermediate species. It must be kept in mind that O_2 also demonstrated a –CH_3 cleaving effect (Fig. IV.3c), but also that its concentration most likely decreases as the gas processes further in the reactor, as a result of its consumption through gas phase and surface reactions. Due to that, it is proposed that the continuous upwards slope of the carbon content in absence of NH_3 in Fig. IV.4c is related to the progressively decreasing concentration of O_2 in the gas phase.

IV.1.1.3. Effect of the TDMSA flow rate

For further investigation, the effect of the TDMSA flow rate on the DR and the film composition is investigated across runs TD3 and TD4, for which NH_3 and O_2 flow rates are kept constant at 20 sccm

and 2 sccm, respectively, and the TDMSA flow is varying from 6 to 2 sccm. The results are presented in Fig. IV.5.
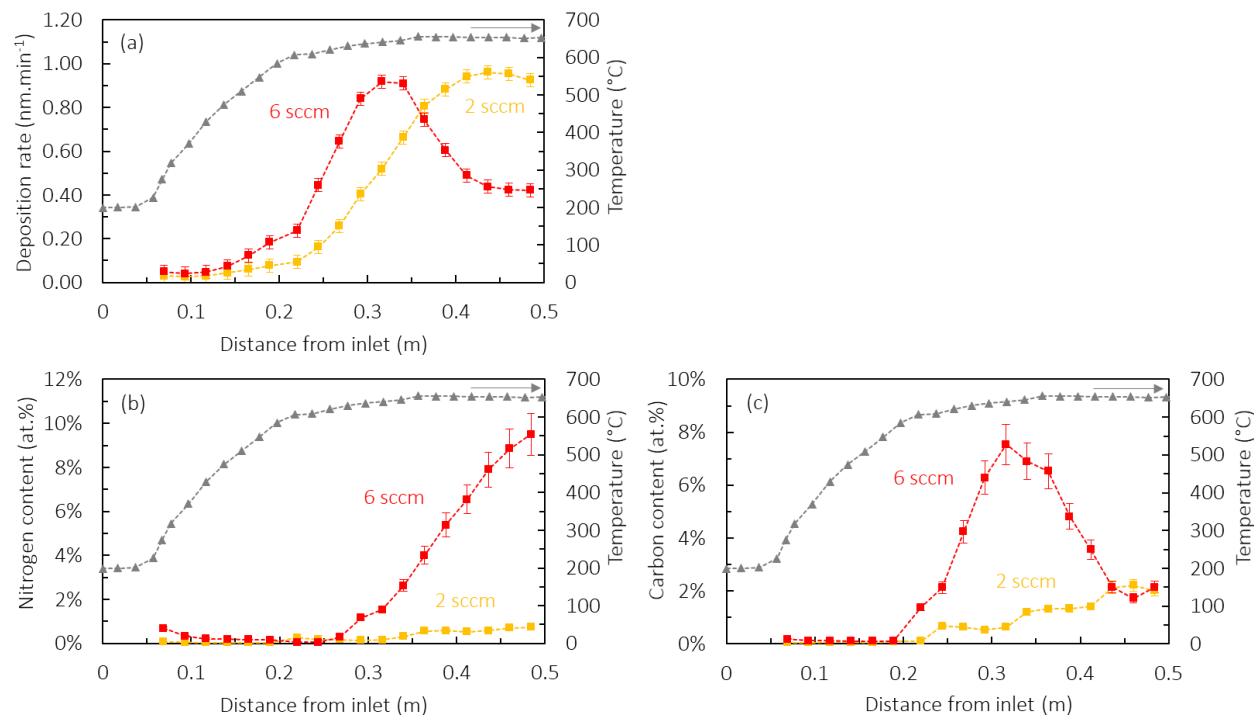
Fig. IV.5. Effect of the TDMSA flow rate on the DR (a), nitrogen (b) and carbon content (c), for runs TD3 and TD4, at SPT 650°C. Thermal profile of SPT 650°C is also included (grey triangles).

Inspecting Fig. IV.5a, it is observed that the maximum DR of both experiments is almost equal, reaching ca. 0.92-0.94 nm.min^{-1}. However, these values are encountered at different positions inside the reactor, namely at around 0.32 m for 6 sccm and 0.42 m for 2 sccm TDMSA. This could be an indication that the increased concentration of TDMSA leads to a quicker consumption of O$_2$ in the gas phase, resulting in the appearance of the maximum DR earlier in the reactor. After the respective maximum value is reached, the DR drops again for both runs, hinting at the consumption of O$_2$.

In terms of nitrogen content, Fig. IV.5b reveals that an increase in TDMSA concentration results in higher nitrogen incorporation in the films. A maximum content of 0.7 at.% N and 9.5 at.% N is probed for 2 and 6 sccm TDMSA, respectively. It is recalled that NH$_3$ supply was constant between the two experiments. These results further confirm the previous proposal, which stated that the nitrogen originates from the TDMSA precursor and not from NH$_3$. Carbon incorporation appears to follow a slightly different behavior. Higher C contents are noted for 6 sccm TDMSA, with values reaching up

to 7.5 at.%. Decrease of the precursor supply reduces carbon incorporation to values up to 2.2 at.%. This behavior of C incorporation, as well as its bell shape noted for 6 sccm TDMSA, is most likely influenced by the $TDMSA/O_2$ and $TDMSA/NH_3$ ratios, and a more efficient cleaving of organic moieties at higher temperatures.

In light of the above results, the addition of NH_3 in the chemistry was questioned: even though it helps to reduce the carbon content in the films, it neither promotes deposition, nor does it contribute to an enrichment in nitrogen. As a result, we removed it from the inlet gas composition, and, in the following sections, executed a parametric analysis based on the effect of the O_2 flow rate in absence of NH_3.

IV.1.2. SiO_xN_y deposition from TDMSA-O_2

The experimental conditions for the parametric analysis investigating the effect of various parameters in absence of NH_3 are summarized in Table IV.2. More specifically, experiments TD7, TD9, TD11 and TD12 examine the influence of the O_2 flow rate under constant TDMSA supply, with the exception of TD11 for which an experimental error in the thermostat resulted in a slightly higher bubbler temperature. Between runs TD14 and TD7, the effect of the SPT is investigated, after fixing all flow rates. Lastly, TD10 follows the same experimental conditions of TD7, with the only adjusted variable being the deposition duration, with the aim to produce thick films with ideally more than 500 nm for mechanical investigation.

Table IV.2. Experimental conditions of the TDMSA-O_2 chemistry tested in the tubular CVD reactor.

Run	SPT (°C)	TDMSA bubbler temperature (°C)	TDMSA flow rate (sccm)	O_2 flow rate (sccm)	Deposition time (min)
TD7	650	80	2	0.6	150
TD9	650	80	2	-	150
TD10	650	80	2	0.6	900
TD11	650	82	2.67	0.3	225
TD12	650	80	2	1.2	150
TD14	625	80	2	0.6	300

IV.1.2.1.   Effect of the O$_2$ flow rate

The effect of the O$_2$ flow rate on the DR and the film composition in absence of NH$_3$ is investigated across experiments TD7, TD9, TD11 and TD12, as presented in Fig. IV.6.
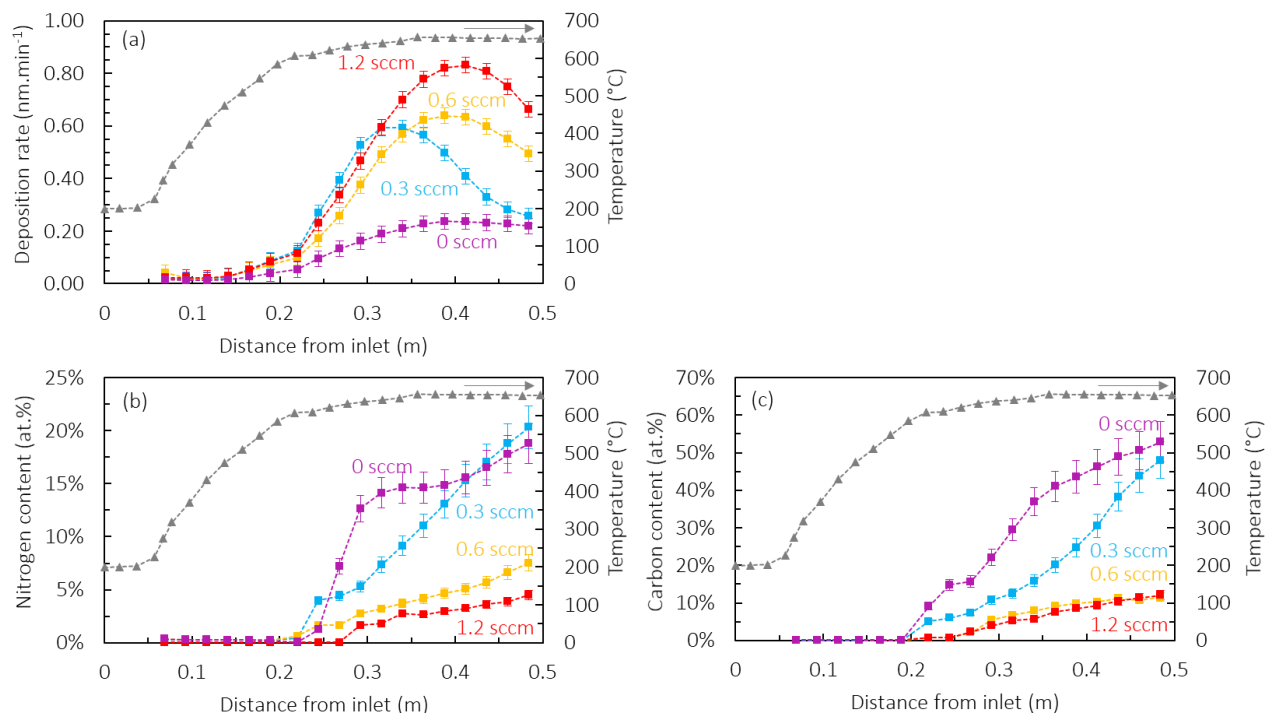

Fig. IV.6. Effect of the O$_2$ flow rate on the DR (a), nitrogen (b) and carbon content (c) across runs TD7, TD9, TD11 and TD12, at SPT 650°C. Thermal profile for SPT 650°C is also included (grey triangles).

Inspecting Fig. IV.6a, it is observed that a higher O$_2$ flow rate enhances the overall DR of the process. This confirms well the deposition-promoting behavior of O$_2$ noted in previous experiments. A maximum DR of 0.83 nm.min^{-1} is measured for 1.2 sccm O$_2$, dropping to 0.24 nm.min^{-1} when no O$_2$ is added in the gas phase. In the latter case, deposition is still observed. This could either be caused by the presence of residual O$_2$ in the deposition chamber, or could indicate that the thermal decomposition of the precursor itself can also lead to deposition. Bell shapes are once again encountered for the three runs utilizing O$_2$, indicating the eventual consumption of O$_2$ or oxygen-containing species in the gas phase. No obvious bell shape is observed for 0 sccm O$_2$.

The effect of the O$_2$ flow rate on the nitrogen content is shown in Fig. IV.6b. Nitrogen is observed for all experiments, confirming that it originates from the TDMSA precursor. The trends are similar to those

observed in presence of NH_3 (Fig. IV.3b), confirming that contribution of NH_3 to the deposition mechanism is low. The maximum N content is observed on the last sample on the array of Si coupons. Globally, the results illustrate well the competitive behavior of O and N incorporation, with high values up to 20.3 at.% N noted for 0 and 0.3 sccm O_2, dropping progressively to a maximum of 7.5 at.% and 4.5 at.% for 0.6 and 1.2 sccm O_2, respectively. Similar trends are noted in terms of carbon content, as shown in Fig. IV.6c. A maximum C content of 52.9 at.% is observed for 0 sccm O_2, decreasing to 12.0 at.% when 1.2 sccm O_2 is supplied. Overall, the higher the applied O_2 flow rate, the lower the carbon incorporation in the films. The results once more confirm the previously noted cleaving effect of organic moieties by O_2.

IV.1.2.2. *Effect of deposition temperature*

The temperature window that allows for SiO_xN_y film formation from the TDMSA-O_2 chemistry is not extensive (only ca. 610 to 650°C). For that reason, the effect of the SPT on the DR and film composition is studied using two SPT close to each other, namely 650°C and 625°C (runs TD7 and TD14), and is presented in Fig. IV.7. The inlet gas composition for both experiments remained the same (Table IV.2).
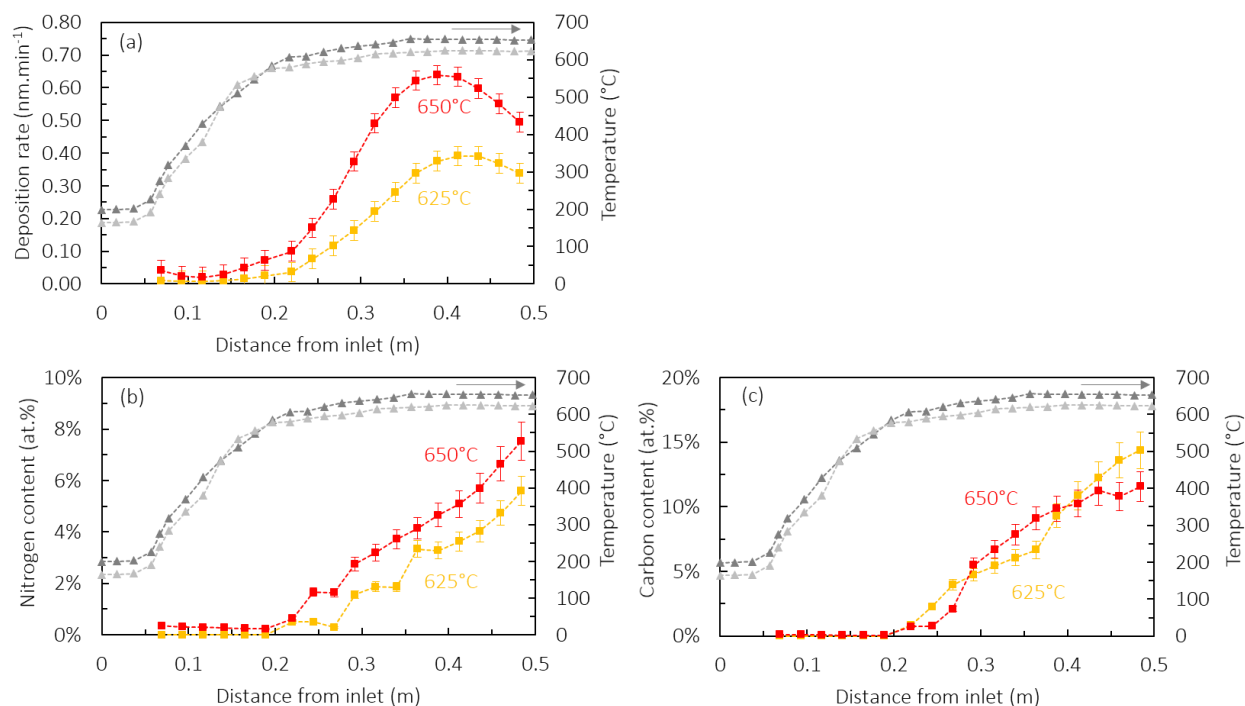

Fig. IV.7. Effect of the SPT on the DR (a), nitrogen (b) and carbon content (c), for runs TD7 and TD14. Respective thermal profiles are included in dark (650°C) and light grey (625°C).

Fig. IV.7a shows a maximum DR of 0.39 nm.min^{-1} for SPT 625°C, which increases to a maximum of 0.64 nm.min^{-1} for SPT 650°C. The DR values per sample are globally higher at the higher SPT. The results illustrate well the thermal dependency of the deposition process, as is expected for endothermic reactions.

The effect of deposition temperature on the N and C content of the films is presented in Fig. IV.7b and c, respectively. Globally, nitrogen incorporation follows a similar trend and shape for both SPTs, namely continuous increase from almost 0 below 600°C to a maximum at the last sample of the array. However, higher contents in N are noted all along the reactor for SPT 650°C, reaching up to 7.5 at.% in contrast to the maximum 5.6 at.% N probed for SPT 625°C. This, once again, illustrates that nitrogen enrichment is favored at higher temperatures. In terms of carbon content, it follows a similar, though more irregular, trend than that of the nitrogen content. However, there is no clear distinction between the two SPT. Carbon incorporation is influenced by multiple factors, such as local temperature, O$_2$ consumption in the gas phase and intermediate species distribution and concentration.

IV.1.3. SiO$_x$N$_y$ films composition by IBA techniques

The previously presented composition results were extracted using an ellipsometry model that can give approximate estimations for the N and C contents in the films. Indeed, this is a useful and timesaving method that allows for a fairly quick analysis of a large number of samples, enabling the extraction of DR and film composition profiles across the whole length of the reactor. Unfortunately, however, ellipsometry is unable to take the presence of hydrogen into account. As such, more accurate composition results are obtained by using Ion Beam Analysis (IBA) techniques, albeit for a limited number of films. The center of sample p2 (Fig. IV.1) is systematically analyzed by IBA to directly compare film composition across experiments, without locality effects. Due to the limitations of the IBA techniques however, only films with a thickness above 75 nm could be probed.

IV.1.3.1.   Composition of TDMSA-NH$_3$-O$_2$ films

Runs TD6, TD7 and TD8 are re-examined by IBA. The effect of the variable NH$_3$ flow rate on the film composition is presented in Fig. IV.8. The trends previously noted by ellipsometry, namely the lack of impact of NH$_3$ on the nitrogen incorporation and the decrease in carbon incorporation for higher NH$_3$ flow rates, are also encountered in the IBA results. Concentrations between 18.8 and 23.1 at.% H are probed. IBA reveals that there is no specific correlation between the NH$_3$ flow rate and the hydrogen content in the

films. Interestingly however, the H concentration follows a reverse trend compared to that of O, and more similar to that of Si.
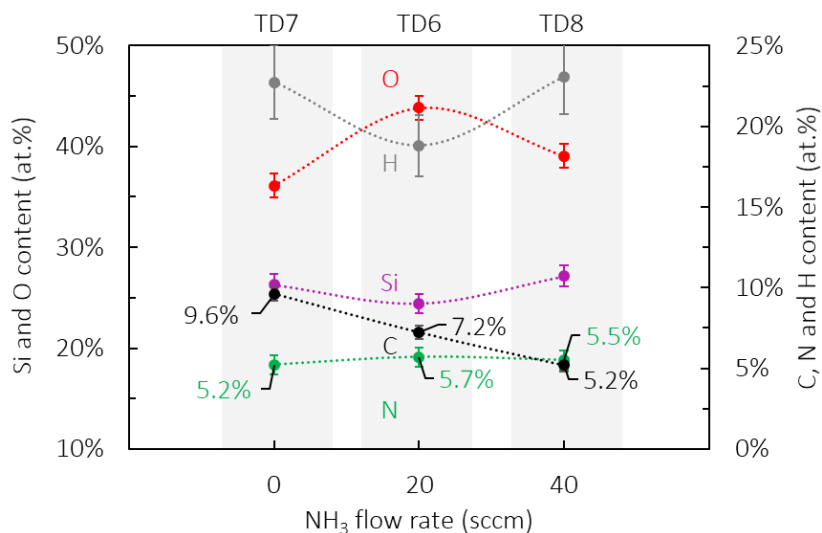

Fig. IV.8. IBA composition results for films produced under various NH$_3$ flow rates.

IV.1.3.2. Composition of TDMSA-O$_2$ films

The effect of the O$_2$ flow rate (runs TD7, TD11, TD12) and the SPT (runs TD14 and TD7) on the composition of the samples are re-examined more closely by IBA in Fig. IV.9. Similarly to the trends previously noted by ellipsometry, IBA confirms once more the competitive incorporation between O and N, as shown in Fig. IV.9a. Carbon incorporation also decreases for higher O$_2$ flow rates. Observing the similar trends in N and C contents, two potential explanations are proposed. The most likely scenario, proposed previously, is that the presence of O$_2$ in the gas phase has a cleaving effect on the methyl moieties of the film-forming intermediates. A second scenario could be that the lower C content originates from the competitiveness between O and N incorporation. If we assume that N and C are inserted in the films through the same intermediate molecule, then it stands to reason that both elements would be in competition with oxygen. Each scenario is non-exclusive of the other, and in fact, both could occur at the same time. If only the second scenario were to take place, then a constant C/N ratio should have been encountered across all runs, which does not seem to be the case.

The IBA results of Fig. IV.9a provide additional information on the hydrogen content of the films. The probed contents vary between 17.2 and 22.7 at.% H. A correlation between the O$_2$ flow rate and H content is noticed only between the two highest O$_2$ flow rates, with lower levels of H observed for 1.2 sccm

O$_2$. Considering the trends of all elements, it is proposed that hydrogen is encountered in multiple forms in the films: N–H, –CH$_x$, adsorbed H$_2$O and potential Si–H. Confirmation of these bonding states relies on FT-IR analysis of the films that is presented later.
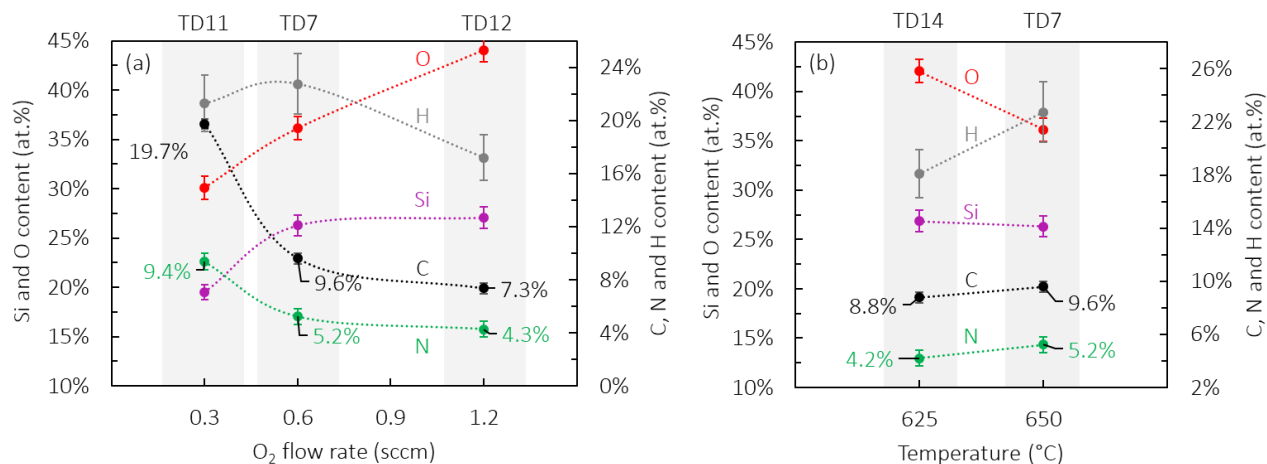

Fig. IV.9. IBA composition results for films produced under various O$_2$ flow rates in absence of NH$_3$ (a), and for a varying SPT at a fixed flow of 0.6 sccm O$_2$ (b).

Changes in film composition from differences in SPT are shown in Fig. IV.9b. The trends of ellipsometry are encountered once more, with higher N incorporation being noted when the temperature is increased. Two speculations can be made at this point: the first one is that the increase of the temperature activates deposition reactions from nitrogen-containing intermediates that require higher activation energy. The second one involves the increase of the concentration of the various nitrogen-containing intermediates produced in the gas phase. Both scenarios can occur at the same time. Regarding carbon, its incorporation is increased at higher SPT. This observation could further indicate a co-deposition of C and N through a common intermediate species. Fig. IV.9b also gives additional insight on the hydrogen content of the films, which increases from 18.1 to 22.7 at.% H between 625 and 650°C. This behavior coincides well with the increase of N and C incorporation and leads to the proposal that the majority of hydrogen is introduced in the films through N–H and/or –CH$_x$ moieties.

A closer inspection also reveals that the C/N ratio of the films seems to decrease slightly with the temperature. It can be proposed that the increase of the temperature enhances the level of decomposition of the precursor and leads to the formation of intermediate species that contain fewer –CH$_3$ ligands. Therefore, globally, even though the carbon content increases with the temperature, the C/N ratio decreases, hinting at

a simultaneous activation of film formation from carbon and nitrogen containing intermediates, along with a parallel enhanced carbon-cleaving effect.

As a closing remark, the N and C contents calculated by ellipsometry are close to those measured by IBA. However, this is expected, given that the ellipsometric model was calibrated using IBA results of run TD7, following the methodology explained in section II.2.2.2 of Chapter II. Without calibration, ellipsometry can on one hand provide relative compositional information in terms of qualitative trends, but fails to give accurate quantitative results. IBA is better suited for accurate compositional analysis, since it also considers hydrogen. Regardless, when both methods used in a complementary manner, a calibrated ellipsometric model is incredibly useful for quickly ascertaining compositional evolutions for a large number of samples and across multiple experiments.

IV.1.4. Chemical bonding in SiO$_x$N$_y$ films

The study of the chemical bonding in SiO$_x$N$_y$ films from the TDMSA-O$_2$ chemistry analyzed by FT-IR was carried out in collaboration with Paris Papavasileiou from the National Technical University of Athens (NTUA), in the frame of his Diploma thesis [269]. Given that films produced from TDMSA are an oxynitride material that contains carbon, various bonds, identified previously in SiO$_2$ and SiO$_x$C$_y$:CH$_3$ films deposited from TEOS and HMDS-TEOS, are encountered once again, in addition to new nitrogen-related ones. A representative FT-IR survey spectrum, taken at the center of sample p1 of run TD7, is shown in Fig. IV.10. The characteristic TO1, TO2 and TO3 modes of a usual SiO$_2$ material are noted, along with the TO3-LO3 pair [99, 187]. Additionally, absorptions relating to organic carbon incorporation are noted as expected, given the presence of –CH$_3$ ligands in the starting TDMSA precursor molecule. Absorptions corresponding to the hydration of the network by Si–OH or H$_2$O can also be observed.

New absorptions are also noted. At ca. 936 cm^{-1}, an absorption evidencing the Si–N bond is found [270, 271]. Further indication of the incorporation of nitrogen is given through the absorptions noted at approximately 470 and 830 cm^{-1}, corresponding to the symmetric and asymmetric stretching modes of the Si–N bond, respectively [272]. According to the literature, an additional absorption appears at ~3400 cm^{-1}, attributed to the N–H stretching vibration [270]. This band appears to be asymmetric and presents a "tail" that extends towards lower wavenumbers. This behavior has been speculated to be caused by hydrogen bonds between the hydrogen atoms of the N–H bond and the lone electrons of nearby nitrogen atoms [273]. The notation given for this specific type of vibration is N–H⋯N and can be found at around 3300 cm^{-1}.
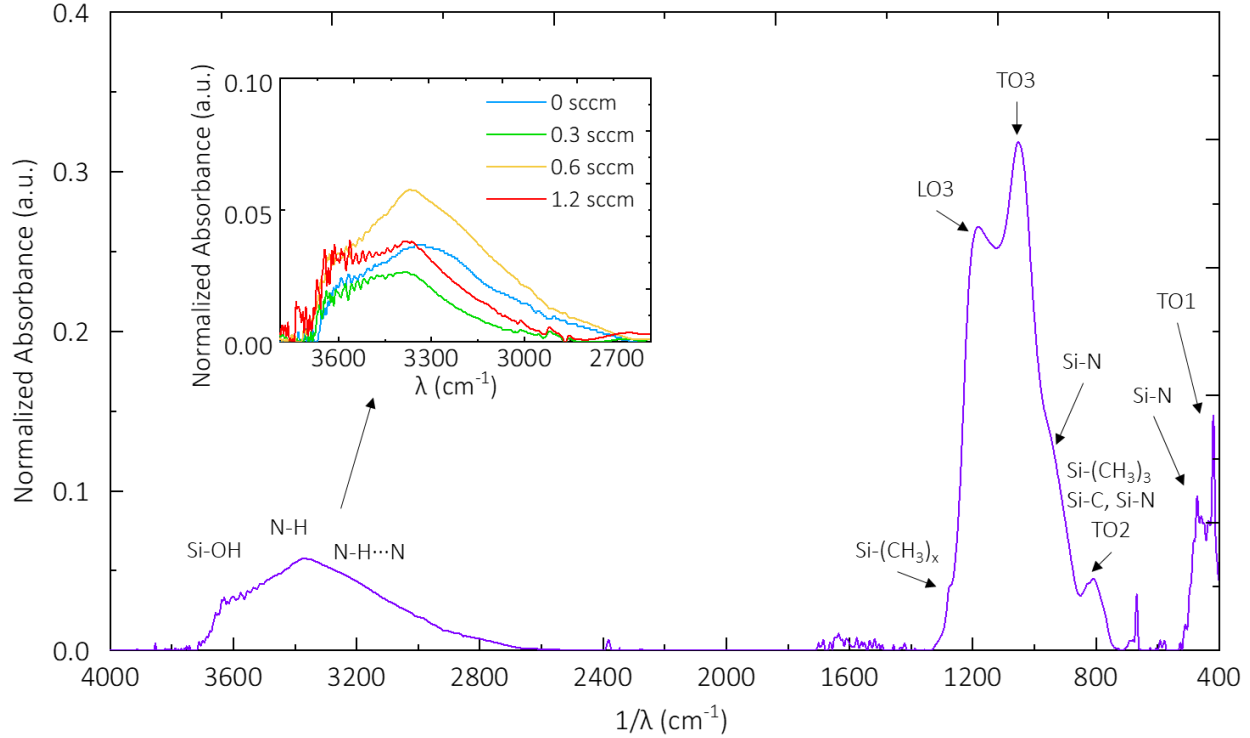
Fig. IV.10. FT-IR survey spectrum of a SiO$_x$N$_y$ film from run TD7, analyzed for an incidence angle of 60°. Inset diagram shows the evolution of hydrogen related bonds in the 2600-3700 cm^{-1} region, as a function of the O$_2$ flow rate (runs TD7, TD9, TD11, TD12).

Given that the present SiO$_x$N$_y$ films are the most complex ones produced in the frame of this thesis, a summary of all encountered absorptions is listed in Appendix 4. Similarly to the produced SiO$_2$ and SiO$_x$C$_y$:CH$_3$ films, the full spectrum can be divided into two main areas of interest: the fingerprint region (400-1400 cm^{-1}) and the hydrated network band (2700-3600 cm^{-1}). An evolution of the latter as a function of the O$_2$ flow rate is presented in the inset of Fig. IV.10. Because of the complexity of the produced SiO$_x$N$_y$ material and the multiple bonds absorbing at these frequencies, the evolution of the hydration state in the films is not instantly obvious. From a first look, it can be noted that the Si–OH absorption at ca. 3650 cm^{-1} increases with the addition of more O$_2$ in the inlet supply. However, no clear observation can be made for the water-bonded Si–OH:H$_2$O peak at around 3400 cm^{-1}, because it overlaps with the N–H stretching bond absorbing at 3400 cm^{-1}, which makes it difficult to discern between the two. Therefore, the hydrated region of the TDMSA films is mainly used in a qualitative manner to confirm the presence of Si–OH and N–H absorptions. Organic –CH$_3$ asymmetric stretching absorptions are noted in the band as well, as evidenced by the weak absorptions (small shoulders) at ca. 2900 cm^{-1}.

IV.1.4.1. Evolution of the SiO$_x$N$_y$ network

The fingerprint region of the SiO$_x$N$_y$ films was analyzed as a function of the O$_2$ flow rate in Fig. IV.11a, by probing p1 samples of runs TD7, TD9, TD11 and TD12. Once more, the overlapping absorptions interfere with a straightforward analysis, but general trends can be observed regardless. The trends are symbolized with arrows indicating the shift of the peak position and its change in intensity.
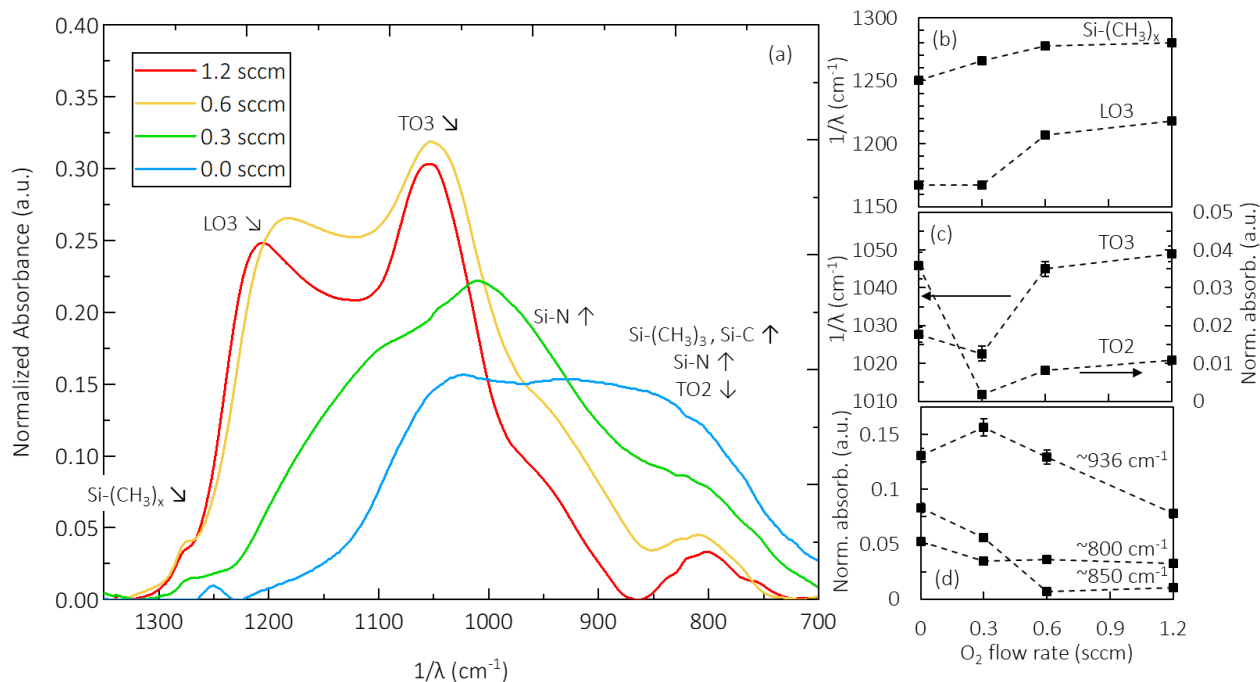
Fig. IV.11. Evolution of the FT-IR spectra of TDMSA-O$_2$ films at SPT 650°C, produced under various O$_2$ flow rates (runs TD7, TD9, TD11, TD12), analyzed for an incidence angle of 60° (a). Supplementary diagrams show evolution of Si–(CH$_3$)$_x$ and LO3 position (b), TO3 position and TO2 intensity (c) and the intensity of various Si–N absorptions (d) as a function of the O$_2$ flow rate, after deconvolution.

It is recalled that a reduction in O$_2$ supply results in films with higher nitrogen and carbon incorporation, as revealed by IBA and ellipsometry. This is reflected in FT-IR with the decrease of the LO3 and TO3 intensities and the parallel increase of the Si–N and Si–C absorptions. Visually, the LO3-TO3 pair is not observed anymore for 0.3 and 0 sccm O$_2$, with the overall spectrum having seemingly "shifted" towards lower wavenumber. Deconvolution is applied to facilitate the identification of the individual absorptions and their position. First, the Si–CH$_3$ peak is identified as the small shoulder around 1270 cm^{-1}. Its position shifts towards higher wavenumbers with the increase of the O$_2$ flow rate (Fig. IV.11b), which

indicates the addition of more O atoms to the Si–(CH$_3$)$_x$ complex [274]. Similarly, the LO3 mode also shifts towards higher wavenumbers at higher O$_2$ flow rates, hinting at the production of a more oxygen-rich film. However, it is noted that its position shifts substantially (from the expected position at ~1250 cm^{-1} to 1170 cm^{-1}) when O$_2$ flow rate is 0.3 sccm or less. It is proposed therefore that the LO3 absorption is potentially not present anymore, and that a different vibration is absorbing around the 1170 cm^{-1} frequency. Referring to Appendix 4, this absorption could be related to the TO4-LO4 pair.

TO3 behaves in a similar manner, absorbing at ca. 1050 cm^{-1} for 1.2 sccm O$_2$ and shifting towards lower wavenumbers for lower O$_2$ flow rates (Fig. IV.11c). The lowest wavenumber noted for TO3 is 1022 cm^{-1}. It is recalled that Si–CH$_2$–Si absorbs at 1000-1020 and 1060 cm^{-1} [247, 250]. Therefore, it could well be that, at the lowest O$_2$ flow rates, a carbon-related absorption is probed instead of the typical TO3 of the Si–O–Si network. This could very likely be the case, given the high C concentrations measured by both IBA and ellipsometry and the potential disappearance of the LO3 mode. Similar observations can be made for the absorption at 820 cm^{-1} (Fig. IV.11c). Both Si–C and Si–O (TO2) absorb at this frequency [214, 275]. A high intensity is noted at 0 sccm O$_2$. Given that the LO3 band has potentially disappeared in absence of O$_2$, and that the TO3 mode in that case is a Si–CH$_2$–Si absorption instead, the peak at 820 cm^{-1} can be attributed to the Si–C bond. Once O$_2$ is added to the inlet gas composition, the intensity at 820 cm^{-1} drops, slowly switching from a Si–C to a Si–O TO2 mode, which starts increasing again for higher O$_2$ flow rates.

The intensity of various Si–N related absorptions is also presented (Fig. IV.11d). Overall, such Si–N absorptions are shown to decrease with the addition of O$_2$. This reflects well the IBA and ellipsometry results presented so far. Interestingly, the three vibrational modes do not follow the exact same trends. This indicates that the nitrogen incorporates differently across the films, a behavior that could potentially be caused by deposition from distinct nitrogen-providing intermediates depending on the O$_2$ flow rate.

The above FT-IR discussion is well supported by X-ray photoelectron spectroscopy (XPS). Table IV.3 presents a synthesis of the chemical environment, as probed by XPS, for SiO$_x$N$_y$ samples produced at SPT 650°C, under varying O$_2$ flow rate, after deconvolution of the spectra based on literature data [253, 276, 277]. Globally, an increase in O$_2$ flow rate is reflected well in the higher oxygen content of the analyzed films (13.54 at.% for 0 sccm O$_2$, increasing to 49.69 at.% for 1.2 sccm O$_2$). The evolutions of the other elements is coherent with the ellipsometry and IBA results as well. The chemical bonding state can be inspected more closely after the deconvolution analysis. More specifically, the environment of Si appears to be changing substantially based on the O$_2$ flow rate. For the highest O$_2$ flow rates, Si appears to be involved primarily in Si(O)$_4$ and O–Si–N configurations. Decreasing the O$_2$ supply at the inlet however results in the transition from Si(O)$_4$ to SiN$_x$, correlating well with the decreased LO3 and TO3 absorptions in FT-IR. XPS results also confirm the presence of the Si–C absorption that was overlapping with TO2.

However, only 4-5 % of the incorporated carbon is found in a Si–C–Si environment. The rest is involved in organic bonds or SiO$_x$C$_x$, which increase with a decrease in O$_2$ flow rate.

Table IV.3. XPS deconvolution analysis of SiO$_x$N$_y$ by TMDSA-O$_2$ at 650°C, for variable O$_2$ flow rates.

Bonding		O$_2$ flow rate (sccm)							
		0		0.3		0.6		1.2	
		Binding energy (eV)	Atomic %	Binding energy (eV)	Atomic %	Binding energy (eV)	Atomic %	Binding energy (eV)	Atomic %
Si2p	Si-C	100.5	0.83	100.5	0.23	100.4	0.76	100.4	0.25
	SiO$_x$C$_x$	101.13	0.42	101.13	0.11	101.03	0.38	101.03	0.12
	SiN$_x$	101.23	26.62	101.39	26.43	-	-	-	-
	N-Si-O	101.86	13.31	102.02	13.21	102.51	25.19	102.6	25.87
	Si(O)$_4$	-	-	-	-	103.14	12.59	103.23	12.93
C1s	Si-C	282.6	1.31	282.6	0.55	282.6	0.67	282.6	0.38
	SiO$_x$C$_x$	283.8	25.62	283.8	25.33	283.94	7.4	283.97	4.63
	CC or CH	285.01	5.83	285	4.16	285	2.86	285	1.53
	C-O	286.3	0.15	286.3	0.5	286.28	0.69	286.17	0.51
	C=O	286.81	0.4	286.7	0.46	286.9	0.45	286.9	0.38
	O=C-O	-	-	289	0.08	289	0.36	289	0.33
N1s	N-Si$_x$	397.74	10.87	397.76	10.36	398.07	4.95	398.02	2.73
	O-N-Si	-	-	-	-	-	-	398.9	0.65
	O-N-Si$_2$	399.18	1.11	399.17	1.16	399.8	0.26	-	-
	O1s	532.05	13.54	532.05	17.44	532.26	43.42	532.26	49.69

IV.1.5. Mechanical properties

It is recalled that nanoindentation analysis requires films with thickness around 500 nm or higher. However, given the very low DR of the tested TDMSA chemistries at the investigated deposition conditions, the technical limitations become clear. Referring back to Table IV.2, only one run (TD10) is performed for the production of thick SiO$_x$N$_y$ films from TDMSA-O$_2$. Despite the execution of only one experiment, the particular evolution of the nitrogen content along the length of the reactor proved beneficial: it allows

correlating in a combinatorial manner the mechanical properties of the films to their composition with just one single experiment. In more detail, samples from the isothermal region are analyzed by nanoindentation to obtain information on their hardness H and elastic modulus E. Given that the temperature remained constant in this region, any change in these mechanical properties can be safely attributed to the change in local film composition and, consequently, the network structure. The evolution of H and E as a function of the nitrogen content, as calculated by ellipsometry, is presented in Fig. IV.12.
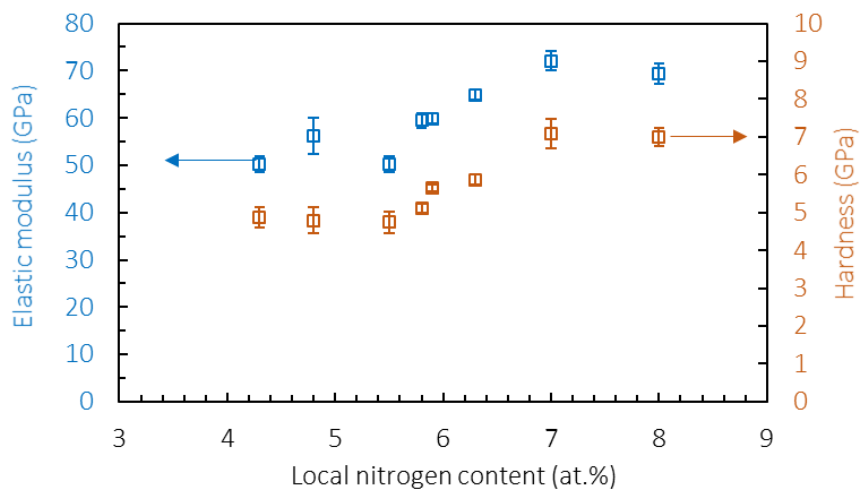

Fig. IV.12. Influence of the local nitrogen content on the elastic modulus E and hardness H of TDMSA-O$_2$ films produced at SPT 650°C (TD10).

Both H and E appear to evolve in a similar manner, slightly increasing with higher incorporation of nitrogen, but seem to stabilize beyond 7.0 at.%. More specifically, sample p1, with a local nitrogen content of 4.3 at.%, exhibits a hardness and elastic modulus of 4.3 and 50.3 GPa, respectively. Further inside the reactor yet still in the isothermal region, sample p5, with a local nitrogen content of 8.0 at.% has its hardness and elastic modulus increase to 7.0 and 69.4 GPa, respectively. Both mechanical properties are comparable to values obtained from PECVD SiO$_x$N$_y$ films with ca. 10 at.% N, for which the elastic modulus and hardness are reported at 78.9 and 7.8 GPa, respectively [278].

Interestingly, the mechanical properties of the SiO$_x$N$_y$ films from TDMSA-O$_2$ are in the same range as those of SiO$_2$ from TEOS-O$_2$/O$_3$. Although SiO$_x$N$_y$ materials are usually more resistant to penetration and deformation than SiO$_2$, the presence of organic moieties in the produced films could potentially explain the similar values noted between the two chemistries. Regardless, the results illustrate well how the partial

and progressive replacement of O atoms by N ones induces a change in the material network and density, improving as a result the mechanical properties of the film, despite the temperature remaining constant.

IV.1.6. Surface wettability

Water wettability measurements on the various SiO$_x$N$_y$ films, which were previously characterized by IBA, are presented in Fig. IV.13. Initial inspection of the results reveals that the global water contact angle (WCA) ranges from 76.9° to 89.4°, but seems to be overall independent from the nitrogen content (Fig. IV.13a). These values are close to the ones reported by Trevino et al. [279], who noted a WCA of 73.6° for a thermally grown SiO$_x$N$_y$ surface with 14.5 at.% N and 14.4 at.% C. Such results illustrate well the multifactorial dependency of the surface wettability. Plotting of the measured WCA values as a function of the carbon and hydrogen contents was also attempted, but no clear correlation was noted. Given the non-linear behavior of the WCA versus the composition in nitrogen, carbon or hydrogen, the wettability behavior is additionally examined as a function of the various process parameters.

More specifically, Fig. IV.13b presents the evolution of the WCA for increasing NH$_3$ flow rate under constant O$_2$ flow of 0.6 sccm (runs TD6, TD7, TD8), and for increasing O$_2$ flow rate in absence of ammonia (runs TD7, TD11, TD12). In the first case, an increase in NH$_3$ flow rate seems to decrease the WCA. This trend could be attributed to the decrease of the organic carbon content in the films through cleaving by NH$_3$, as was revealed by IBA (Fig. IV.8). It is known that higher organic concentrations in silicon oxide and nitride films tend to increase the hydrophobic character of the films. In the case of nitrides, Arafat et al. [280] presented an increase of the WCA from ca. 60° to approximately 83° for the surface termination of Si$_3$N$_4$ with an organic monolayer. Similarly, Saengdee et al. [281] noted an increase of the WCA of Si$_3$N$_4$ from 73° to ca. 86° after replacement of surface –OH groups by organic carbon ones. Another potential connection could be made with the introduction of further surface NH$_2$ groups or –N–H bonds in the films for higher NH$_3$ flow rates. It is noted that Si–NH–Si bonds are hydrophilic due to their polarity and their quick reaction with water in the air [282]. However, no such correlation was possible when plotting the WCA as a function of the NH$_2$ or NH absorbance at 3300 to 3400 cm^{-1} from the respective FT-IR spectra.

An increase of the O$_2$ flow rate in absence of ammonia (runs TD7, TD11, TD12) appears to increase the WCA slightly (Fig. IV.13b). A similar behavior is shown in Fig. IV.13c, where an increase in O$_2$ flow rate under a constant NH$_3$ flow of 20 sccm (runs TD6, TD4) also increases the WCA. This behavior is unexpected, since increase of the O$_2$ flow rate decreases nitrogen incorporation and enhances the oxide character of the films. Hong et al. [283] specifically mention that lower nitrogen incorporation in silicon

oxynitride films can make the surface more negatively charged and hydrophilic, by facilitating dipole interaction and hydrogen bonding between silanols and water. The slight increase in WCA is therefore difficult to explain, but could be caused due to a replacement of the hydrophilic NH or NH$_2$ groups by, slightly less hydrophilic, Si–OH ones.
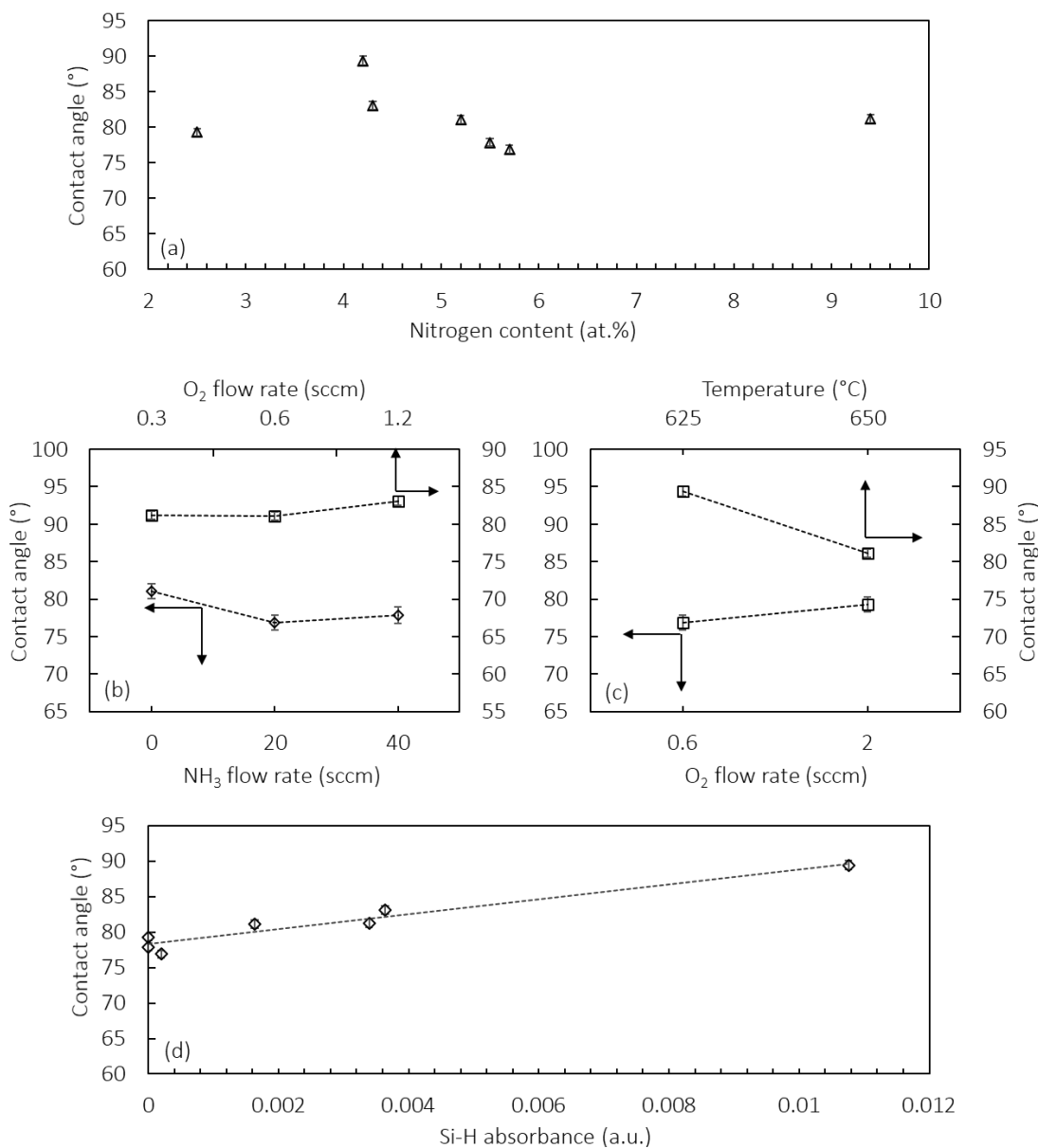

Fig. IV.13. Water wettability results for various SiO$_x$N$_y$ films from runs TD6, TD8, TD7, TD11, TD12 and TD14. Evolution of the contact angle as a function of the N content of the films (a), NH$_3$ flow rate and O$_2$ flow rate in absence of NH$_3$ (b), O$_2$ flow rate in presence of NH$_3$ and temperature (c), and Si–H absorption at ca. 630 to 650 cm^{-1} (d).

Even though the analysis of only two points was possible, the effect of the SPT is also considered (Fig. IV.13c). It appears that an increase of 25°C leads to more hydrophilic films. It is recalled that N film concentration is higher at 650°C compared to 625°C making it possible that a relatively higher amount of NH$_x$ bonds is also present, increasing the wetting phenomenon. At the same time however, a closer inspection of the FT-IR data of these particular samples reveals that the methyl related absorptions increase at 650°C, which is in contrast to the lower WCA value noted at this temperature.

Considering all the above, it is once again apparent that the surface wettability depends on a large number of factors, including film composition, surface termination, roughness and surface energy, as was discussed in Chapter III. In the case of silicon nitride materials, surface termination is affected by –OH, –NH$_2$ and –CH$_3$ groups. Tsukruk and Bliznyuk reported a contact angle of 42°, 53° and 75° for –OH, –NH$_2$ and –CH$_3$ terminated silicon nitrides, respectively [284]. Other authors however also place importance on the Si–H content, mentioning that replacement of –OH by Si–H reduces wettability [285]. In a similar sense, it was also noted that replacement of NH or NH$_2$ surface sites by the less polar Si–H surface bonds through HF etching also increases the contact angle of Si$_3$N$_4$ films [280]. In the case of oxynitride materials, Zhang et al. produced SiO$_x$N$_y$ coatings with high Si–H contents and noted WCAs between 98 and 110° [282]. As such, a closer inspection was given to the evolution of the Si–H absorption across the films. Even though this specific bond absorbs very weakly between 630 and 650 cm^{-1} in the FT-IR spectra, tracing the measured WCA values as a function of its absorbance yielded an almost linear behavior (Fig. IV.13d). Of course, that is not to exclude the impact of the other factors mentioned previously. Regardless, the increase of WCA with the Si–H content reflects well the reports in the literature.

IV.1.7. *Wet etching corrosion resistance of SiO$_x$N$_y$ films*

In a first step, the wet corrosion resistance of a TDMSA-NH$_3$-O$_2$ film produced at 650°C (run TD3) is assessed by P-etch. The results reveal a significant improvement in corrosion resistance with a remarkably low P-etching rate of 0.2 Å.s^{-1} noted for the SiO$_x$N$_y$ film. This value measures at least one order of magnitude lower than the TEOS (9.1-19.1 Å.s^{-1}) and HMDS-TEOS (14.8-60.4 Å.s^{-1}) films produced so far, even when compared to films that underwent annealing post-treatment at 550°C (ca. 4.0 Å.s^{-1}). This vastly improved corrosion resistance cannot be attributed merely to the increase of the temperature from 550°C to 650°C. This is also supported by the record-low etching rate of 2 Å.s^{-1} for SiO$_2$ films produced at 800°C [177]. If it were merely an effect of the temperature, the etching rate at 650°C would be expected to fall between 2 and 4 Å.s^{-1}. Therefore, it becomes clear that this significant improvement is to be attributed to the change in film composition, and more specifically to the partial replacement of O atoms by higher

coordinated N ones. Another interesting point is that the presence of organic carbon, as was identified by FT-IR, does not seem to be detrimental to the P-etch behavior of the SiO$_x$N$_y$ films.

It must be noted, however, that such low etching rate values render it difficult to discern between SiO$_x$N$_y$ films with variable nitrogen contents, especially when wishing to establish a link between the composition and the corrosion resistance. For that reason, a chemical etching solution that is more suitable for the resistant silicon nitride materials must be utilized. A literature review on the various etchants used for the chemical etching of silicon nitride and silicon oxynitride films is presented in Table IV.4.

Table IV.4. Buffered oxide etching solutions, process parameters and etching rates noted in the literature.

Ref.	Material	Etchant	Chemistry	Method	P (mTorr)	T°C	Notes	BOE etching rate (Å.s^{-1})
[286]	SiN$_x$	BOE 6:1	SiH$_4$/N$_2$/Ar	ECR-PECVD	<1	<120°C	-	0.8-25
[179]	SiO$_x$N$_y$	BOE 6:1	SiH$_4$/N$_2$/Ar	ECR-PECVD	<0.9	<120°C	15 at.% C	1.6-17
[287]	SiN$_x$	BOE 7:1	SiH$_4$/N$_2$/Ar	ICPE-CVD	1-20	150°C	15-20 at.% H	6-20
[287]	SiN$_x$	BOE 7:1	SiH$_4$/N$_2$/Ar	PECVD	1-20	150°C	25-30 at.% H	83
[288]	SiN$_x$	BOE 9:1	SiH$_4$/N$_2$/Ar	ECR-PECVD	1.5	90°C	24-31 at.% H	3-28
[289]	Si$_3$N$_4$	BOE 10:1	Commercial Si$_3$N$_4$ mask	-	-	-	-	0.1
[290]	SiN$_x$	BOE 10:1	SiH$_4$/NH$_3$/H$_2$	PECVD	500	150°C	2.10^{22} cm^{-3} H	61
[180]	SiN$_x$, SiO$_x$N$_y$	BOE 10:1	Si$_3$N$_4$ target	RF Sputtering	<1	-	-	8-295
[291]	SiN$_x$	Misc.	SiH$_4$/NH$_3$	Photo-CVD	300-1400	100-400°C	-	10-150

The most commonly utilized solution for etching nitrogen-rich films is a Buffered oxide etchant (BOE) solution. A key difference from the P-etch solution is that the BOE solution contains NH$_4$F, which helps maintain (buffer) the HF concentration and pH value of the solution, aiding in the continuous etching of the nitride films [289]. Oftentimes this solution is also referred to as Buffered hydrogen fluoride (BHF)

solution. No standard composition has been proposed in the literature for the screening of silicon nitride films, with the scientific community using various ratios of NH$_4$F:HF. Nonetheless, it is noted that the BOE 10:1 solution is the most widely used one in the semiconductor industry and encountered in the majority of the patents concerning Si$_3$N$_4$ films for MEMS and semiconductor devices. Despite that, given that the BOE 6:1 solution is more aggressive than BOE 10:1, the former (6:1) is used to better screen the produced SiO$_x$N$_y$ films among each other.

Fig. IV.14 presents the evolution of the BOE 6:1 etching rate of various SiO$_x$N$_y$ films as a function of their nitrogen content, as calculated by ellipsometry. SiO$_2$ and SiO$_x$ films from the TEOS and HMDS-TEOS chemistries produced at 550°C are also etched with this solution for comparison. A nitrogen content of 0 at.% is assigned to them in this figure.
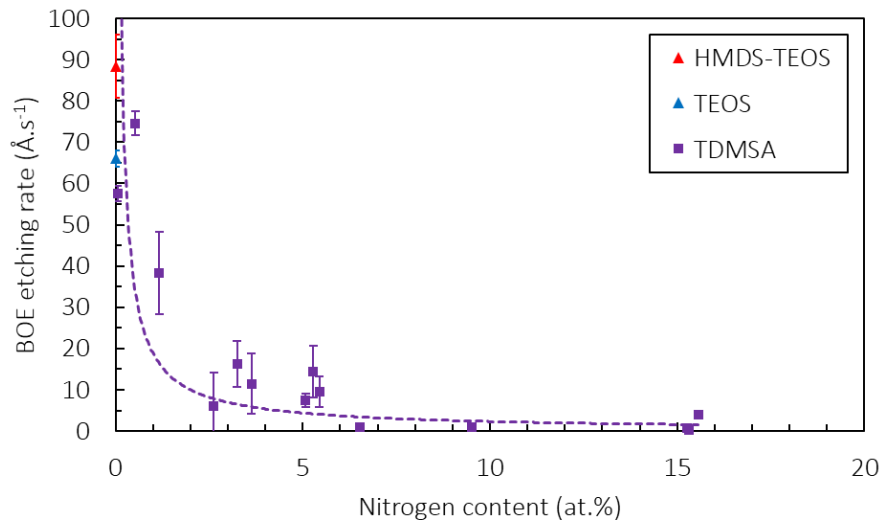

Fig. IV.14. BOE etching rate of SiO$_x$N$_y$ films from TDMSA chemistries, as well as SiO$_2$ and SiO$_x$ films from TEOS and HMDS-TEOS, respectively. Power curve added for visual aid.

Fig. IV.14 reveals a BOE etching rate of around 88 Å.s^{-1} and 66 Å.s^{-1} for HMDS-TEOS and TEOS films, respectively. It is recalled that at this temperature (550°C), these two films correspond to a sub-stoichiometric and stoichiometric SiO$_2$, respectively. Similar to the P-etch results, the film from TEOS presents a better resistance to the corrosive BOE solution in comparison to the HMDS-TEOS film. Beyond that, incorporation of nitrogen in the silica network results in BOE etching rate values ranging from 74 Å.s^{-1} down to 0.1 Å.s^{-1} depending on the nitrogen content. The measured values are comparable to those noted in the literature (Table IV.4), with even lower etching rate values observed for most of the produced films.

Another interesting point is that the etched oxynitride films in the present thesis have a nitrogen concentration below 15 at.% N, yet perform as well, if not better, as some of the nitride films studied in the literature. Additionally, the power curve added for visual aid reveals that the SiO$_x$N$_y$ films from TDMSA converge to values below 4 Å.s^{-1} beyond approximately 7 at.% N. This result is significant in establishing a link between the operating conditions, film composition and corrosion resistance. Based on the above information, it seems that films with around 7 at.% N are sufficient in achieving an excellent corrosion resistance. Further incorporation of nitrogen beyond this point does not appear to be necessary. This information is important when defining operating conditions with a targeted corrosion resistance behavior in mind.

It is recalled that the etching rates of Fig. IV.14 are measured from films that have been processed under a variety of operating conditions. Since the link to the nitrogen content is well established, a closer look at how the specific operating conditions affect the etching rate is presented in Fig. IV.15.
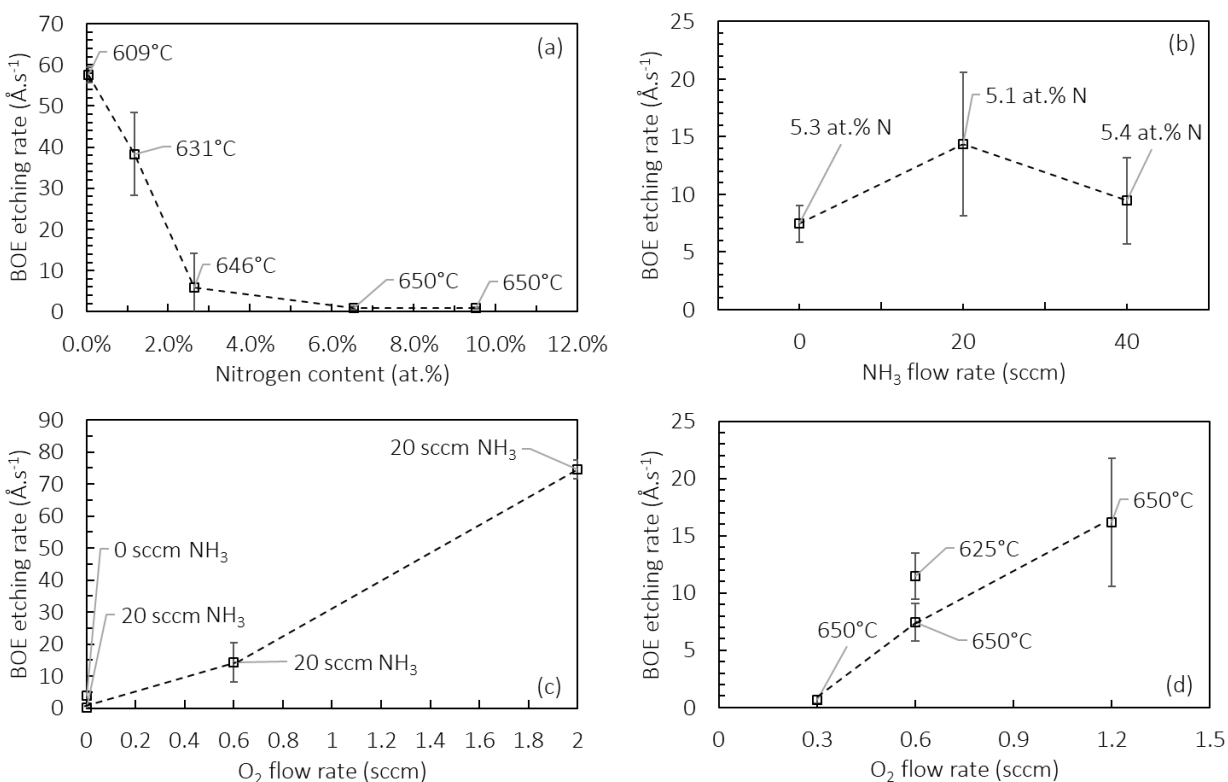

Fig. IV.15. BOE etching rate of SiO$_x$N$_y$ films from TDMSA, plotted as a function of the nitrogen content along the length of the reactor (a), the NH$_3$ flow rate under constant O$_2$ flow of 0.6 sccm (b), the O$_2$ flow rate for 0 and 20 sccm of NH$_3$ (c) and the O$_2$ flow rate in absence of NH$_3$ (d).

Fig. IV.15a examines the evolution of the etching rate across 5 samples from run TD3 as a function of their nitrogen concentration. Since a thermal gradient exists along the length of the reactor, the local temperature of each sample is also noted. For a sample produced outside the isothermal region, with a local temperature of 609°C and a nitrogen concentration of 0.1 at.%, a BOE etching rate of 57.5 Å.s^{-1} is noted. When examining a sample of the isothermal region, produced at a local temperature of 650°C and having a nitrogen concentration of 9.5 at.%, the etching rate drops to 0.9 Å.s^{-1}. A decreasing trend is observed overall for a simultaneous increase in temperature and nitrogen content. This behavior was also noted by Rathi et al. [291], the results of whom illustrated a decrease in etching rate when substrate temperature was increased from 100 to 400°C. The authors attributed this evolution to a loss in hydrogen of the films, followed by densification of the network as a result of the higher deposition temperatures.

Additionally, the BOE evolution in Fig. IV.15a presents a break in its slope: a steep decrease is noted between 0 and 2.5 at.% N, explained as an effect of the temperature. As was presented in Chapter III, an increase in temperature greatly aids the densification of the network, through desorption of hydrated species and reorganization of the Si–O–Si bridges. After the break, a milder slope is observed between 2.5 and 10 at.% N. The temperature remains constant in that case, but the nitrogen concentration increases. It can therefore be said that the etching rate depends strongly on the process temperature on one hand, which on the other hand is a process parameter that also influences the level of nitrogen incorporation.

Fig. IV.15b examines the effect of the NH$_3$ flow rate on the BOE etching rate, under a constant O$_2$ flow of 0.6 sccm (runs TD6, TD7, TD8). The nitrogen content of the films is also noted. No specific behavior is observed, with all values falling within the error bars, ranging between 7.4 to 14.3 Å.s^{-1}. This could be explained by the fact that a change in NH$_3$ does not affect the nitrogen content of the films enough in order to lead to a change of their corrosion resistance. Instead, NH$_3$ has been mostly seen to influence the carbon content of the films (Fig. IV.8). However, as was noted previously, the presence of CH$_3$ does not seem to greatly influence the etching rate in the case of SiO$_x$N$_y$ films. Similar observations were mentioned by Trevino et al. [279], who studied the surface modification of SiO$_x$N$_y$ containing ca. 14 at.% C and noted that their applied HF dip process do not impact carbon. It is therefore not surprising that changes in the NH$_3$ flow rate do not reveal any specific trend in the BOE etching rate.

Fig. IV.15c examines the effect of the O$_2$ flow rate on the BOE etching rate, with (TD4, TD5, TD6) and without NH$_3$ (TD9). When no O$_2$ is added in the inlet gas composition, a BOE etching rate of 3.9 and 0.1 Å.s^{-1} is noted for 0 and 20 sccm NH$_3$, respectively. An increase of the O$_2$ flow rate to 2 sccm worsens the corrosion resistance of the film, with its BOE etching rate increasing drastically to 74.6 Å.s^{-1}. Similar results were presented by Volkov and Satunkina [180], who studied the etching rate of Si$_3$N$_4$ films and its evolution for increasing addition of O$_2$ in the inlet gas composition. The authors noted that the BOE etching

rate of their silicon nitride films increased dramatically with gradual increase in oxygen incorporation. An approximately 83 times higher BOE etching rate was measured once the material had fully transitioned from Si$_3$N$_4$ to SiO$_2$. A similar trend is also encountered when examining the effect of the O$_2$ flow in absence of NH$_3$ in Fig. IV.15d. When a 0.3 sccm O$_2$ is used, a BOE etching rate of 0.7 Å.s^{-1} is noted. This value increases to 16.2 Å.s^{-1} for a higher O$_2$ flow of 1.2 sccm. Once again, the decreased corrosion resistance is attributed to the loss in nitride character (i.e. gain in oxide character) of the films under higher O$_2$ flow rates.

Two additional points are discussed. First, in Fig. IV.15c, the etching rate of a film produced only from TDMSA, namely in absence of O$_2$ and NH$_3$ (run TD9), has a BOE etching rate of 3.9 Å.s^{-1}. Considering the results, it is revealed that the addition of 20 sccm of NH$_3$ in absence of O$_2$ (Fig. IV.15c), or the addition of 0.3 sccm O$_2$ in absence of NH$_3$ (Fig. IV.15d), result in a lower etching rate than the one noted from TDMSA alone. Thus, the addition of at least one of the two gases (O$_2$ or NH$_3$) in the inlet composition, preferably O$_2$, is beneficial to the corrosion behavior of the films. This could be potentially linked to the ability of NH$_3$ and O$_2$ to cleave methyl ligands or hydrogen atoms from TDMSA and/or its intermediates in the gas phase, leading as a result to the production of films with a denser network. Lastly, the additional point in Fig. IV.15d is included to compare two films that have been produced under the same inlet gas composition, but at different SPT (runs TD7 and TD14). When deposition is performed at 625°C (run TD14), a BOE etching rate of 11.5 Å.s^{-1} is noted, decreasing to 7.4 Å.s^{-1} when the SPT is raised to 650°C (runs TD7). These results reflect well the behavior previously discussed in Fig. IV.15a, pointing once more at the combined effect of higher temperatures and at.% N in improving the corrosion resistance of the films.

The above results illustrate well the excellent performance of the SiO$_x$N$_y$ films and their improved wet etching corrosion resistance in comparison to SiO$_2$. At the same time however, they also underline the grand effect of the operating conditions on the resulting material. Factors such as gas phase composition, local temperature, and their subsequent effect on the resulting film composition and structure, play a big role in the final material performance. Chapter III demonstrated well how a deposition process governed by the precursor molecule differs from that driven by its intermediate molecules. The nature of the film-forming compound greatly affects the composition and the various properties of the resulting film. Given that the TDMSA precursor is rarely studied, very little information exists about it in the literature. Thus, the following section attempts to shed light on the details of its deposition mechanism. Gas phase analyses are used to identify film-forming species and elaborate on potential deposition pathways, with parallel consideration of the solid phase data presented so far.

IV.2. Gas-phase analysis of the SiO$_x$N$_\gamma$ deposition process

Analysis of the gas phase is executed in order to identify the gaseous species that are present during the SiO$_x$N$_y$ deposition process. The three analyses, namely ESR, GC-MS and NMR, are carried out by sampling the gas phase at the outlet of the reactor, as was described in section II.2.1 of Chapter II. All three methods are implemented at the same time and systematically used for all runs of Table IV.1 and 2. Additional experiments are also performed to replicate selected experimental runs and confirm reproducibility, for calibration, or in order to extract additional information. This methodology was developed and implemented by engineer Laura Decosterd in the frame of the ANR project HEALTHYGLASS, supervised by Prof. Marie-Joëlle Menu.

The results of section IV.1 have illustrated how the presence of NH$_3$ in the gas phase does not benefit the aim of the present thesis: no enrichment in nitrogen or increase in DR was observed. Additionally, the wet etching corrosion results showed that samples produced under a TDMSA-O$_2$-NH$_3$ chemistry have a lower corrosion resistance, compared to samples produced using TDMSA-O$_2$. For this reason, the current section focuses principally on the gas phase results of the TDMSA-O$_2$ chemistry, in order to propose potential chemical reactions that can be used as the basis for the development of a deposition mechanism. Gas-phase results of experimental runs that utilize NH$_3$ are included in Appendix 5.

IV.2.1. Analysis of radical species by ESR

Electron Spin Resonance (ESR) study is performed in order to gain insight into the species that are the most difficult to probe; namely the very reactive, radical species that are described by very short lifetimes. In order to observe them, the spin-trap molecule POBN is encapsulated in a KBr pellet and placed within the reactor, as described in section II.2.1.1 of Chapter II. After ESR analysis, it is observed that the same radical species is systematically trapped across all runs, independently of the reaction conditions (presence of NH$_3$, O$_2$ flow rate, or SPT) as is discussed below.

First, Fig. IV.16a shows typical ESR spectra obtained in liquid and solid states. It is recalled that "liquid state" refers to an analysis after dissolution of the pellet in toluene, while "solid state" corresponds to analysis of the POBN encapsulated in the solid KBr matrix as is. For both states, a *g*-factor equal to 2.0059 is noted. The signal of the solid state is observed to be anisotropic, with 2 parallel *g* values: g_x= 2.021 and g_z=1.984. In the liquid state, the free rotation of the molecules gives rise to a triplet with *g*=2.0059. The liquid state also gives access to the hyperfine constants a_N=14.6 G and a_H, the latter of which is confounded in the bandwidth and cannot be calculated.

Fig. IV.16b shows liquid state ESR spectra for all runs. Differences in the intensities of the spectra are attributed to external factors. Despite that, the similarity between them indicates the generation of a common radical molecule. Additionally, analysis of the gas phase under presence of only TDMSA (run TD9) resulted in the trapping of the same molecule as for all other runs. It can therefore be deduced that the trapped species originates from the precursor and is independent from the other reactants used in the inlet gas composition.
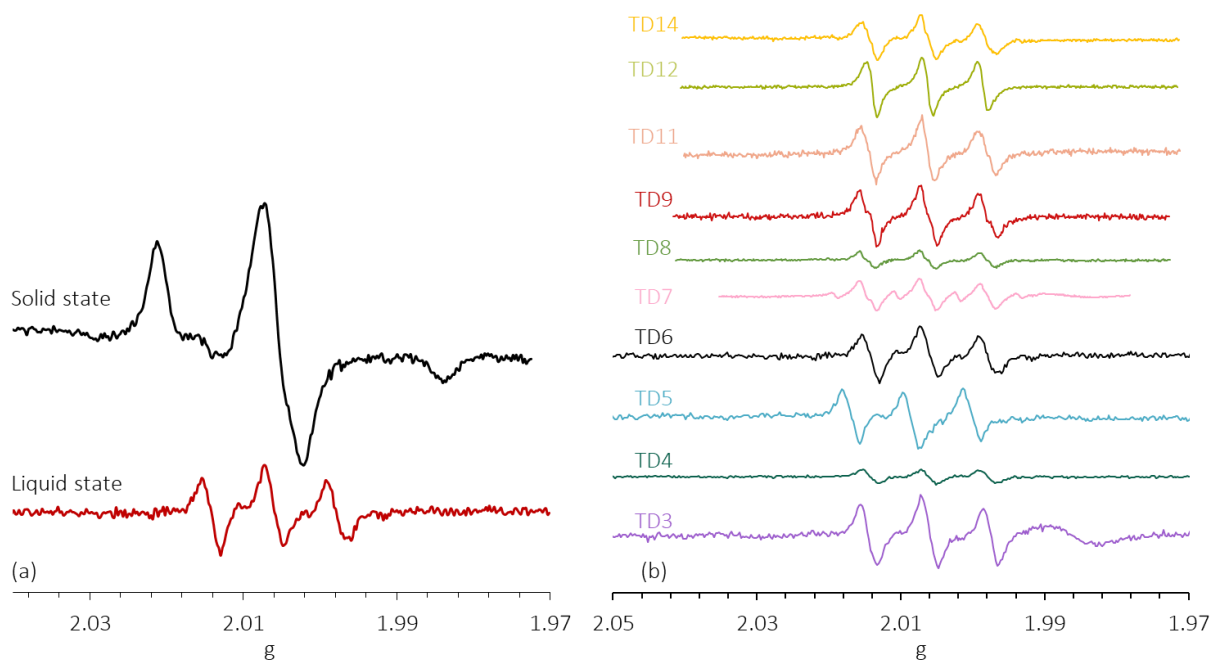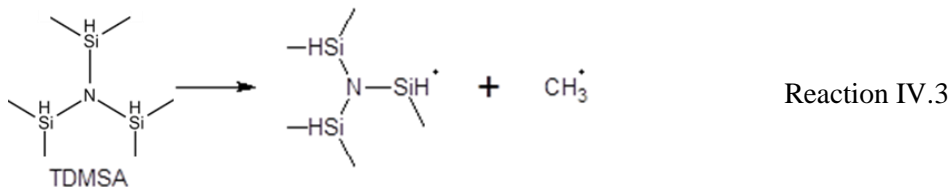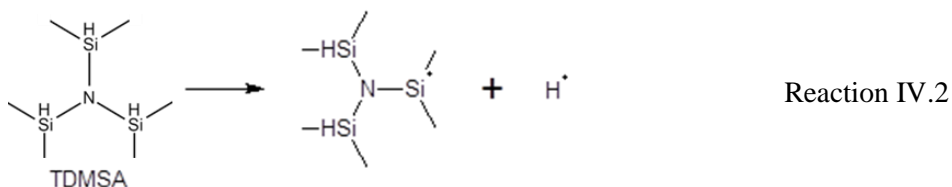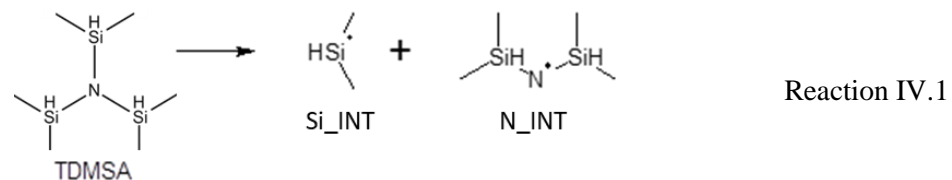

Fig. IV.16. ESR spectra obtained in liquid and solid state (run TD6) (a).

Liquid state ESR spectra across all runs (b).

Given the complex structure of the TDMSA molecule, its decomposition can follow multiple pathways based on the homolytic dissociation of the different bonds. For example, the homolytic breaking of the Si–N bond (Reaction IV.1) would result in the formation of two intermediate radical species Me$_2$HSi$^\bullet$ and (Me$_2$HSi)$_2$N$^\bullet$, which are noted Si_INT and N_INT hereinafter, respectively. Reaction IV.2 on the other hand proposes the homolytic dissociation of the Si–H bond, which would form a H$^\bullet$ and a Si-centered radical. Finally, if the pathway is initiated at a Si–C bond (Reaction IV.3), it would produce a CH$_3$$^\bullet$ and another Si-centered radical, as detailed below.

Reaction IV.1

Reaction IV.2

Reaction IV.3

Reaction IV.1 to 3 illustrate the multiple possible radical species that can be produced through the thermal decomposition of TDMSA. However, only one species is trapped by ESR. One could speculate that only one of the proposed reactions is taking place. However, each of the reactions produces two radical species and such a speculation can thus not explain why the second radical is not trapped. As a result, it is suggested that only the radical molecule with the highest remaining concentration and longer lifetime is trapped. The production of the other radicals is not excluded. However, they are not trapped either because they are formed in lower concentrations, or because they have already reacted in the gas phase.

A close inspection of the hyperfine structure of the signal and comparison to literature data reveals that CH$_3$$^\bullet$, H$^\bullet$ and (Me$_2$HSi)$_2$N$^\bullet$ radicals are not the trapped species [292, 293]. Based on the proposed Reaction IV.1 to 3, it is deduced that the species observed by ESR is a silicon-centered radical. Chandra et al. reported values for multiple Si-centered radicals, such as Me$_2$HSi$^\bullet$ or Me$_3$Si$^\bullet$, trapped by α-phenyl-N-tert-butyl nitrone (PBN) spin-trap [294, 295]. The g-factor for these Si-centered radical species was always 2.0059±0.0001, which coincides well with the values observed for all runs in the present thesis. Additionally, because of their large, hindered structure, the Si-centered radicals resulting from the Si–C and Si–H bond cleaving of Reaction IV.2 and 3 are unlikely to be trapped. Considering all of the above results and literature data, it is proposed that the trapped radical concerns the Me$_2$HSi$^\bullet$ molecule. As a result, is it also proposed that Reaction IV.1 is the primary decomposition reaction followed by the TDMSA precursor, leading to the formation of the Si_INT (Me$_2$HSi$^\bullet$) and N_INT (Me$_2$HSi)$_2$N$^\bullet$) radical intermediate species. As such, it is expected that these two intermediates will be encountered as the building blocks of the various

non-radical by-products present in the gas phase. To confirm this, GC-MS and NMR analyses are carried out, in order to identify the stable compounds at the exhaust of the reactor.

IV.2.2. Analysis of stable species

IV.2.2.1.   Gas-phase analysis by GC-MS

GC-MS analysis of the gas phase is executed as was described in Chapter II. Three different campaigns are carried out. The first campaign focuses on calibrating the GC-MS apparatus in regards to the analyzed quantity of TMDSA. The second campaign is executed in order to obtain information on the thermal decomposition of TDMSA, in absence of O_2 and NH_3. The third and last campaign pertains to the analysis of the gas phase for the experimental runs detailed in Table IV.2.

IV.2.2.1.1.   TMDSA calibration curve

In order to quantify the amount TDMSA exiting the reactor for a given condition, it is mandatory to establish a calibration curve. For this purpose, specific flow rates of TDMSA are introduced in the reactor at room temperature, under constant N_2 dilution (4028 sccm). After GC-MS analysis of the sampling bags, the areas beneath the TMDSA and N_2 peaks in the GC-MS spectra are calculated. The area of the TDMSA peak (A_{TDMSA}) is divided by that of the N_2 peak (A_{N2}) and plotted versus the applied flow rate of the precursor. The resulting calibration curve is presented in Fig. IV.17.
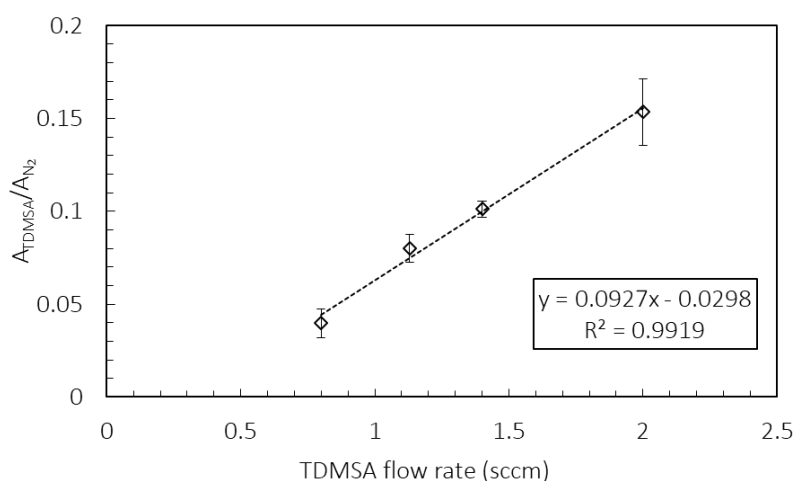

Fig. IV.17. GC-MS calibration curve for the TDMSA precursor.

The calibration curve of Fig. IV.17 was further verified by additional GC-MS analyses that probed the gas phase under TDMSA flow rates inside (interpolation) and outside (extrapolation) the range of the calibration curve. The results were coherent, with less than 10 % deviation from the values predicted by the calibration curve. Through this, the calibration curve is validated and used systematically in the following sections for measuring the amount of TMDSA at the exit of the reactor and calculating its conversion percentage.

IV.2.2.1.2.   Thermal decomposition of TDMSA

The thermal decomposition of TDMSA is analyzed by fixing the TDMSA flow at 2 sccm for a constant dilution of 4028 sccm N$_2$, in absence of O$_2$ and NH$_3$. Four different SPTs are applied in the reaction chamber, namely 580, 625, 650 and 700°C. Through utilization of the calibration curve established in Fig. IV.17, the conversion of TDMSA at the exhaust of the reactor is calculated and plotted versus the temperature in Fig. IV.18, as a means to study the decomposition of the precursor.
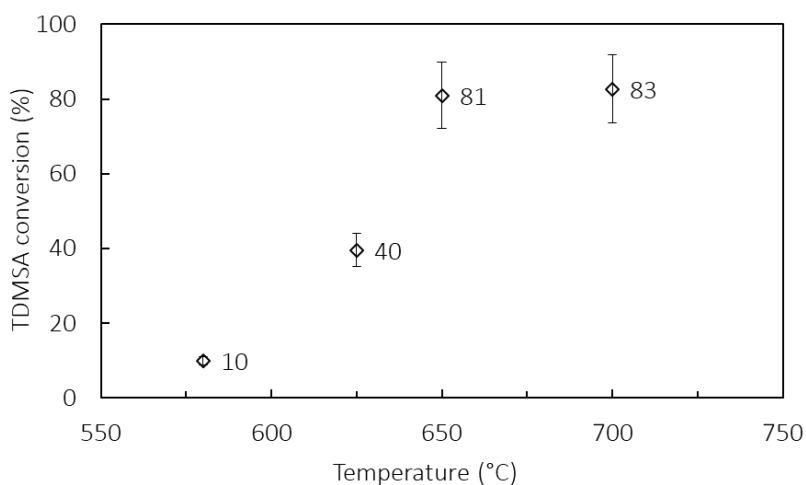

Fig. IV.18. TDMSA conversion as a function of the SPT.

As shown in Fig. IV.18, only 10 % of the available TDMSA is decomposed at 580°C. Increasing the temperature to 650°C increases the precursor decomposition to 81 %, illustrating the thermal dependency of this process. However, further increase of the temperature up to 700°C does not significantly influence the TDMSA conversion, increasing it only slightly from 81 to 83 %. A potential explanation could be the recombination of the produced radical species into TDMSA. Regardless, the results illustrate

the high temperatures at which the thermal decomposition of TDMSA can be activated and explain the very low DR noted for temperatures below 580°C that were discussed in section IV.1.

The decomposition by-products identified by GC-MS for each SPT are listed in Table IV.5, along with their enumeration, semi-developed formula, abbreviation and GC retention time. A first observation is that all by-products result from the previously mentioned Si_INT and N_INT building blocks. Additionally, it is noted that some of them contain one additional H atom or –CH$_3$ group, which are not encountered in the starting TDMSA molecule or in the two primary Si_INT and N_INT intermediates. For example, compound TMDSz *(7)* is the result of the addition of a H atom to N_INT. Similarly, the identified trimethylsilanol *(4)* is the result of a reaction between Si_INT, a –CH$_3$ group and O$_2$.

Thus, it can be concluded that all three TDMSA decomposition reactions proposed previously are taking place in the reactor (Reaction IV.1 to 3), albeit with different reaction rates. This also means that the various radical species produced through these reactions are indeed present in the gas phase at some point, but are not trapped by POBN and observed by ESR due to their participation in subsequent reactions. Moreover, since compounds with additional H atoms and –CH$_3$ groups are identified for all of the tested temperatures, it is difficult to discern which decomposition pathway takes place under which conditions, or which has the higher reaction rate.

Another interesting point is that compounds containing oxygen are identified. It is recalled that no O$_2$ was added in the inlet gas composition for these decomposition experiments. It is speculated that the O$_2$ originated either from a small leak, or from incompletely desorbed water on the solid surfaces. Another possibility could be the purity of the TDMSA precursor, which is fairly low (95 %). Upon closer inspection, it is observed that compounds dimethylsilanol *(1)*, trimethylsilanol *(4)* and HMTSo *(11)* are systematically probed for all decomposition temperatures. This indicates that they can be produced even under very low amounts of O$_2$ and that a temperature of 580°C is already sufficient for their formation.

Compounds TMDSo *(3)* and tetramethyldisiloxan-1-ol *(9)* are identified only at 580°C. Compared to the previously mentioned by-products, tetramethyldisiloxan-1-ol *(9)* contains two atoms of oxygen. It is assumed that at higher temperatures, the small quantity of oxygen in the gas phase has already reacted to produce by-products containing one O atom, leaving insufficient quantity for the production of TMDSo *(3)* and tetramethyldisiloxan-1-ol *(9)*. Following this logic, it could also be proposed that dimethylsilanol *(1)*, trimethylsilanol *(4)* and HMTSo *(11)* require a lower energy of formation (*Δ*$_f$) compared to the TMDSo *(3)* and tetramethyldisiloxan-1-ol *(9)* compounds.

Table IV.5. By-products identified by GC-MS after TDMSA decomposition at various temperatures.

	GC-MS by-product information			Decomposition temperature (°C)			
No#	Formula	Abbreviation	Retention time (min)	580	625	650	700
0	H$_2$O	-		-	-	-	-
1		-	2.03-2.16	✓	✓	✓	✓
2		MeOTMS		-	-	-	-
3		TMDSo	2.50	✓	-	-	-
4		-	2.46-2.50	✓	✓	✓	✓
5		-		-	-	-	-
6		PMDSo		-	-	-	-
7		TMDSz	4.80-4.81	-	✓	✓	✓
8		PMDSz	6.58-6.61	-	-	✓	✓
9		-	7.67	✓	-	-	-
10		HMDSz	9.72-9.76	-	-	✓	✓
11		HMTSo	10.36-10.44	✓	✓	✓	✓
12		HMCTSo		-	-	-	-
13		-		-	-	-	-
14		TDMSA	12.40	✓	✓	✓	✓
15		-		-	-	-	-

Nitrogen containing by-products such as disilazanes and silanamines are also detected. More specifically, TMDSz *(7)*, PMDSz *(8)* and HMDSz *(10)* are probed at 650°C and 700°C. At 625°C, only TMDSz *(7)* is present, while no nitrogen-containing by-products are found at 580°C. This correlates well with the absence of nitrogen in films produced at local temperatures below 600°C, as was presented in Fig. IV.3 to 7. The formation of compounds *(8)* and *(10)* only at higher temperatures is explained by their molecular structures. Both compounds contain –SiMe$_3$ moieties, which require more energy and additional reaction steps to be formed from the precursor and its intermediates. Therefore, it is proposed that the sequence of formation based on the amount of required energy is TMDSz *(7)*< PMDSz *(8)* < HMDSz *(10)*, with additional –CH$_3$ groups translating into higher energy requirements. Lastly, inspecting the results also reveals that oxygen-containing compounds are formed much easier than the nitrogen-containing ones.

The above gas-phase results are coherent with the solid-phase ones and explain well why deposition from TDMSA leads first to an oxygen rich material, which is progressively enriched in nitrogen with the increase of the local temperature (Fig. IV.3 to 7).

IV.2.2.1.3. *Compounds identified for the TDMSA-O$_2$ chemistry*

Runs utilizing TDMSA and O$_2$ in the inlet gas composition are analyzed by GC-MS in order to study the impact of the O$_2$ flow rate and the temperature on the formation of the various by-products. The compounds identified for these experiments are listed in Table IV.6. First, three by-products containing oxygen, namely dimethylsilanol *(1)*, trimethylsilanol *(4)* and HMTSo *(11)*, are identified for 0 sccm O$_2$. This could again be the result of a small leak or H$_2$O desorption from solid surfaces. Other by-products identified for 0 sccm O$_2$ are nitrogen-containing compounds TMDSz *(7)*, PMDSz *(8)*, and HMDSz *(10)*, for which the N_INT intermediate serves as the building block. These results were discussed previously for Table IV.5. Naturally, low O$_2$ concentration in the gas phase translates to lower oxidation of the Si–C or Si–N bonds of N_INT. As such, N_INT can participate in the formation of *(7)*, *(8)* and *(10)*. The presence of these compounds, which contain –N–SiMe$_2$ and/or –N–SiMe$_3$ moieties, in the gas phase explains well the higher nitrogen and carbon content of the films at 0 or 0.3 sccm O$_2$.

At 0.3 sccm O$_2$, additional oxygen-containing compounds MeOTMS *(2)* and TMDSo *(3)* are produced. It is proposed that the energy required for their formation is higher than that of products *(1)* and *(11)*. As a result, when O$_2$ concentration is low, only *(1)* and *(11)* are formed, while *(2)* and *(3)* appear only after sufficient oxygen is present in the gas phase, to cover for the production of all oxygen-containing by-products. Interestingly, upon addition of 0.3 sccm O$_2$, trimethylsilanol *(4)* is not detected. It is possible that it is still present, but its concentration is too low to be probed, potentially due to its participation in other O$_2$-activated homogeneous and/or heterogeneous reactions.

Higher concentrations of oxygen in the gas phase lead to the identification of additional compounds. More specifically, for 0.6 sccm, trimethylsilanol *(4)* is probed once more, in addition to dimethylsilanediol *(5)*, PMDSo *(6)*, tetramethyldisiloxan-1-ol *(9)* and HMCTSo *(12)*. By-products *(5)*, *(9)* and *(12)* contain more than one oxygen atom in their structure, which explains well why they are produced only beyond a specific concentration of O$_2$ in the gas phase. Moreover, two new silanamine compounds, N-(dimethylsilyl)-1-(methoxy)-1,1-dimethylsilanamine *(13)* and N-(dimethylsilyl)-1-[(dimethylsilyl)oxy]-1,1-dimethylsilanamine *(15)*, are detected at 0.6 sccm O$_2$, containing a N–Si–O sequence.

Further increase of the oxygen in the gas phase composition has multiple effects. At 1.2 sccm O$_2$, the disappearance of TMDSo *(3)*, dimethylsilanediol *(5)*, PMDSo *(6)* and tetramethyldisiloxan-1-ol *(9)* is observed. It is proposed that the higher concentration of O$_2$ results in a cascade of reactions, which eventually lead to the production of molecules with longer siloxane chains, such as HMTSo *(11)* and HMCTSo *(12)*. Regarding the nitrogen-containing by-products, the silazanes TMDSz *(7)* and PMDSz *(8)* are also not encountered in the gas phase. An explanation similar to the one given previously for HMDSz *(10)* is proposed: N_INT, the common building block of *(7)*, *(8)* and *(10)*, reacts readily with oxygen and leads to the production of the silanamine derivative *(13)*, reducing its available concentration for the formation of *(7)* or *(8)*. This confirms once more that the silanamine derivative *(13)* has a lower energy requirement for its formation compared to TMDSz *(7)*, PMDSz *(8)*, or HMDSz *(10)*. On a related note, it is pointed out that the second silanamine derivative *(15)* is not probed anymore for 1.2 sccm O$_2$, despite it being very similar to *(13)*. It is noted that *(15)* seems to originate from a reaction path involving N_INT, O$_2$ and Si_INT. Both compounds *(13)* and *(15)* are present for 0.6 sccm O$_2$, therefore O$_2$ cannot be the limiting reactant at 1.2 sccm. It is therefore speculated that at 1.2 sccm O$_2$, N_INT and/or Si_INT have reacted in the gas phase towards the production of other molecules, and that their concentration is decreased to a point where they become rate-limiting species for the production of *(15)*. It is difficult to conclude which one of the two intermediates, N_INT or Si_INT is the rate-limiting one. The presence of *(13)* at 1.2 sccm O$_2$ also indicates that it has lower energy requirements for formation compared to *(15)*. This is confirmed by replication of the experiment utilizing 0.6 sccm O$_2$ at 625°C instead of 650°C. Inspection of the last column of Table IV.6 reveals that the silanamine derivative *(13)* is detected at both 625°C and 650°C, while *(15)* is only present at 650°C. In general, the low number of nitrogen-containing by-products for an inlet flow of 1.2 sccm O$_2$ reflects well the production of nitrogen-poor films, with a more pronounced oxide character as was revealed by FT-IR (Fig. IV.11).

Ultimately, consideration of all the results listed in Table IV.6 leads to a proposed sequence of compounds, starting from those requiring lower (left) and moving towards higher energies for formation:

(1), *(4)* < *(9)* ≈ *(2)*, *(3)* ≈ *(12)*, *(13)* ≈ *(11)* < *(5)*, *(6)* < *(7)*, *(8)* < *(10)* ≈ *(15)*
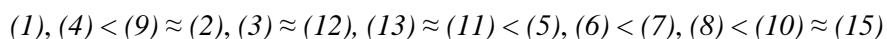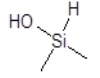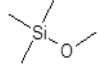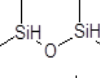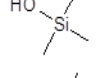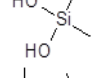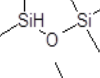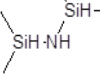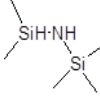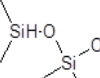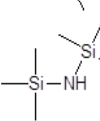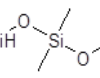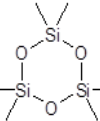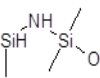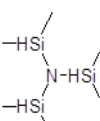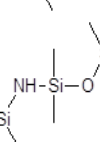
Table IV.6. Identified GC-MS by-products of the TDMSA-O$_2$ chemistry, for varying O$_2$ flow rates.

	GC-MS by-product information			O$_2$ flow rate (sccm)				T (°C)
No#	Formula	Abbreviation	Retention time (min)	0	0.3	0.6	1.2	625°C
1	*(structure)*	-	2.03-2.15	✓	✓	✓	✓	✓
2	*(structure)*	MeOTMS	2.27-2.35	-	✓	✓	✓	-
3	*(structure)*	TMDSo	2.44	-	✓	✓	-	-
4	*(structure)*	-	2.42-2.48	✓	-	✓	✓	✓
5	*(structure)*	-		-	-	✓	-	-
6	*(structure)*	PMDSo	2.51	-	-	✓	-	-
7	*(structure)*	TMDSz	4.80-4.81	✓	✓	✓	-	-
8	*(structure)*	PMDSz	4.28-6.58	✓	✓	✓	-	-
9	*(structure)*	-	7.71-7.74	-	-	✓	-	✓
10	*(structure)*	HMDSz	9.72-9.76	✓	✓	-	-	-
11	*(structure)*	HMTSo	10.27-10.63	✓	✓	✓	✓	-
12	*(structure)*	HMCTSo	11.22-11.42	-	-	✓	✓	✓
13	*(structure)*	-	8.39-11.80	-	-	✓	✓	✓
14	*(structure)*	TDMSA	12.40	✓	✓	✓	✓	✓
15	*(structure)*	-	11.40	-	-	✓	-	-

The presence of TDMSA is confirmed for all experiments (Table IV.6). Table IV.7 presents the conversion percent of TDMSA at the exit of the reaction chamber. The TDMSA conversion at 650°C averages 82.5 % and appears to be independent from gas-phase composition, for the tested range of O_2 flow rate (0-1.2 sccm). This compares favorably to the proposed TDMSA decomposition reactions (Reaction IV.1 to 3), in which O_2 does not participate as a reactant. It could be proposed that the temperature seems to be the only parameter to impact the TDMSA conversion rate. However, an interesting behavior is observed at lower SPT. It is recalled that at 625°C and in absence of O_2, the thermal decomposition of TMDSA resulted in a conversion of 40 % (Fig. IV.18). However, upon addition of 0.6 sccm O_2 in the inlet gas composition (TD14), the conversion increases to 59 %.

Table IV.7. TDMSA conversion at the exhaust for each experiment from the TDMSA-O_2 chemistry.

Run	SPT= 650°C				SPT= 625°C	
	TD9	TD11	TD7	TD12	Fig. IV.18	TD14
O_2 flow rate (sccm)	0	0.3	0.6	1.2	0	0.6
TDMSA conversion (%)	81	86	81	82	40	59

On one hand, both conversion at SPT 625°C are lower than the ones noted at 650°C, which is coherent with the lower deposition rates observed at SPT 625°C (Fig. IV.7a). On the other hand, the above results indicate that at temperatures lower than 650°C, the utilization of an oxidizing atmosphere can lead to a higher conversion of TDMSA. Globally, fewer by-products are detected in the gas phase for SPT 625°C (Table IV.6), potentially since the majority of the compounds require higher energies to be formed. Therefore, it can be speculated that this leaves a proportionally higher quantity of O_2 in the gas phase, available to react with TDMSA. On the contrary, at higher SPT, TDMSA has decomposed significantly into the various intermediates and the supplied energy is sufficient for them to react with O_2. The suspected participation of oxygen in the precursor conversion at lower temperatures potentially hints at a different reaction pathway compared to the one followed at 650°C. This information is kept in mind for later.

IV.2.2.2.   NMR analysis

Fig. IV.19a presents exemplary results of the 1H NMR analysis of the gas effluent of run TD6. At a first glance, the DMSO-d_6 solvent is detected, along with water. The presence of water is not surprising,

given that the silanols detected by GC-MS in the gas phase can lead to the production of siloxanes and water through condensation reactions [296]. Beyond that however, further analysis is more complex and difficult due to the variety and multitude of gaseous products. Despite that, it is noted that the 1H NMR spectra systematically show two main zones: one encountered around 4.60-4.72 ppm, associated with the presence of Si–H fragments (Fig. IV.19b), and the other at approximately -0.01-0.22 ppm corresponding to Si–CH$_3$ moieties (Fig. IV.19c). In the Si–CH$_3$ zone, singlets are assigned to a trimethyl substituent. Doublets on the other hand indicate a H–Si(CH$_3$)$_2$ sequence due to the presence of the J^3_{HH} coupling constant between both types of H atoms.
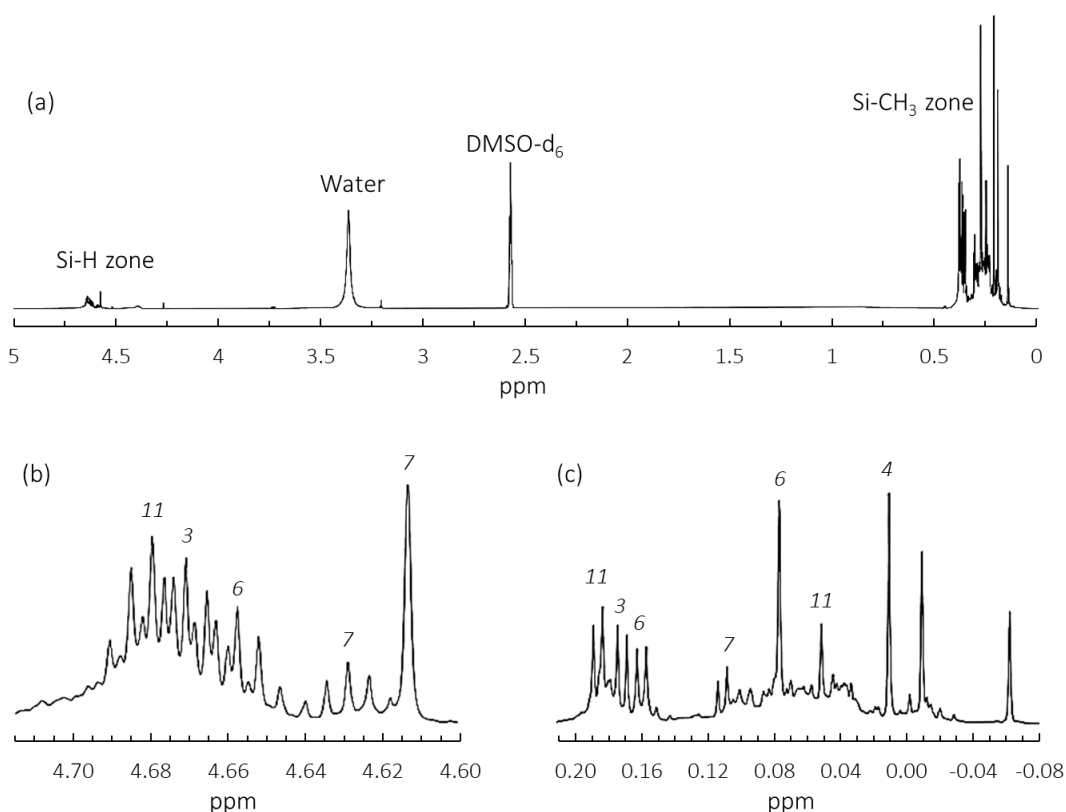
Fig. IV.19. Typical 1H NMR spectrum (a), with zoom in the 4.60-4.72 ppm (b) and -0.01-0.22 ppm (c) range, recorded at 500 MHz in DMSo-d$_6$.

Through utilization of the above, it is possible to confirm numerous compounds that have been observed previously by GC-MS. More specifically, compounds *(3)*, *(4)*, *(6)*, *(7)* and *(11)* are confirmed. Given the multiple by-products identified by GC-MS, other by-compounds are also present in the NMR spectra, however their identification is difficult since their respective peaks are obscured underneath others.

In the present sub-section, an apparent deposition mechanism is proposed based on all previously discussed gas phase and solid phase results, alongside parallel consideration of the literature. For the gas phase, the proposed starting step concerns the homolytic dissociation of the Si–N bond through Reaction IV.1 towards the production of Si_INT and N_INT. Moreover, the presence of trimethyl-containing compounds *(4)*, *(6)* and *(10)*, among others, indicates a supplementary Si–CH$_3$ bond dissociation through Reaction IV.3. Similarly, compounds *(7)* and *(15)* possess one additional H atom resulting potentially from a Si–H bond homolytic cleaving through Reaction IV.2. As a result, we propose that Reaction IV.1 is the primary pathway, with Reaction IV.2 and 3 also taking place in parallel, albeit at lower rates.

With Si_INT, N_INT, H˙ and CH$_3$˙ resulting from the decomposition of TDMSA through Reactions IV.1 to 3, multiple other reactions can take place in the gas phase. Being under an oxidizing atmosphere, H˙ could form water after reaction with O$_2$. H$_2$O was indeed detected by NMR for all experiments. The produced water can then react with Si_INT to form compound *(1)* through Reaction IV.4:

$$\text{Si\_int} \quad + \quad \text{H}_2\text{O} \quad \longrightarrow \quad \text{SiH·OH} \quad + \quad \text{H}^\bullet \qquad \qquad \text{Reaction IV.4}$$
$$\text{1}$$
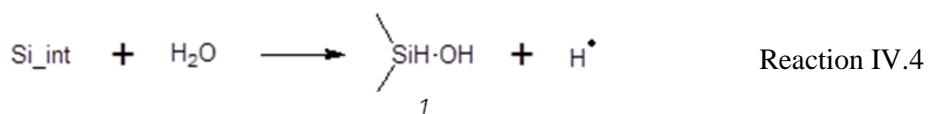
As was mentioned previously, the condensation of two silanol molecules, produced through Reaction IV.4, can then result in the formation of TMDSo *(3)* through Reaction IV.5.

$$2 \ \text{SiH·OH} \quad \longrightarrow \quad \text{SiH-O-SiH} \quad + \quad \text{H}_2\text{O} \qquad \qquad \text{Reaction IV.5}$$
$$\text{1} \qquad\qquad\qquad \text{3}$$
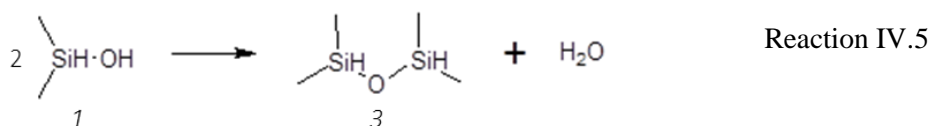
As suggested by Pola et al. [297], siloxane molecules can disproportionate into a silanone and a radical species when given enough energy. The produced species can then participate in the polymerization of other siloxane molecules. Following this proposition, the siloxane compound TMDSo *(3)* is assumed to disproportionate into a dimethylsilanone and the radical species Si_INT and H˙ through Reaction IV.6:

$$\text{SiH-O-SiH} \quad \longrightarrow \quad \text{Si=O} \quad + \quad \text{Si\_int} \quad + \quad \text{H}^\bullet \qquad \qquad \text{Reaction IV.6}$$
$$\text{3}$$
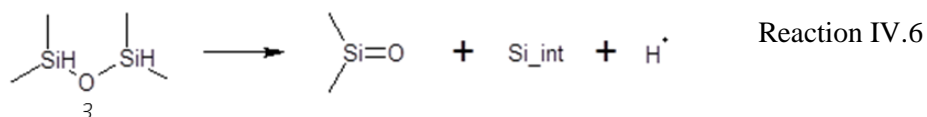
H˙ and Si_INT can also react together to form a dimethylsilane. This compound is not observed in the gas phase, however, given its high reactivity, its formation is not excluded. Moreover, being in an

oxidizing atmosphere, dimethylsilane is potentially quickly oxidized into silanol compounds such as the identified dimethylsilanol *(1)* and dimethylsilanediol *(5)*. The newly formed silanols can in turn participate once more in the formation of the siloxane compound TMDSo *(3)* through Reaction IV.5, resulting in a continuous cycle between Reaction IV.5 and 6. Moreover, the silanone formed through Reaction IV.6 can in turn be used to polymerize TMDSo *(3)* into HMTSo *(11)* through Reaction IV.7
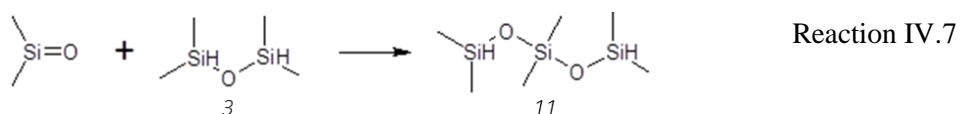
Reaction IV.7

It is recalled that TDMSA decomposition through Reaction IV.1 also yields N_INT. This radical compound can undergo a 1,2 H-shift yielding a new Si-centered radical [152] as illustrated in Reaction IV.8, or react with H˙ leading to the formation of TMDSz *(7)* (Reaction IV.9).

Reaction IV.8

Reaction IV.9
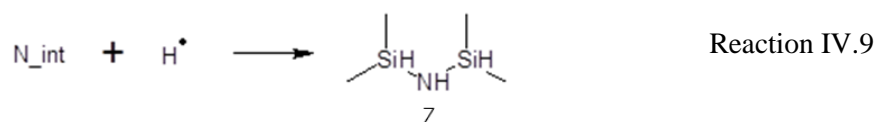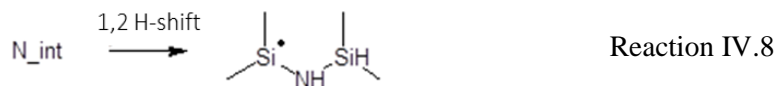
The formation of the new Si-centered radical after the 1,2 H-shift in the N_INT radical could in fact explain why only Si-centered species were identified by ESR. Moreover, it explains well the probing of N–H bonds by FT-IR. Additionally, following the same reasoning as for TMDSo *(3)*, we propose that TMDSz *(7)* can also disproportionate and lead to the production of a silanimine, a Si_INT and a H˙ radical, as shown in Reaction IV.10. The produced silanimine can in turn be used to polymerize siloxanes and drive the formation of bi-functional compounds with a N–Si–O sequence, such as the silanamine derivative *(15)*, through Reaction IV.11.

Reaction IV.10
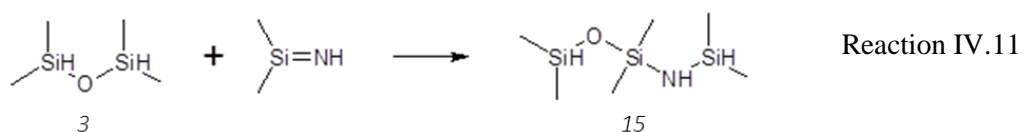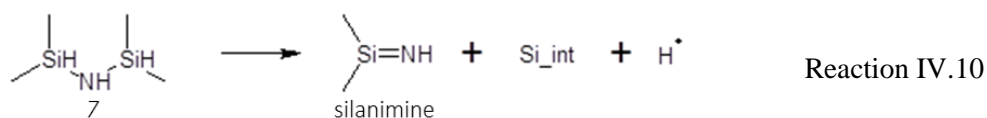
Reaction IV.11

The produced stable by-products and radical intermediate species in the gas phase naturally influence the film formation on the solid phase, through their participation in heterogeneous reactions. Firstly, it is noted that the Si_INT intermediate is present in large concentrations in the gas phase, formed from Reaction IV.1, 6 and 10. It is proposed that Si_INT is able to form a silica film through Reaction IV.12 and 13 as follows: first, Si_INT reacts with the silanol-terminated surface sites of the Si-substrate to form a siloxane sequence (Reaction IV.12). Following that, the formed siloxane sequence can then be oxidized by the O$_2$ of the gas phase, before reacting with the geminal silanol on the Si-substrate (Reaction IV.13). It is noted that both Reaction IV.12 and 13 involve the production of H$_2$O.

Reaction IV.12
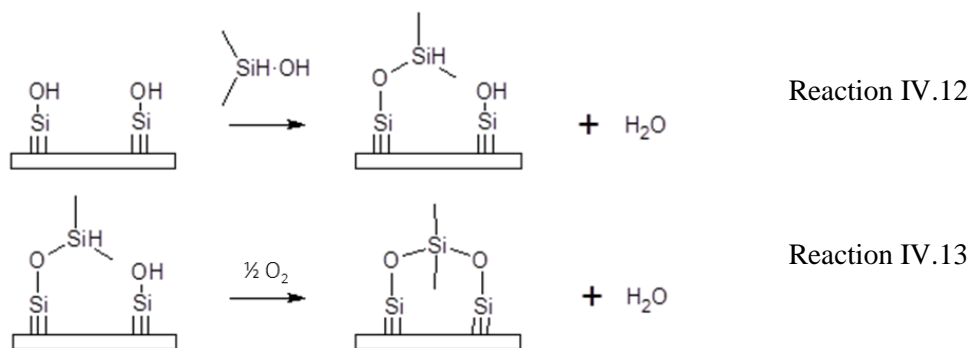
Reaction IV.13

The various identified siloxane compounds (*(3)*, *(6)*, *(9)* and *(11)*) can all participate in film formation through Reaction IV.12 and 13. In contrast, only few nitrogen-containing compounds are identified (*(13)* and *(15)*), translating into lower N incorporation in comparison to O, which is well reflected by the solid-phase results of section IV.1. Reaction IV.14 proposes a general mechanism for the formation of SiO$_x$ or SiO$_x$N$_y$ film from compounds with an O-Si-X sequence. In cases where X=O, the reacting compound is trisiloxane *(11)* leading to SiO$_x$ deposition. If X=NH the reacting compound is the silanamine derivative *(15)*, leading to SiO$_x$N$_y$ production. The adsorption and oxidation mechanism of these molecules onto the Si-substrate is similar to Reaction IV.12 and 13. In the case of SiO$_x$N$_y$ formation, the silanamine *(15)* reacts with an OH terminated surface site after desorption (Reaction IV.14). The formed O–Si bond acts as the driving force of the deposition mechanism.

Reaction IV.14
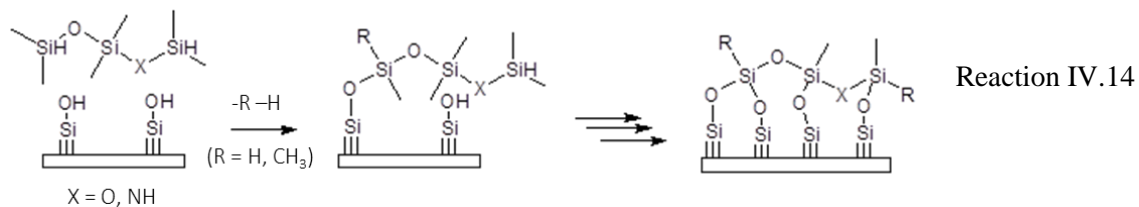
Given the numerous formed gaseous by-products, the number of reactions that would be required to describe their formation, as well as all potential solid phase reactions they could be participating in,

would be very large. Moreover, if the process were to be studied through simulation, the implementation of a large number of homogeneous and heterogeneous reactions would require high computation times. As such, the following section uses Reaction IV.1 to 14 as the basis for the development of a simplified chemical model. Its implementation in the simulation environment of FLUENT® is executed with the aim to replicate the deposition process by utilization of a small, though representative, number of apparent chemical reactions.

IV.3. Development of an apparent chemical model for the deposition of SiO_xN_γ films from TDMSA-O_2

The development of the apparent mechanism is based on the parallel consideration of both gas phase and solid phase results. More specifically, average-per-sample ellipsometry and local IBA results are used for the definition of solid phase reactions and their respective kinetics, while GC-MS, NMR and ESR results are used for the definition of the homogeneous reactions, the produced species and intermediates in the gas phase.

As noted in Chapter I, no apparent chemical models and CFD calculations for the SiO_xN_y deposition have been reported in the literature so far, even more so from a silanamine precursor or in absence of NH_3. Therefore, the apparent model has to be built from scratch. The strategy behind the development of this novel chemical model follows the idea of starting form a basic system and slowly enriching it. As a result, the initial kinetic constants calculated for the various reactions progressively undergo further refinements whenever the chemical model is enriched with the addition of new reactions, until a satisfactory agreement with the experimental results is reached. A compromise has to be found between the complexity of the kinetic model, the computational load of the numerical simulations and the model accuracy.

With the above in mind, the chemical model is initially described by one volumetric reaction, referred to as V1, corresponding to the decomposition reaction of TDMSA. Alongside it, heterogeneous reactions are introduced, accounting for film deposition. It is recalled that the produced material is a SiO_xN_y film containing a non-negligible amount of carbon. An ambitious attempt during the development process of the deposition mechanism is to not only simulate local DR values, but also the local composition in N and C. Fig. IV.6 and 7 illustrated that the C and N incorporation evolves along the length of the reactor, impacted by the local temperature and gas phase composition. Thus, it would be incorrect to define film formation through one single surface reaction, because this would translate into a constant film composition.

In that case, the only variable would be the film thickness. Therefore, at least two surface reactions are required: one leading to the formation of silicon oxide, and one to the formation of silicon nitride. Obviously, the deposited material is a homogeneous, amorphous SiO$_x$N$_y$ as revealed by HRTEM analysis (Appendix 6), not the conglomeration of SiO$_2$ and Si$_3$N$_4$. Despite that, the definition of separate, apparent, surface reactions for each material allows for the independent tweaking of their respective deposition rates, which in turn influences the resulting film composition. Ellipsometry results are used extensively for the definition of these solid-phase reactions and their respective kinetic constants. It is recalled that the applied ellipsometry model considers the material as a homogeneous mixture of three components, namely SiO$_2$, Si$_3$N$_4$ and amorphous carbon. Moreover, it provides local information on the volumetric fraction of each component, along with the total film thickness. Therefore, multiplying the respective volumetric fractions with the total film thickness and dividing by the deposition duration can give information on the individual SiO$_2$ and Si$_3$N$_4$ DR. It is noted that hydrogen is also incorporated in the films, but given the limited number of IBA samples and the inability of ellipsometry to provide at.% H values, its presence is not considered.

For each step, the calculated results are compared to the experimental ones. Deviations from the experimental data are discussed with the aim of proposing additional reactions that help better reproduce the experimental DR and composition profiles. New reactions are then formulated after consideration of the GC-MS results, justifying their introduction in the chemical model. It is recalled that up to 15 species were identified by GC-MS. Considering all of them would be time consuming. For simplicity, the identified species are first categorized into families (silanols, siloxanes, silanamines, etc.) and their implementation is done in a stepwise manner and only if it appears that the chemical model reaches a point that requires further elaboration. Quantitative results for gaseous compounds apart from TDMSA are not available. Therefore, the identified by-products can provide only qualitative information. The initial kinetic constants for each new reaction that is added, as well as subsequent refinements, are calculated through a combination of mass balance equations and manual fitting, by utilizing DR results from ellipsometry and species concentrations provided by FLUENT®. Part of the following work was carried out in collaboration with Tryfon Tsiros from the National Technical University of Athens (NTUA), supervised by Hugues Vergnes and Brigitte Caussat, in the frame of his Diploma thesis [298].

In its final version, the model involves a total of 12 species and 8 chemical reactions. The physical properties and Lennard Jones (L-J) parameters of the species are listed in Appendix 7. Those of O$_2$, N$_2$, CH$_4$ and H$_2$O are taken from the FLUENT® database. The CHEMKIN database is consulted for those of CH$_3$OH [239]. Due to lack of concrete values in the literature, the L-J parameters of the remaining species are assumed equal to those of molecules with similar chemical structure. The L-J parameters of silanone and the N_INT2 intermediate are set equal to silanol (σ = 5.25 Å and ε/k = 522.7 K) [239]. The L-J

parameters of TDMSA and its intermediates are set equal to TEOS ($\sigma = 7.03$ Å and $\varepsilon/k = 78.6$ K). Lastly, those of the siloxane and silanamine by-products are set equal to octamethylcyclotetrasiloxane ($\sigma = 3.54$ Å and $\varepsilon/k = 1182.43$ K) taken from the literature [299].

IV.3.1. Definition of initial reactions: TDMSA decomposition and SiO_2 film formation

The decomposition reaction of TDMSA is considered as the driving reaction of the model. The Si_INT intermediate, i.e. Me$_2$HSi$^•$, was identified by ESR in section IV.2.1. Out of the previously proposed TDMSA decomposition pathways, only Reaction IV.1 leads to the production of Si_INT and is therefore the one considered. For the simulations, it will be referred to as the volumetric reaction V1, leading to the production of the two Si_INT and N_INT intermediates as follows:

$$TDMSA \rightarrow Si\_INT + N\_INT \qquad (V1)$$

Since the addition of O_2 does not influence TDMSA conversion at 650°C, V1 is defined with TDMSA as the sole reactant, and is considered to be independent from the presence of O_2. Following that, the conversion of TDMSA in Fig. IV.18 is considered for the calculation of the kinetic constant k_{VI} of V1. Since recombination of the intermediates towards the production of TDMSA is possible at 700°C, this point was excluded from the calculations. From the resulting Arrhenius plot, shown in Fig. IV.20a, an activation energy of $E_{a,VI} = 2.49 \cdot 10^2$ kJ.mol^{-1} and a pre-exponential factor of $A_{o,VI} = 1.68 \cdot 10^{14}$ s^{-1} are deduced. Following the decomposition of TDMSA through reaction V1, the produced radical intermediates Si_INT and N_INT are considered as the main reactants that participate in subsequent reactions. For the purpose of simulating the system in a simplified manner, initially the direct contribution of Si_INT and N_INT to the solid film is considered.

In a first version of the chemical model, two apparent surface reactions are considered, referred to as S1 and S2. They produce a SiO_2 and a Si_3N_4 material from Si_INT and N_INT, respectively, as follows:

$$Si\_INT + O_2 \rightarrow SiO_2 + by\text{-}products \qquad (S1)$$

$$4\ N\_INT \rightarrow Si_3N_4 + by\text{-}products \qquad (S2)$$
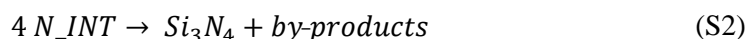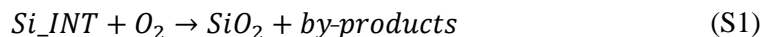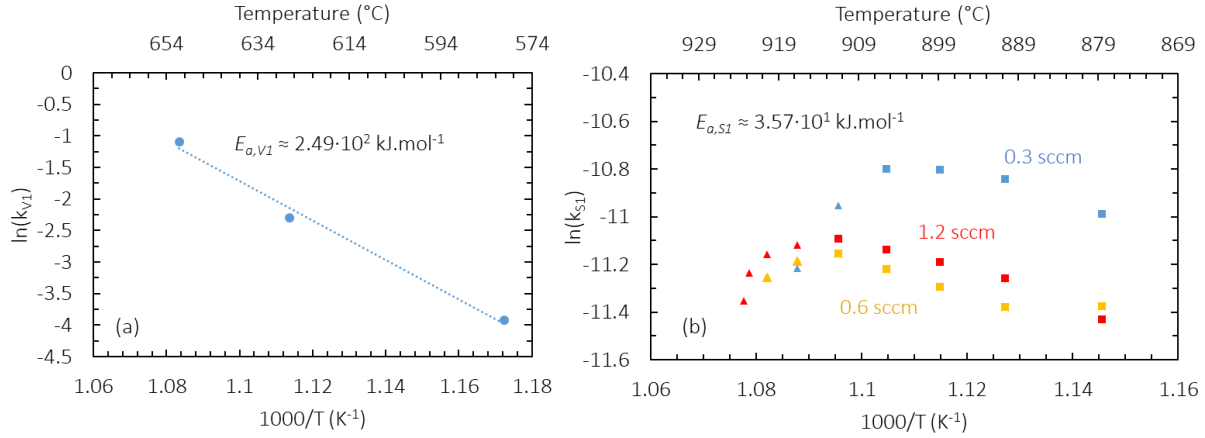
Fig. IV.20. Arrhenius plot for decomposition of TDMSA through V1, calculated from quantitative GC-MS analysis of TDMSA at the exhaust of the reactor (a). Arrhenius plot for SiO$_2$ production through S1, calculated for selected samples from runs using varying O$_2$ flow rates at SPT 650°C (b).

However, formulated like this, the two reactions do not account for the incorporation of C. Previous discussion on the ellipsometry and IBA results gave rise to the speculation that C and N are incorporated through the same intermediate species. Therefore, the volumetric fraction of the amorphous carbon calculated by ellipsometry is added to that of the Si$_3$N$_4$ component, in order to represent a carbonated Si$_3$N$_4$ "phase". The deposition of a nitride material that includes carbon is discussed in more detail later. Regarding the oxide material, the DR of the SiO$_2$ component for runs TD7, TD11 and TD12 are plotted in an Arrhenius expression as presented in Fig. IV.20b, based on the rate law of S1 ($S1 = k1[Si\_INT]^a[O_2]^b$). First order kinetics are considered initially. Concentrations are extracted from simulation of reaction V1 using FLUENT®. Only samples between 0.2 m and 0.4 m were considered (square symbols), since significant O$_2$ consumption is taking place beyond 0.4 m, as reflected in the decreasing DR values at higher temperatures (triangle symbols). From the slope, an initial activation energy of $E_{a,s1}= 3.57 \cdot 10^7$ J.kmol^{-1} and a pre-exponential factor $A_{o,S1}= 1.79 \cdot 10^{-3}$ s^{-1} are deduced.

After the definition of V1 and S1, representing the decomposition of TDMSA and the SiO$_2$ film formation respectively, both reactions are implemented into FLUENT®. The total mass flow rate and the mass fractions of all species at the inlet are fixed to the experimental values (Appendix 8). The resulting simulations are presented in Fig. IV.21 and are compared to the experimental results by ellipsometry.

Inspecting Fig. IV.21, the simulation manages to somewhat fit the experimental results from 0.2 to 0.37 m for the two highest O$_2$ flow rates. However, beyond 0.37 m the simulated DR profile overestimates the experimental values for all three O$_2$ flow rates. Given that the thermal profile remains constant in that

region (isothermal region: 0.36-0.5 m), the lower DRs measured experimentally are the result of decreasing concentrations of the film-forming reactants. For O_2 flow rates below 0.6 sccm, it is assumed that O_2 is the rate-limiting species. In a more oxygen-rich gas phase (1.2 sccm, Fig. IV.21), the rate-limiting species at the end of the reactor could be the Si_INT intermediate instead, but this does not exclude the effect of a potential O_2 deficit. As such, the introduction of at least one O_2 and Si_INT consuming reaction is proposed.
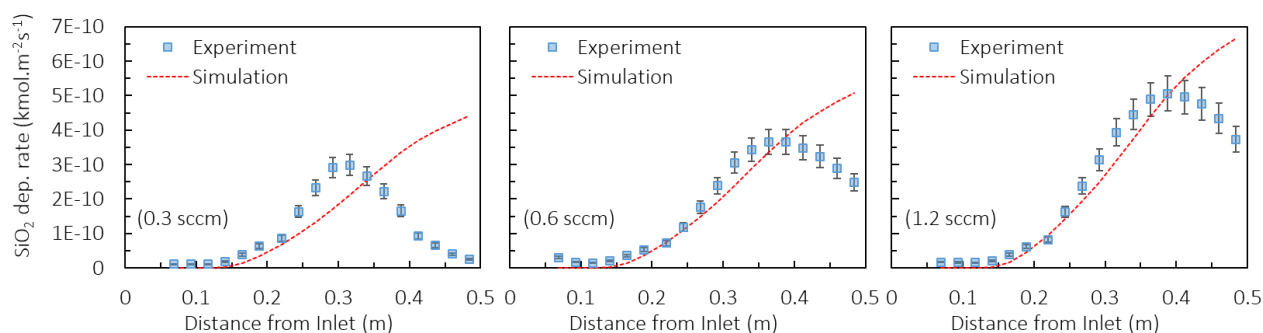
Fig. IV.21. Comparison of SiO_2 DR between simulations using S1 and V1 and experimental ellipsometry results, for varying O_2 flow rates at SPT 650°C (runs TD7, TD11, TD12).

The above proposal is justified when taking into account the multiple oxygen-containing by-products identified by GC-MS (Table IV.6), for which the Si_INT intermediate clearly acts as the building block. For simplicity however, the production of only one family of by-products is considered, accounting for multiple volumetric reactions in one single apparent reaction. This reaction is referred to as V2. Since the aim is to reduce the concentrations of O_2 and Si_INT in order to limit SiO_2 production, these two molecules are considered as the reactants in V2. Through this, Reaction IV.2, the production of water through H$^\bullet$ and O_2, and Reactions IV.4, 5, 6 and 7 are accounted for in one single reaction V2, defined as:

$$4\ Si\_INT + 2O_2 \rightarrow siloxane + by\text{-}products \qquad\qquad (V2)$$
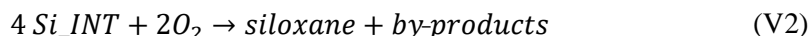
The siloxane compound HMTSo *(11)* is considered as the representative product of V2, with H_2O and silanone as the by-products. Since no quantitative results for HMTSo *(11)* are available, the kinetic constant k_{V2} of the volumetric reaction V2 is calculated through a reverse mass balance, by utilizing the overestimated difference between the simulated S1 and the experimental SiO_2 deposition in the 0.37-0.50 m region. An initial activation energy of $E_{a,V2}= 7.05\cdot10^1$ kJ.mol^{-1} is deduced for V2. The introduction of V2

also required slight re-adjustment of S1 kinetics. After these actions, the enriched chemical model is simulated once more, resulting in the profiles of Fig. IV.22.

Inspecting Fig. IV.22, it is observed that the general bell shape noted at 0.3 sccm O$_2$ is successfully reproduced through simulation, although it overestimates the experimental results. In comparison, the simulations do not fully replicate the DR profile for 0.6 sccm and completely underestimate the experimental results for 1.2 sccm O$_2$.

Plotting of the O$_2$ and Si_INT concentration profiles revealed that the Si_INT species has become the rate-limiting reactant for SiO$_2$ deposition at 1.2 sccm O$_2$, with its concentration decreasing to very low values beyond 0.3 m. This means that if an attempt were made to fit the DR profile for 0.3 sccm by increasing the rate of V2 or decreasing that of S1, it would result in an even more pronounced underestimation of the DR profiles at 0.6 and 1.2 sccm O$_2$. Various combinations of O$_2$ and Si_INT partial order exponents for V2 and S1 were attempted, but yielded unsatisfactory results. As such, it becomes clear that the present model is unable to reproduce the experimental data and requires the addition of further reactions, which will bring the simulated gas phase composition closer to the real one.
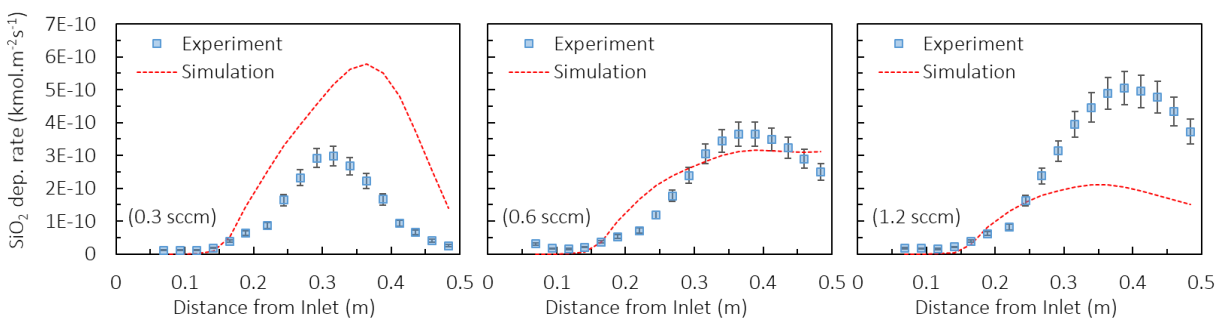
Fig. IV.22. Comparison of SiO$_2$ DR between simulations using S1, V1, and V2, and experimental ellipsometry results, for varying O$_2$ flow rates at SPT 650°C (runs TD7, TD11, TD12).

The low concentration of Si_INT in the gas phase needs to be addressed. An option would be to increase the rate of its production through V1, but this idea was abandoned since an increase of V1 would result in a higher TDMSA conversion, compared to the one measured experimentally through GC-MS in Table IV.7. Reduction of the rate of V2 is also not recommended, as it would translate into further overestimation of the DR for 0.3 sccm O$_2$. Therefore, it is proposed that, at the highest O$_2$ concentrations, the rate-limiting Si_INT species is produced through an additional reaction other than V1.

Looking back at the list of reactions proposed in section IV.2, Reactions IV.6 and IV.10 are highlighted, both leading to the production of a Si_INT molecule. They justify therefore the addition of a supplementary volumetric reaction that produces Si_INT. This reaction is referred to as V3 hereinafter. However, a choice must be made regarding which one of the two Si_INT-producing reactions, Reactions IV.6 or IV.10, shall be implemented. Before deciding however, the homogeneous and heterogeneous reactions eventually leading to the deposition of the carbonated Si_3N_4 phase are formulated first.

IV.3.2. Introduction of nitrogen-involving gas phase and solid phase reactions

In order to formulate representative, apparent, reactions for the deposition of a carbonated Si_3N_4 "phase", the C/N atomic ratio calculated by ellipsometry is considered initially, to assess if carbon and nitrogen are introduced through the same species.

Fig. IV.23 presents the evolution of the C/N ratio along the reaction chamber for runs TD7, TD11 and TD12. At 1.2 sccm O₂, the C/N ratio appears constant at around 2.9 from 0.35 to 0.5 m, indicating that potentially, a nitrogen-containing intermediate with three –CH₃ ligands is responsible for film formation. Between 0 and 0.35 m, the C/N atomic ratio is lower than 2.9 and presents an increasing trend. This could be potentially related to the higher local O₂ concentrations in that region, resulting in more efficient oxidation of the organic ligands of the intermediate. In the same zone, the C/N atomic ratio evolves similarly for 0.3 and 0.6 sccm O₂.
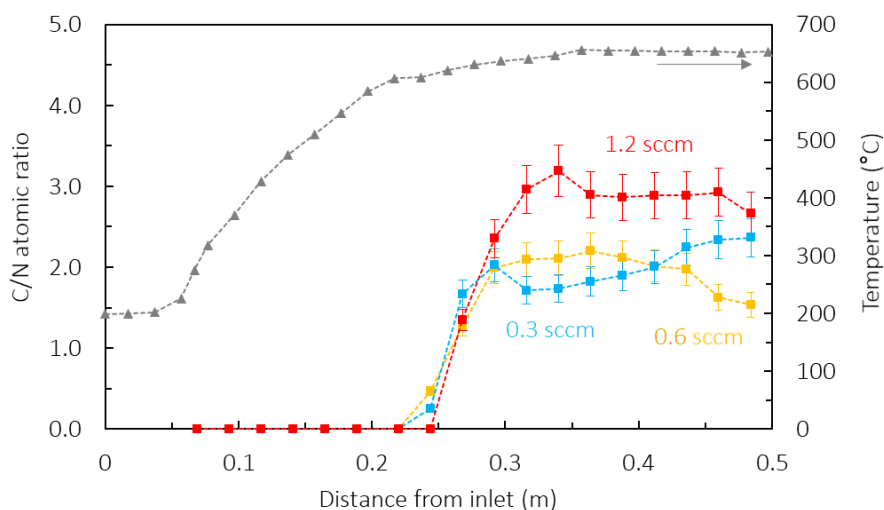
Fig. IV.23. Atomic C/N ratio for varying O₂ flow rates (runs TD7, TD11 and TD12) at SPT 650°C.

Interestingly, the average C/N values in the 0.35-0.5 m region are 2.1 and 1.9 for 0.3 and 0.6 sccm, respectively. Both are lower than the value noted at 1.2 sccm, something which is contrary to the proposal that higher O$_2$ flow leads to more efficient –CH$_3$ cleaving. This point will be addressed shortly. The general evolution of the C/N ratio could indicate two things: in a first scenario, the CH$_3$-cleaving step is taking place in the gas phase prior to deposition, meaning that the nitrogen-containing intermediate, N_INT, "loses" some of its methyl moieties before participating in film-forming reactions. In a second scenario, two nitrogen-containing intermediates, each containing a different number of carbon atoms, participate in film formation and result in varying incorporations of carbon. The problem with the first scenario is that it relies on O$_2$ to cleave the carbon of the N_INT. However, the higher C/N ratio at the highest O$_2$ flow rate (1.2 sccm) does not support this proposal. Therefore, the second scenario is considered, and two apparent surface reactions are assumed, S2 and S3, defined as follows:

$$4\,N\_INT + O_2 \; \rightarrow Si_3N_4 + \textit{by-products} \tag{S2}$$

$$4\,N\_INT \; \rightarrow carb\_Si_3N_4 + \textit{by-products} \tag{S3}$$
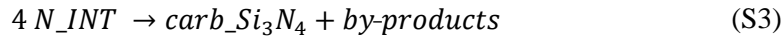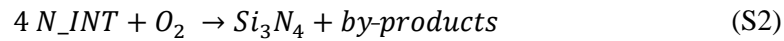
S2 results in the deposition of a nitride material with no carbon, while S3 leads to the deposition of a carbonated Si$_3$N$_4$ material. From Fig. IV.23, the C/N ratio for 1.2 sccm O$_2$ remains constant at 2.9. Therefore, a stoichiometry of Si$_3$N$_4$C$_{12}$ is assigned to the carbonated nitride material produced through S3. Reaction S3 is then considered as the primary reaction taking place under 1.2 sccm O$_2$. An initial activation energy of $E_{a,S3}= 1.97{\cdot}10^2$ kJ.mol^{-1} is deduced from the ellipsometry data of the total Si$_3$N$_4$ "phase" (i.e. Si$_3$N$_4$ + amorphous-C volumetric fractions) at 1.2 sccm O$_2$. Then, the difference in Si$_3$N$_4$ deposition noted between 1.2 and 0.3 sccm O$_2$ is used to extract an initial activation energy of $E_{a,S2}= 3.51{\cdot}10^1$ kJ.mol^{-1} for S2. The simulation of V1, V2, S1, S2 and S3 resulted in the DR profiles presented in Fig. IV.24a.

Comparing them to the total Si$_3$N$_4$ (i.e. Si$_3$N$_4$ + amorphous-C) experimental DR profiles by ellipsometry (Fig. IV.24) reveals that the simulations greatly miscalculate the global behavior. Ellipsometry indicates namely that the DR of the total nitride material decreases with increasing O$_2$ flow rates in the inlet supply. In contrast, the simulations show higher DRs under higher O$_2$ flow rates. This is logical, because S2 is formulated with O$_2$ participating as a reactant in the production of Si$_3$N$_4$. The simulation results make it therefore clear that O$_2$ should not participate in the surface reaction S2, and that the cleaving of –CH$_3$ groups of the N_INT species should instead preferably happen through a volumetric reaction involving N_INT and O$_2$.
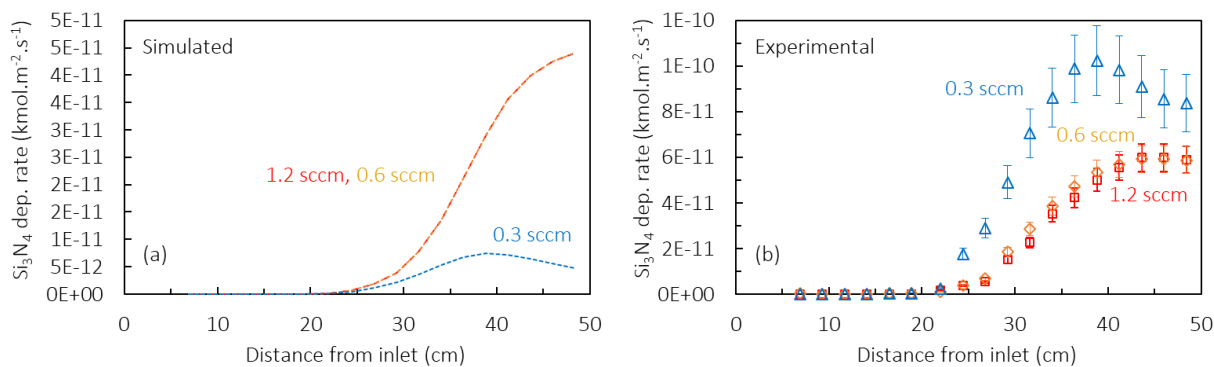
Fig. IV.24. Simulation of the total Si$_3$N$_4$ DR from S2 and S3 (runs TD7, TD11, TD12) (a). DRs for 0.6 and 1.2 sccm O$_2$ coincide. Experimental DR of the total Si$_3$N$_4$ phase provided by ellipsometry (b).

IV.3.3. Introduction of a –CH$_3$ cleaving and Si_INT producing reaction

So far, two main issues have been encountered. The first one involves the underestimation of SiO$_2$ deposition at higher O$_2$ flow rates, being the result of a deficit in Si_INT concentration in the gas phase. The second issue is that the cleaving of the methyl moieties of the N_INT intermediate should happen in the gas phase, instead of the solid phase. Previously, no decision was made on whether the first issue should be addressed through Reactions IV.6 or IV.10. Both lead to the production of a Si_INT molecule. However, only Reaction IV.10 involves N_INT, and by extent, the production of a nitrogen-containing intermediate with fewer carbon atoms. In light of these arguments, Reaction IV.10 is chosen, as it helps address both points at the same time. Thus, reaction V3 is defined as:

$$N\_INT + O_2 \rightarrow N\_INT2 + Si\_INT + by\text{-}products \qquad (V3)$$
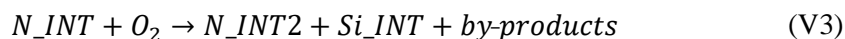
V3 leads to the production of a second nitrogen-containing intermediate N_INT2, containing less carbon atoms than the original N_INT species. The produced N_INT2 is defined as an intermediate from a family of molecules related, but not exclusive to, silanimines. Consequently, reactions S2 and S3 are reformulated, with the silanimine N_INT2 molecule being the one leading to carbonated film formation:

$$4\,N\_INT \rightarrow Si_3N_4 + by\text{-}products \qquad (S2)$$

$$4\,N\_INT2 \rightarrow carb\_Si_3N_4 + by\text{-}products \qquad (S3)$$
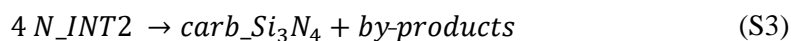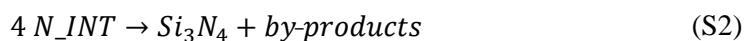
However, in that case, we would arrive at the same problem: higher concentrations of O$_2$ would translate into higher production of N_INT2 through V3, and therefore higher DRs of the nitride material through S3. For this reason, the introduction of an additional volumetric reaction is proposed, with the aim to consume quantities of the N_INT species and reduce its available concentration in the gas phase for higher O$_2$ flow rates. Following this logic, O$_2$ should be participating as a reactant in this new volumetric reaction, named V4, in order to compensate for the lower Si$_3$N$_4$ DRs at higher O$_2$ flow rates.

In order to define V4, the GC-MS results are revisited, with a focus on identifying by-products that contain a N–Si–O sequence. Two such compounds are detected from Table IV.6, namely the silanamine derivatives *(13)* and *(15)*, justifying the presence of a reaction between N_INT and O$_2$. This reaction is apparent and combines the involvement of the previously proposed Reactions IV.4, 5 8, 9, 10, 11, as well as the initial production of water through a reaction between H$^\bullet$ and O$_2$, after Reaction IV.2. As such, reaction V4 is formulated in a summarized manner as:

$$N\_INT + O_2 \rightarrow silanamine + by\text{-}products \qquad\qquad (V4)$$
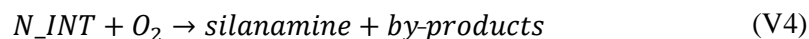
The silanamine derivative *(13)* is chosen to define the produced silanamine. It is assumed that *(13)* does not participate in the formation of Si$_3$N$_4$, since this would defeat the purpose of reaction V4. A schematic representation of all reactions proposed so far is presented in Fig. IV.25.
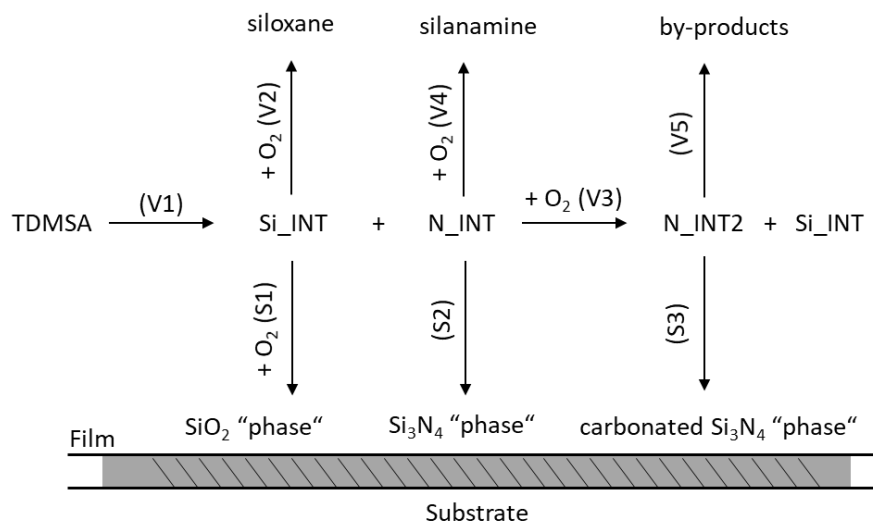
Fig. IV.25. Schematic representation of proposed volumetric and surface reactions for the deposition of a carbon-containing SiO$_x$N$_y$ material from the TDMSA-O$_2$ chemistry.

To summarize, reaction V1 represents the decomposition of TDMSA, in order to produce the two main building blocks, Si_INT and N_INT, which are encountered in all gaseous by-products. Reaction V2 serves for the consumption of O$_2$ and Si_INT to produce the family of siloxane by-products, and reduce the SiO$_2$ DR at the later parts of the reactor. Reaction V3 compensates for the Si_INT deficit by producing it under high O$_2$ concentrations, and simultaneously serves the production of a less-carbonated nitrogen-containing intermediate, N_INT2. V4 represents the consumption of N_INT through reaction with O$_2$ to produce the silanamine family of by-products, with the main aim to decrease the global available N_INT quantity in the gas phase at higher O$_2$ flow rates and replicate the reduced Si$_3$N$_4$ DRs for 0.6 and 1.2 sccm. It is noted that the underestimation of SiO$_2$ deposition at higher O$_2$ flows could be alternatively addressed through introduction of a surface reaction involving the siloxane species produced through V2, as was suggested in Reaction IV. 14. However, since V3 addresses two points at the same time, it was chosen instead. Reaction V5 shown in Fig. IV.25 is addressed later.

The present enrichment of the model and the involvement of O$_2$ in multiple reactions requires further refinement for the majority of the kinetic constants. After numerous iterations and use of mass balance calculations, an adjusted (but not final) version of the model is implemented in FLUENT®, the results of which are shown in Fig. IV.26.
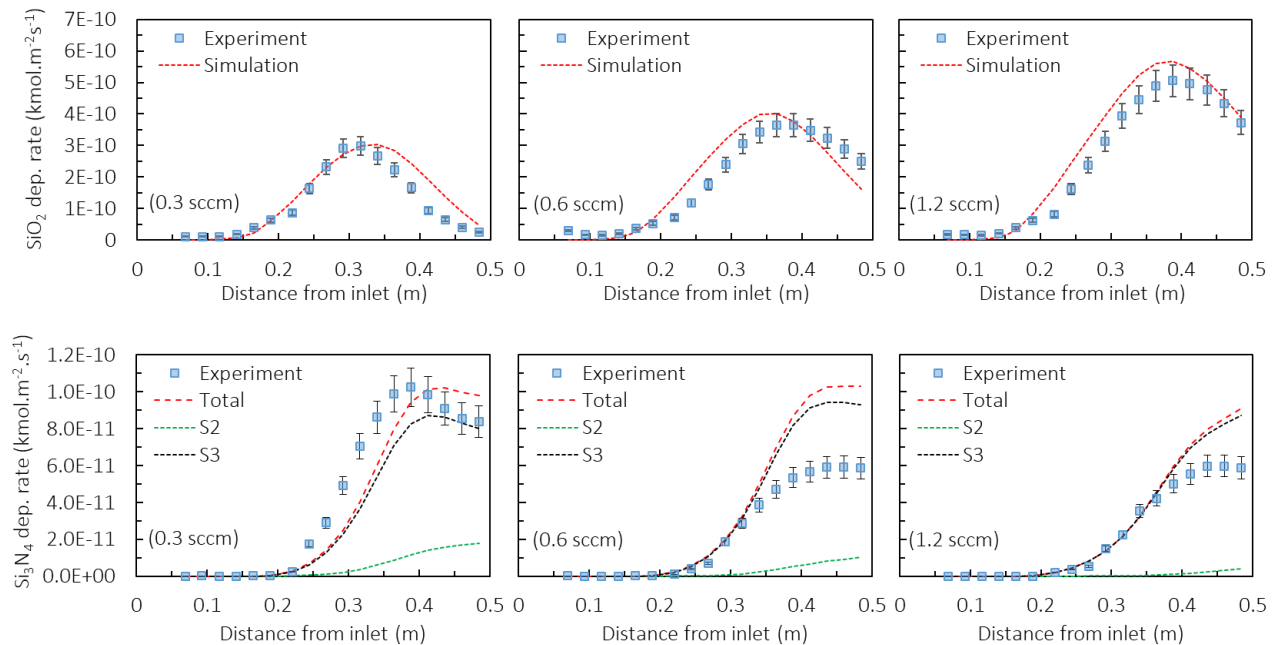
Fig. IV.26. Comparison of SiO$_2$ DR (top row) and Si$_3$N$_4$ DR (bottom row) between simulations using V1-V4, S1-S3 and experimental ellipsometry results, for varying O$_2$ flow rates at SPT 650°C (runs TD7, TD11, TD12).

After implementation of the enriched SiO$_x$N$_y$ model, a satisfactory agreement is reached for the SiO$_2$ DR profiles as presented in Fig. IV.26. The bell shape is reproduced successfully for all three experiments. Slight deviations exist, albeit at different regions, meaning that further refinement would require the adjustment of more than one reaction. Regarding the nitride phase, the total Si$_3$N$_4$ DR is underestimated between 0.2 and 0.4 m at 0.3 sccm O$_2$, while for 0.6 and 1.2 sccm O$_2$ an overestimation between 0.35 and 0.5 m is observed instead. It is obvious that the simple increase of S2 or S3 to fit the DR profile at 0.3 sccm O$_2$ would result in bigger discrepancies for the two other experiments. Similarly, a reduction of the S2 and S3 reaction rates could potentially result in a good agreement of the Si$_3$N$_4$ DR for high O$_2$ flow rates, but would also translate into further underestimation for 0.3 sccm O$_2$.

Fig. IV.27 examines the simulated incorporation of nitrogen and carbon in the films. Globally, the simulations have managed to reproduce the composition within the same order of magnitude. Individually examined, the curve of the C and N contents are reproduced for 0.3 sccm O$_2$, albeit underestimated. This underestimation stems from the lower simulated total Si$_3$N$_4$ deposition at 0.2-0.4 m. Between 0.4-0.5 m, a good agreement for the Si$_3$N$_4$ deposition is achieved, however the composition of C and N is still underestimated because of the overestimated SiO$_2$ deposition in that region.

Fig. IV.27. Comparison of nitrogen (top row) and carbon (bottom row) contents between simulations using V1-V4, S1-S3 and experimental ellipsometry results, for varying O$_2$ flow rates at SPT 650°C (runs TD7, TD11, TD12).

In the case of 0.6 sccm O_2, a mixed behavior is observed regarding the composition. Below 0.4 m, the simulated carbon and nitrogen contents are slightly underestimated, as the result of the overestimation in SiO_2 DR in that region. Beyond 0.4 m, the composition in C and N is overestimated as a result of the overestimation in total Si_3N_4 DR from S2 and S3. This is further accentuated by the slight underestimation of SiO_2 DR in that region. For 1.2 sccm O_2, the nitrogen and carbon contents approach a closer agreement with the experimental values, although they are slightly underestimated, because of the global overestimation of the SiO_2 DR.

The above results make it clear that a good agreement of the simulated DR profiles is important for the subsequent simulation of the composition. The definition of the carbonated Si_3N_4 stoichiometry also plays a role, as it affects the corresponding incorporation of N and C. Further refinements were attempted to fit the SiO_2 and Si_3N_4 DR profiles, either by adjusting the kinetic constants or the partial order exponents of the various species. Despite that, discrepancies continued to be present. This is expected, given the fact that all considered reactions are apparent and represent multiple others. Moreover, it is recalled that only a few of the gaseous by-products identified by GC-MS are accounted for in the model and potential supplementary deposition reactions by them are ignored.

For a final refinement, the addition of a fifth volumetric reaction is attempted. As illustrated in Fig. IV.26, the total Si_3N_4 deposition is overestimated for the highest O_2 flow rates. This overestimation is attributed to S3 and is the result of the increased production of the N_INT2 intermediate through reaction V3, when sufficient O_2 quantity is present in the gas phase. For that reason, a new volumetric reaction, V5, is added, with the aim to consume the N_INT2 intermediate at higher O_2 flow rates and help regulate the total Si_3N_4 deposition. It is noted that Reaction IV.11, proposed previously in section IV.2, involved the consumption of the silanimine intermediate to produce the identified silanamine compound *(15)*, which justifies the addition of V5. A similar reaction between the silanimine intermediate and a silanol, diol, or methoxysilane compound, for example *(1)*, *(2)*, *(4)* or *(5)*, can be conceptualized to produce the silanamine *(13)*. V5 can therefore represent any of the above. Naturally, the apparent reaction V5 would require the addition of an oxygen-containing species, such as a silanol, siloxane or O_2, as co-reactant. In order not to influence other reactions involving O_2 however, the N_INT2 intermediate was used as the sole reactant and V5 was formulated as:

$$N\_INT2 \rightarrow by\text{-}products \qquad\qquad (V5)$$

The results upon implementation of V5 into the chemical model are shown in Fig. IV.28. Inspecting Fig. IV.28, the addition of V5 did not affect the SiO_2 deposition, just as desired, and instead resulted only in changes for the Si_3N_4 DR profile. Consumption of the silanimine N_INT2 intermediate by V5 globally

decreased the deposition from S3. This translated in further underestimation of the total Si$_3$N$_4$ deposition for 0.3 sccm O$_2$, though the shape of the curve is close to the desired one. At 0.6 sccm O$_2$, the simulations approach the experimental data a bit closer, though a slight inconsistency in the shape of the Si$_3$N$_4$ deposition curve is noted beyond 0.35 m. The effect of V5 becomes clear here: its addition has managed to decrease the available concentration of the N_INT2 intermediate, decreasing as a result the Si$_3$N$_4$ production from S3. For 1.2 sccm O$_2$, even though V5 is once again consuming the silanimine intermediate, the higher concentration of O$_2$ in the gas phase compensates with continuous N_INT2 production through V3. As a result, V3 and V5 balance each other out, and help regulate S3. An excellent agreement is noted between the total calculated and experimental Si$_3$N$_4$ profiles for 1.2 sccm O$_2$.
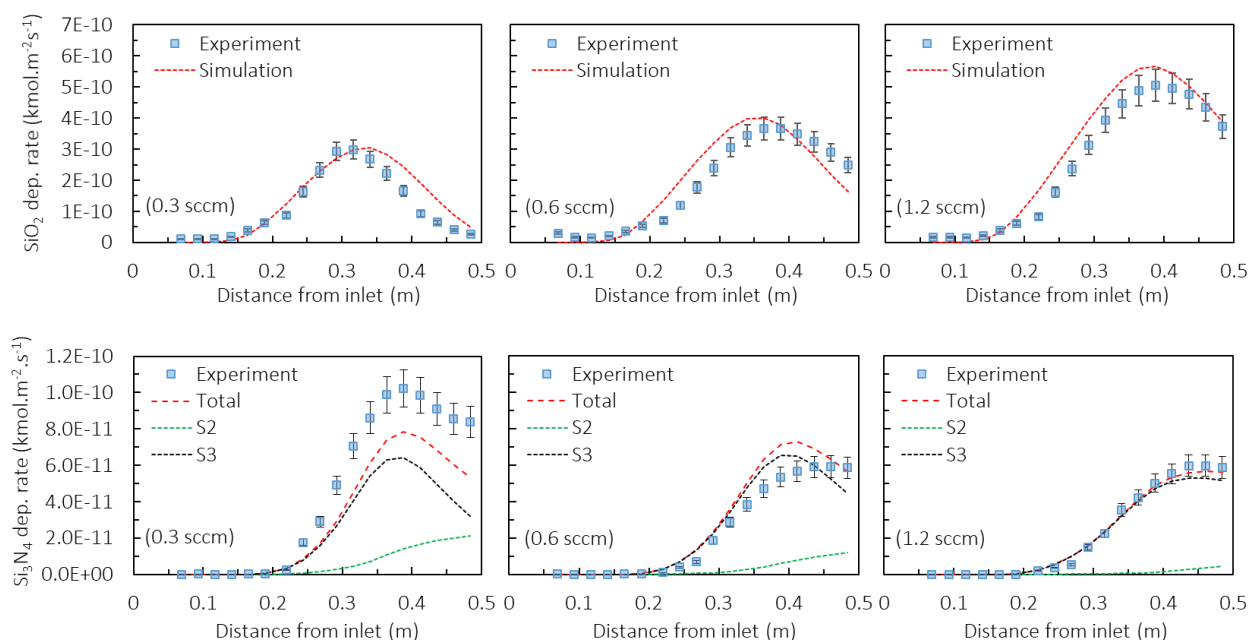
Fig. IV.28. Comparison of SiO$_2$ DR (top row) and Si$_3$N$_4$ DR (bottom row) between simulations using V1-V5, S1-S3 and experimental ellipsometry results, for varying O$_2$ flow rates at SPT 650°C (runs TD7, TD11, TD12).

The effects of the V5 addition on the composition are shown in Fig. IV.29. The reduction of rate of S3 through the consumption of the silanimine N_INT2 intermediate by reaction V5 resulted in a decrease of the C content for all three runs, which is visible through comparison between the carbon contents of Fig. IV.27 and Fig. IV.29. After introduction of V5 (Fig. IV.29), for 0.3 sccm O$_2$, incorporation of N and C is underestimated, as expected due to the lower total Si$_3$N$_4$ DR. For 0.6 sccm O$_2$, the slight deviations in the

SiO_2 and Si_3N_4 DR profiles cancel each other out and result in a good reproduction of the composition profiles.
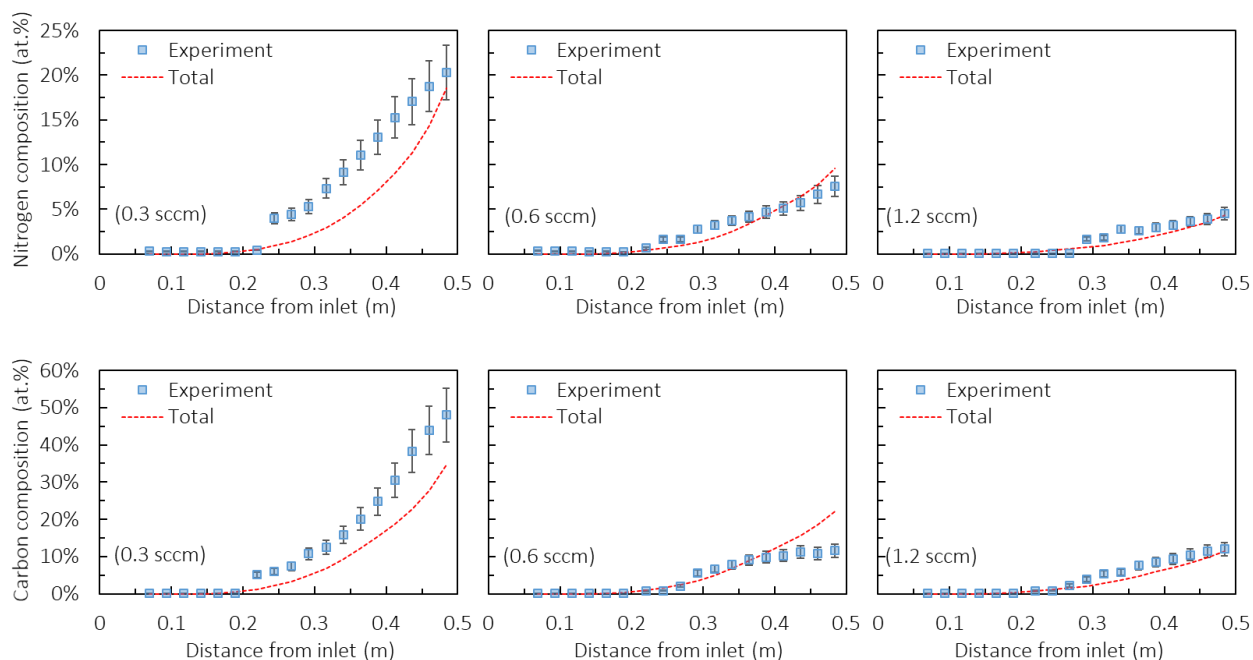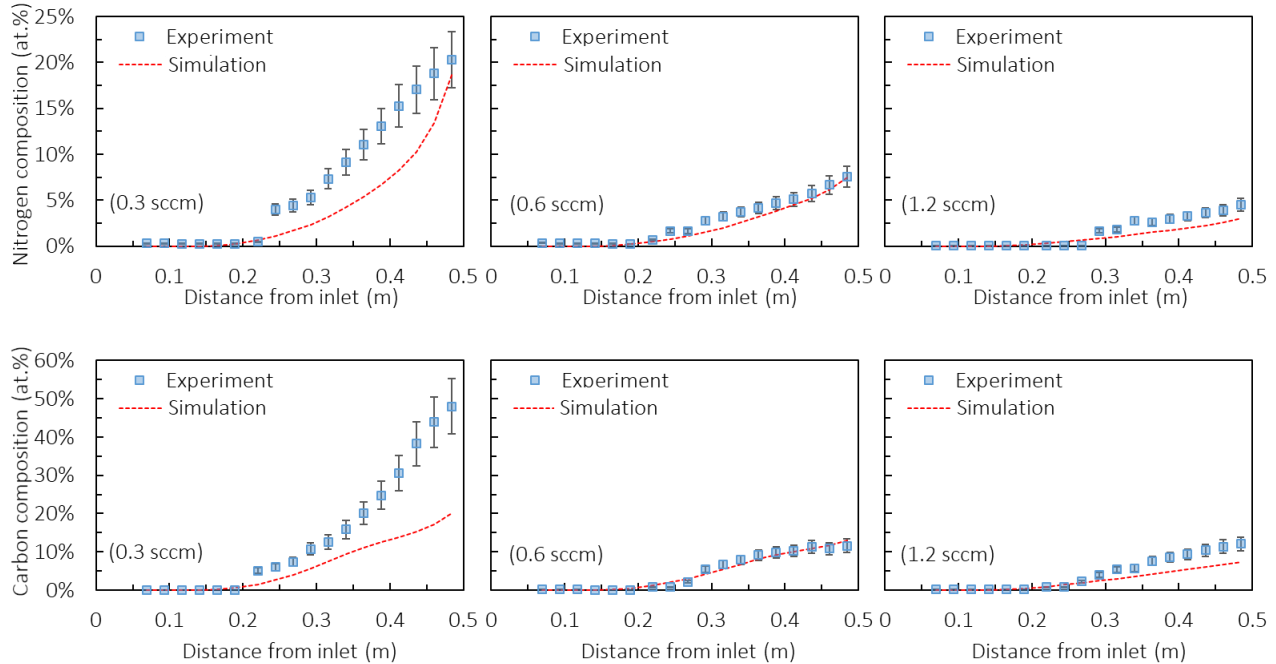

Fig. IV.29. Comparison of nitrogen (top row) and carbon (bottom row) contents between simulations using V1-V5, S1-S3 and experimental ellipsometry results, for varying O_2 flow rates at SPT 650°C (runs TD7, TD11, TD12).

For 1.2 sccm O_2, an interesting observation is made: the N and C concentration profiles are underestimated by around 1.5 at.% for N and 5 at.% for C, even though the total Si_3N_4 deposition was simulated with very close agreement to the experimental data. This could be the result of the slight overestimation in SiO_2, which translates in higher concentrations of O and Si, reducing as a result those of C and N. However, these results could indicate that potential deviations are also caused by the chosen stoichiometry. It is recalled that the deposition of pure SiO_2 and Si_3N_4 is considered for S1 and S2 respectively, while S3 represents the production of a $Si_3N_4C_{12}$ material. It is therefore possible to arrive at closer agreements of the composition by redefinition of the stoichiometries and redistribution of the incorporated carbon into the other "phases". Various calculation attempts were carried out, revealing that consideration of a SiO_2C_1 stoichiometry drastically increases the incorporation of carbon along the whole length of the reactor. Only when decreasing it to $SiO_2C_{0.05}$ was a satisfactory fit achieved, with parallel consideration of a $Si_3N_4C_2$ stoichiometry for S2, and $Si_3N_4C_{12}$ for S3. However, deviations from the experimental composition profiles are still observed, and are primarily the result of DR profile discrepancies.

The developed chemical model in its final iteration and the kinetic constants of each reaction are presented in Table IV.8. Gas velocity, temperature and species mass fraction contours are shown in Appendix 9.

Table IV.8. Proposed apparent chemical model for SiO$_x$N$_y$ deposition from TDMSA-O$_2$ chemistry, with list of reactions and their respective kinetic laws and constants.

	Reaction	Rate law	Kinetic constants[a]
	Volumetric Reactions (kmol.m^{-3}.s^{-1})		
V1	$TDMSA \rightarrow Si\_INT + N\_INT$	$k_1[TDMSA]$	$k_1 = 1.68 \times 10^{14} \times exp\left(-\dfrac{29954.1}{T(K)}\right)$
V2	$4\ Si\_INT + 2\ O_2 \rightarrow siloxane + bp$[b]	$k_2[Si\_INT]^a[O_2]^b$ $a = 0.50, b = 1.00$	$k_2 = 1.98 \times 10^{14} \times exp\left(-\dfrac{25201.1}{T(K)}\right)$
V3	$N\_INT + O_2 \rightarrow N\_INT2 + Si\_INT + bp$	$k_3[N\_INT]^a[O_2]^b$ $a = 0.80, b = 0.85$	$k_3 = 2.96 \times 10^{18} \times exp\left(-\dfrac{29808.7}{T(K)}\right)$
V4	$N\_INT + O_2 \rightarrow silanamine + bp$	$k_4[N\_INT]^a[O_2]^b$ $a = 0.45, b = 1.26$	$k_4 = 2.96 \times 10^{20} \times exp\left(-\dfrac{32334.4}{T(K)}\right)$
V5	$N\_INT2 \rightarrow bp$	$k_5[N\_INT2]$	$k_5 = 6.276 \times 10^{28} \times exp\left(-\dfrac{59575.2}{T(K)}\right)$
	Surface Reactions (kmol.m^{-2}.s^{-1})		
S1	$Si\_INT + O_2 \rightarrow SiO_2 + bp$	$k_{s1}[Si\_INT]_s^a[O_2]_s^b$ $a = 0.40, b = 0.37$	$k_{s1} = 7.25 \times 10^{-2} \times exp\left(-\dfrac{7598.5}{T_s(K)}\right)$
S2	$4\ N\_INT \rightarrow Si_3N_4 + bp$	$k_{s2}[N\_INT]_s^a$ $a = 0.70$	$k_{s2} = 6.27 \times 10^6 \times exp\left(-\dfrac{29080.4}{T_s(K)}\right)$
S3	$4\ N\_INT2 \rightarrow Si_3N_4C_{12} + bp$	$k_{s3}[N\_INT2]_s^a$ $a = 0.50$	$k_{s3} = 8.61 \times 10^6 \times exp\left(-\dfrac{29065.5}{T_s(K)}\right)$

[a] T_s is the temperature of the solid surface; [b] The notation *bp* stands for "by-products".

IV.3.4. Comparison and validation of the simulations with local experimental results

Let us recall that ellipsometry results, averaged from 5 points on each Si coupon, were used to develop the model. After conceptualization and implementation, the chemical model implemented into the CFD code FLUENT® is compared in shape and value to the experimental results, as a means of indirect validation. Firstly, the simulated local deposition profiles are visually compared to the experimental ones. It is recalled that the observed iridescences are caused by interaction of the film with the light and signify changes in thickness. Moreover, since we are dealing with a SiO$_x$N$_y$ material with evolving composition, the produced color palette deviates from that of pure SiO$_2$ or Si$_3$N$_4$ materials. Given that the iridescences

from Si_3N_4 films appear more vibrant than those of SiO_2 [185], brighter colors on the coated Si substrates could not only indicate higher thicknesses, but also potentially higher N incorporation. With this point in mind, the experimental and simulated deposition profiles are presented in Fig. IV.30 and are discussed below.
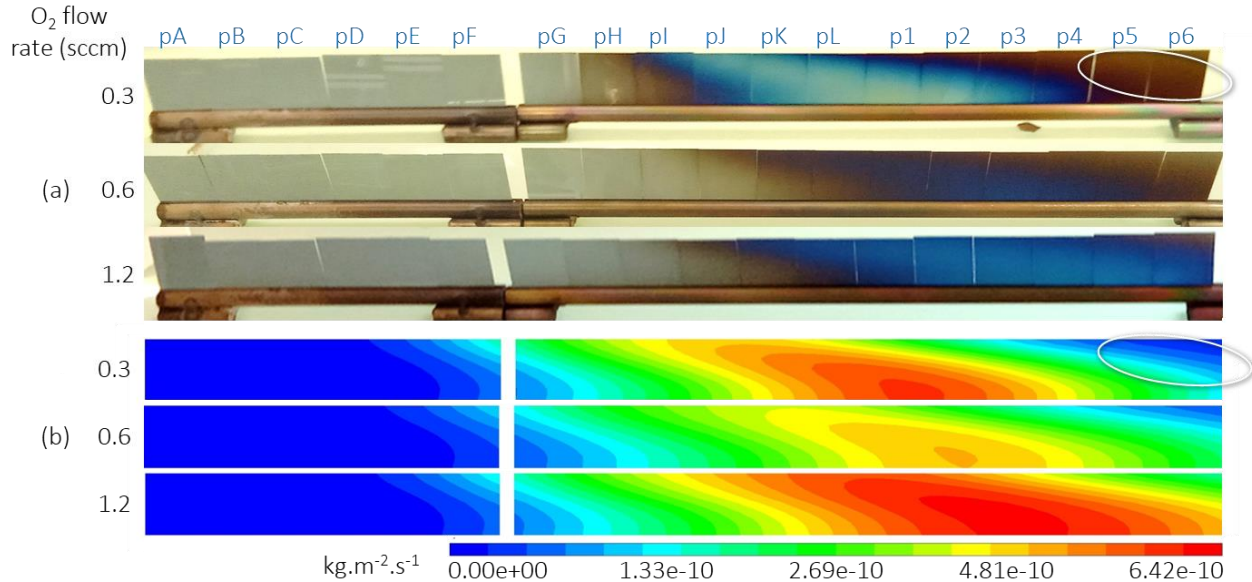
Fig. IV.30. Visual validation in shape for the developed SiO_xN_y model. Photographs of array of samples after deposition (a) and simulated total DR profiles (b) at various O_2 flow rates (runs TD7, TD11, TD12).

Fig. IV.30a shows photographs of the coated Si coupons for the three runs (TD7, TD11, TD12) that were used as the basis for the development of the chemical model. Samples pA to pG present the typical silver color, indicating that little to no film has been produced on them. Deposition starts to take place beyond sample pH for 0.3 sccm O_2. It is recalled that the deposition duration for 0.3 sccm O_2 was longer than for the other two experiments (Table IV.2), resulting in more material production, with the film becoming visible more easily. This explains why deposition is encountered seemingly downhill for 0.6 and 1.2 sccm O_2. For all three runs, a characteristic half-arrow shape is observed due to the high total gas flow rate and the progressive film formation thanks to the thermal gradient. The appearance of the "tip" of the arrow is connected to the decrease in deposition (circled in white) and is caused by the consumption of O_2 and other film forming species.

Globally, it is observed that the simulations (Fig. IV.30b) reproduce well the general shape of the experimental profiles, validating the model in shape. The "tip" of the arrow is also encountered, with the

simulations correctly representing its occurrence earlier for 0.3 sccm O$_2$ (at samples p3/p4) and its extension towards the right-most samples (p5/p6) for 1.2 sccm O$_2$. It is also noted that the iridescence of 0.3 sccm O$_2$ appears brighter. On one hand, this could be attributed to the higher thickness of the films. However, the thickness of TD12 is also comparable yet appears less vividly. Therefore, the more vibrant color at 0.3 sccm O$_2$ is linked to the higher nitrogen incorporation [185].

Fig. IV.31 presents a comparison of local DR and composition profiles for 1.2 sccm O$_2$ (run TD12). The local experimental values are extracted from local measurements taken by ellipsometry, by probing the point (3) located in the middle of the substrate, as indicated in Fig. II.7. A line passing across the middle of all samples is plotted in FLUENT® to extract the respective calculated values.

Fig. IV.31. Comparison of local SiO$_2$ (a) and total Si$_3$N$_4$ (b) DR, as well as nitrogen (c) and carbon (d) composition profiles, plotted from ellipsometry probing point (3) and the equivalent local values from simulations, for 1.2 sccm O$_2$ at SPT 650°C (run TD12).

As shown in Fig. IV.31a and b, the DR profiles of the SiO$_2$ and total Si$_3$N$_4$ depositions are well represented, with the bell shape of the SiO$_2$ profile being reproduced with small deviations noted between 0.2 and 0.4 m. The total Si$_3$N$_4$ profile on the other hand presents an excellent agreement between the

calculated and experimental local data. The comparison between the composition in C and N are shown in Fig. IV.31c and d. Similarly to what was discussed previously for Fig. IV.29, the gradually increasing trends are well represented, although a general underestimation is noted for both elements. This underestimation is attributed to the overestimation of the SiO_2 deposition, with Si and O occupying as a result larger composition percentages of the film in relation to C and N. For the six samples located in the isothermal region (0.36-0.5 m) an average deviation of 9 and 3 % is calculated for the overestimated SiO_2 and underestimated Si_3N_4 DR, respectively. The resulting deviations of the underestimated N and C contents are 42 and 37 %, respectively, meaning that the model is able to represent the local DR but gives less accurate results regarding the film composition.

IV.3.4.1.   Validation for different process temperature

So far, the chemical model was developed from experiments with a variable O_2 flow rate and was validated partially by comparing local values. Certainly, the local temperature also varies within the reactor due to the presence of a thermal gradient. However, it is of interest to see how the model performs for an experimental run with different operating conditions. For this purpose, run TD14 (Table IV.2) is simulated, described as a deposition under a SPT of 625°C instead of 650°C. Although SPT 625°C is not too far from the SPT for which the model was developed, it does constitute an extrapolation, which might result in lower accuracy. Comparison of the calculated and experimental DR and composition values is shown in Fig. IV.32.

Indeed an underestimation of the SiO_2 and Si_3N_4 DR profiles is noted in Fig. IV.32a and b, respectively. This indicates that the developed chemical model encounters difficulties in reproducing the DR profiles for SPT lower than 650°C. However, an important point uncovered in section IV.2 is recalled: the addition of 0.6 sccm O_2 at SPT 625°C resulted in higher TDMSA conversion than when no O_2 was present. Reaction V1 however has been formulated as being dependent only on the concentration of TDMSA and the temperature. The higher TDMSA conversion (and as a result, higher production of Si_INT and N_INT) that takes place in reality for SPT 625°C can thus not be accounted for by V1. This explains well why the current simulations underestimate the SiO_2 and Si_3N_4 deposition. Additionally, due to the underestimation of the total Si_3N_4 deposition, the composition in N and C is underestimated as well.

The results reveal that the deposition mechanism is obviously more complex and in reality involves multiple reactions that were not accounted for. Additionally, as all apparent kinetic models, it is only valid in the range of deposition conditions for which it has been developed. As illustrated for the run at SPT 625°C, deposition at temperatures lower than 650°C follows a different mechanism and the kinetic

constants of at least one reaction need to be adjusted, in order to have an agreement between the calculated and the experimental values. Regardless, the developed model constitutes a significant first step towards the simulation of complex ternary SiO$_x$N$_y$ systems containing non-negligible amounts of carbon.
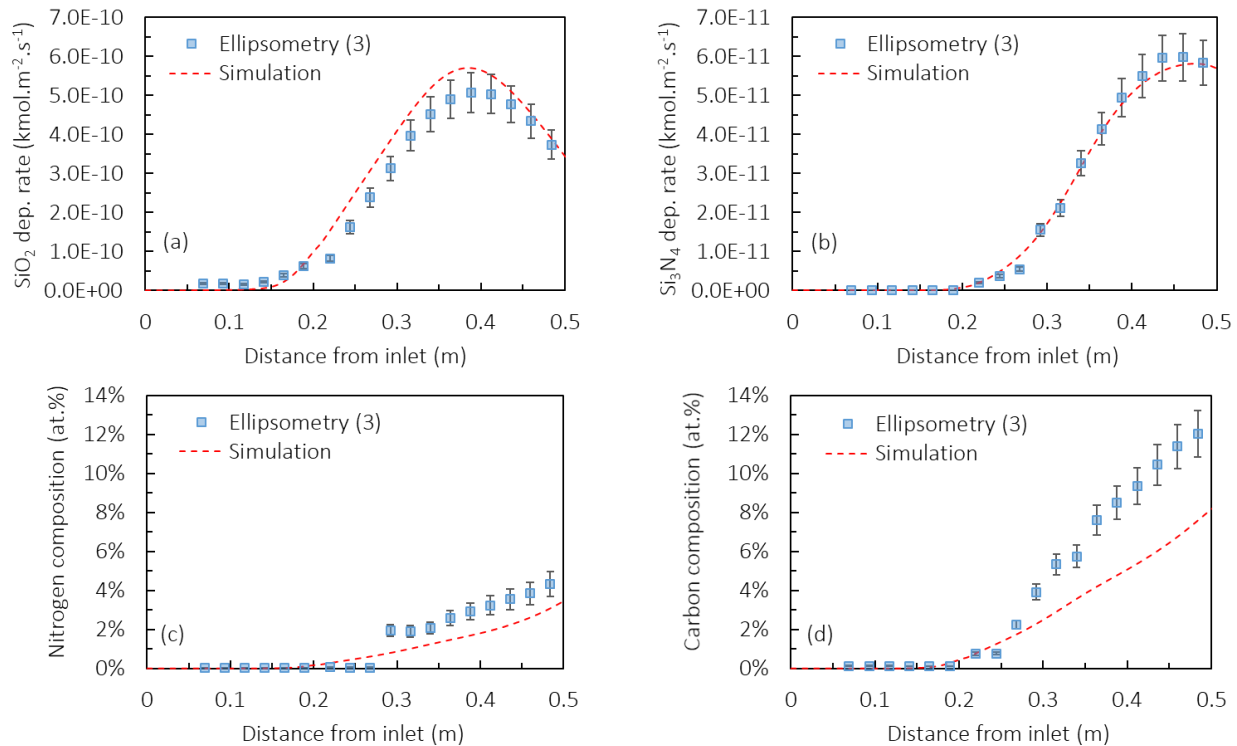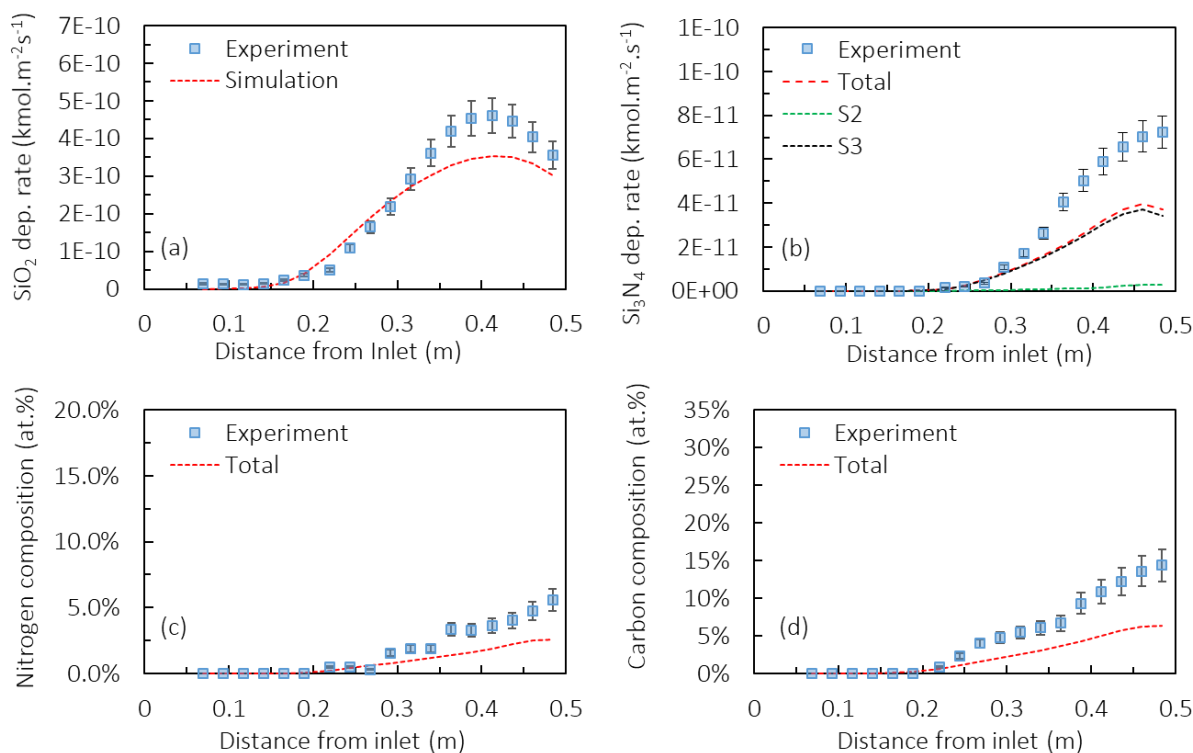

Fig. IV.32. Comparison of local SiO$_2$ (a) and Si$_3$N$_4$ (b) DR, and nitrogen (c) and carbon (d) composition profiles, plotted from ellipsometry probing point (3) and the equivalent local composition from simulations, for run TD14 at SPT 625°C.

IV.3.5. SiO$_x$N$_y$ deposition in vials: experiment and process simulation

Following the excellent corrosion resistance of the SiO$_x$N$_y$ films as revealed from the P-etch and BOE wet etching corrosion results (Fig. IV.14), coating of pharmaceutical vials is undertaken using the TDMSA-O$_2$ chemistry. Based on the BOE results, a concentration of maximum 7 at.% N is considered sufficient for excellent corrosion resistance. However, incorporation of N from TDMSA is taking place only for temperatures higher than 621°C. Moreover, under 0.6 sccm of O$_2$, the desired content of 7 at.% N is reached at 650°C (Fig. IV.6). This temperature is above the glass transition temperature of the Type I pharmaceutical vials and could pose deformation problems during the deposition process. Despite that, deposition is attempted at SPT 650°C (thermal profile shown in Appendix 10), by applying a gradual and

very slow temperature increase of 1°C.min^{-1}, to avoid deformation. Cooling after deposition is performed at the same rate until 500°C, after which the vial is cooled with a rate of 10°C.min^{-1}. The applied flow rates are detailed in section II.1.1.2 of Chapter II. To recall them, the total flow rate is fixed at ca. 2219 sccm, with O_2, total $N_{2-dilution}$ and $N_{2-bubbler}$ supplies being 0.3, 2195 and 24 sccm, respectively. A photograph of the vial after SiO_xN_y deposition for 1 h is presented in Fig. IV.33.
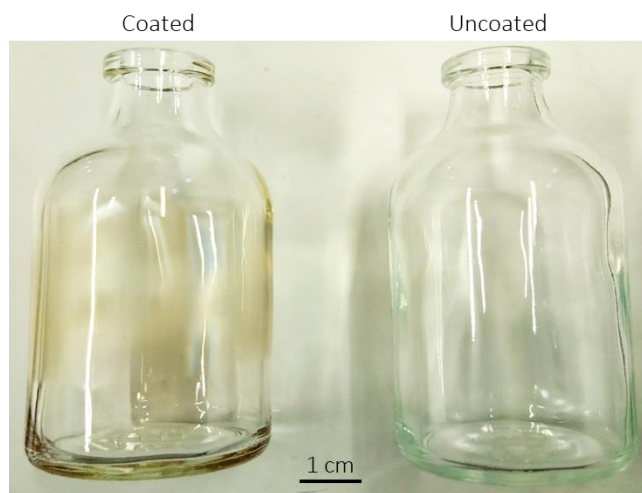
Fig. IV.33. Type I pharmaceutical vial after application of SiO_xN_y coating (left) and uncoated (right).

The treated Type I pharmaceutical vial coated with a film of approximately 122 nm SiO_xN_y is shown on the left side of Fig. IV.33. Compared to an uncoated vial (right), which appears transparent, the SiO_xN_y treated glass substrate shows a yellow hue on the body of the vial, indicating the production of a barrier coating. The average DR deduced from weighing measures 2.02 nm.min^{-1} for an assumed SiO_xN_y density of 2.65 g.cm^{-3} and considering deposition on both the internal and external surfaces (external base surface is excluded). This value is three times higher than the maximum DR noted on planar Si-substrates treated under the same conditions (Fig. IV.6a, 0.6 sccm). A potential explanation could be the difference in reactor configuration (impinging jet) and substrate geometry (confined space), which results in different gas velocity profiles and residence times compared to the generally unobstructed gas flow in the tubular reactor.

The developed chemical model is implemented in the vial geometry for further investigation. The total mass flow rate and the mass fractions of all species at the inlet are fixed to the experimental values (Appendix 8). Through this, predictions regarding the hydrodynamic, thermal and mass transfer properties of the gas phase and the involved species are obtained. Fig. IV.34 presents the calculated gas velocity and

temperature distribution profiles. Fig. IV.34a shows the full range of the velocity profile. Similarly to depositions from TEOS, the maximum velocity is noted at the tip of the injector nozzle. In the case of the TDMSA chemistry, it reaches around 210 m.s^{-1}, a value logically higher than the one obtained for the runs at SPT 550°C (Fig. III.24a). In order to aid the visualization of the impinging jet, the velocity range is clipped at a maximum of 20 m.s^{-1} (Fig. IV.34b). The vortex at the bottom of the vial becomes visible now. A smaller vortex is observed near the vial shoulder. Globally, the gas velocity profile is similar to the profiles observed previously (section III.2.7).
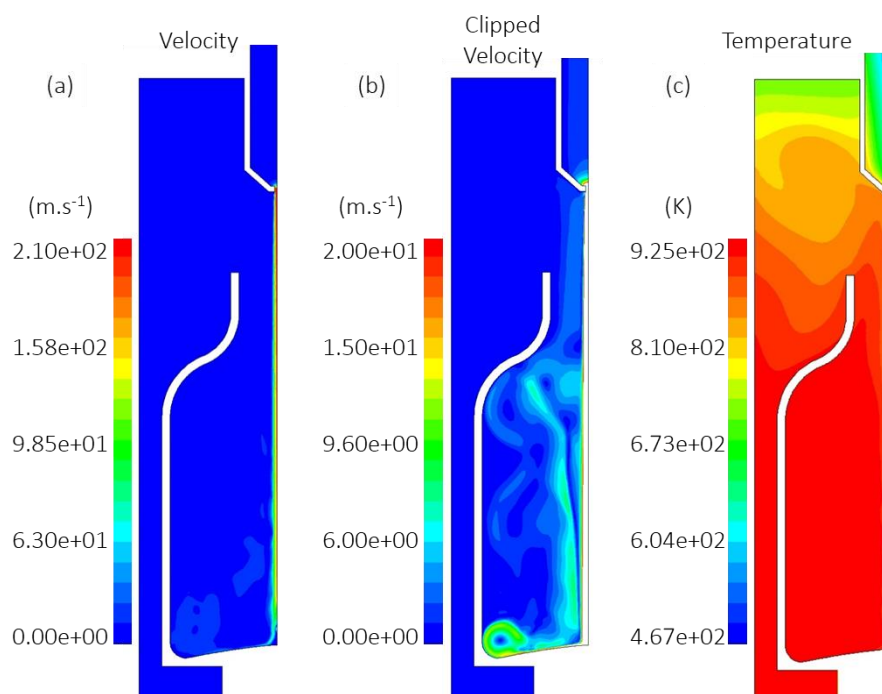
Fig. IV.34. Gas velocity profile at full range (a) and clipped to a maximum value of 20 m.s^{-1} (b), as well as temperature distribution profile (c), for a SPT of 650°C.

The thermal profile imposed on the solid walls and the simulated thermal distribution in the gas phase is shown in Fig. IV.34c. The cooler jet and the subsequent heating of the gas upon impact on the hotter surfaces of the vial are noted. Globally, it is observed that temperatures above 600°C are reached only after the gas has exited the nozzle and met the hotter base of the vial. This indicates that deposition of a nitrogen-containing film is first initiated within at region contained within the vial, as is desired. The difference in thermal profile between the tubular and vial reactors can be an additional reason why a higher DR was observed in the vial reactor: no consumption of film-forming species is taking place before the gas enters the vial. In the tubular reactor on the other hand, deposition on the gradually heated quartz wall,

substrates and substrate holder is observed, even before the gas manages to reach the isothermal region. As a result, the concentration of the film-forming species in the isothermal region of the tubular reactor is lower compared to the equivalent vial configuration, where the gas phase is heated more abruptly. This is reflected in the mass fractions of the main species shown in Fig. IV.35.
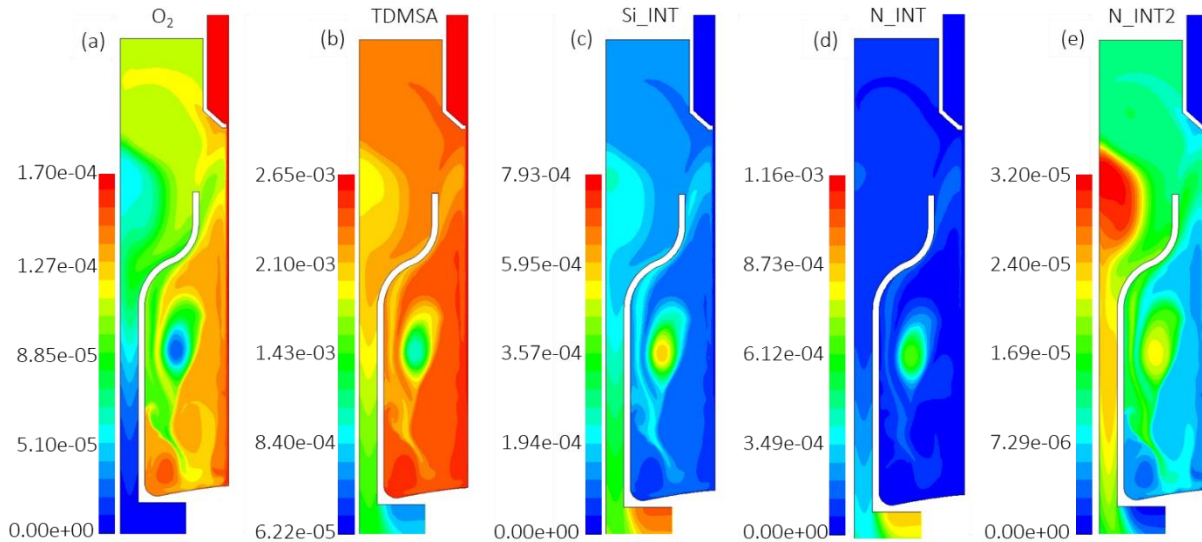
Fig. IV.35. Local mass fraction profiles of O_2 (a), TDMSA (b), Si_INT (c), N_INT (d) and the silanimine N_INT2 intermediate (e) from simulation at SPT 650°C.

Fig. IV.35 shows the local mass fraction distributions of O_2, TDMSA, Si_INT, N_INT and the N_INT2 intermediate. The mass fractions of O_2 and TDMSA remain unchanged until the incoming gas flow impacts on the bottom of the vial. Beyond this point, the gas phase is heated abruptly and a series of reactions is taking place in quick succession. TDMSA is first decomposed to produce Si_INT and N_INT through V1. Si_INT then reacts with O_2 to produce siloxane compounds and the solid SiO_2 film through reactions V2 and S1, respectively. At the same time, N_INT reacts with O_2 to produce the silanimine N_INT2 intermediate. The species exhibit non-uniform mass fraction profiles and seem to be greatly affected by the vortexes present in the gas phase. This is especially emphasized in the vortex close to the shoulder of the vial, where an important consumption of TDMSA and O_2 is taking place. Additionally, only O_2 is completely consumed, while a quantity of unreacted TDMSA is noted at the exhaust. Despite that, the TDMSA conversion within the reactor is calculated at 97 % and the deposition yield (considering only the vial) at 0.7 %. Both values are higher than the respective ones calculated for the tubular reactor (85 % and 0.2 %, respectively). A similar behavior was also observed for the TEOS-O_2/O_3 chemistry. Once again, it

is confirmed that the change in reactor configuration and substrate geometry has led to a more efficient utilization of the supplied precursor quantity. The constrained thermal profile also plays an important role in increasing deposition on regions of interest.

The simulated distribution of SiO$_2$ (reaction S1) and total Si$_3$N$_4$ deposition (reactions S2 and S3) on the internal and external surfaces of the vial is presented in Fig. IV.36. The simulations indicate that SiO$_2$ deposition (Fig. IV.36a) is taking place across the whole surface of the vial and appears relatively uniform thanks to the distribution of the Si_INT and O$_2$ mass fractions close to the vial wall. A decreased DR is noted at the external heel region, which is attributed to the consumption of O$_2$ in the gas phase (Fig. IV.35a). Deposition of Si$_3$N$_4$ (Fig. IV.36b) is noted to be more pronounced on the external surface of the vial, predominantly at the body and heel regions. Inspection of the mass fractions from Fig. IV.35 shows that both N_INT and N_INT2 are indeed present at the exterior of the vial. On the internal surface on the other hand, a sharp change in DR is noted around the middle of the vial body region. This distribution of the Si$_3$N$_4$ deposition rate is visibly linked to the evolution of the local N_INT2 mass fraction (Fig. IV.35e).
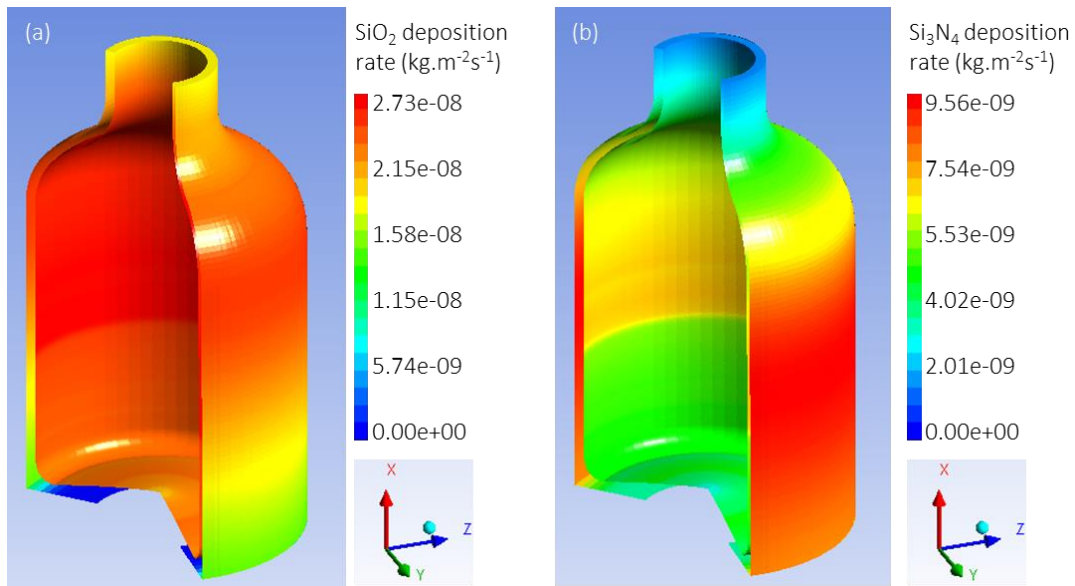
Fig. IV.36. Simulated SiO$_2$ DR profile from S1 (a), Si$_3$N$_4$ DR from S2 and S3 (b) on the external and internal surfaces of a vial simulation from the TDMSA-O$_2$ chemistry at SPT 650°C (run VTD1).

The evolution of the DRs from each individual heterogeneous reaction on the internal surface of the vial are presented in Fig. IV.37. A steep increase is observed for all three reactions at the region where the sharp change in DR appears. The steepest increase is observed for the DR of carbonated Si$_3$N$_4$ through

reaction S3 (dependent on the mass fraction of N_INT2), the trend of which is naturally closely followed by the evolution of the carbon content. The calculated carbon incorporation spans from 4.3 to 6.1 at.%, while the nitrogen content ranges between 1.7 and 2.3 at.%. Although the accuracy of these values depends on validation of the model after being transposed into the vial reactor, they still serve to demonstrate how simulation can be used to acquire compositional information on surfaces that would otherwise be difficult to examine non-destructively. Additionally, the model could also help finding new deposition conditions that would allow for more uniform film thickness and composition inside the vial. One possible route could be to decrease the total flow rate, so as to minimize the recirculation patterns inside the vial.
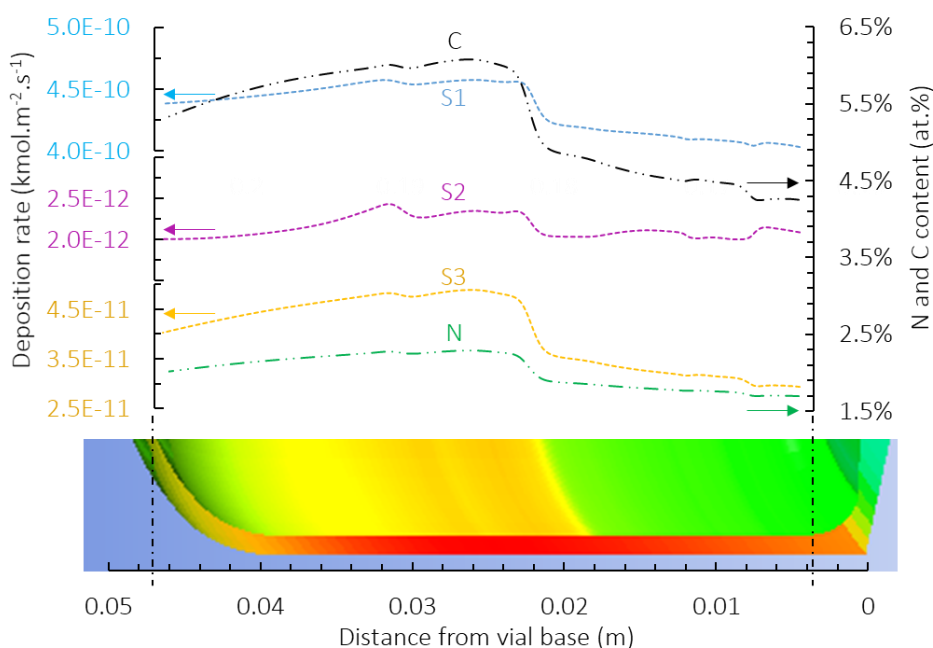
Fig. IV.37. Evolution of simulated DR from reactions S1(SiO$_2$), S2 (Si$_3$N$_4$) and S3 (Si$_3$N$_4$C$_{12}$) (dashed lines), as well as C and N composition (dash-dotted lines) along the body of the vial.

Lastly, an important piece of information is pointed out. Even though a gradual and very slow increase and decrease of the temperature was applied during the heating and cooling steps of the deposition process, the glass container deformed regardless as soon as the temperature exceeded ca. 600°C. More specifically, the vial sagged by 2-4 mm, with one side deforming more than the other. The asymmetric deformation made the crown of the vial shift out of axial alignment below the injector nozzle, a change that cannot be simulated. This is why no direct comparison is possible between experimental and simulated deposited mass. Moreover, the altered and unknown volume of the vial renders it difficult to correctly

follow the UPS<660> protocol. The above results underline well the requirement of treating vials within the specified temperature margins. At the same time though, the fact that deposition of nitrogen-containing films from the TDMSA chemistry is possible only above ca. 621°C is an obstacle. Thus, it is clear that the challenges remain: novel, more reactive chemistries are necessary in order to carry out SiO$_x$N$_y$ deposition at lower temperatures, compatible with the glass transition temperature of Type I pharmaceutical vials.

IV.4. Conclusions

The deposition of SiO$_x$N$_y$ films from the rarely reported TDMSA precursor was explored in the present chapter. Chemistries involving NH$_3$ and O$_2$ were investigated, resulting in successful incorporation of nitrogen, a landmark achievement for the present thesis. The reactivity of the precursor enabled SiO$_x$N$_y$ deposition below the 750-900°C temperature range encountered in conventional thermal CVD processes. After extensive parametric analysis, it was uncovered that TDMSA fulfills a dual role as Si and N provider. NH$_3$ aids in decreasing organic carbon in the films but does not benefit DR or film enrichment in N. O$_2$ has a substantial film-promoting role. However, a trade-off exists in terms of film nitridation: incorporation reactions of O and N are highly competitive to each other. Hydration of the network is encountered as N–H, Si–OH and –CH$_3$, with IBA measuring 17-23 at.% H and 5-20 at.% C. Despite their presence, the films exhibited an exceptionally low P-etching rate (0.2 Å.s^{-1}), at least one order of magnitude lower than any of the silica films produced so far. Screening using BOE showed that this remarkable corrosion resistance is attributed to the presence of nitrogen and to the network densification induced by its incorporation. It was revealed that ca. 7-8 at.% N is sufficient for the production a SiO$_x$N$_y$ film with excellent corrosion resistance. This result is significant and helps frame the previously mentioned trade-off between film growth and nitridation.

Gas phase analysis revealed that the deposition process is initiated through the thermal decomposition of TDMSA into radical species. The (Me)$_2$HSi$^\bullet$ radical was trapped systematically. Compounds from the silanol, silanamine, siloxane and alkoxysilane families were also identified. It was observed that the (Me)$_2$HSi$^\bullet$ and (Me)$_2$SiHN$^\bullet$ radicals, originating from the thermal decomposition of TDMSA, are the main building blocks for all detected by-products, with additional indications on the presence of CH$_3$$^\bullet$ and H$^\bullet$ radicals. At least 14 distinct reactions were proposed to describe the deposition process and suggest pathways for the production of the various identified compounds. Among them, 8 reactions were used for the formulation of an apparent mechanism, implemented for the first time for the

simulation of a SiO_xN_y material with non-negligible amounts of carbon. An innovative methodology combining results from ellipsometry, IBA, GC-MS, ESR, NMR and process simulation by CFD was applied. The developed model is valid for low O_2 flow rates (up to 1.2 sccm) at 650°C and provides predictions regarding SiO_xN_y film thickness and composition. An extrapolated comparison with deposition at 625°C was carried out. Discrepancies were observed, which can however be traced back to a difference in deposition mechanism at this temperature.

Unfortunately, the TDMSA chemistries failed to conform to the operating constraints. Nitrogen incorporation from this precursor requires a temperature of at least 620°C, rendering this chemical pathway incompatible with pharmaceutical Type I vials. Thus, the following chapter focuses on addressing this challenge by exploring SiO_xN_y deposition through a more reactive, novel trisilylamine-derivative precursor, developed and provided by Air Liquide.

Chapter V. Deposition of SiO$_x$N$_\gamma$ films from a novel trisilylamine derivative precursor

The present chapter pertains to research on the deposition of silicon oxynitride films from a trisilylamine derivative compound. This molecule, referred to as TSAR, is a novel, proprietary precursor developed by Air Liquide. This study was conducted during the final months of the thesis, in an attempt to further challenge the thermal chemical vapor deposition of SiO$_x$N$_y$ films and achieve film formation at temperatures lower than 600°C.

The experimental exploration of this new compound was conducted in absence of ammonia, using a TSAR-O$_2$ chemistry. In a first step, a parametric analysis investigating the effect of the temperature and O$_2$ flow rate is executed. Focus is placed on the minimum temperature required for deposition, the respective deposition rates, as well as the nitrogen and carbon contents of the films. In a second step, the produced SiO$_x$N$_y$ films from TSAR are compared to those from TDMSA in terms of deposition rates, composition and chemical structure.

In a final step, the corrosion resistance behavior of the films obtained from the TSAR-O$_2$ chemistry is investigated. Similarly to TDMSA, improvements in performance are explained by linking them to the densification of the network caused by additional enrichment in nitrogen and/or increase in deposition temperature. A comparison of all silica-based materials produced in this thesis allows drawing important conclusions regarding the correlation between the process-composition-structure triptych and the resulting barrier performance of each material. Lastly, differences in possible deposition mechanisms and incorporated moieties are discussed.

V.1. SiO$_x$N$_\gamma$ deposition from TSAR on planar substrates

Based on the results of Chapter IV, it appears that, for the range of operating conditions tested, a chemistry including NH$_3$ does not result in improvements regarding the deposition rate of the films or their enrichment in nitrogen. For that reason, the production of SiO$_x$N$_y$ films from TSAR was studied using a TSAR-O$_2$ chemistry. The operating conditions of the various experiments performed are summarized in Table V.1. Flow rates of 3960 sccm and 68 sccm were applied for the N$_2$-dilution and N$_2$-bubbler lines respectively, remaining unchanged across all experiments. For these conditions and by keeping the bubbler temperature at 60°C, a TSAR flow rate of ca. 2 sccm was supplied in the reactor.

Table V.1. Experimental conditions of the TSAR-O$_2$ chemistry tested in the tubular CVD reactor.

Run	SPT (°C)	O$_2$ flow rate (sccm)	Deposition time (min)
AR1	650	0.6	25
AR4	625	0.6	15
AR3	580	0.6	41
AR2	550	0.6	50
AR5	550	0.3	67
AR6	550	-	58
AR7	650	0.6	80

The effect of the set point temperature (SPT), as well as the lowest possible temperature for deposition of SiO$_x$N$_y$ films from the TSAR-O$_2$ chemistry, are investigated through experiments AR1 to AR4. Afterwards, the effect of the O$_2$ flow rate for a SPT of 550°C is investigated through experiments AR2, AR5 and AR6. Run AR7 is performed to obtain thick SiO$_x$N$_y$ films for nanoindentation analysis.

V.1.1. Deposition from TSAR-O$_2$ and comparison with TDMSA-O$_2$

Fig. V.1 shows that successful deposition of material was achieved for AR1 conditions (2 sccm TSAR, 0.6 sccm O$_2$, at 650°C). Similar to previous experiments, the iridescence reveals changes in thickness. Interestingly, the minimum temperature required for film formation is noted to be around 510°C,

much lower than the 585-610°C required for the TDMSA chemistry. These results translate into lower thermal requirements and improved compatibility of the process with pharmaceutical vials.
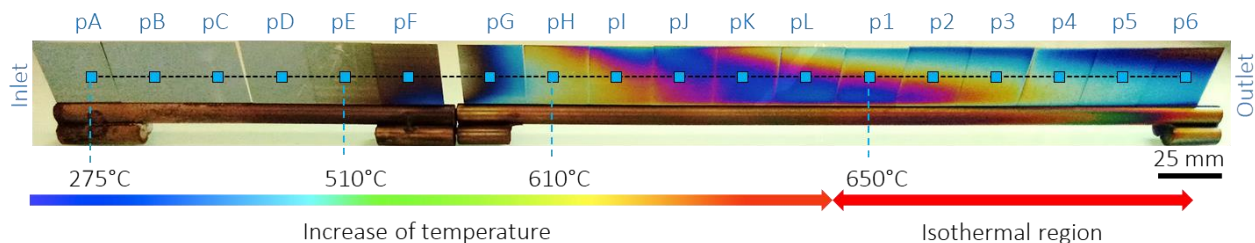
Fig. V.1. Photograph of substrates after deposition for 2 sccm TSAR and 0.6 sccm O$_2$ (AR1), with local temperature indicated for selected samples.

Following deposition, the samples are analyzed by ellipsometry to assess if nitrogen incorporation was successful. Similarly to TDMSA, application of models based on SiO$_2$ (Fig. II.8b) failed to give a satisfactory fit between the measured and simulated ellipsometric spectra. Application of the material-independent Cauchy and Sellmeier models (Fig. II.8a) revealed a refractive index (RI) of 1.78 for sample p6. Once again, this value is well above the value of stoichiometric silica (1.458) and close to that of SiO$_x$N$_y$ material with around 30 at.% of nitrogen (i.e. 1.85, [263]). The successful incorporation of nitrogen is further confirmed by a fit of the ellipsometry spectra to a SiO$_2$+Si$_3$N$_4$ BEMA model (Fig. II.8c), with an R^2 over 0.99. In comparison to TDMSA, which includes 6 Si–CH$_3$ groups in its structure, the TSAR precursor features Si–H bonds instead (Table II.1). For that reason, the consideration of a carbon-containing component in the BEMA model (Fig. II.8d) was not required. The deposition rate (DR) and nitrogen content results for AR1 are shown in Fig. V.2. Results of the TDMSA-O$_2$ chemistry, for an experiment carried out under the same flow rates and temperature conditions (i.e. 2 sccm TDMSA, 0.6 sccm O$_2$, SPT 650°C) is also included for comparison.

Fig. V.2a reveals a big difference in DR between the two precursors. A maximum DR of 10.3 nm.min^{-1} is reached at ca. 635°C for TSAR, a value that is at least one order of magnitude higher than the maximum DR noted for TDMSA under similar conditions. The reactivity of the TSAR molecule thanks to the multiple Si–H bonds is apparent and drastically increases material growth rate. Beyond the point at which the maximum DR is achieved, the rate of film production decreases similarly to what was observed for TDMSA. This behavior has been attributed to the consumption of one or multiple reactants. Fig. V.2b reveals that, just like TDMSA, the TSAR precursor can also act as a nitrogen source. Moreover, higher nitrogen incorporation is encountered for TSAR. When this trisilylamine derivative molecule is used as the

precursor, nitrogen is first probed beyond 0.15 m from the inlet, corresponding to a local temperature of around 520°C. Similarly to what was previously observed for TDMSA, the nitrogen content of the films increases continuously, despite the deceleration of the DR beyond its maximum. Based on the information revealed in Chapter IV and the literature regarding the competition between O and N incorporation, this behavior is attributed to the consumption of O$_2$ in the gas phase and/or to the depletion of oxygen containing species that participate in film formation [179, 180, 247, 264].
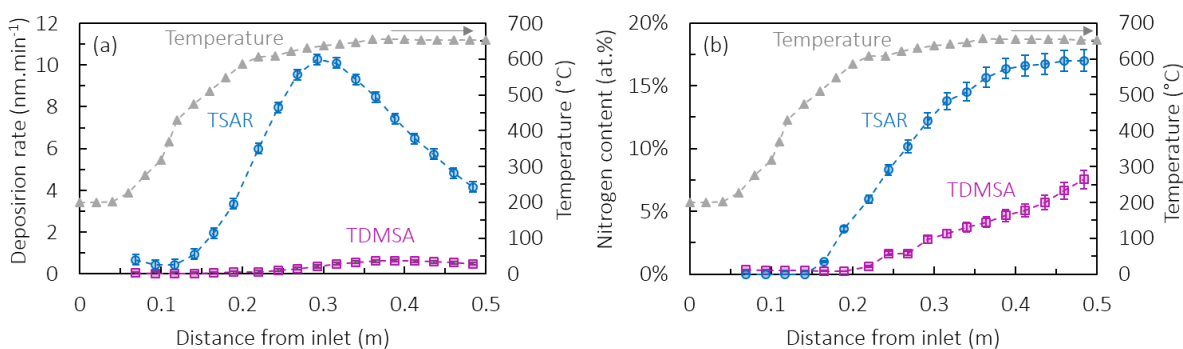
Fig. V.2. Average deposition rate of films (a) and nitrogen content (b) per sample measured by ellipsometry, for films produced under 0.6 sccm O$_2$ for a SPT of 650°C.

Ellipsometry revealed that a maximum percentage of 17.4 at.% N is reached on the last sample (p6) for films produced from the TSAR precursor. This value is lower than the one calculated previously (ca. 30 at.% N) from correlation of the RI to the composition, as provided by the literature [263]. A possible explanation could be the presence of Si–Si bonds in the films. Since the RI of Si=3.949 > Si$_3$N$_4$=2.044 > SiO$_x$N$_y$ > SiO$_2$=1.458 [300-302], a high RI does not necessarily translate to a high nitrogen content. Instead, it could be biased by the presence of Si–Si bonds, shifting the RI towards higher values. This assumption is investigated further through FT-IR, IBA and XPS analyses in section V.2.

For the same operating conditions and on the same sample (p6), deposition from TDMSA resulted in lower nitrogen incorporation, reaching a maximum of 7.5 at.% N. This could be explained by the difference in the atomic N:Si ratio in the precursor molecules, which is 1:3 for TDMSA and 2:3 for TSAR. However, nitrogen incorporation from TSAR on sample p6 is more than double that of TDMSA. Therefore, the increased N content in films from TSAR cannot be solely attributed to the higher N:Si ratio in the starting molecule. It indicates a better efficiency in film nitridation from this particular precursor.

V.1.2. Effect of the deposition temperature

Following the above, a parametric analysis studying the deposition at four different SPTs, namely 550°C, 580°C, 625°C and 650°C is conducted (runs AR1 to AR4, Table V.1). The evolution of the DR and the content in N along the reactor (averaged per sample), as measured by ellipsometry (SiO$_2$+Si$_3$N$_4$ BEMA model, Fig. II. 9c), is presented in Fig. V.3.
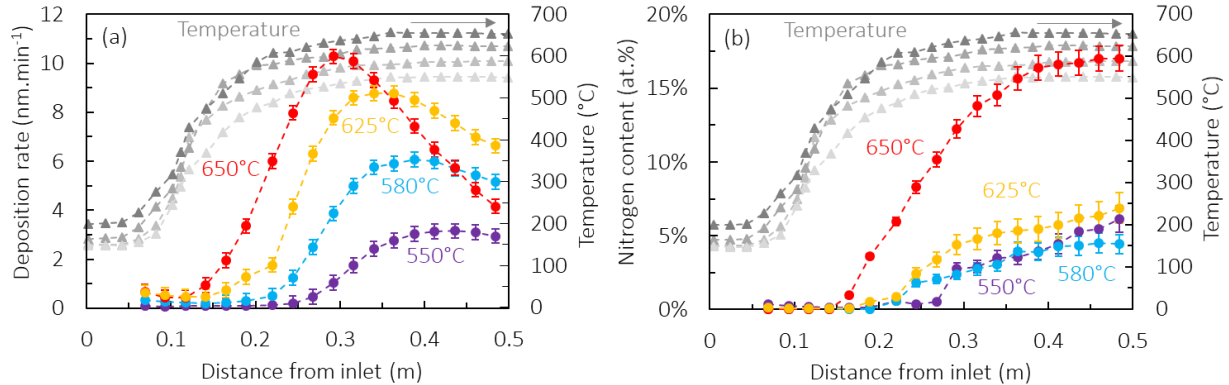
Fig. V.3. Investigation of the SPT on the DR (a) and nitrogen content (b). Respective thermal profiles are added in grey triangles.

Fig. V.3a shows that for a SPT of 650°C, deposition is initiated at ca. 510°C, with an average DR of 0.9 nm.min^{-1}. The maximum DR at this SPT is 10.3 nm.min^{-1}, reached at ca. 635°C. As the SPT decreases, so does the global DR profile of each experiment, with the corresponding maximum DR values measuring 8.8, 6.1 and 3.1 nm.min^{-1} for SPT 625°C, 580°C and 550°C, respectively. This behavior is expected for thermally activated processes. Additionally, it is noted that the maximum DR is observed closer to the inlet for higher SPT, which is explained by the offset between the thermal profiles. Faster heating of the gas phase at higher SPT leads naturally to increased activation of the various gas phase and surface reactions. Beyond the maximum DR, the deposition decreases for all experiments, due to the consumption of one or multiple reactants, as was previously mentioned.

Fig. V.3b reveals that for SPT 650°C, nitrogen is first encountered beyond 0.15 m from the inlet, corresponding to a local temperature of around 520°C. Nitrogen incorporation is initiated further inside the reactor for lower SPT, as a result of the thermal profile offset. The nitrogen content of the films increases continuously, attributed to the consumption of O$_2$ and/or oxygen-containing species in the gas phase. Deposition at SPT lower than 650°C results in the decrease of nitrogen incorporation, with maximum values

of approximately 6.9, 4.1 and 6.4 at.% N noted for SPT 625°C, 580°C and 550°C, respectively. Interestingly, most of the values for 580°C and 550°C overlap, even though clear differences in their respective DRs were shown in Fig. V.3a. This can indicate that, between 550°C and 580°C, deposition and N incorporation proceed through the same intermediate species. Above 580°C, and especially at 650°C, the deposition mechanism appears to be changing, with deposition being potentially carried out by multiple intermediate species that likely feature higher N:Si atomic ratios.

V.1.3. Effect of the O$_2$ flow rate

The first set of experiments discussed in the previous section illustrated the ability of the TSAR precursor to successfully lead to SiO$_x$N$_y$ deposition featuring multiple advantages. Firstly, high DRs of up to 10.3 nm.min^{-1} were noted. More importantly, deposition at temperatures as low as 510°C was achieved, with successful nitrogen incorporation at 520°C and above. This feature is seminal for the deposition of SiO$_x$N$_y$ coatings at conditions that are compatible with the glass transition temperature of Type I pharmaceutical vials. Following the achievement of SiO$_x$N$_y$ deposition at temperatures lower than 600°C, a parametric analysis based on the O$_2$ flow rate for a constant SPT of 550°C is executed (runs AR2, AR5 and AR6, Table V.1). The results in terms of DR and nitrogen incorporation under variable O$_2$ flow rates are presented in Fig. V.4.
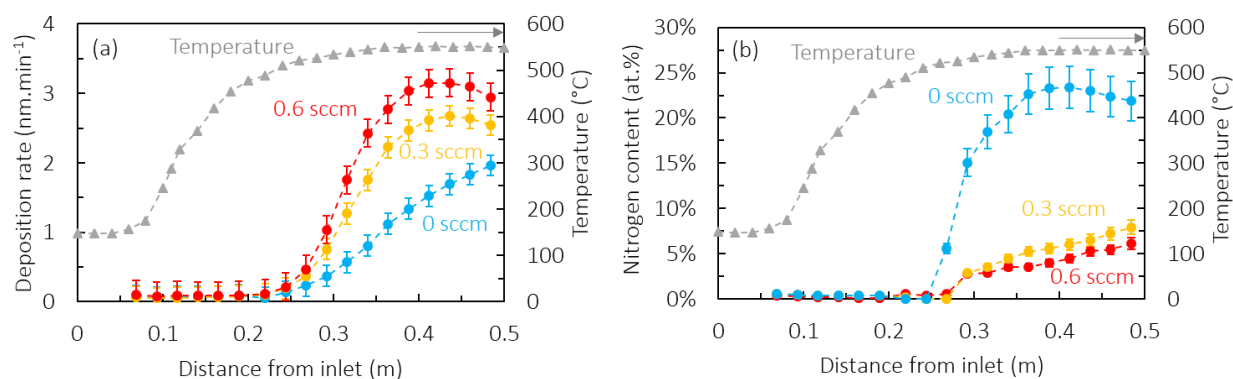
Fig. V.4. Investigation of the effect of the O$_2$ flow rate on the DR (a)
and nitrogen content (b), at SPT 550°C. Thermal profile is included in grey.

From Fig. V.4a it is observed that a higher O$_2$ flow rate increases the overall DR of the process. In absence of O$_2$, a maximum 2.0 nm.min^{-1} is noted. This value increases to 2.7 and 3.1 nm.min^{-1} for 0.3 and

0.6 sccm O$_2$, respectively, illustrating the deposition-promoting effect of O$_2$. Similarly to TDMSA, film formation is observed even in absence of O$_2$ in the inlet gas composition, indicating that the TSAR precursor can dissociate and produced film-forming intermediates on its own. The fact that the measured ellipsometry spectra fit to a SiO$_2$+Si$_3$N$_4$ model suggests also the presence of O in the films for 0 sccm O$_2$. The cause could be an O$_2$ leak, or the desorption of O$_2$/H$_2$O from the reactor walls. It is however pointed out that no bell shape is noted for the experiment carried out in absence of O$_2$, a shape that is typically encountered in experiments with O$_2$ in the inlet gas composition, even at 0.3 sccm. Thus, if an O$_2$ leak is the cause for oxygen incorporation at 0 sccm O$_2$, it can be concluded that its flow rate is much lower than 0.3 sccm.

The effect of the O$_2$ flow rate on the nitrogen content is shown in Fig. V.4b. Nitrogen incorporation is encountered for all experiments. Similarly to before, the maximum N content is observed on the last sample, measuring 6.1 at.% N at 0.6 sccm O$_2$. This value increases to 7.9 and 21.9 at.% N for 0.3 and 0 sccm O$_2$, respectively. Like for TDMSA, the results illustrate clearly the competitive behavior of O and N incorporation, with nitrogen incorporation increasing for lower O$_2$ inlet supply. Because of the continuous consumption of O$_2$ in the gas phase, a progressive increase in N concentration is noted along the length of the reactor. However, at 0 sccm, a bell curve for the nitrogen content is observed for the first time. Given that the DR continues to increase, it is speculated that film formation in this region proceeds through multiple species, each containing different atomic N:Si ratios. The depletion of a species with high N:Si ratio, along with the prevalence of an intermediate with lower N:Si ratio, could explain the decrease in nitrogen content and concomitant increase in DR between 0.4 and 0.5 m.

V.2. Chemical bonding state and composition of SiO$_x$N$_y$ from TSAR-O$_2$

V.2.1. Infrared analysis

The chemical bonding state of the films produced by the TSAR precursor is probed with FT-IR. Since the material is a silicon oxynitride, the majority of the identified peaks have already been previously encountered in TDMSA films and are listed in Appendix 4. The following sections focus on the evolution of the FT-IR spectra as a function of the temperature and the O$_2$ flow rate, presenting results by zooming at the two main areas of interest, the fingerprint region (600-1400 cm^{-1}) and the region of the hydrated network (2800-3700 cm^{-1}).

V.2.1.1. Effect of the temperature on the SiO$_x$N$_y$ network

The evolution of the SiO$_x$N$_y$ network as function of the SPT is shown in Fig. V.5, after FT-IR analysis performed at 60°. Multiple overlapping absorptions are once again encountered in this fingerprint region, but general trends can be observed visually. Similarly to what was presented for TDMSA (Fig. IV.11), the trends are symbolized with arrows indicating the shift of the peak position and the change in its intensity. The characteristic TO3-LO3 pair of the –Si–O–Si– network is noted as expected for oxide-type films [99, 187]. Interestingly, the Si–(CH$_3$)$_x$ absorption at ca. 1270 cm^{-1} is also noted, despite the TSAR precursor featuring predominantly Si–H bonds. It is proposed that the methyl moieties originate from the alkylamine chain found in the precursor molecule. The Si–N stretching vibration is also noted as a shoulder appearing at ca. 940 cm^{-1} [270, 271]. Various overlapping absorptions at 800 cm^{-1} are also observed,

The ellipsometry results of section V.1 revealed higher contents of nitrogen for films produced at the higher temperatures. This is reflected in the FT-IR spectra through the decrease of the LO3 and TO3 intensities and the parallel increase of the Si–N absorptions. Visually, the LO3-TO3 pair is not observed anymore for 650°C. At this temperature, the spectrum appears to be "shifted" towards lower wavenumbers. This is a result of the disappearance of absorptions above 1200 cm^{-1} and the increase in intensity of bonding states vibrating at frequencies lower than 1000 cm^{-1}.

The position and intensity of the separate absorptions are identified after deconvolution. As shown in Fig. V.5a, the LO3 mode shifts towards lower wavenumbers for increasing SPT and is not detected anymore at 650°C. For TO3, its position moves from 1034 to 1036 cm^{-1} from 550°C to 625°C. It then shifts down to 1006 cm^{-1} for 650°C. The TO3 component has been reported at this exact wavenumber in the literature, for silicon oxycarbide and carbonitride films by PECVD [303]. Additionally, referring back to Appendix 4, a peak at 1006 cm^{-1} could also be attributed to a Si–CH$_2$–Si stretching absorption, found normally at 1000-1020 and 1060 cm^{-1} [247, 250]. This assumption could correlate well with the disappearance of the LO3 component at 650°C and would translate in the decrease of the number of Si(O)$_4$ tetrahedra and the appearance of tetrahedra where at least one oxygen is substituted by carbon. A second assumption could be made, suggesting that the supplied quantity of O$_2$ is potentially already consumed in the gas phase by the time the gas reaches the sample probed by FT-IR (sample p1, local temperature: 650°C). Since the maximum DR is encountered at ca. 635°C for this SPT, that is, prior to sample p1, and because the DR begins to drop beyond that point, this proposal, i.e. that O$_2$ is potentially already consumed at the location where sample p1 is found, seems reasonable. The above-described decrease in Si(O)$_4$ tetrahedra is kept in mind and is discussed again in later sections.
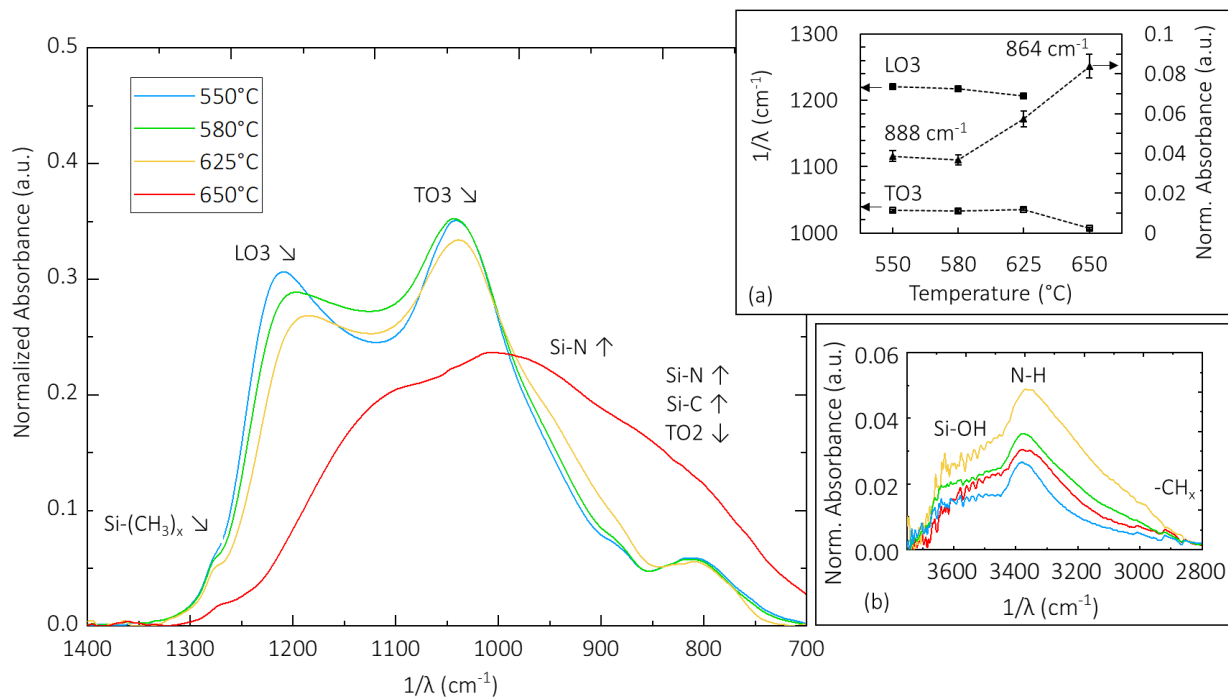
Fig. V.5. Evolution of the FT-IR fingerprint spectra of TSAR-O$_2$ films as a function of the SPT, analyzed for an incidence angle of 60°. Supplementary diagrams show evolution of LO3 and TO3 position and the intensity of the 888-864 cm^{-1} absorption after deconvolution (a), as well as the evolution of the hydrated network region (b).

In addition to the above, a new absorption is also noted at around 890 cm^{-1}, appearing as a small shoulder for SPT 550°C to 625°C. This shoulder has not been observed for any of the TDMSA films, but appears consistently for those produced from TSAR. Tracing its evolution after deconvolution of the spectra (Fig. V.5a) reveals that its intensity increases for higher SPT. In parallel, its position shifts from 888 to 864 cm^{-1}. This absorption has been associated with the asymmetric stretching of Si–N in Si–NH–Si groups or the Si–H wagging vibrational mode [304] in the literature and has been seen to shift by more than 50 cm^{-1}. Multiple articles mention its appearance at 840 cm^{-1} even and correlate it to Si$_3$N$_4$ [305, 306]. According to Behrens et al. [307], two local structures for SiO$_x$N$_y$ are suggested: the random mixture model (RMM) and the random binding model (RBM). RMM is identified by a mixture of randomly distributed SiO$_2$ and Si$_3$N$_4$ phases leading macroscopically to an amorphous SiO$_x$N$_y$. In RBM, "the bonds between Si, O and N constitute a fourfold coordination and represent a homogeneous Si–O–N network in five different tetrahedral configurations of SiO$_v$N$_{4-v}$, where v=0-4" [16, 307]. Multiple authors have correlated the appearance of the aforementioned asymmetric stretching Si–N absorption to Si$_3$N$_4$, and by extension to the RMM model. It is recalled that this newly appearing absorption was not observed for SiO$_x$N$_y$ films from

TDMSA. Based on the above information, it could be suggested that SiO$_x$N$_y$ from TDMSA follows the RBM and is comprised of various SiO$_v$N$_{4-v}$ tetrahedral configurations, while SiO$_x$N$_y$ from TSAR follows the RMM and is comprised of randomly mixed SiO$_2$ and Si$_3$N$_4$ "phases". Supplementary information from other characterization techniques is required to confirm this assumption, a point that is touched upon later.

The evolution of the spectra in the 2800-3700 cm^{-1} region, relating to the hydration of the network, is shown in Fig. V.5b. Since both Si–OH and N–H bonds absorb in this frequency range, no clear trend can be observed due to overlap. Ellipsometry revealed higher N incorporation at elevated temperatures, which could translate in larger concentrations of N–H. Overall, the intensity of the whole band appears to be increasing from 550°C to 625°C, beyond which it drops again for 650°C. It could therefore be assumed that from 550°C to 625°C the continuous enrichment of the films in nitrogen also introduces additional N–H bonds, increasing the intensity of the N–H stretching mode at 3400 cm^{-1} [270, 271, 281]. For high temperatures however (650°C), the additional supply of energy aids in the breaking of N–H bonds, facilitating network dehydration and densification. According to that scenario, the intensity of the whole band decreases due to lower N–H concentrations. This in turn also results in lower –N–H···N– hydrogen bonds, which are responsible for the "tail" appearing at ~3300-3400 cm^{-1}. Alternatively, it is also possible that deposition at 650°C proceeds through intermediates that do not contain N–H. This point is kept in mind for later. The Si–OH bonded to H$_2$O and the free Si–OH stretching modes absorbing at around 3500 and 3650 cm^{-1} respectively are also noted [8, 270, 271]. No clear evolution with the temperature can be discerned. Lastly, weak absorptions at 2800-3000 cm^{-1} are also observed [89, 214, 308], further indicating the slight incorporation of methyl moieties from the alkylamine chain.

V.2.1.2. Effect of the O$_2$ flow rate on the SiO$_x$N$_y$ network

An investigation similar to the one above is also carried out for films produced by the TSAR-O$_2$ chemistry, under O$_2$ flow rates varying between 0 and 0.6 sccm at a constant SPT of 550°C. The evolution of the various bonding states is shown in Fig. V.6.

The characteristic TO3-LO3 pair is encountered once more in the two experiments utilizing O$_2$ in the inlet gas composition, but disappears for 0 sccm O$_2$. The spectrum appears to shift towards lower wavenumbers for decreasing concentrations of O$_2$. Previously, this behavior was encountered for 650°C, a temperature at which the network is rich in nitrogen. Similarly, the nitrogen content of the films is also increased for 0 sccm O$_2$, and a FT-IR spectrum with no LO3-TO3 is probed. After deconvolution, the position of the LO3 and TO3 components is identified (Fig. V.6a). The LO3 mode shifts towards lower wavenumbers for lower O$_2$ flow rates and is not probed anymore for 0 sccm O$_2$. The LO3 disappearance

was previously noted for 650°C (Fig. V.5a). This behavior is attributed to the reduction in oxide character in the films and the gain in nitrogen content. For TO3, its position decreases from 1034 to 1029 cm^{-1} for 0.6 and 0.3 sccm respectively. At 0 sccm O$_2$, the vibration shifts significantly down to 1006 cm^{-1}. The exact same vibration was probed previously for 650°C. Thus, the same assumptions are made, proposing that the TO3 shift down to 1006 cm^{-1} relates to a decrease in Si(O)$_4$ tetrahedra and the potential appearance of a Si–CH$_2$–Si mode. This is highly likely, considering the disappearance of the LO3 component for 0 sccm O$_2$. The similarity of this absorption between the spectra of 650°C and 0 sccm O$_2$ could confirm that the O$_2$ in the gas phase for SPT 650°C has already been consumed once the gas reaches the isothermal region.
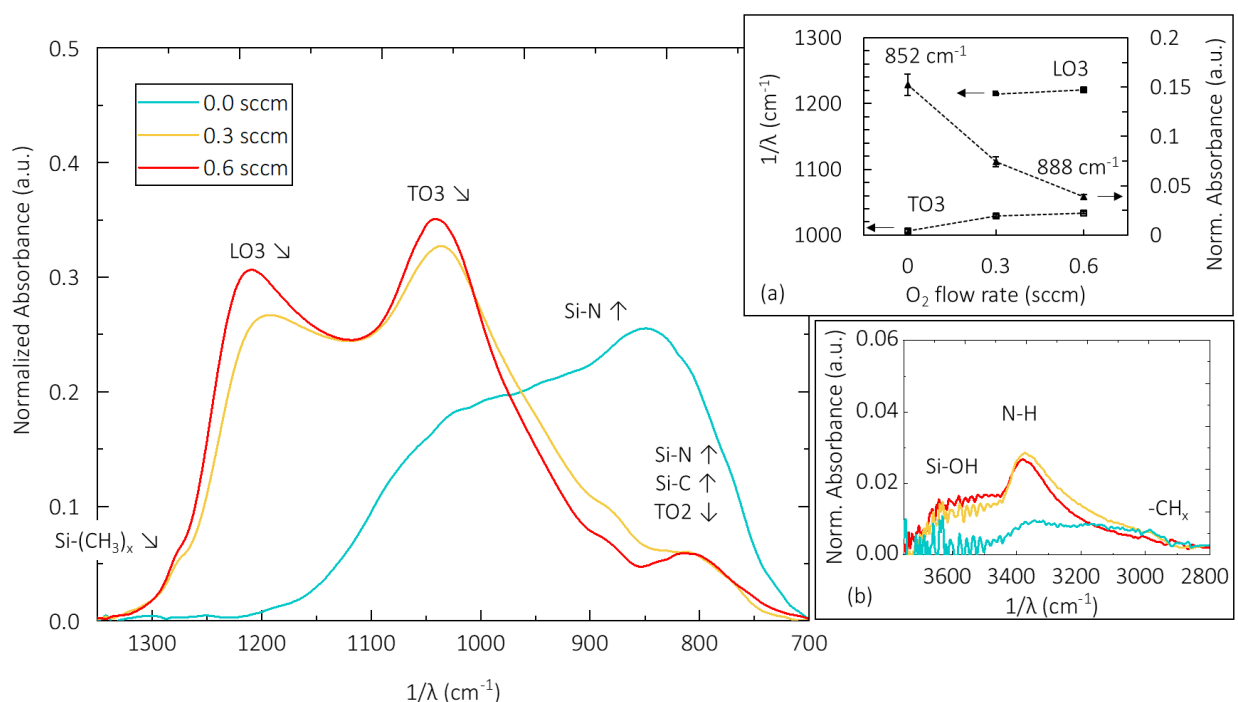
Fig. V.6. Evolution of the FT-IR fingerprint spectra of TSAR-O$_2$ films produced under various O$_2$ flow rates, analyzed for an incidence angle of 60°. Supplementary diagrams show evolution of LO3 and TO3 position and the intensity of the 888-852 cm^{-1} absorption after deconvolution (a), as well as the evolution of the hydrated network (b) as a function of the O$_2$ flow rate.

Fig. V.6 also reveals the Si–(CH$_3$)$_x$ absorption appearing as a shoulder at around 1280 cm^{-1}. Its intensity drops significantly at 0 sccm O$_2$, with its position having shifted from 1280 to 1250 cm^{-1}. In terms of nitrogen incorporation, the Si–N stretching vibration is once again noted as a shoulder appearing at around 940 cm^{-1} [270, 271], next to the newly reported asymmetric stretching Si–N absorption appearing

as a second shoulder at ca. 890 cm^{-1} [304]. Tracing of its evolution after deconvolution (Fig. V.6a) shows once more increasing intensities for lower O$_2$ flow rates, a trend that can be correlated to the increase in nitrogen incorporation. Reduction of the O$_2$ supply in the gas phase also shifts this absorption position from 888 cm^{-1} (at 0.6 sccm) to 852 cm^{-1} (at 0 sccm). As previously mentioned, the appearance of this asymmetric stretching Si–N absorption could indicate a RMM configuration, comprised of randomly mixed SiO$_2$ and Si$_3$N$_4$.

The evolution of the spectra relating to the hydration of the network is shown in Fig. V.6b. Once again, a clear trend is difficult to observe due to the simultaneous contributions of Si–OH and N–H bonds in this frequency range. However, the spectra present a distinctly different shape for 0 sccm O$_2$. The intensity of the whole band is greatly reduced, which is a bit unexpected given that the higher N content of the film should result in a relative increase of the N–H absorption. Since the temperature was kept constant, the decrease in N–H is directly correlated to the absence of O$_2$ in the gas phase. It could therefore be speculated that incorporation of nitrogen, when in an oxidizing gas phase, proceeds through an intermediate that contains N–H groups, which fits the description of the nitrogen contained in the alkylamine chain. This assumption correlates in fact well with the higher Si–(CH$_3$)$_x$ absorption noted under higher O$_2$ flow (Fig. V.6), and means that, under oxidizing atmospheres, the N–H$_x$ and –CH$_3$ groups of the alkylamine chain are introduced in the films through the same intermediate.

Lastly, the plateau between 3450 and 3650 cm^{-1} (Si–OH:H$_2$O and free Si–OH absorptions) is also noted, appearing almost constant at 0.6 sccm, but presenting a more prominent slope when the O$_2$ supply in the inlet gas composition is decreased. At 0 sccm O$_2$, even though the spectra show a lot of noise, the Si-OH stretching mode found at 3650 cm^{-1} appears to have decreased significantly, as expected for a film produced under an oxidant-free atmosphere.

V.2.1.3. Presence of Si–H

Given that the TSAR precursor contains more Si–H bonds in its structure compared to the TDMSA molecule, a closer inspection of the two main regions where this bond absorbs, is advised, in order to investigate if higher incorporation of Si–H is taking place. These two regions pertain first to the 620-650 cm^{-1} range, where the wagging/rocking Si–H vibrational mode is encountered [309, 310], and then to the 2000-2250 cm^{-1} range, where the Si–H stretching mode is found to absorb more prominently [275]. Fig. V.7 shows FT-IR spectra of TSAR-O$_2$ films produced under different conditions, focusing on the 2000-2250 cm^{-1} range. A TDMSA-O$_2$ film produced at SPT 650°C (run TD7) is also included for comparison.
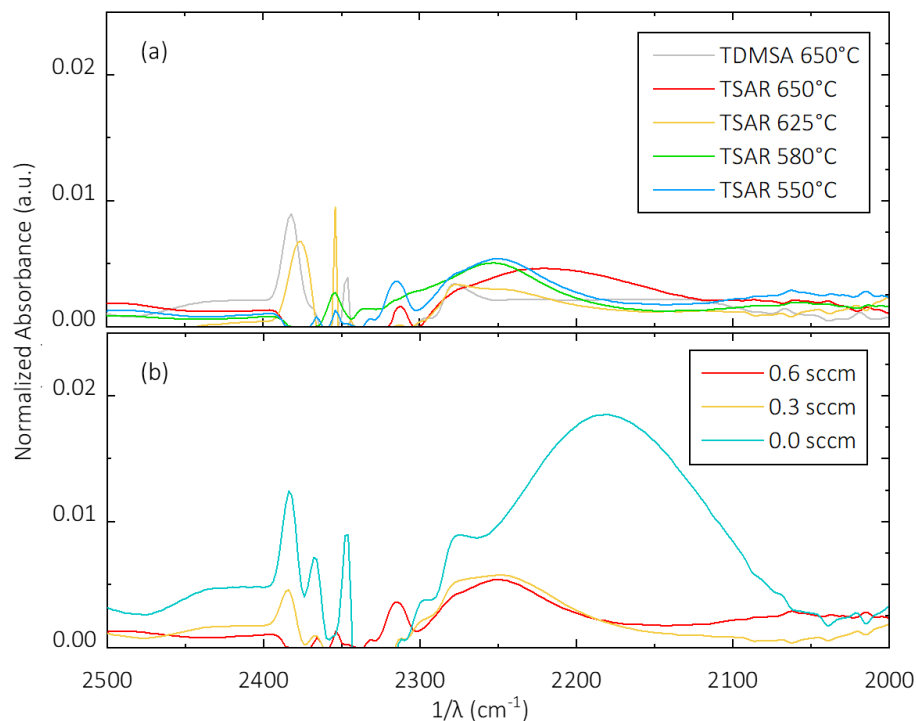
Fig. V.7. Evolution of the Si–H stretching mode in SiO$_x$N$_y$ films from TSAR and TDMSA as a function of the SPT, under a constant O$_2$ flow rate of 0.6 sccm (a). Influence of the O$_2$ flow rate on the Si–H stretching mode in SiO$_x$N$_y$ films from TSAR, produced at a constant SPT of 550°C (b).

In the first set of results (Fig. V.7a), no Si–H absorption is noted for the TDMSA film. The small peak appearing at around 2280 cm^{-1} is attributed to the incompletely removed CO$_2$ background signal from the atmosphere [195, 196]. Broad absorption bands are noted for the TSAR films however, spanning between 2100 and 2300 cm^{-1}. No clear trend exists for the Si–H stretching mode as a function of the temperature. The very broad absorption for 650°C is noteworthy.

When inspected as a function of the O$_2$ flow rate at a constant SPT of 550°C (Fig. V.7b), a clearer trend for the Si–H absorption is observed. It appears to increase in intensity with decreasing O$_2$ supply, showing a very prominent absorption for the sample produced in absence of O$_2$ in the gas phase. Thus, it can be concluded that the presence of O$_2$ gas tends to dehydrogenate the species contributing to film formation. Moreover, when O$_2$ is supplied in the gas phase (0.3 and 0.6 sccm), the Si–H absorption is centered around 2250 cm^{-1}. Under an oxidant-free atmosphere however, its position visibly shifts to lower wavenumbers and its intensity increases. The same behavior is noted for the Si–H absorption from TSAR at SPT 650°C (Fig. V.7a), the center of which appears to have shifted down to ca. 2225 cm^{-1}. This shift could indirectly indicate that a considerable consumption of the supplied O$_2$ takes place for 650°C. This

assumption correlates well the previous discussions on how the similarity between the SPT 650°C and 0 sccm O$_2$ spectra indicate a significant O$_2$ consumption in the gas phase of the former.

V.2.2. SiO$_x$N$_y$ composition from IBA techniques

More accurate composition results are obtained by Ion beam analysis (IBA) techniques. The p2 sample position was systematically analyzed to compare compositional changes across experiments directly, without locality effects. An additional sample, pG (Fig. V.1), produced for SPT 650°C and 0.6 sccm O$_2$ (run AR1) was also analyzed, to compare the influence of the sample position between it and sample p2. Since sample pG is located outside the isothermal region, its local temperature for SPT 650°C is 605°C. Thus, interconnected effects from sample position, local temperature and local gas phase composition are expected.

The influence of a variable deposition temperature (runs AR1 to AR4) on the atomic percentage for each element is presented in Fig. V.8a. The presence of carbon is noted. Given that carbon is encountered only in the alkylamine chain, the IBA results confirm that this part of the precursor is indeed involved in the deposition process. Low percentages spanning from 3.1 to 5.3 at.% C are noted between 550°C and 625°C. The relatively low content in carbon explains why the utilized ellipsometry model did not require the addition of a carbon component. However, incorporation of carbon increases visibly at 650°C, reaching 12.5 at.%. Similar behavior is noted for hydrogen, with its atomic percentage increasing from 5.0 at.% at 550°C, to 15.4 at.% at 650°C. The similar trend across these two elements could indicate that they are inserted in the film through a common intermediate species. At the same time, it is recalled that low absorptions of Si–(CH$_3$)$_x$ were indeed probed by FT-IR, along with Si–H and N–H absorptions.

Nitrogen incorporation on the other hand follows a non-monotonous behavior. The same evolution, although reversed, is noted for oxygen, illustrating well the competitive incorporation between O and N. A nitrogen content between 7.1 and 16.9 at.% is probed. The lack of linearity, evident in the spike at 605°C, potentially hints at the incorporation of nitrogen through different intermediates, depending on the temperature and the local gas phase composition.

The drop in oxygen content at 650°C is also pointed out. This result correlates well with previous discussions of the FT-IR data, where the disappearance of the LO3 peak and the shift of the TO3 position to 1006 cm^{-1} was speculated to be caused by the consumption of O$_2$ in the gas phase and a decrease in the oxide character of the films. In parallel, the IBA results at 650°C reveal that the decrease of O$_2$ in the gas phase allows incorporation of N, C and H, which is expected, given the N/O and C/O competition. Interestingly, the Si content of the films decreases with increasing temperature.
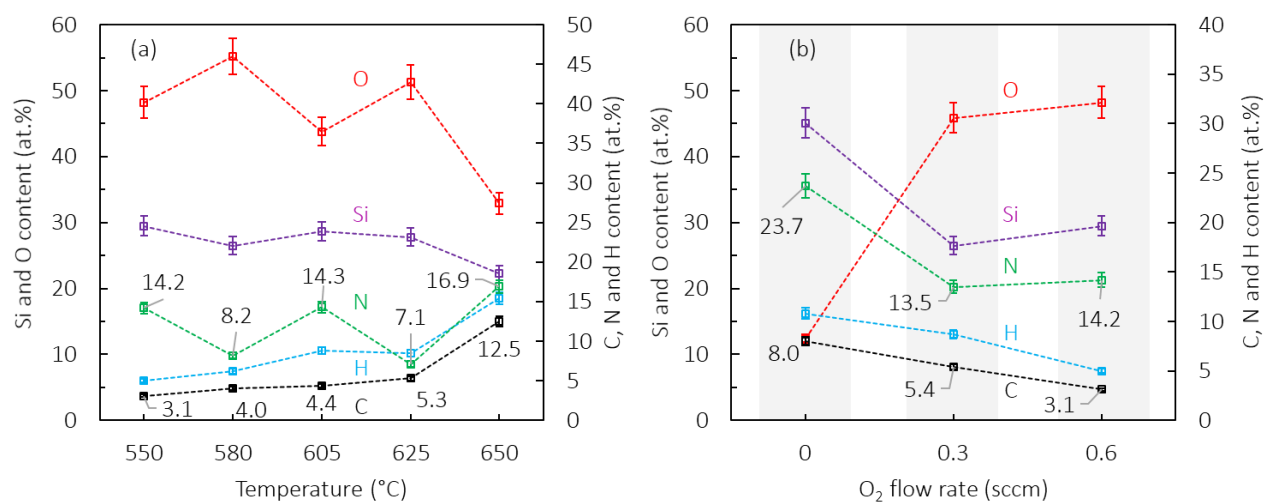
Fig. V.8. Evolution of film composition by IBA. Influence of the local temperature under a constant O$_2$ flow rate of 0.6 sccm (a). Influence of the O$_2$ flow rate, at 550°C (b).

The effect of the O$_2$ flow rate (runs AR2, AR5 and AR6) on the atomic percentages of each element is investigated more closely in Fig. V.8b, by keeping the deposition temperature fixed at 550°C. Almost linear trends are noted for H and C, with their percentages decreasing as more O$_2$ is added in the inlet gas composition. It is concluded that O$_2$ reduces carbon incorporation and/or cleaves organic moieties, as is well known in CVD. Nitrogen and silicon on the other hand follow a non-monotonous behavior, which is however very comparable between the two elements. The discussion of Fig. V.3 proposed that, at temperatures up to 580°C, incorporation of N and Si is taking place through the same species. The IBA results reveal that this could indeed be the case, with the two elements following very similar trends. Nitrogen content spans from 13.5 to 23.7 at.% N. Oxygen content on the other hand ranges from 48.2 at.% at 0.6 sccm O$_2$, down to 12.4 at.% at 0 sccm O$_2$. The presence of oxygen in the films, despite the O$_2$-free inlet gas composition, could be the result of a leak or O$_2$/H$_2$O desorption from the reactor walls, as was previously discussed. It could also original from surface oxidation upon exposure to air. The low oxygen content is in alignment with the FT-IR results of Fig. V.6 that illustrated the decreased oxide character of the films based on the disappearance of the LO3 component and the shift of the TO3 position to lower wavenumbers.

The (O+N+C)/Si atomic ratio is also briefly discussed. At 0.6 and 0.3 sccm O$_2$, this ratio is equal to 2.2 and 2.4, respectively. At 0 sccm O$_2$ however, the (O+N+C)/Si atomic ratio drops to 1. Indeed, the Si content increases from 29.5 at.% at 0.6 sccm O$_2$, to 45.1 at.% at 0 sccm. It is concluded that the absence of

oxygen in the inlet gas composition results in silicon-rich films. Since similarities have been observed between the films at 0 sccm O$_2$ and the films at 650°C, one could assume that films produced in the isothermal of SPT 650°C are also slightly rich in silicon, as a result of the consumed O$_2$ in the gas phase. This correlates well with the discussion at the start of this chapter, where it was proposed that the higher refractive indexes measured by ellipsometry could be induced by a silicon-rich network instead of being solely the result of high nitrogen content.

V.2.3. X-ray photoelectron spectroscopy

XPS analyses were carried out by Takashi Teramoto at Air Liquide, Innovation Campus Tokyo, Japan. Although in-depth analysis of the results is still in progress at the time of the present writing, some initial information is discussed, as it can help confirm previous assumptions made during the discussions of the ellipsometry, FT-IR and IBA results. Additional information on the incorporation of carbon is also provided.

Elemental analysis by XPS is performed after an etching of the surface for 240 s, in order to assure analysis in the bulk of the material. Globally, the produced results replicate the trends revealed by ellipsometry and IBA, namely that nitrogen incorporation increases with the deposition temperature and decreases for higher O$_2$ flow rates. At the highest O$_2$ flow rate, the films have a predominant Si–O–Si character. In terms of carbon content, 3.7 at.% C is probed at 550°C, increasing to 14.1 at.% for 650°C. These values are very close to the ones noted by IBA in Fig. V.8a. Under varying O$_2$ flow rates, the 3.7 at.% C probed previously at 550°C for 0.6 sccm O$_2$ increase to 9.8 at.% when no O$_2$ is supplied in the inlet gas composition. XPS slightly overestimates the 8.0 at.% C probed by IBA for this experiment, but such deviations are expected given that the former technique does not consider hydrogen.

XPS also provides valuable information on the chemical environment of the elements. Deconvolution analysis was executed by Jerome Esvan (CIRIMAT, ENSIACET, Toulouse), with the aid of the CasaXPS$^©$ software. Table V.2 includes a list of all considered bonding states identified with the help of the literature [253, 276, 277, 311].

The deconvolution results allow the tracking of Si–O$_x$–C$_x$, O–Si–N–O and other bonding states. Consideration of the spectra as a function of the O$_2$ flow rate reveals that the Si(O)$_4$ bonding state decreases when O$_2$ supply is decreased from 0.6 to 0.3 sccm, in favor of an increase in Si–O$_x$–C$_x$, O–N–Si and O–Si–N–O. The competitive incorporation of N and O is once more encountered. At 0 sccm O$_2$, no Si(O)$_4$ bonding state is probed anymore, which is favorably coherent with the absence of the LO3 component in the FT-IR spectra (Fig. V.5 and Fig. V.6) and the "shift" of the TO3 bond to 1006 cm^{-1}.

Table V.2. XPS deconvolution analysis of SiO_xN_y films produced by TSAR-O_2 at 550°C under variable O_2 flow rates.

Bonding state		O$_2$ flow rate (sccm)					
		0.6		**0.3**		**0**	
		Binding energy (eV)	Atomic %	Binding energy (eV)	Atomic %	Binding energy (eV)	Atomic %
Si2p	Si-Si/Si-Si-C	-	-	-	-	100.20	4.20
	SiO$_x$C$_x$ (x≈2)	101.40	0.66	101.41	0.85	101.50	9.36
	SiN$_x$	-	-	-	-	102.23	35.84
	O-N-Si-O	102.40	4.16	102.60	5.96	-	-
	Si(O)$_4$	103.45	29.52	103.67	27.90	-	-
C1s	Si-C	-	-	-	-	281.95	0.25
	SiO$_x$C$_x$ (x≈2)	283.70	0.68	283.69	0.59	283.89	8.33
	CC or CH	284.76	1.39	284.65	2.43	-	-
	C-C	-	-	-	-	285.11	1.28
	C-O	286.15	0.93	286.00	0.93	-	-
	C=O	287.98	0.40	287.51	0.75	286.78	0.21
	O=C-O	289.49	0.31	289.60	0.47	-	-
N1s	N-Si$_x$	-	-	-	-	398.18	25.73
	O-N-Si	398.84	4.47	398.89	6.18	-	-
	O-N-Si$_2$	-	-	-	-	399.70	0.94
	N-O	401.19	0.14	401.06	0.25	-	-
	O1s	533.02	57.32	533.06	53.68	532.50	13.84

In light of the XPS results, one can safely conclude that the absorption at 1006 cm^{-1} should rather be attributed to the Si–CH$_2$–Si absorption instead. Additionally, the N–Si bonding state appears in the N1s and Si2p spectra for 0 sccm O$_2$. A noticeable increase in Si–O$_x$–C$_x$ in both Si2p and C1s spectra is observed in oxidant-free atmospheres too, confirming the previous assumption that the shift of the TO3 component down to 1006 cm^{-1} relates to a decrease in Si(O)$_4$ coordination and potential insertion of carbon in the tetrahedra (Fig. V.5a and Fig. V.6a). This is in agreement with the appearance of the Si–C bonding state for the C1s spectrum at 0 sccm O$_2$. Another new state appears in the spectral deconvolution of the Si2p and

C1s spectra, namely Si–Si–C. The presence of a Si–Si–C bonding state at these conditions correlates well with the silicon-rich composition revealed by the IBA results and confirms the initial assumption made at the start of section V.1, where it was proposed that the higher RI was biased by high Si contents. Ultimately, it appears that the presence or absence of O$_2$ in the gas phase plays a key role in the chemical structure of the film-forming intermediates and consequently the chemical environment of the resulting SiO$_x$N$_y$ material.

V.2.4. *Influence of composition on wettability and mechanical properties*

V.2.4.1. Mechanical properties

Nanoindentation analysis is performed on samples taken from the isothermal region, that is, a local temperature of 650°C, of experiment AR7 (Table V.1). The particular evolution of the nitrogen content along the length of the reactor as a result of the evolving gas-phase composition is utilized to extract multiple measurements from just one single experiment. Results on the hardness H and elastic modulus E of the SiO$_x$N$_y$ films from TSAR-O$_2$ are shown in Fig. V.9.
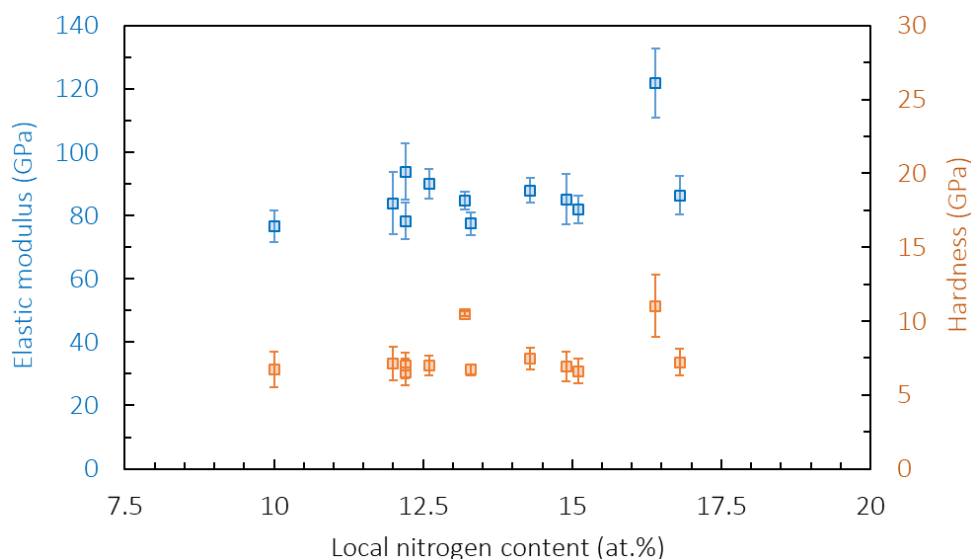
Fig. V.9. Influence of the local nitrogen content on the elastic modulus E and hardness H of TSAR-O$_2$ films produced at 650°C and 0.6 sccm O$_2$.

Given that the temperature remained constant in this region, any change in mechanical properties can be safely attributed to the change in local film composition and, consequently, the resulting network

structure. However, regardless of the evolving composition and increasing nitrogen content along the length of the reactor, both H and E values appear to remain constant within certain ranges. Hardness values span between 6.6 and 11.0 GPa, while elastic modulus values measure from 76.6 up to 121.8 GPa. Both values are higher than those measured for the TDMSA precursor at the same temperature and O_2 flow rate. If the "outliers" are ignored, it could be assumed that the relatively flat behavior is due to the nitrogen content surpassing a minimum required value. It is recalled H and E results from TDMSA (Fig. IV.12) increased with increasing nitrogen incorporation up to ca. 7 at.%, after which they seemed to stabilize. Perhaps a similar behavior is exhibited with TSAR and the flat evolution is the result of the nitrogen content exceeding 7 at.%. On the other hand, the measured mechanical properties are notably lower than those of Si_3N_4 produced by PECVD [312], which is to be expected given the stiffer network structure of stoichiometric Si_3N_4. Regardless, they are comparable to values obtained from PECVD SiO_xN_y films with up to 10 at.% N [278].

The dispersion of the acquired values is also discussed. It is speculated that this is the result of local compositional inhomogeneities. The previous discussion of the FT-IR results of section V.2.1 is recalled. Samples produced either at 550°C and 0 sccm O_2 (run AR2), or at 650°C and 0.6 sccm O_2 (runs AR1 and AR7), the latter of which applies for the nanoindentation films, showed the appearance of an asymmetric stretching Si–N bond that has been linked to the Random Mixture Model (RMM). It is therefore proposed that the deviations and spikes of the H and E values originate from regions rich in a Si_3N_4 "phase". A co-existence of amorphous oxynitride and crystalline Si_3N_4 phases in SiO_xN_y films produced by PECVD was recently reported in the literature [278]. The authors additionally mention the appearance of silicon-rich compositions. This is coherent with our XPS and IBA results that revealed an excess of Si content and the presence of a Si–Si bonding state under an oxidant-free atmosphere. High-resolution TEM (HRTEM) analysis is currently underway to provide further information.

V.2.4.2. Surface wettability

Water wettability measurements performed on various SiO_xN_y films of the TSAR-O_2 chemistry are presented in Fig. V.10. The global water contact angle (WCA) of samples produced at different temperatures is measured between 53.5 and 57.0° (Fig. V.10a). The films are globally hydrophilic and present a relatively flat behavior with most values lying within the error bars. No particular behavior in terms of deposition temperature can be concluded. When deposition temperature is fixed at 550°C, WCA values range between 55.9 and 63.2° depending on the O_2 flow rate (Fig. V.10b). Comparing all of the above values for SiO_xN_y films from TSAR to those from TDMSA (76.9-89.4°) reveals that the latter are

less hydrophilic. The difference in the wettability behavior of these two oxynitride types lies most probably in their different organic content, although multiple other factors such as surface roughness also play a role.
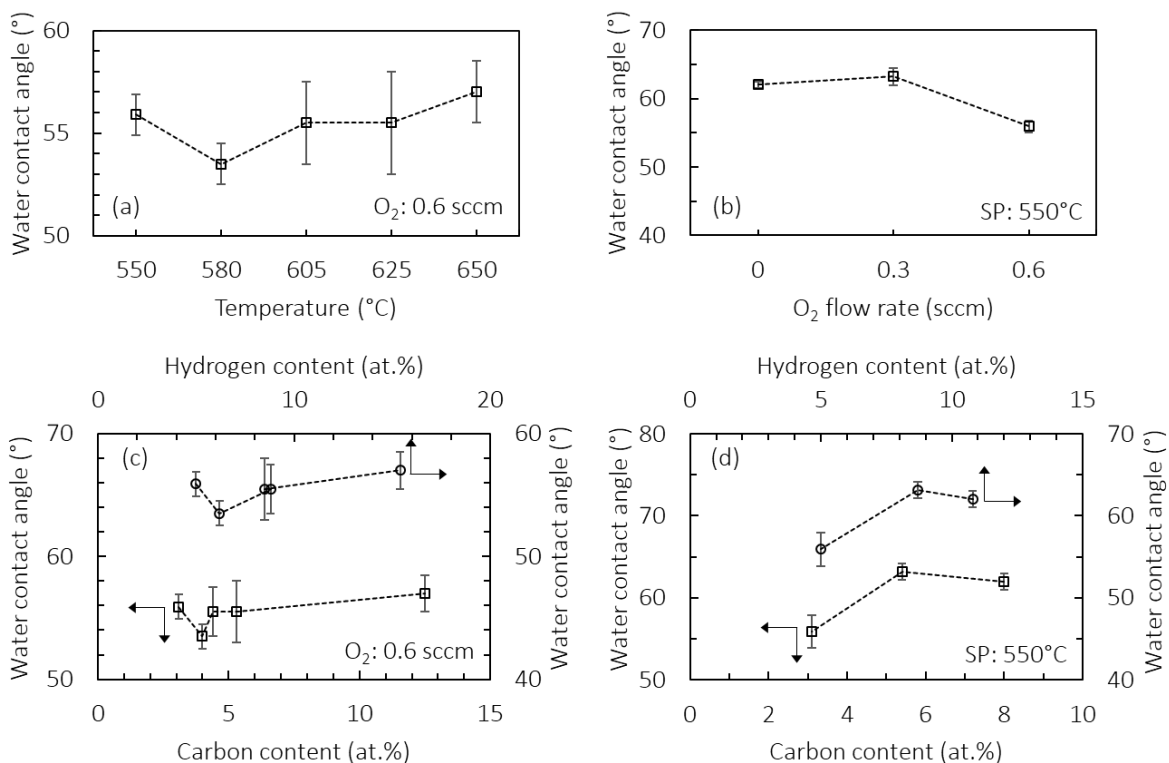
Fig. V.10. Water wettability of multiple SiO$_x$N$_y$ films from TSAR-O$_2$. Evolution of the contact angle as a function of the temperature for a constant 0.6 sccm O$_2$ flow rate (a), and the O$_2$ flow rate for a constant temperature of 550°C (b). Representation of wettability results as a function of the carbon and hydrogen content (c) and O$_2$ flow rate variable results (d).

Plotting of the above WCA values from TSAR-O$_2$ SiO$_x$N$_y$ films as a function of the nitrogen content was attempted, but no clear correlation was found. In contrast, trends can be inferred when the two sets of results are plotted based on the atomic C and H percentages (Fig. V.10c and d). It appears that for both sets, i.e. a variable temperature or a variable O$_2$ flow rate, WCA increases with the C and H contents. This is not surprising given that the presence of organic –CH$_3$ moieties tends to increase the contact angle [280]. The trends are not completely linear, which is not a surprise since carbon and hydrogen are involved in multiple species (Si–C–Si, N–H, Si–H, Si–OH) and are not found solely in organic moieties. Lastly, although the presence of Si–H has been linked to a reduction in wettability (i.e. higher WCA) [282, 285],

no such correlation was found, and plotting of the WCA versus the absorbance at 2100-2250 cm^{-1} (Si–H) showed great dispersion.

V.3. Corrosion resistance of SiO$_x$N$_\gamma$ films from TSAR

V.3.1. Global Buffered Oxide Etchant (BOE) results

The wet corrosion resistance of films from the TSAR-O$_2$ chemistry is assessed by immersion in the buffered oxide etchant (BOE) 6:1 solution, with the aim to compare them directly to the other chemistries studied previously in section IV.1.7. The global results are presented in Fig. V.11, featuring the etching rates obtained from all film types produced in this thesis, under various deposition temperatures and conditions, plotted as a function of their atomic content in nitrogen as measured by ellipsometry.
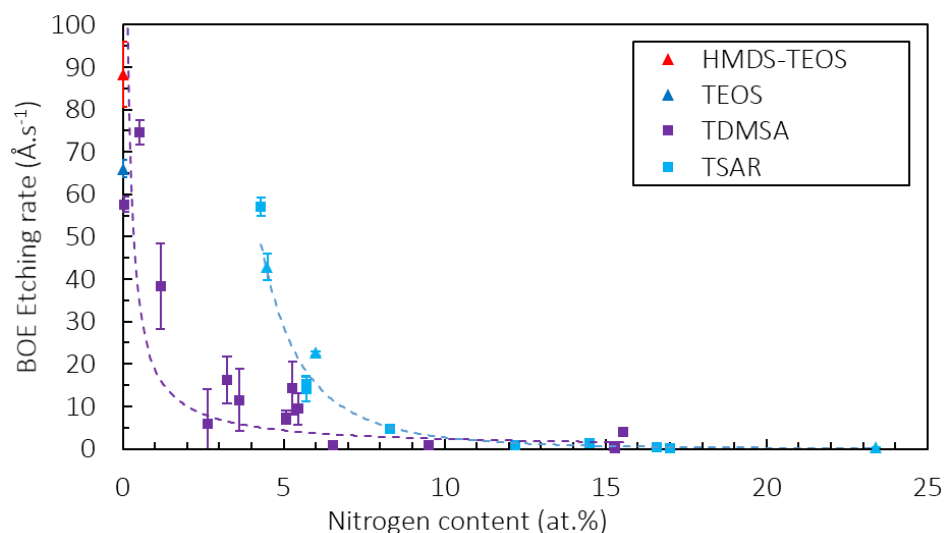
Fig. V.11. BOE etching rate of SiO$_x$N$_y$ films from TSAR (light blue squares and triangles), TDMSA (purple squares), as well as SiO$_2$ and SiO$_x$ films from TEOS (dark blue triangle) and HMDS-TEOS (red triangle), respectively. Power trend lines added for visual aid. All triangle symbols refer to a deposition temperature of 550°C.

Fig. V.11 reveals that the BOE etching rates of the TSAR precursor are overall lower than those of the HMDS-TEOS (ca. 88 Å.s^{-1}) and TEOS samples (ca. 66 Å.s^{-1}). Similarly to the etching rates observed

for TDMSA, progressive incorporation of nitrogen in the silica network results in decreasing BOE etching rate values for TSAR as well, ranging from 57 Å.s^{-1} down to 0.2 Å.s^{-1}, depending on the nitrogen content and the specific deposition conditions. Although produced at different conditions and from a different chemistry, the measured etching rates of the SiO$_x$N$_y$ films from TSAR are in the same order of magnitude as those noted in the literature (Table IV.4). For the TSAR chemistry, the BOE etching rates start converging towards values below 4 Å.s^{-1} at approximately 9 at.% N. The equivalent convergence is reached earlier for the TDMSA chemistry, at ca. 7 at.%. The power trend lines serve as a visual guide to illustrate this. These results indicate that below 9 at.% N, films from the TDMSA precursor present an improved and more efficient corrosion resistance compared to those from TSAR. This behavior can be attributed to multiple factors. One could be the higher DR from TSAR, which could translate to less dense films with larger amounts of nanoporosities. Thus, even if the nitrogen content is at a similar value, the TSAR films are more susceptible to corrosive attack by a hydrofluoric solution. However, beyond 9 at.% N, both chemistries behave similarly and present an excellent corrosion resistance. Further incorporation of nitrogen beyond this point does not appear to be necessary. Moreover, in contrast to TDMSA, TSAR allowed the study of the corrosion behavior of SiO$_x$N$_y$ films at lower deposition temperatures (<600°C), which are appropriate to coat pharmaceutical vials. Thus, the above information can help define operating conditions for performance optimization. Obviously, multiple factors influence the BOE etching rate, such as SPT, inlet gas composition and flow rates. The following section breaks down the above results into sets of data, each studying the effect of different operating conditions on the etching rate.

V.3.2. *Effect of deposition conditions and comparison to TDMSA*

The etching rates of Fig. V.11 were measured from films that have been processed under a variety of operating conditions. Although the link to the nitrogen content is well established, it shall be mentioned that plotting of the BOE values versus the DR did not yield any clear correlation. For further analysis, a closer look at how the specific experimental conditions affect the BOE etching rate is presented in Fig. V.12. Comparisons with films from TDMSA are also drawn.

Fig. V.12a examines the evolution of the etching rate across 6 samples from the same experiment (AR1, SPT 650°C, 0.6 sccm O$_2$) as a function of their nitrogen concentration. The local temperature of each sample is also noted, in order to consider the thermal gradient existing along the length of the reactor. For a sample produced outside the isothermal region with a local temperature of 560°C and a nitrogen content of 5.7 at.%, a BOE etching rate of 15.3 Å.s^{-1} is noted. Then, samples closer to and within the isothermal region (646 and 650°C), show etching rates below 1.2 Å.s^{-1}. Their content in nitrogen exceeds 14.5 at.%. Globally, a decreasing trend is observed for a simultaneous increase in temperature and nitrogen content,

similarly to what was noted previously from TDMSA and the literature [291]. The improvement in corrosion resistance is attributed to the lower hydration of the network and the resulting densification at higher deposition temperatures, with the parallel increase in nitride character. No clear break in the slope is observed, contrary to the respective results from TDMSA (Fig. IV.15a).
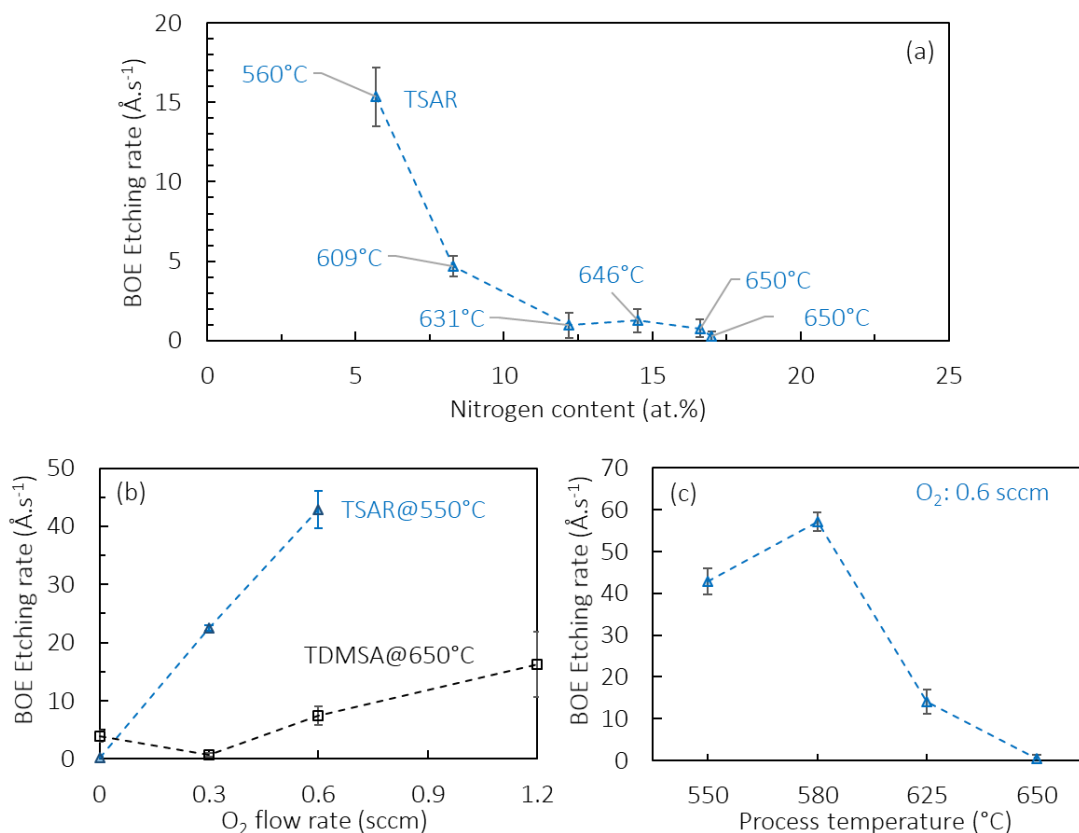
Fig. V.12. BOE etching rate of SiO$_x$N$_y$ films from TSAR-O$_2$, produced at SPT 650°C and an O$_2$ flow rate of 0.6 sccm (AR1), plotted as a function of the nitrogen content along the length of the reactor (a). BOE etching rate of SiO$_x$N$_y$ films from TSAR and TDMSA for variable O$_2$ flow rates (b), and of TSAR-O$_2$ films for 0.6 sccm O$_2$, as a function of the SPT (c).

Fig. V.12b examines the effect of the O$_2$ flow rate on the BOE etching rate, under a constant deposition temperature. When no O$_2$ is added in the inlet gas composition, a BOE etching rate of 0.2 Å.s^{-1} is noted for films from TSAR at 550°C. It is recalled that, although IBA revealed 12.4 at.% O in these films, XPS and FT-IR results respectively showed the absence of the Si(O)$_4$ bonding state and the LO3-TO3 pair. Thus, this low etching rate can be linked to the higher nitride character of the film. An increase of the O$_2$

supply to 0.6 sccm reduces the corrosion resistance of the films, with the BOE etching rate increasing abruptly to 42.8 Å.s^{-1}. A similar upwards trend is also followed by the TDMSA-O$_2$ chemistry. The increase of the BOE etching rate with the O$_2$ flow rate reflects the reports in the literature [180]. It is worth noting that the slope from TDMSA is less steep than the one noted for TSAR. Examining this slope can help assess how sensitive the film corrosion resistance from each chemistry is to further addition of O$_2$. The steeper slope observed for TSAR illustrates that films produced from this precursor are more strongly impacted by the addition of O$_2$ in the gas phase. This could be related to the lower deposition temperature (550°C). The overall upwards trend under higher O$_2$ flow rates (Fig. V.6b) can also be linked to the higher hydrogenation of the incorporated nitrogen (i.e. –N–H), which is speculated to be taking place through film formation characterized by the participation of the alkylamine chain, as was discussed in section V.2.1. Given that the presence of N–H groups has been reported to be detrimental to the corrosion resistance of SiN$_x$ films [313] and translates to a less dense network, the higher BOE etching rates for TSAR noted at increasing O$_2$ flow rates are coherent with this assumption.

Lastly, Fig. V.12c presents the corrosion performance of the films as a function of the SPT, for a contant O$_2$ flow rate of 0.6 sccm. When deposition is performed at 550°C, a BOE etching rate of 42.8 Å.s^{-1} is noted, increasing to 57.1 Å.s^{-1} at 580°C. This result is unexpected, since higher temperature normally results in increased densification of the network. To better understand this behavior, the IBA composition results are recalled (Fig. V.8a). The film at 580°C was noted to contain lower nitrogen (8.2 at.%) than the one at 550°C (14.2 at.%). This difference could explain the decreased corrosion resistance of the former. Upon further increase of the temperature, the BOE etching rate decreases once more, reaching 0.5 Å.s^{-1} at 650°C. These results reflect well the combined effect of the deposition temperature and N incorporation in the performance of the films against corrosion.

V.4. Conclusion

This final chapter explored anew the deposition of SiO$_x$N$_y$ films, with the goal to go below the usual thermal ranges for SiO$_x$N$_y$ film production by thermal CVD. A novel chemistry was utilized, based on a proprietary trisilylamine-derivative precursor, TSAR, developed by Air Liquide. The presence of multiple Si–H bonds in this precursor molecule increased its reactivity by up to one order of magnitude and enabled film formation at temperatures much lower than those noted when using TDMSA. More specifically, high DRs of up to 10.3 nm.min^{-1} were achieved, a value that is rarely encountered in thermal

CVD of SiO_xN_y films at temperatures below 700°C. Incorporation of nitrogen was successful as well, starting at temperatures as low as 520°C. Similarly to TDMSA, the TSAR precursor fulfills a dual role as silicon and nitrogen provider and showed a more efficient nitridation of the films. A parametric analysis was executed to investigate the effect of the deposition temperature and the O_2 flow rate on the film composition and material properties. With increasing deposition temperatures, the films are enriched in nitrogen and film formation takes place at a higher rate. Increase of the O_2 flow rate also promotes deposition, but reduces nitrogen incorporation, due to the competitive pathways for O and N insertion in the films.

The above transition from an oxide to a nitride character and vice versa was also confirmed by FT-IR. The participation of the alkylamine chain in the deposition process was confirmed through the detection of N–H and –CH_3 bonds. Higher N–H contents were probed for higher O_2 flow rates, indicating a potential reaction between the alkylamine chain and O_2. Additionally, a new absorption was probed at ca. 888 cm^{-1}, attributed most likely to an asymmetric stretching Si–N vibration and is speculated to hint at a random mixture model (RMM) configuration of the network. In contrast to TDMSA, films produced from TSAR also revealed clear absorptions of the Si–H stretching vibrational mode at 2000-2250 cm^{-1}, which became more prominent under O_2-deficient or O_2-free atmospheres. Additionally, the disappearance of the LO3 mode was observed, in parallel to a "shift" of the TO3 mode from its usual 1070-1030 cm^{-1} range down to 1006 cm^{-1}. XPS analysis confirmed that this "shift" related in fact to the disappearance of the TO3 mode and the appearance of Si–CH_2–Si instead, given the disappearance of Si(O)$_4$ bonding state to the benefit of SiO_xC_x and various Si–N bonding states.

SiO_xN_y films from TSAR were found to be more hydrophilic compared to the SiO_xN_y films from TDMSA, with WCA values ranging between 53.5 and 63.2°, potentially related to the lower amounts of incorporated methyl moieties. The mechanical properties were found to be relatively insensitive to the nitrogen content of the films. However, dispersions in both hardness and elastic modulus results were noted. The lowest H and E values (6.6 and 76.6 GPa) that were measured fit with literature values on SiO_xN_y films, while the highest values (11.0 and 121.8 GPa) approach those observed for non-stoichiometric SiN_x. Thus, it is assumed that the dispersion of results originates from a compositional and structural inhomogeneity, caused by individual SiO_2 and Si_3N_4 phases. This assumption correlates well with the RMM configuration proposed through the FT-IR results, but needs to be confirmed with supplementary characterizations.

Lastly, SiO_xN_y films from TSAR-O_2 revealed an excellent corrosion resistance, with BOE etching rate values as low as 0.2 A.s^{-1}. The etch resistance of the films globally improved for higher deposition temperature and/or lower O_2 flow rates, both of which translate to higher incorporation of nitrogen. SiO_xN_y films from the TSAR precursor proved to be slightly more susceptible to corrosion upon addition of O_2 in

the gas phase than those from TDMSA. This is however expected, given that lower deposition temperatures were used for TSAR. Overall, TSAR films were slightly less resistant than TDMSA ones, a behavior that can be potentially attributed to their much higher deposition rate or lower deposition temperatures, both of which lead to less dense network structures. Despite that, a nitrogen incorporation of 9 at.% was sufficient to reduce the etching rate at extremely low values and result in excellent corrosion resistance. It is once again illustrated how the partial replacement of O by the higher coordinated N leads to better performance, regardless of the precursor used. The positive BOE etching rate results, combined with the ability of TSAR to produce SiO$_x$N$_y$ films by thermal CVD at temperatures below 600°C, managed to address the previously faced challenges. Although USP <660> and <1660> tests are underway and will be the direct indicator of hydrolytic performance, the challenge in terms of process temperature compatibility with the pharmaceutical glass container was overcome successfully, constituting a major step towards reaching the ANR objective.

GENERAL CONCLUSIONS

The various types of pharmaceutical glass exhibit distinct functionalities and hydrolytic resistance. The network forming and modifying elements composing these amorphous materials are involved in covalent and ionic bonds respectively, influencing, among others, the density and workability of the glass. When in an aqueous environment (e.g. during the storage of liquids), ion exchange takes place between the water molecules and the network modifying ions of the glass. Under prolonged contact with the aqueous solution, ion exchange progresses to a stage where the water molecules diffuse to an extent that leads to the hydrolysis of the covalent bonds of the network. Elements diffuse from the glass surface towards the solution, altering the composition and concentration of the liquid, while also augmenting its pH. At progressed stages of glass alteration, delamination of whole glass flakes can occur, posing sanitary risks.

Barrier coatings deposited on the internal surface of pharmaceutical vials have attracted attention as a solution to the above. When applied by CVD processes, which have the advantage of uniform coverage of such complex 3D substrates, barrier coatings can effectively limit the interaction between the container and the stored solution. The composition of the coatings is key to their hydrolytic resistance: absence of modifying elements (Na, K, etc.) in a vitreous network results in reduced alteration kinetics, while low concentrations of hydrated species (Si–OH, Si–H, etc.) lead to denser lattices. In that context, current commercial products (e.g. SCHOTT AG) are based on the application of pure silica (SiO_2) coatings, offering good hydrolytic resistance when subjected to accelerated ageing tests described in the USP <660> recommendation. However, when subjected to more aggressive assessments like those proposed in the USP <1660> chapter, the covalent bonds of the SiO_2 network fail to withstand hydrolysis and the coating is eventually dissolved in the solution. Ponton in his thesis (2019) demonstrated how the hydrolytic performance of SiO_2 barrier coatings, applied via a thermal CVD process using TEOS-O_2, is tightly linked to the process parameters. Operating conditions such as inlet gas composition and process temperature can lead to enhanced network densification and improve hydrolytic resistance.

In the present thesis, a similar approach was pursued initially, namely the deposition of SiO_2 barrier coatings from a TEOS-O_2/O_3 chemistry by thermal CVD. The motivation lied in achieving comparable, if not better, hydrolytic resistance to TEOS-O_2, with the addition of O_3 enabling this feat at much lower temperatures. Indeed, the use of reactive O_3-based chemistries allowed SiO_2 deposition at temperatures as low as 150°C. Evolution of the refractive index and infrared spectra indicated that films elaborated above 500°C are stoichiometric. Additionally, they contain lower concentrations of hydrated species in comparison to films produced from TEOS-O_2 and global hydrogen content ranges between 4.5 and 7.8 at.%. Their resistance to P-etch chemical abrasion is comparable. A chemical model was also developed to provide additional information regarding the deposition process, gain understanding of the phenomena involved and find optimized deposition conditions for other substrate geometries and/or reactor configurations in its range of validity. This part of the thesis was published in 2020 [314]. SiO_2-coated vials from the TEOS-O_2/O_3 chemistry demonstrated excellent barrier properties, with up to 92 % less extractable elements being probed in the solution in comparison to uncoated vials. The results indicated that the ionic exchange, i.e. the initiating step of the hydrolysis mechanism, is taking place at reduced rates when a SiO_2 barrier coating is applied. Unfortunately, despite efforts made in Ponton's and the present thesis to deposit dense SiO_2 coatings from different chemistries and operating conditions, hydrolysis of the SiO_2 barrier was still observed. Concentrations of Si were probed in the solution, indicating that the coating dissolved after a hydrolysis reaction between the hydroxide ions and the covalent bonds of the silica network. Thus, a key point was underlined: the SiO_2 material is at its performing limit. If further network densification is to be induced, solutions should be sought in alternative compositions.

In this context, the project HEALTHYGLASS financed by ANR was conceptualized, proposing the deposition of denser silica-based coatings through the partial replacement of O^{2-} divalent anions by higher coordinated trivalent N^{3-} and/or tetravalent C^{4-} ones. A partnership between three laboratories (LGC, CIRIMAT INPT and UPS, and CEMHTI) embarked on this endeavor. The goal to deposit silicon oxynitride (SiO_xN_y) and silicon oxycarbide (SiO_xC_y) coatings inside a pharmaceutical vial proved to be challenging however. The barrier coating must on one hand be dense enough to withstand alteration, but also be deposited at conditions compatible with the glass fabrication process and the container itself on the other. Thus, certain constrictions are imposed: operation at atmospheric pressure is advised to facilitate transfer to production lines, while deposition temperatures ideally below 600°C are imperative to ensure compatibility with the glass container. These limitations constrict the production of SiO_xN_y and SiO_xC_y coatings, given the fact that, thermally, they are conventionally deposited at temperatures well above 700°C.

To tackle this challenge, careful selection of precursor molecules and reacting chemistries has been executed. The strategy developed for this selection process was validated by an exploratory chemistry using

hexamethyldisilazane (HMDS), tetraethylorthosilicate (TEOS) and O_2/O_3 gas mixtures. No nitrogen was detected in the films from HMDS-TEOS-O_2/O_3, proving that the presence of Si–O bonds in the precursor molecule (TEOS) and the use of highly reactive oxidants (O_3) impedes the incorporation of nitrogen. On the other hand, incorporation of carbon was observed for temperatures equal to or below 450°C, albeit in organic form. The inserted carbon originated from the incomplete decomposition of the HMDS precursor and resulted in substantial reduction of the films corrosion resistance, and by extension the integrity of the material network. This part of the thesis was published in 2021 [315]. In light of these findings, novel silanamine precursors were selected on the basis of avoiding Si–O bonds and preferably including Si–N ones. Additionally, O_3 was excluded from SiO_xN_y-producing chemistries and NH_3 was added as an external nitrogen source. In order to address deposition of SiO_xN_y at moderate temperatures, precursor molecules with multiple Si–H bonds were prioritized, as they demonstrate increased reactivity. Following this strategy, two silanamine precursors were selected: the rarely reported tris(dimethylsilyl)amine (TDMSA) and a novel proprietary trisilylamine-derivative precursor (TSAR) developed and provided by Air Liquide. The consequent CVD routes are innovative regarding the state-of-the art.

Using a thermal CVD process, SiO_xN_y films were successfully produced from TDMSA-NH_3-O_2 and TDMSA-O_2 chemistries. It was revealed that, for the conditions tested, the incorporated nitrogen originates in fact from the precursor molecule and that NH_3 mainly serves to cleave –CH_3 moieties from the film-forming intermediate species. Moreover, a trade-off between deposition rate and nitrogen incorporation was underlined. The former is promoted for higher O_2 flow rates, while the latter is impeded. The structure and composition of the produced SiO_xN_y films were characterized extensively and their resistance to wet etching corrosion induced by hydrofluoric solutions was evaluated. Etching results from SiO_2 and SiO_x films were used as reference points to compare the performance among the various material types. A clear dependency between the level of nitrogen incorporation, and the network densification induced through it, was established. Films with a higher nitride character were almost unaffected by the etching solutions, exhibiting exceptionally low etching rates down to 0.1 Å.s^{-1}. A limit level of nitrogen incorporation was also defined: it appeared that up to 7 at.% N in silica-based films is sufficient for excellent corrosion resistance. Further densification is induced by increasing the deposition temperature, which acts as a means to enhance nitrogen incorporation and decrease the concentration of hydrated species in the network.

Given the novelty of the chemistry and the lack of data in the literature, deposition experiments were coupled with gas phase analyses to shed more light into the homogeneous and heterogeneous reactions describing this particular chemical pathway. By an innovative approach combining three gas-phase characterizations, the radical species (Me)$_2$HSi$^{\bullet}$ and up to fifteen stable by-products were identified. Parallel

consideration of solid phase results allowed the proposal of a comprehensive deposition mechanism. This specific part of the thesis is currently in press. These results were used as the basis for the development of an apparent chemical model for the deposition of SiO_xN_y and its application in numerical simulations through an original methodology combining gas phase analysis, solid phase ellipsometry results and CFD codes. The model consisted of eight chemical reactions and was able to predict local deposition rates and film composition profiles of N and C in a SiO_xN_y system with non-negligible amounts of carbon. Film formation was described by three surface reactions defined by Arrhenius-type kinetic laws and based on the contribution of three intermediate species: the detected $(Me)_2HSi^•$ radical, a $((Me)_2SiH)_2N^•$ radical, and a fictitious intermediate species N_INT2. The deposition process was defined as a simultaneous formation of SiO_2, Si_3N_4 and carbonated Si_3N_4 "phases", homogeneously distributed towards the formation of a global carbonated SiO_xN_y material. Controlling the respective deposition rates of each "phase" allowed for the modulation of the resulting film composition in N and C. The model also accounted for the competitive incorporation of N and O by including homogeneous reactions that reduce the available concentration of nitrogen-containing species in the gas phase when in presence of O_2. After validation, the apparent model was transferred to the vial reactor and demonstrated its utility in estimating, non-destructively, local deposition rates and film composition in hollow bodies. To the best of our knowledge, such a model has not been reported in the literature to this date. A publication on the above aspects is under preparation.

However, chemistries involving the TDMSA precursor failed to adhere to the defined prerequisites of the application targeted within this thesis and the overarching HEALTHYGLASS project. Production of SiO_xN_y films from TDMSA demanded namely a minimum temperature of ca. 620°C, rendering this chemistry incompatible with Type I pharmaceutical vials, which visibly creeped when subjected to such temperatures. Thus, it became clear that the operating limitations must be strictly respected. These constraints were addressed through the selection of a second, more reactive, novel molecule; the trisilylamine-derivative TSAR, developed and provided by Air Liquide. Similarly to TDMSA, TSAR also fulfilled a dual role as silicon and nitrogen provider. Thermal CVD of SiO_xN_y from this precursor was successful at temperatures as low as 520°C. Similar trends with the TDMSA chemistries were noted, with the competitive incorporation of O and N being at the forefront. Additionally, films from TSAR were found to be rich in silicon when deposited under O_2-impoverished atmospheres. By parallel consideration of multiple characterization techniques, Si–O–Si, O–N–Si–O and Si–O_x–C_x bonds were identified. For an O_2-deficit in the gas phase, the disappearance of the SiO_4 tetrahedra was noted, evidenced through the lack of the $Si(O)_4$ bonding state by XPS and the absence of the TO3-LO3 pair by FT-IR. These changes benefited an increase in Si–N states. Wet etching corrosion results revealed the requirement of ca. 9-10 at.% N for excellent corrosion resistance. The above characteristics enabled by the reactive TSAR precursor render SiO_xN_y barrier coatings as a promising alternative for the hydrolytic protection of pharmaceutical vials.

PERSPECTIVES

Multiple chemistries were tested in the frame of the present thesis. The wealth of results, be they from characterizations or numerical simulations, allows the proposal of various perspectives for further research, even beyond the scope of a pharmaceutics-centered application. Each chemistry is addressed in its own dedicated paragraph.

Deposition of SiO_2 from TEOS-O_2/O_3 is generally considered a conventional deposition pathway and has been well documented in the literature. Its respective kinetic model was adapted to unexplored conditions in hot-wall CVD reactor configurations and was modified to define all surface reactions with thermal dependency. An improved understanding of the SiO_2 deposition mechanisms can be gained through it, which can be used as a tool of process optimization in diverse applications. The model can be improved by expanding its range of validity in terms of total flow rate and operating pressure. Additional deposition reactions from INT can be considered to address discrepancies beyond 520°C. In its current state, the model can be used for optimization studies involving different reactor and substrate geometries. However, it must be noted that since the model is apparent and is strongly influenced by mass transport, transposing it to different reactor configurations must always be accompanied by validation experiments. Optimization-wise, multiple O_3 inlets for higher deposition yield could be investigated for the tubular reactor. Such a configuration could likely increase the occurrence of powdering phenomena common to chemistries utilizing high O_3 concentrations. Thus, installation of a condensation particle counter (CPC, or condensation nucleus counter, CNC) at the exhaust of the reactor, similarly to Okuyama et al.'s [114] or Fujimoto et al.'s [316] studies, could be implemented as a means to monitor particle size and population. For the vial reactor, the exploration of different nozzle characteristics (diameter, distance, etc.) and thermal profiles could be undertaken to achieve more uniform coverage. The gas-phase analysis methodology established in Chapter IV could also be applied to the TEOS-O_2/O_3 chemistry: the identification, qualitative or quantitative, of radical species and stable by-products could confer additional accuracy to the model. The low deposition temperatures enabled by O_3 could also warrant the placement of spin-trap pellets closer to the inlet instead of the exhaust of the reactor, allowing for the identification of radical species with shorter lifetimes.

The HMDS-TEOS-O_2/O_3 chemistry resulted in the production of films that transitioned from SiO_x to SiO_xC_y:CH_3 with decreasing process temperature. Carbon was incorporated mostly in organic form, evidently increasing the water contact angle of the films. Although their corrosion resistance was low, coatings from this chemistry could find application in other fields such as in sacrificial silica-based films, often encountered in the fabrication process of MEMs devices [317, 318]. Another alternative relates to the storage of lyophilized products. The TopLyo® product marketed by SCHOTT AG is based on the concept of using hydrophobic Si-O-C-H coatings on the internal surface of vials, which can reduce fogging, decrease residual volumes and improve dosing accuracy [319]. A contact angle of 110° and reduced protein aggregation is advertised. In that context, the tunability of the HMDS-TEOS-O_2/O_3 films can prove beneficial for desired functionalities and performance. Investigation of higher HMDS:TEOS flow ratios can be explored to achieve hydrophobic wetting behavior and test the resulting corrosion resistance, which is reported to decrease surfaces with lower wettability [320].

Deposition of SiO_xN_y from chemistries using TDMSA was eventually proven to be incompatible with the glass transition temperature of Type I pharmaceutical vials. However, this does not exclude their application for the treatment of less heat sensitive substrates, like those used in the semiconductor, optics, energy harvesting or gas separation industries. Apart from the desired nitrogen, carbon was also incorporated in the films. Interestingly, its presence did not affect their corrosion resistance. Investigation using XPS and solid NMR analysis could aid in identifying the elemental environment more accurately and clarifying the bonding characteristics that led to network densification. ESR analysis of the solid film would also prove insightful. Normally used for the identification of lattice defects [321], ESR could be applied for analysis of radical species potentially trapped in the solid film during deposition. From a process point-of-view, experiments with higher NH_3:TDMSA ratios could be performed. Given the demonstrated –CH_3 cleaving effect of NH_3, higher NH_3 flow rates could be explored for the production of carbon-free SiO_xN_y films. From a mechanistic point-of-view, section IV.2.2.3 described a series of gas phase reactions, none of which however include the involvement of O_2. Instead, it was suggested that O_2 forms H_2O, which in turn reacts with the $(Me)_2HSi^•$ radical towards the production of silicon-containing compounds that eventually lead to film deposition. The formation of H_2O however requires the presence of $H^•$ radicals. It is possible that the $H^•$ generation through a seemingly slow homolytic breaking of the TMDSA precursor at the Si-H bond could be a rate-limiting step. This would well explain the low deposition rates noted for this chemistry. As an alternative, TDMSA-H_2O gas mixtures could be investigated, given that the involvement of water vapor in ALD and CVD processes has been documented to promote the growth rate of SiO_2 and SiO_xN_y films [118, 322].

Further improvements can be proposed in relation to the gas phase analyses and the kinetic model. Additional information on the radical species could be gained by selection of an ESR spin-trap molecule with higher decomposition temperature, with the goal to enable trapping of short-lived radical species at critical regions and illuminate the various TDMSA decomposition pathways. For GC-MS analysis, external calibration using standards of identified compounds is proposed, in order to obtain valuable quantitative information on the concentration of each species and better define the kinetic parameters of the respective homogeneous reactions. Further improvements to the model could be introduced by considering a siloxane by-product as a co-reactant in reaction V5. Such a formulation is in fact very likely given Reaction IV.11. In its current state, reaction V5 serves to reduce nitride deposition through consumption of the N_INT2 intermediate. It is balanced out by reaction V3 (production of N_INT2) at higher O_2 flow rates, but as a consequence, nitride deposition is underestimated at lower O_2 flow rates. Adding a siloxane co-reactant to V5 would help address this discrepancy by modulating the consumption of N_INT2 in relation to the O_2 flow rate. Further amelioration can be achieved by considering different kinetic constants for V1 depending on the temperature. By defining this reaction through a UDF, the change in deposition mechanism below SPT 650°C could be accounted for. Global improvements to the model could also be made by basing its development on IBA results directly. In the present thesis, ellipsometry was used for this purpose, since it can provide compositional information for a large number of samples relatively rapidly. If the same task could be executed through IBA, accuracy would increase and hydrogen incorporation could also be considered.

The SiO_xN_y films produced from TSAR-O_2 demonstrate effective nitrogen incorporation at temperatures compatible with the pharmaceutical Type I glass and other heat sensitive substrates. Thus, it is of great interest to assess their hydrolytic resistance under the USP <660> and <1660> tests. Deposition on vials and USP tests are planned in 2021, serving as demonstrators for the main objective of the ANR HEALTHYGLASS project. Additionally, although organic carbon incorporation is below 13 at.%, it could be minimized through the addition of NH_3 in the chemistry. A parametric analysis studying the TSAR-NH_3-O_2 chemistry would also be of interest to investigate the effect of the NH_3 flow rate on the deposition rate and the global composition in C, N and H. The high deposition rates noted from this chemistry also render it attractive for industrial implementation, provided that the security and environmental aspects are mastered. Since scale-up is anchored to in-depth understanding of the deposition process, application of the methodologies established in Chapter IV could aid in the analysis of the gas phase and the subsequent development of a kinetic model from this chemistry. This model could be used for numerical simulation and optimization of the deposition from TSAR, or even open the possibility for application of this original CVD chemical pathway to other fields.

Lastly, general suggestions for further research are proposed. For all utilized chemistries, the precursor flow rate calculated by Hersee and Ballingall's equation [161] deviated, oftentimes substantially, from the values measured experimentally. These discrepancies can be well explained by the incomplete liquid exchange between the carrier-gas and the precursor liquid in the bubbler, as well as by the non-infinite conductance of the gas lines that connect the bubbler to the reactor volume. More detailed calculations, considering these characteristics, are available [323] and can be used in its place. Available experimental weight data before and after deposition could be utilized to adjust these equations for each precursor molecule. From a materials perspective, the variety of produced films allows for the proposal of multilayered barrier coatings [324], such as SiO_2/SiO_xN_y or SiO_xN_y/SiC_xN_y, with the extreme surface ideally being hydrophobic, so as to reduce the contact surface between coating and stored solution. Finally, it is recalled that the production of a carbidic network could prove beneficial to the hydrolytic resistance. Gumpher et al. [73] noted that incorporation of highly covalent Si-C bonds can reinforce the nitride network, leading to improved etching resistance. Thus, production of silicon carbonitride (SiC_xN_y) and SiO_xC_y coatings, poor in organic content, could be explored. The strategy for the selection of appropriate precursor molecules and chemistries developed in this thesis could be used and transposed for the production of SiC_xN_y and SiO_xC_y at moderate temperatures. Chemistries involving a reactive Si-C precursor containing multiple Si-H bonds such as dimethylsilane [123] could be investigated. As a closing remark, it is important to underline that the utilized chemistries were primarily investigated on Si substrates instead of glass, one of the reasons being the exploratory nature of the majority of the experiments. Another reason was practicality, since, in the case of SiO_xN_y films from TDMSA, their deposition was impossible on glass due to the high temperatures (>600°C). Given that depositions at temperatures compatible with glass are enabled through the TSAR precursor, it is now possible to coat this heat-sensitive substrate. An in-depth characterization of the elemental diffusion at the coating-to-glass interface, as well as potential incubation effects due to the different substrate composition, would be of interest.

Oral communications

- K. C. Topka, S. Ponton, H. Vergnes, D. Samelor, D. Sadowski, V. Turq, R. Laloo, C. Genevois, H. Lecoq, B. Caussat, C. Vahlas. "A comparative study of Chemical Vapor Deposited SiO_2 thin films from TEOS-O_2 and TEOS-O_2/O_3". 93rd Annual Meeting of the German Society of Glass Technology (DGG) in conjunction with the Annual Meeting of the French Union for Science and Glass Technology Union pour la science et la technologie verrières (USTV), 13–15 May 2019, Nürnberg, Germany.

- K. C. Topka, S. Ponton, H. Vergnes, D. Samelor, D. Sadowski, V. Turq, R. Laloo, C. Genevois, H. Lecoq, C. Vahlas, B. Caussat. "Advanced chemical vapor deposition routes for the production of SiO_2 barrier films at moderate temperature". 44th International Conference and Expo on Advanced Ceramics and Composites (ICACC2020), 26–31 January 2020, Daytona Beach, Florida, USA.

- K. C. Topka, G. A. Chliavoras, H. Vergnes, D. Samelor, D. Sadowski, C. Vahlas, B. Caussat. "Development of a kinetic model for the moderate temperature chemical vapor deposition of SiO_2 films from TEOS-O_2/O_3". 44th International Conference and Expo on Advanced Ceramics and Composites (ICACC2020), 26–31 January 2020, Daytona Beach, Florida, USA.

- K. C. Topka, L. Decosterd, T. Tsiros, M.-J. Menu, H. Vergnes, C. Vahlas, B. Caussat. "An innovative methodology for the determination of an apparent kinetic model for the chemical vapor deposition of multifunctional SiO_xN_y films". International Congress of Chemical and Process Engineering (CHISA), 15–18 March 2021, Virtually.

Publications

- K. C. Topka, G. A. Chliavoras, F. Senocq, H. Vergnes, D. Samelor, D. Sadowski, C. Vahlas, B. Caussat. "Large temperature range model for the atmospheric pressure chemical vapor deposition

of silicon dioxide films on thermosensitive substrates". *Chemical Engineering Research and Design*, 161 (2020) 146-158.

- K. C. Topka, B. Diallo, D. Samelor, R. Laloo, D. Sadowski, C. Genevois, T. Sauvage, F. Senocq, H. Vergnes, V. Turq, N. Pellerin, B. Caussat, C. Vahlas. "Tunable SiO_2 to SiO_xC_yH films by ozone assisted chemical vapor deposition from tetraethylorthosilicate and hexamethyldisilazane mixtures". *Surface and Coatings Technology*, 407 (2021) 126762.

- N. Pellerin, B. Diallo, K. C. Topka, M. Puyo, C. Lebesgue, C. Genevois, R. Laloo, D. Samelor, H. Lecoq, M. Allix, H. Vergnes, F. Senocq, P. Florian, V. Sarou-Kanian, T. Sauvage, M.-J. Menu, B. Caussat, V. Turq, C. Vahlas. "Network hydration, ordering and composition interplay of chemical vapor deposited amorphous silica films from tetraethyl orthosilicate". *Journal of Materials Research and Technology*. Accepted April 2021. In press.

- M. Puyo, K. C. Topka, B. Diallo, R. Laloo, C. Genevois, P. Florian, T. Sauvage, D. Samelor, F. Senocq, H. Vergnes, B. Caussat, M.-J. Menu, N. Pellerin, C. Vahlas, V. Turq. "Beyond surface nanoindentation: combining static and dynamic nanoindentation to assess intrinsic mechanical properties of CVD amorphous silicon oxide (SiO_x) and silicon oxycarbide (SiO_xC_y) thin films". *Thin Solid Films*, Under review.

- L. Decosterd, K. C. Topka, B. Diallo, D. Samelor, H. Vergnes, F. Senocq, B. Caussat, C. Vahlas, M.-J. Menu. "A GC-MS, NMR and ESR Combined Investigation of the Gas Phase during Chemical Vapor Deposition of Silicon Oxynitrides from Tris(dimethylsilyl)amine". *Physical Chemistry Chemical Physics*. Accepted April 2021. In press.

- Three more manuscripts on the following parts of the present thesis are currently subject to preparation and submission:

  o Kinetic model and numeric simulations of SiO_xN_y from the TDMSA-O_2 chemistry;

  o SiO_xN_y material characterization from TDMSA chemistries;

  o Deposition of SiO_xN_y films at moderate temperatures using the novel TSAR precursor.

Appendix 1   Comparative FT-IR spectra (60°) of SiO$_2$ films deposited at 550°C from different TEOS chemistries
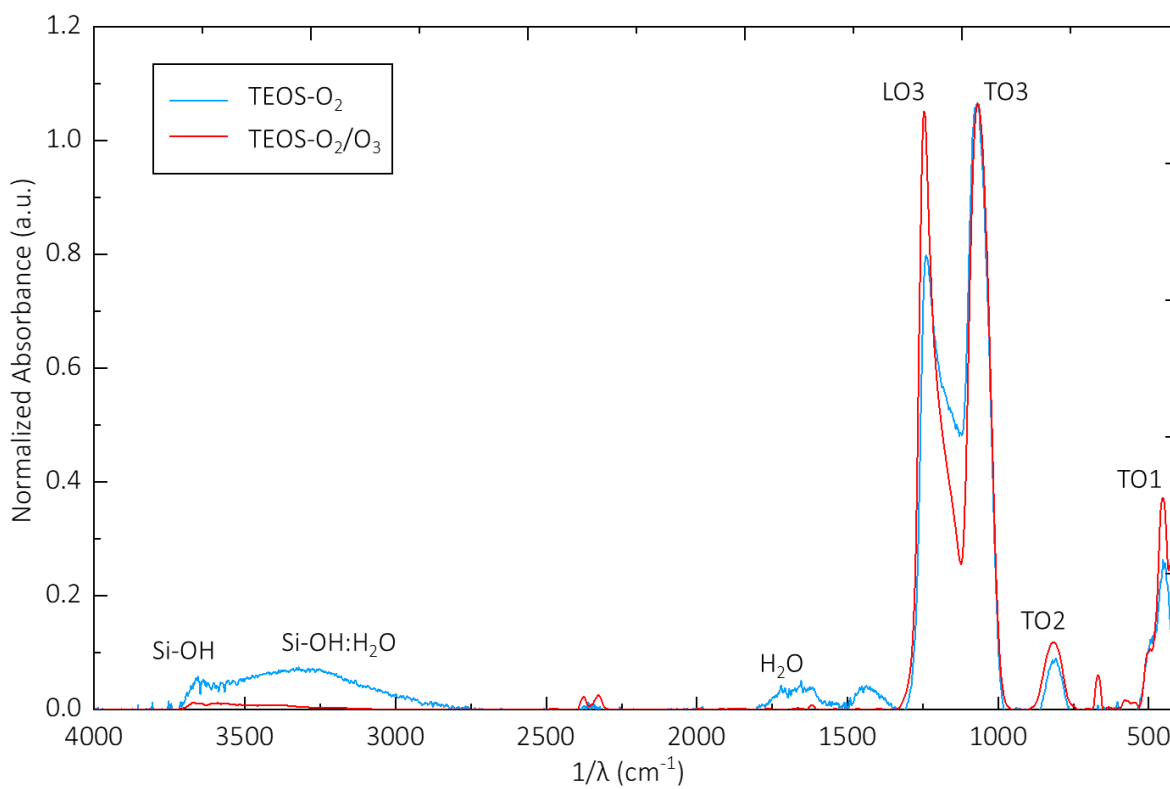
Appendix 2 Apparent chemical reactions and respective kinetic laws in the TEOS-O₂/O₃ model developed by Nieto et al. [158]

	Chemical reactions	Reaction Rate and Kinetic constants
Volumetric Reactions $(kmol/m^3 s)$	(R1) $\quad O_3 + M \rightarrow O_2 + O^{\cdot} + M$	$k_1[O_3][M]$ $k_1 = 2.5 \times 10^{11} \times exp\left(-\dfrac{11430}{T(K)}\right)$
	(R2) $\quad O_3 + O^{\cdot} \rightarrow 2O_2$	$k_2[O_3][O^{\cdot}]$ $k_2 = 10^{10} \times exp\left(-\dfrac{2090}{T(K)}\right)$
	(R3) $\quad 2O^{\cdot} + M \rightarrow O_2 + M$	$k_3[O^{\cdot}]^2[M]$ $k_3 = 4 \times 10^8 \times exp\left(+\dfrac{720}{T(K)}\right)$
	(R4) $\quad O_3 + TEOS + M \rightarrow INT + R + M$	$k_4[O_3][TEOS][M]$ $k_4 = 4 \times 10^{17} \times exp\left(-\dfrac{14099}{T(K)}\right)$
	(R5) $\quad INT \rightarrow by\text{-}products$	$k_5[INT]$ $k_5 = 5 \times 10^3 \times exp\left(-\dfrac{5539}{T(K)}\right)$
Surface Reactions $(kmol/m^2 s)$	(R6) $\quad TEOS + 6O_3 \rightarrow SiO_2 + O_2 + by\text{-}products$	$k_6[TEOS]_s^a[O_3]_s^b$ $k_6 = 4.1 \times 10^{-4}$ $a = 0.4, b = 0.25$
	(R7) $\quad INT \rightarrow SiO_2 + by\text{-}products$	$k_7[INT]_s/(1 + k_8[INT]_s)$ $k_7 = 1.2 \times exp\left(-\dfrac{4053}{Ts(K)}\right)$ $k_8 = 1.482 \times 10^6 \times exp\left(-\dfrac{2578}{Ts(K)}\right)$

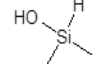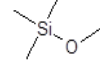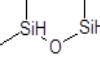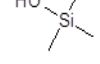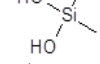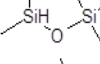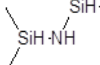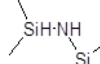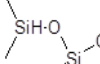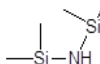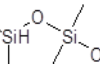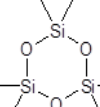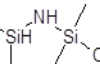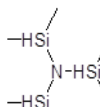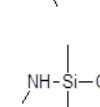# Appendix 3 FT-IR spectra (0°) of SiO_xC_y:CH_3 film deposited at 360°C from HMDS-TEOS-O_2/O_3, before and after annealing at 550°C
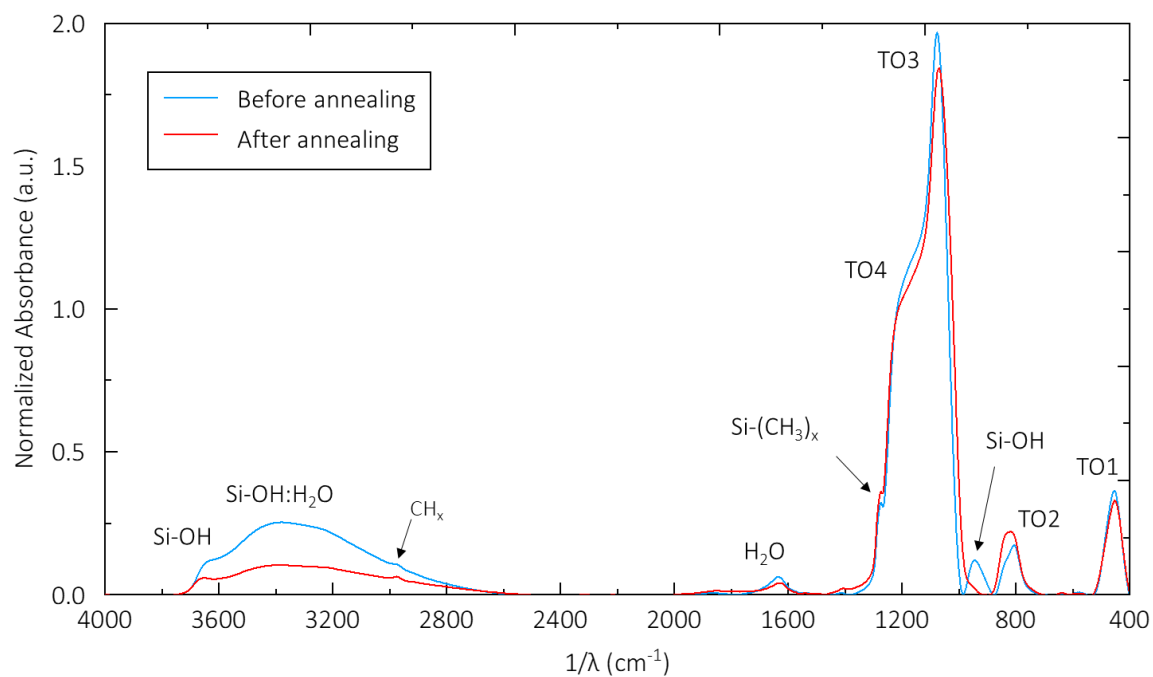
Appendix 4 List of FT-IR absorptions encountered in SiO_xN_y films produced from TDMSA

Bond family	Bond	Vibrational mode	$1/\lambda$ (cm^{-1})	Ref.
Organic carbon	C-H	Stretching	2800-3000	[89, 214, 308]
	CH$_3$	Rocking in Si(CH$_3$)$_2$ groups	800	[246]
	CH$_3$	Asym. stretching	2970	[242]
	CH$_3$	Sym. Bending in Si-(CH$_3$)$_x$ groups	1260-1278	[216, 245] [325]
	CH$_3$	Rocking in Si-(CH$_3$)$_3$ groups	845	[242, 246]
	=CH$_2$	Stretching	3050	[308, 326]
Oxide	Si-O-Si	TO1 rocking	455	[270, 271, 275]
	Si-O-Si	TO2 stretching or bending	805-820	[275]
	Si-O-Si	TO3 asymmetric stretching	1080	[275]
	Si-O-Si	TO4 asymmetric stretching	1160-1180	[270, 271, 327]
	Si-O-Si	LO4 asymmetric stretching	1165	[327]
	Si-O-Si	LO3 asymmetric stretching	1254	[327]
Nitride	Si-N	Symmetric stretching	490	[272]
	Si-N	Stretching of locally distorted Si-N configurations	790-800	[272]
	Si-N	Asymmetric stretching	850	[272]
	Si-N	Stretching	940	[270, 271]
Carbide	Si-C	Stretching	790-820	[214, 328, 329]
	Si-CH$_2$-Si	Stretching	1000-1020	[247, 250]
	CH$_2$	Wagging in Si-CH$_2$-Si groups	1060	[247]
	Si-O-C	Stretching	1100	[249]
Network Hydration	Si-H	Wagging or rocking	620-650	[309, 310]
	Si-OH	Stretching	940-960	[8, 188]
	Si-H	Stretching	2000-2150	[275]
	N-H	Stretching	3250, 3400	[270, 271, 281]
	N-H⋯N	Hydrogen-bonded, asymmetric stretching	3320-3350	[273, 281]
	Si-OH:H-OH	Silanol bonded with water, stretching	3400-3500	[8, 200, 270, 271]
	Si-OH	Stretching	3600-3650	[8, 270, 271]
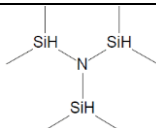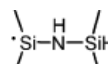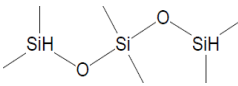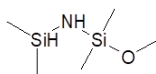
Appendix 5   Identified GC-MS by-products from TDMSA-NH₃-O₂

GC-MS by-product information				NH₃ flow rate (sccm)				T (°C)
No#	Formula	Abbreviation	Retention time (min)	TD3	TD4	TD5	TD6	TD8
1		-	1.82-2.15	✓	✓	✓	✓	✓
2		MeOTMS	-	-	-	-	-	-
3		TMDSo	1.76	✓	✓	✓	✓	✓
4		-	2.42-2.45	✓	✓	✓	✓	✓
5		-	-	-	-	-	-	-
6		PMDSo	2.51	✓	-	✓	-	-
7		TMDSz	-	-	-	-	-	-
8		PMDSz	-	-	-	-	-	-
9		-	7.71-7.74	✓	✓	✓	✓	✓
10		HMDSz	-	-	-	-	-	-
11		HMTSo	10.27-10.63	✓	✓	✓	✓	✓
12		HMCTSo	11.22-11.42	-	✓	✓	-	✓
13		-	13.06	-	✓	-	-	-
14		TDMSA	12.40	✓	✓	✓	✓	✓
15		-	11.40	✓	✓	✓	✓	✓

Appendix 6 HRTEM-EELS of SiO$_x$N$_y$ film from TDMSA-NH$_3$-O$_2$ (TD3-p6)

EELS Spectroscopy

ADF Image

O spectrum

N spectrum

Overlay O-N

FFT of Si substrate [110]

FFT of SiO$_x$N$_y$ film
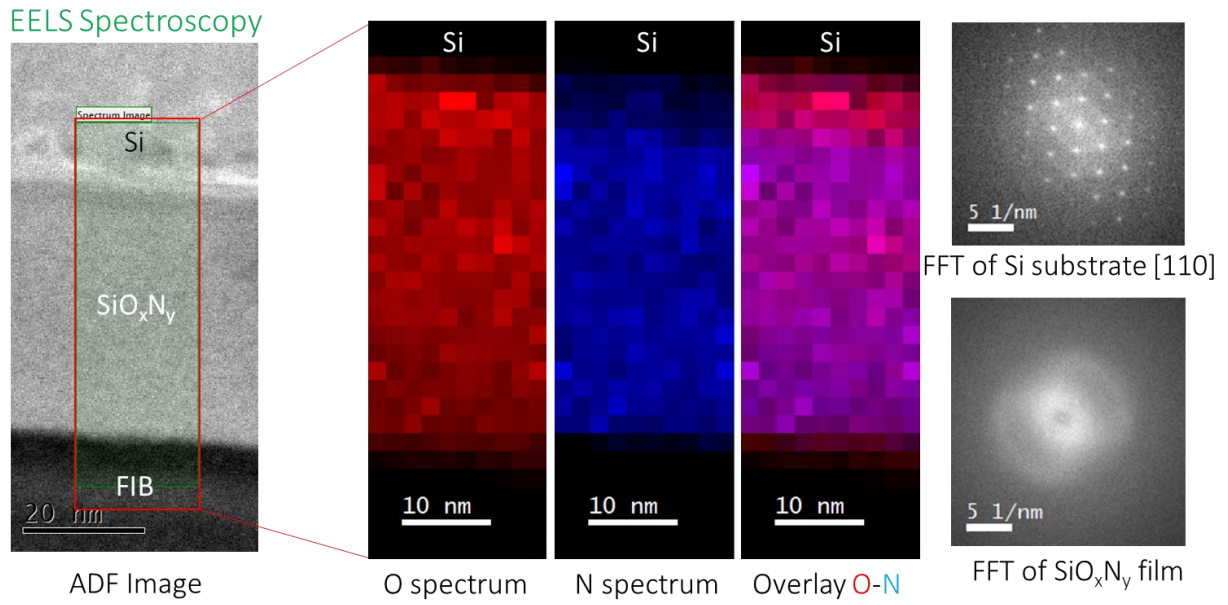
Appendix 7   Species used in the TDMSA-O₂ chemical model and their respective L-J parameters

Species (abbreviated name)	Full compound name	Matched chemical structure	Mr (g.mol⁻¹)	σ (Å)	ε/k (K)
TDMSA	Tris(dimethylsilyl)amine		191.492	3.71	78.6
Si_INT	Dimethylsilyl radical		59.162	3.71	78.6
N_INT	1,1,3,3-tetramethyl disilazane radical		132.330	3.71	78.6
Siloxane	1,1,3,3,5,5-hexamethyltrisiloxane		208.476	3.54	1182.4
Silanamine	N-(dimethylsilyl)-1-(methoxy)-1,1-dimethylsilanamine		163.364	3.54	1182.4
Silanone	Dimethyl silanone		74.153	5.25	522.7
N_INT2	Dimethylsilanimine (Imine-family intermediates)		72.161	5.25	522.7
CH₃OH	Methanol		32.041	3.63	481.8
CH₄	Methane		31.077	3.76	148.6
H₂O	Water vapor		18.015	2.61	572.4
O₂	Oxygen gas		31.999	3.46	107.4
N₂	Nitrogen gas		28.013	3.62	97.5

Appendix 8   Inlet boundary conditions for FLUENT® simulations

Precursor	Runs	Inlet mass flow rate [a] $(kg.s^{-1})$	Inlet mass fractions			
Tubular reactor						
			Precursor[b]	O_2	O_3	N_2
TEOS	E1, E4-E6	$9.19653 \text{ e}10^{-5}$	0.00181	0.50534	0.02414	0.46871
TDMSA	TD11	$8.39434 \text{ e}10^{-5}$	0.00353	0.00009	-	0.99638
TDMSA	TD7	$8.28763 \text{ e}10^{-5}$	0.00265	0.00017	-	0.99718
TDMSA	TD12	$8.39017 \text{ e}10^{-5}$	0.00278	0.00034	-	0.99688
TDMSA	TD14	$8.39319 \text{ e}10^{-5}$	0.00331	0.00017	-	0.99652
Vial reactor						
			Precursor[b]	O_2	O_3	N_2
TEOS	V1-V6	$5.06537 \text{ e}10^{-5}$	0.00219	0.50515	0.02413	0.46853
TDMSA	VTD1	$4.62568 \text{ e}10^{-5}$	0. 00265	0.00017	-	0.99718

[a] Values correspond to the whole inlet surface area and do not account for symmetry.

[b] Supply of precursor measured experimentally by weighing the respective bubbler system before and after deposition.

Appendix 9   Gas velocity, temperature and species mass fraction profiles in the gas volume (XZ plane) and reaction rates near the samples surface (YZ plane) for TDMSA-O₂ chemistry, run TD12.
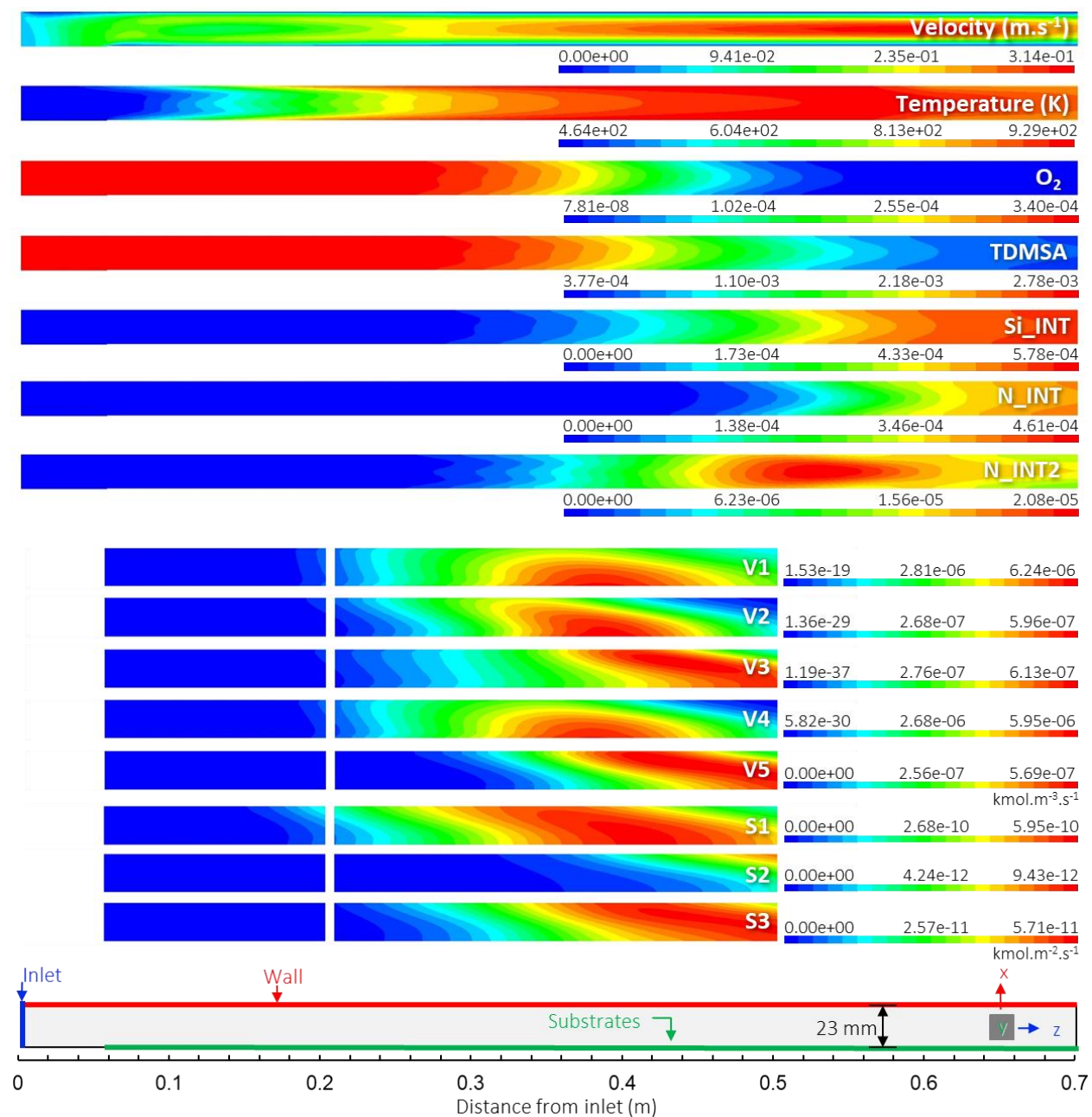
V1 to V5: Volumetric reactions; S1 to S3: Surface reactions

Appendix 10   Thermal profile of the vial reactor, measured experimentally for various SPT.
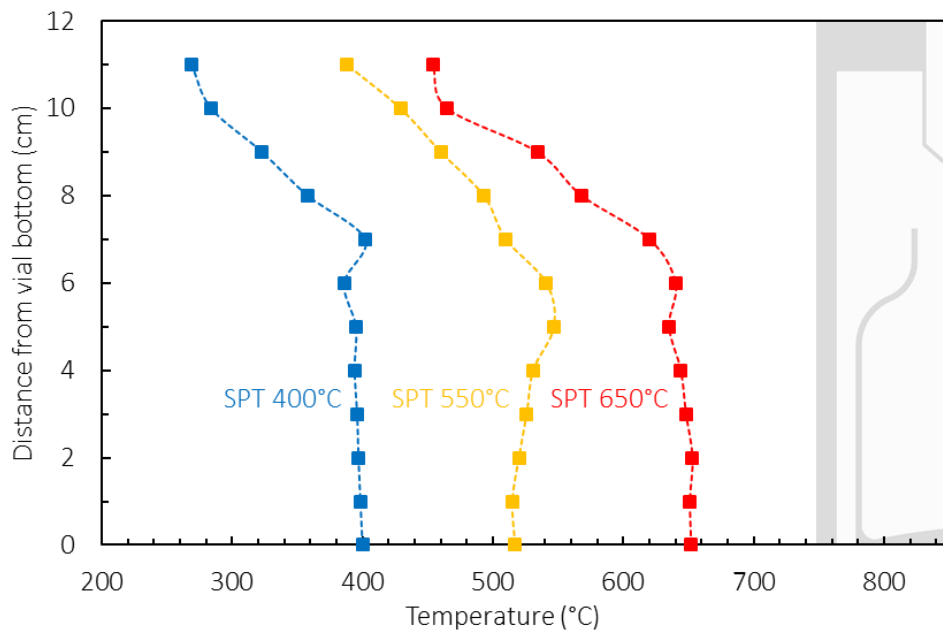
REFERENCES

[1]   R.A. Schaut, W.P. Weeks, Historical review of glasses used for parenteral packaging, *PDA J Pharm Sci Technol*, 71 (2017) 279-296.

[2]   Food and Drug Administration, Advisory to Drug Manufacturers: Formation of Glass Lamellae in Certain Injectable Drugs, Food and Drug Administration: Silver Spring, MD, 2011.

[3]   S.A. Tawde, Particulate matter in injectables: main cause for recalls, *J. Pharmacovigil*, 3 (2014) 1-2.

[4]   USP, Committee of Revision, Chapter <660> Glass Containers. The United States Pharmacopeia Thirtyninth Revision, 2016.

[5]   USP, Chapter <1660> Evaluation of the Inner Surface Durability of Glass Containers, 2012.

[6]   SCHOTT AG, SCHOTT TopLine Options for Superior Shelf Life, available at https://www.us.schott.com/pharmaceutical_packaging/english/products/vials/top-line-options/type-1-plus.html?wss_setorigin=1&wss_iso=en-US , Last Accessed: 23 January 2021.

[7]   S. Ponton, Dépôt chimique en phase vapeur de silice amorphe en tant que revêtement barrière pour flacons pharmaceutiques, PhD Thesis, Institut national polytechnique de Toulouse, France, 2019.

[8]   S. Ponton, F. Dhainaut, H. Vergnes, D. Samelor, D. Sadowski, V. Rouessac, H. Lecoq, T. Sauvage, B. Caussat, C. Vahlas, Investigation of the densification mechanisms and corrosion resistance of amorphous silica films, *J Non-Cryst Solids*, 515 (2019) 34-41.

[9]   ANR, Surfaces de verre performantes et durables pour la pharmacie – HEALTHYGLASS, Available at: https://anr.fr/Projet-ANR-17-CE08-0056, Last Accessed: 23 January 2021.

[10]   N. Alford, J. Amouroux, D. Barbier, G. Bauer, A. Borg, J.P. Conde, A. Gonzalez-Elipe, H. Grimmeiss, A. Jäger-Waldau, D. Jarvis, T. Lippert, S. Maier, H.-J. Müssig, E. Olsson, J. Perrière, L. Pfitzner, F. Priolo, H. Richter, A.C. Ritschkoff, C. Vahlas, Materials for Key Enabling Technologies, 2011.

[11]   Y. Shi, L. He, F. Guang, L. Li, Z. Xin, R. Liu, A review: preparation, performance, and applications of silicon oxynitride film, *Micromachines*, 10 (2019) 552.

[12]   A.G. Erlat, B.-C. Wang, R.J. Spontak, Y. Tropsha, K.D. Mar, D.B. Montgomery, E.A. Vogler, Morphology and gas barrier properties of thin SiO_x coatings on polycarbonate: Correlations with plasma-enhanced chemical vapor deposition conditions, *J Mater Res*, 15 (2000) 704-717.

[13]   H.M. Park, J.Y. Lee, K.Y. Jee, S.-I. Nakao, Y.T. Lee, Hydrocarbon separation properties of a CVD-deposited ceramic membrane under single gases and binary mixed gas, *Sep Purif Technol*, 254 (2021) 117642.

[14]   M. Li, J. Feng, K. Huang, S. Tang, R. Liu, H. Li, F. Ma, X. Meng, Amino group functionalized SiO_2@graphene oxide for efficient removal of Cu(II) from aqueous solutions, *Chem Eng Res Des*, 145 (2019) 235-244.

[15]   J.-H. Zhang, Y.-S. Wang, J.-H. Liang, D.-S. Wuu, Effect of the polymer overcoat on the performance of the SiN_x/SiO_x multilayer barrier for OLED gas barrier applications, in: 2015 International Symposium on Next-Generation Electronics (ISNE), IEEE, 2015, pp. 1-4.

References

[16] M. Shahpanah, S. Mehrabian, M. Abbasi-Firouzjah, B. Shokri, Improving the oxygen barrier properties of PET polymer by radio frequency plasma-polymerized SiO_xN_y thin film, *Surf Coat Technol*, 358 (2019) 91-97.

[17] S. Hampshire, Oxynitride glasses, their properties and crystallisation – a review, *J Non-Cryst Solids*, 316 (2003) 64-73.

[18] E.K. Park, S. Kim, J. Heo, H.J. Kim, Electrical evaluation of crack generation in SiN_x and SiO_xN_y thin-film encapsulation layers for OLED displays, *Appl Surf Sci*, 370 (2016) 126-130.

[19] N. Brinkmann, D. Sommer, G. Micard, G. Hahn, B. Terheiden, Electrical, optical and structural investigation of plasma-enhanced chemical-vapor-deposited amorphous silicon oxynitride films for solar cell applications, *Sol Energy Mater Sol Cells*, 108 (2013) 180-188.

[20] W.H. Zachariasen, The atomic arrangement in glass, *J Am Chem Soc*, 54 (1932) 3841-3851.

[21] J. Kawamura, R. Asayama, N. Kuwata, O. Kamishima, Ionic transport in glass and polymer: Hierarchical structure and dynamics, *Phys. Solid State Ionics*, 81 (2006) 193-246.

[22] C.W. Sinton, W.C. LaCourse, Experimental survey of the chemical durability of commercial soda-lime-silicate glasses, *Mater Res Bull*, 36 (2001) 2471-2479.

[23] D.E. Clark, M. Dilmore, E. Ethridge, L. Hench, Aqueous corrosion of soda-silica and soda-lime-silica glass, *J Am Ceram Soc*, 59 (1976) 62-65.

[24] D.E. Clark, E.L. Yen-Bower, Corrosion of glass surfaces, *Surface Science*, 100 (1980) 53-70.

[25] B. Bunker, Molecular mechanisms for corrosion of silica and silicate glasses, *J Non-Cryst Solids*, 179 (1994) 300-308.

[26] A. Putnis, Sharpened interface, *Nature Materials*, 14 (2015) 261-262.

[27] E. Ruiz-Agudo, C.V. Putnis, C. Rodriguez-Navarro, A. Putnis, Mechanism of leached layer formation during chemical weathering of silicate minerals, *Geology*, 40 (2012) 947-950.

[28] C. Cailleteau, F. Angeli, F. Devreux, S. Gin, J. Jestin, P. Jollivet, O. Spalla, Insight into silicate-glass corrosion mechanisms, *Nature materials*, 7 (2008) 978-983.

[29] T. Geisler, A. Janssen, D. Scheiter, T. Stephan, J. Berndt, A. Putnis, Aqueous corrosion of borosilicate glass under acidic conditions: A new corrosion mechanism, *J Non-Cryst Solids*, 356 (2010) 1458-1465.

[30] B.C. Bunker, G.W. Arnold, E.K. Beauchamp, D. Day, Mechanisms for alkali leaching in mized-Na·K silicate glasses, *J Non-Cryst Solids*, 58 (1983) 295-322.

[31] B. Parruzot, P. Jollivet, D. Rébiscoul, S. Gin, Long-term alteration of basaltic glass: Mechanisms and rates, *Geochim Cosmochim Acta*, 154 (2015) 28-48.

[32] R.G. Iacocca, M. Allgeier, Corrosive attack of glass by a pharmaceutical compound, *J Mater Sci*, 42 (2007) 801-811.

[33] R.G. Iacocca, N. Toltl, M. Allgeier, B. Bustard, X. Dong, M. Foubert, J. Hofer, S. Peoples, T. Shelbourn, Factors affecting the chemical durability of glass used in the pharmaceutical industry, *AAPS PharmSciTech*, 11 (2010) 1340-1349.

[34] R.D. Ennis, R. Pritchard, C. Nakamura, M. Coulon, T. Yang, G.C. Visor, W.A. Lee, Glass vials for small volume parenterals: influence of drug and manufacturing processes on glass delamination, *Pharm Dev Technol*, 6 (2001) 393-405.

[35] J.S. Bee, T.W. Randolph, J.F. Carpenter, S.M. Bishop, M.N. Dimitrova, Effects of Surfaces and Leachables on the Stability of Biopharmaceuticals, *J Pharm Sci*, 100 (2011) 4158-4170.

[36] E. Guadagnino, D. Zuccato, Delamination Propensity of Pharmaceutical Glass Containers by Accelerated Testing with Different Extraction Media, *PDA J Pharm Sci Technol*, 66 (2012) 116.

[37] V. Rupertus, B. Hladik, U. Rothhaar, V. Scheumann, A Quick Test To Monitor the Delamination Propensity of Glass Containers, *PDA J Pharm Sci Technol*, 68 (2014) 373.

[38] SCHOTT AG, SCHOTT TopLine Options for Superior Shelf Life, SCHOTT EVERIC™, Video available at: https://www.us.schott.com/pharmaceutical_packaging/english/products/vials/top-line-options/schott-vials-dc.html , Last Accessed: 23 January 2021

[39] L. Lachman, H.A. Lieberman, J.L. Kanig, The theory and practice of industrial pharmacy, Lea & Febiger, Philadelphia, USA, 1986.

[40] E. Guadagnino, A. Chillon, D. Zuccato, F. Nicoletti, Testing the glass material to predict delamination in pharmaceutical glass containers, *Glass Technol: Eur J Glass Sci Technol, Part A*, 58 (2017) 179-188.

[41] T.J. Roseman, J.A. Brown, W.W. Scothorn, Glass for parenteral products: A surface view using the scanning electron microscope, *J Pharm Sci*, 65 (1976) 22-29.

[42] B.C. Bunker, G.W. Arnold, D.E. Day, P.J. Bray, The effect of molecular structure on borosilicate glass leaching, *J Non-Cryst Solids*, 87 (1986) 226-253.

[43] R.A. Schaut, J.S. Peanasky, S.E. DeMartino, S.L. Schiefelbein, A New Glass Option for Parenteral Packaging, *PDA J Pharm Sci Technol*, 68 (2014) 527.

[44] P. Brix, Boron-Free Glass, U.S Patent 8,629,072, 2014.

[45] Nippon Electric Glass, Press Release 2015: Two New Materials of Glass Tubing for Pharmaceutical Containers Developed, available at: http://www.neg.co.jp/uploads/sites/2/news_20150325_release_en.pdf, Last Accessed: 18 January 2021.

[46] T. Rong, S. Conzone, M.L. Panchula, Fused quartz tubing for pharmaceutical packaging, U.S. Patent 2012/0148770 A1, 2012.

[47] Corning Incorporated, Delamination resistant pharmaceutical glass containers containing active pharmaceutical ingredients, U.S. Patent WO 2013/063258 A1, 2013.

[48] SCHOTT AG, EVERIC™ pure, available at: https://www.us.schott.com/d/pharmaceutical_packaging/9b089502-185a-4135-bd05-5ab5c77dd0b9/1.0/schott-everic-drug-stability-low-fill-english-us-17022020.pdf, Last Accessed: 23 January 2021.

[49] Corning Incorporated, Methods for forming delamination resistant glass containers, U.S. 9,346,707 B2, 2016.

[50] K. Ahn, G. Xu, M. Panchula, S. Conzone, T. Rong, K.S. Zuyev, Y. Zhou, Fused quartz tubing for pharmaceutical packaging, U.S. Patent 9,919,948 B2, 2018.

[51] D. Samélor, A.-M. Lazar, M. Aufray, C. Tendero, L. Lacroix, J.-D. Béguin, B. Caussat, H. Vergnes, J. Alexis, D. Poquillon, N. Pébère, A. Gleizes, C. Vahlas, Amorphous Alumina Coatings: Processing, Structure and Remarkable Barrier Properties, *J Nanosci Nanotechnol*, 11 (2011) 8387-8391.

[52] A.S. da Silva Sobrinho, M. Latrèche, G. Czeremuszkin, J.E. Klemberg-Sapieha, M.R. Wertheimer, Transparent barrier coatings on polyethylene terephthalate by single- and dual-frequency plasma-enhanced chemical vapor deposition, *J Vac Sci Technol A*, 16 (1998) 3190-3198.

[53] R. Murakami, K. Fujikawa, D. Yonekura, Improvement of Oxidation Property of SUS304 by Gas Barrier Coating, in: Key Eng Mater, Trans Tech Publ, 2007, pp. 1879-1882.

[54] M. Nocuń, D. Burcon, S. Siwulski, Sodium diffusion barrier coatings prepared by sol-gel method, *Optica Applicata*, 38 (2008) 171.

[55] P.-L. Etchepare, Revêtements barrière d'alumine amorphe appliqués à l'intérieur de flacons pharmaceutiques en verre, par le procédé de dépôt chimique en phase vapeur, PhD Thesis, Institut national polytechnique de Toulouse, France, 2015.

[56] P.-L. Etchepare, H. Vergnes, D. Samélor, D. Sadowski, B. Caussat, C. Vahlas, Modeling a MOCVD process to apply alumina films on the inner surface of bottles, *Surf Coat Technol*, 275 (2015) 167-175.

[57] F. Guanghui, D. Jiafeng, P. Donghui, H. Ouli, The migration of alkali ions from glass substrates coated with sol-gel barrier films, *J Non-Cryst Solids*, 112 (1989) 454-457.

[58] H. Nagayama, H. Honda, H. Kawahara, A New Process for Silica Coating, *J Electrochem Soc*, 135 (1988) 2013-2016.

[59] A.S. Yersak, R.J. Lewis, J. Tran, Y.C. Lee, Characterization of Thin Film Dissolution in Water with in Situ Monitoring of Film Thickness Using Reflectometry, *ACS Appl Mater Interfaces*, 8 (2016) 17622-17630.

[60]   M. Klause, U. Rothhaar, M. Bicker, W. Ohling, Dissolution of thin SiO_2-coatings–Characterization and evaluation, *J Non-Cryst Solids*, 356 (2010) 141-146.

[61]   Y.T. Yang, B.S. Park, T.K. Won, S.Y. Choi, J.M. White, Amorphous-silicon thin-film transistor on soda-lime glass, *J Soc Inf Disp*, 17 (2009) 317-321.

[62]   J. Palm, V. Probst, A. Brummer, W. Stetter, R. Tölle, T.P. Niesen, S. Visbeck, O. Hernandez, M. Wendl, H. Vogt, H. Calwer, B. Freienstein, F. Karg, CIS module pilot processing applying concurrent rapid selenization and sulfurization of large area thin film precursors, *Thin Solid Films*, 431-432 (2003) 514-522.

[63]   H. Koo, H. You, K.-E. Ko, O.J. Kwon, S.-H. Chang, C. Park, Thermochromic properties of VO_2 thin film on SiN_x buffered glass substrate, *Appl Surf Sci*, 277 (2013) 237-241.

[64]   J.W. Osenbach, S.S. Voris, Sodium diffusion in plasma-deposited amorphous oxygen-doped silicon nitride (a-SiON:H) films, *J Appl Phys*, 63 (1988) 4494-4500.

[65]   E. Song, H. Fang, X. Jin, J. Zhao, C. Jiang, K.J. Yu, Y. Zhong, D. Xu, J. Li, G. Fang, Thin, transferred layers of silicon dioxide and silicon nitride as water and ion barriers for implantable flexible electronic systems, *Adv Electron Mater*, 3 (2017) 1700077.

[66]   M. Saarniheimo, E. Seppäläinen, Undercoat process for fluorine-doped tin oxide type transparent conductive oxide coating, *Thin Solid Films*, 532 (2013) 31-35.

[67]   E. Aubry, M. Ghazzal, V. Demange, N. Chaoui, D. Robert, A. Billard, Poisoning prevention of TiO_2 photocatalyst coatings sputtered on soda-lime glass by intercalation of SiN_x diffusion barriers, *Surf Coat Technol*, 201 (2007) 7706-7712.

[68]   C. Dussarrat, J.-M. Girard, T. Kimura, Method for producing silicon nitride films, U.S. Patent 8,357,430 B2, 2013.

[69]   E. Scheid, L. Kouassi, R. Henda, J. Samitier, J. Morante, Silicon nitride elaborated by low pressure chemical vapour deposition from Si_2H_6 and NH_3 at low temperature, *J Mater Sci Eng B*, 17 (1993) 185-189.

[70]   J.W. Smith, S.M. Seutter, R.S. Iyer, Thermal Chemical Vapor Deposition of Bis (Tertiary-Butylamino) Silane-based Silicon Nitride Thin Films: Equipment Design and Process Optimization, *J Electrochem Soc*, 152 (2005) G316.

[71]   M. Tanaka, S. Saida, Y. Tsunashima, Film Properties of Low-k Silicon Nitride Films Formed by Hexachlorodisilane and Ammonia, *J Electrochem Soc*, 147 (2000) 2284.

[72]   T. Oyaidu, Y. Ogawa, K. Tsurumaki, K. Ohdaira, H. Matsumura, Formation of gas barrier films by Cat-CVD method using organic silicon compounds, *Thin Solid Films*, 516 (2008) 604-606.

[73]   J. Gumpher, W. Bather, N. Mehta, D. Wedel, Characterization of low-temperature silicon nitride LPCVD from bis (tertiary-butylamino) silane and ammonia, *J Electrochem Soc*, 151 (2004) G353.

[74]   W.-J. Lee, Y.-H. Choa, Highly conformal carbon-doped SiCN films by plasma-enhanced chemical vapor deposition with enhanced barrier properties, *Thin Solid Films*, 657 (2018) 32-37.

[75]   V.A. Gritsenko, J.B. Xu, R.W.M. Kwok, Y.H. Ng, I.H. Wilson, Short Range Order and the Nature of Defects and Traps in Amorphous Silicon Oxynitride Governed by the Mott Rule, *Phys Rev Lett*, 81 (1998) 1054-1057.

[76]   W. Ding, L. Li, L. Zhang, D. Ju, S. Peng, W. Chai, An XPS study on the chemical bond structure at the interface between SiO_xN_y and N doped polyethylene terephthalate, *J Chem Phys*, 138 (2013) 104706.

[77]   G.M. Renlund, S. Prochazka, R.H. Doremus, Silicon oxycarbide glasses: Part II. Structure and properties, *J Mater Res*, 6 (1991) 2723-2734.

[78]   C.G. Pantano, A.K. Singh, H. Zhang, Silicon oxycarbide glasses, *J Sol-Gel Sci Technol*, 14 (1999) 7-25.

[79]   G.D. Sorarù, S. Modena, E. Guadagnino, P. Colombo, J. Egan, C. Pantano, Chemical durability of silicon oxycarbide glasses, *J Am Ceram Soc*, 85 (2002) 1529-1536.

[80]   S. Walter, G. Soraru, H. Brequel, S. Enzo, Microstructural and mechanical characterization of sol gel-derived Si–O–C glasses, *J Eur Ceram Soc*, 22 (2002) 2389-2400.

[81]   G.D. Sorarù, E. Dallapiccola, G. D'Andrea, Mechanical Characterization of Sol–Gel-Derived Silicon Oxycarbide Glasses, *J Am Ceram Soc*, 79 (1996) 2074-2080.

[82]   Stevanato Group, High Performance Converting Lines, Available at: https://www.stevanatogroup.com/en/offering/glass-converting/, Last Accessed: 23 January 2021.

[83]   C. Vallée, A. Goullet, A. Granier, A. van der Lee, J. Durand, C. Marlière, Inorganic to organic crossover in thin films deposited from O_2/TEOS plasmas, *J Non-Cryst Solids*, 272 (2000) 163-173.

[84]   K. Pfeiffer, S. Shestaeva, A. Bingel, P. Munzert, L. Ghazaryan, C. van Helvoirt, W.M.M. Kessels, U.T. Sanli, C. Grévent, G. Schütz, M. Putkonen, I. Buchanan, L. Jensen, D. Ristau, A. Tünnermann, A. Szeghalmi, Comparative study of ALD SiO_2 thin films for optical applications, *Opt Mater Express*, 6 (2016) 660-670.

[85]   S. Suh, S.W. Ryu, S. Cho, J.-R. Kim, S. Kim, C.S. Hwang, H.J. Kim, Low-temperature SiON films deposited by plasma-enhanced atomic layer deposition method using activated silicon precursor, *J Vac Sci Technol A*, 34 (2016) 01A136.

[86]   S.S. Cho, K.H. Joo, I.-S. Yeo, I. Chung, Study On Charge Trap Layers In Charge Trap Metal–Oxide–Semiconductor Field Effect Transistor, *Jpn J Appl Phys*, 48 (2009) 021201.

[87]   A. Hashimoto, M. Kobayashi, T. Kamijoh, H. Takano, M. Sakuta, Properties of PECVD SiO_xN_y Films as Selective Diffusion Barrier, *J Electrochem Soc*, 133 (1986) 1464-1467.

[88]   Y.-S. Lin, Y.-H. Liao, M.-S. Weng, Enhanced scratch resistance of polycarbonate by low temperature plasma-polymerized organosilica, *Thin Solid Films*, 517 (2009) 5224-5230.

[89]   A. Walkiewicz-Pietrzykowska, J. Cotrino, A.R. González-Elipe, Deposition of Thin Films of SiO_xC_yH in a Surfatron Microwave Plasma Reactor with Hexamethyldisiloxane as Precursor, *Chem Vap Deposition*, 11 (2005) 317-323.

[90]   V.K. Tomar, D.K. Gautam, Deposition and characterization of Si-rich silicon oxide films using HMDS for integrated photonics, *Mater Sci Semicond Process*, 10 (2007) 200-205.

[91]   E. Halova, S. Alexandrova, A. Szekeres, M. Modreanu, LPCVD-silicon oxynitride films: interface properties, *Microelectron Reliab*, 45 (2005) 982-985.

[92]   B. Kaghouche, F. Mansour, C. Molliet, B. Rousset, P. Temple-Boyer, Investigation on optical and physico-chemical properties of LPCVD SiO_xN_y thin films, *Eur Phys J: Appl Phys*, 66 (2014) 20301.

[93]   B. Morana, G. Pandraud, J. Creemer, P. Sarro, Characterization of LPCVD amorphous silicon carbide (a-SiC) as material for electron transparent windows, *Mater Chem Phys*, 139 (2013) 654-662.

[94]   I. Kleps, A. Angelescu, LPCVD amorphous silicon carbide films, properties and microelectronics applications, *J Phys IV*, 9 (1999) Pr8-1115-Pr1118-1122.

[95]   K.S. Lee, J.Y. Park, W.-J. Kim, G.W. Hong, Effect of microstructure of SiC layer on the indentation properties of silicon carbide–graphite system fabricated by LPCVD method, *J Mater Sci Lett*, 20 (2001) 1229-1231.

[96]   R. Taylor, B. Scott, Hexachlorodisilane as a precursor in the LPCVD of silicon dioxide and silicon oxynitride films, *J Electrochem Soc*, 136 (1989) 2382.

[97]   T. Kanashima, R. Nagayoshi, M. Okuyama, Y. Hamakawa, Optical characterizations of photo-induced chemical vapor deposition produced SiO_2 films in vacuum ultraviolet, ultraviolet, and visible region, *J Appl Phys*, 74 (1993) 5742-5747.

[98]   T. Kawahara, A. Yuuki, Y. Matsui, A study on the behavior of SiO_2 film precursors with trench deposition method for SiH_4/O_2 low pressure chemical vapor deposition, *Jpn J Appl Phys*, 30 (1991) 431.

[99]   H. Nagasawa, T. Minamizawa, M. Kanezashi, T. Yoshioka, T. Tsuru, Microporous organosilica membranes for gas separation prepared via PECVD using different O/Si ratio precursors, *J Membr Sci*, 489 (2015) 11-19.

[100]   Y.S. Kim, J.H. Lee, J.T. Lim, J.B. Park, G.Y. Yeom, Atmospheric pressure PECVD of SiO_2 thin film at a low temperature using HMDS/O_2/He/Ar, *Thin Solid Films*, 517 (2009) 4065-4069.

[101]   B. Park, R. Conti, L. Economikos, A. Chakravarti, J. Ellenberger, Characterization of bis (tertiary-butylamino) silane-based low-pressure chemical vapor deposition silicate glass films, *J Vac Sci Technol B*, 19 (2001) 1788-1795.

[102]   S. Kamiyama, T. Miura, Y. Nara, Comparison between SiO_2 films deposited by atomic layer deposition with $SiH_2[N(CH_3)_2]_2$ and $SiH[N(CH_3)_2]_3$ precursors, (2006) 1517-1521.

[103]   S.M. Aman, D. Koretomo, Y. Magari, M. Furuta, Influence of Deposition Temperature and Source Gas in PE-CVD for SiO_2 Passivation on Performance and Reliability of In–Ga–Zn–O Thin-Film Transistors, *IEEE Trans Electron Devices*, 65 (2018) 3257-3263.

[104]   A. Meshkova, F. Elam, S. Starostin, M. van de Sanden, H. de Vries, The role of carrier gas flow in roll-to-roll AP-PECVD synthesized silica moisture barrier films, *Surf Coat Technol*, 339 (2018) 20-26.

[105]   I. Blaszczyk-Lezak, A.M. Wrobel, M.P. Kivitorma, I.J. Vayrynen, Silicon carbonitride films produced by remote hydrogen microwave plasma CVD using a (dimethylamino) dimethylsilane precursor, *Chem Vap Deposition*, 11 (2005) 44-52.

[106]   W. Jang, H. Jeon, H. Song, H. Kim, J. Park, H. Kim, H. Jeon, The effect of plasma power on the properties of low-temperature silicon nitride deposited by RPALD for a gate spacer, *Phys Status Solidi A*, 212 (2015) 2785-2790.

[107]   T. Sorita, S. Shiga, K. Ikuta, Y. Egashira, H. Komiyama, The Formation Mechanism and Step Coverage Quality of Tetraethylorthosilicate - SiO_2 Films Studied by the Micro/Macrocavity Method, *J Electrochem Soc*, 140 (1993) 2952-2959.

[108]   B. Shokri, M.A. Firouzjah, S.I. Hosseini, FTIR analysis of silicon dioxide thin film deposited by metal organic-based PECVD, in: Proceedings of 19th international symposium on plasma chemistry society, Bochum, Germany, 2009.

[109]   H. Juárez, M. Pacio, T. Díaz, E. Rosendo, G. Garcia, A. García, F. Mora, G. Escalante, Low temperature deposition: properties of SiO_2 films from TEOS and ozone by APCVD system, in: Journal of Physics: Conference Series, 2009, pp. 012020-012021.

[110]   C.K. Wong, H. Wong, C.W. Kok, M. Chan, Silicon oxynitride prepared by chemical vapor deposition as optical waveguide materials, *J Cryst Growth*, 288 (2006) 171-175.

[111]   C. Chang, T. Abe, M. Esashi, Trench filling characteristics of low stress TEOS/ozone oxide deposited by PECVD and SACVD, *Microsyst Technol*, 10 (2004) 97-102.

[112]   I. Shareef, G. Rubloff, M. Anderle, W. Gill, J. Cotte, D. Kim, Subatmospheric chemical vapor deposition ozone/TEOS process for SiO_2 trench filling, *J Vac Sci Technol B*, 13 (1995) 1888-1892.

[113]   V.H. Nguyen, A. Sekkat, C.A. Masse de la Huerta, F. Zoubian, C. Crivello, J. Rubio-Zuazo, M. Jaffal, M. Bonvalot, C. Vallée, O. Aubry, H. Rabat, D. Hong, D. Muñoz-Rojas, Atmospheric Plasma-Enhanced Spatial Chemical Vapor Deposition of SiO_2 Using Trivinylmethoxysilane and Oxygen Plasma, *Chem Mater*, 32 (2020) 5153-5161.

[114]   K. Okuyama, T. Fujimoto, T. Hayashi, M. Adachi, Gas-phase nucleation in the tetraethylorthosilicate (TEOS)/O_3 APCVD process, *AIChE journal*, 43 (1997) 2688-2697.

[115]   K. Fujino, Y. Nishimoto, N. Tokumasu, K. Maeda, Silicon Dioxide Deposition by Atmospheric-Pressure and Low-Temperature CVD Using TEOS and Ozone, *J Electrochem Soc*, 137 (1990) 2883-2887.

[116]   I.A. Shareef, G.W. Rubloff, W.N. Gill, Role of gas phase reactions in subatmospheric chemical-vapor deposition ozone/TEOS processes for oxide deposition, *J Vac Sci Technol B*, 14 (1996) 772-788.

[117]   S.W. Benson, A.E. Axworthy, Mechanism of the Gas Phase, Thermal Decomposition of Ozone, *J Chem Phys*, 26 (1957) 1718-1726.

[118]   O. Mittov, N. Ponomareva, I.Y. Mittova, E. Novikova, T. Gadebskaya, M. Bezryadin, Deposition of Al_2O_3 and SiO_2 films via pyrolysis of aluminum acetylacetonate and hexamethyldisiloxane in the presence of nitrogen compounds, *Inorg Mater*, 36 (2000) 1243-1250.

[119]   V. Tomar, D. Patil, D. Gautam, Deposition and characterization of SiON films using HMDS for photonics applications, *Semicond Sci Technol*, 22 (2006) 43.

[120] N. Fainer, A. Plekhanov, Y.M. Rumyantsev, E. Maximovskii, V. Shayapov, Films of hydrogenated silicon oxycarbonitride. Part I. Chemical and phase composition, *Glass Phys Chem*, 40 (2014) 570-577.

[121] S. Guruvenket, S. Andrie, M. Simon, K.W. Johnson, R.A. Sailer, Atmospheric-pressure plasma-enhanced chemical vapor deposition of a-SiCN: H films: role of precursors on the film growth and properties, *ACS Appl Mater Interfaces*, 4 (2012) 5293-5299.

[122] T. Aoki, T. Ogishima, A.M. Wróbel, Y. Nakanishi, Y. Hatanaka, Silicon nitride film growth by remote plasma CVD using Tris (dimethylamino) silane, *Vacuum*, 51 (1998) 747-750.

[123] A.M. Wrobel, A. Walkiewicz-Pietrzykowska, I. Blaszczyk-Lezak, Reactivity of organosilicon precursors in remote hydrogen microwave plasma chemical vapor deposition of silicon carbide and silicon carbonitride thin-film coatings, *Appl Organomet Chem*, 24 (2010) 201-207.

[124] L. Kleps, F. Caccavale, G. Brusatin, A. Angelescu, L. Armelao, LPCVD silicon carbide and silicon carbonitride films using liquid single precursors, *Vacuum*, 46 (1995) 979-981.

[125] V. Tomar, L. Patil, D. Gautam, Deposition and characterization of silicon nitride films using HMDS for photonics applications, *J Optoelectron Adv Mater*, 10 (2008) 2657-2662.

[126] W. Jang, H. Jeon, C. Kang, H. Song, J. Park, H. Kim, H. Seo, M. Leskela, H. Jeon, Temperature dependence of silicon nitride deposited by remote plasma atomic layer deposition, *Phys Status Solidi A*, 211 (2014) 2166-2171.

[127] L. Du, Y. Bai, W. Chu, Y. Ding, Synthesis of two aminosilanes as CVD precursors of SiC_xN_y films: Tuning film composition by Molecular Structures, *Phosphorus, Sulfur, Silicon Relat Elem*, 193 (2018) 568-573.

[128] Z. Tijanić, D. Ristić, M. Ivanda, I. Bogdanović-Radović, M. Marciuš, M. Ristić, O. Gamulin, S. Musić, K. Furić, A. Chiasera, Low Temperature Deposition of SiNx Thin Films by the LPCVD Method, *Croat Chem Acta*, 85 (2012) 97-100.

[129] B. Semmache, M. Lemiti, C. Chanelière, C. Dubois, A. Sibai, B. Canut, A. Laugier, Silicon nitride and oxynitride deposition by RT-LPCVD, *Thin Solid Films*, 296 (1997) 32-36.

[130] F. Martí, A. Castro, J. Olivares, C. Gómez-Aleixandre, J. Albella, Deposition of ternary silicon based compounds by CVD techniques, *J Phys IV*, 9 (1999) Pr8-101-Pr108-107.

[131] A.M. Wrobel, A. Walkiewicz-Pietrzykowska, M. Ahola, I.J. Vayrynen, F.J. Ferrer-Fernandez, A.R. Gonzalez-Elipe, Growth Mechanism and Chemical Structure of Amorphous Hydrogenated Silicon Carbide (a-SiC: H) Films Formed by Remote Hydrogen Microwave Plasma CVD From a Triethylsilane Precursor: Part 1, *Chem Vap Deposition*, 15 (2009) 39-46.

[132] Applied Materials Inc., Process of filling the high aspect ratio trenches by co-flowing ligands during thermal CVD, U.S. Patent 2016/0293483 A1, 2016.

[133] V.E. Vamvakas, R. Berjoan, S. Schamm, D. Davazoglou, C. Vahlas, Low pressure chemical vapor deposition of silicon oxynitride films using tetraethylorthosilicate, dichlorosilane and ammonia mixtures, *J Phys IV*, 11 (2001) Pr3-231-Pr233-238.

[134] S.K. Ray, C.K. Maiti, N.B. Chakrabarti, Low-Temperature deposition of dielectric films by microwave plasma enhanced decomposition of hexamethyldisilazane, *J Electron Mater*, 20 (1991) 907-913.

[135] J.A. Prybyla, C.M. Chiang, L.H. Dubois, Investigations of the Growth of TiN Thin Films from Ti(NMe2)4 and Ammonia, *J Electrochem Soc*, 140 (1993) 2695-2702.

[136] L.H. Dubois, Model studies of low temperature titanium nitride thin film growth, *Polyhedron*, 13 (1994) 1329-1336.

[137] C. Vahlas, Chemical Vapor Deposition of Metals: from Unary Systems to Complex Metallic Alloys, in: Surface Properties and Engineering of Complex Intermetallics, Wolrd Scientific, 2010, pp. 49-81.

[138] J.-H. Park, T. Sudarshan, Chemical vapor deposition, ASM international, Metals Park, OH, 2001.

[139] E.J. Kim, W.N. Gill, Analytical Model for Chemical-Vapor-Deposition of SiO_2-Films Using Tetraethoxysilane and Ozone, *J Cryst Growth*, 140 (1994) 315-326.

References

[140] H. Vergnes, D. Samélor, A.N. Gleizes, C. Vahlas, B. Caussat, Local Kinetic Modeling of Aluminum Oxide Metal-Organic CVD From Aluminum Tri-isopropoxide, *Chem Vap Deposition*, 17 (2011) 181-185.

[141] C.R. Kleijn, Computational modeling of transport phenomena and detailed chemistry in chemical vapor deposition – a benchmark solution, *Thin Solid Films*, 365 (2000) 294-306.

[142] S. Alexandrov, A. Kovalgin, D. Krasovitskiy, A study of CVD of gallium nitride films by in situ gas-phase UV spectroscopy, *J Phys IV*, 5 (1995) C5-183-C185-190.

[143] K. Kachel, D. Siche, S. Golka, P. Sennikov, M. Bickermann, FTIR exhaust gas analysis of GaN pseudo-halide vapor phase growth, *Mater Chem Phys*, 177 (2016) 12-18.

[144] T. Ohba, T. Suzuki, H. Yagi, Y. Furumura, T. Hatano, Decomposition property of methylhydrazine with titanium nitridation at low temperature, *J Electrochem Soc*, 142 (1995) 934.

[145] W.G. Zhang, K.J. Hüttinger, CVD of SiC from methyltrichlorosilane. Part II: Composition of the gas phase and the deposit, *Chem Vap Deposition*, 7 (2001) 173-181.

[146] J. Arnó, Z. Yuan, S. Murphy, Fourier Transform Infrared Characterization of Downstream Gas-Phase Species Generated by Tetraethylorthosilicate/Ozone Atmospheric Pressure Reactions, *J Electrochem Soc*, 146 (1999) 276-280.

[147] M. Yoshimoto, K. Takubo, M. Komoda, H. Matsunami, Gas phase reactions diagnosed by mass analysis in photo-assisted chemical vapor deposition of silicon nitride, *Appl Surf Sci*, 79 (1994) 264-269.

[148] T. Sorita, T. Satake, H. Adachi, T. Ogata, K. Kobayashi, Mass Spectrometric and Kinetic Study of Low-Pressure Chemical Vapor Deposition of Si_3N_4 Thin Films from SiH_2Cl_2 and NH_3, *J Electrochem Soc*, 141 (1994) 3505.

[149] T. Satake, T. Sorita, H. Fujioka, H. Adachi, H. Nakajima, Detection of Intermediates in Thermal Chemical Vapor Deposition Process Using Tetraethoxysilane, *Jpn J Appl Phys*, 33 (1994) 3339-3342.

[150] T. Kawahara, A. Yuuki, Y. Matsui, Reaction-Mechanism of Chemical Vapor-Deposition Using Tetraethylorthosilicate and Ozone at Atmospheric-Pressure, *Jpn J Appl Phys, Part 1*, 31 (1992) 2925-2930.

[151] Y. Tsutsumi, M. Ikegawa, T. Usui, Y. Ichikawa, K. Watanabe, J. Kobayashi, Molecular beam sampling to analyze the reaction mechanism of chemical vapor deposition, *J Vac Sci Technol A*, 14 (1996) 2337-2342.

[152] W. Knolle, L. Wennrich, S. Naumov, K. Czihal, L. Prager, D. Decker, M.R. Buchmeiser, 222 nm Photo-induced radical reactions in silazanes. A combined laser photolysis, EPR, GC-MS and QC Study, *Phys Chem Chem Phys*, 12 (2010) 2380-2391.

[153] G. Schoof, C. Kleijn, H. Van Den Akker, T. Oosterlaken, H. Terhorst, F. Huussen, Simulation and validation of SiO_2 LPCVD from TEOS in a vertical 300 mm multi-wafer reactor, in: Journal de Physique IV (Proceedings), EDP sciences, 2002, pp. 51-61.

[154] M. Adachi, T. Fujimoto, Y. Itoh, K. Okuyama, Numerical simulations of films formed by cluster/particle co-deposition in atmospheric-pressure chemical vapor deposition process using organic silicon vapors and ozone gas, *Jpn J Appl Phys*, 39 (2000) 3542.

[155] S. Romet, M.F. Couturier, T.K. Whidden, Modeling of silicon dioxide chemical vapor deposition from tetraethoxysilane and ozone, *J Electrochem Soc*, 148 (2001) G82-G90.

[156] D.M. Dobkin, S. Mokhtari, M. Schmidt, A. Pant, L. Robinson, A. Sherman, Mechanisms of Deposition of SiO_2 from Teos and Related Organosilicon Compounds and Ozone, *J Electrochem Soc*, 142 (1995) 2332-2340.

[157] N. Zhou, A. Krishnan, V. Kudriavtsev, Y. Brichko, Numerical study of $TEOS/O_3$ CVD mechanism in an industrial reactor, in: Fifth International Conference on Advanced Thermal Processing of Semiconductors, RTP, 1997, pp. 257-268.

[158] J.P. Nieto, L. Jeannerot, B. Caussat, Modelling of an industrial moving belt chemical vapour deposition reactor forming SiO_2 films, *Chem Eng Sci*, 60 (2005) 5331-5340.

[159] S.-W. Hu, Y. Wang, X.-Y. Wang, T.-W. Chu, X.-Q. Liu, Gas-Phase Reactions between Silane and Ammonia: A Theoretical Study, *J Phys Chem A*, 107 (2003) 9189-9196.

[160] K. Yacoubi, C. Azzaro-Pantel, J.P. Couderc, Analysis and Modeling of Low Pressure CVD of Silicon Nitride from a Silane-Ammonia Mixture: II. Deposition Modeling, *J Electrochem Soc*, 146 (1999) 3018-3027.

[161] S.D. Hersee, J.M. Ballingall, The operation of metalorganic bubblers at reduced pressure, *J Vac Sci Technol A*, 8 (1990) 800-804.

[162] M.G.M. Van Der Vis, E.H.P. Cordfunke, Tetraethoxysilane, $Si(OC_2H_5)_4$ - Vapor-Pressure Measurements at Temperatures from 323 to 442 K by Means of a Bourdon Spoon Gauge, *Thermochim Acta*, 265 (1995) 129-134.

[163] M.G.M. Van Der Vis, E.H.P. Cordfunke, R.J.M. Konings, The thermodynamic properties of tetraethoxysilane (TEOS) and an infrared study of its thermal decomposition, *J Phys IV*, 03 (1993) C3-75-C73-82.

[164] M. Kato, H. Tanaka, Ebulliometric Measurement of Vapor Liquid Equilibria for 4 Binary-Systems - Methanol + Silicon Tetramethoxide, Methanol + Silicon Tetraethoxide, Ethanol + Silicon Tetramethoxide, and Ethanol + Silicon Tetraethoxide, *J Chem Eng Data*, 34 (1989) 206-209.

[165] S.J. Jang, S.-D. Lee, J.H. Kim, S.G. Kim, D.Y. Kim, B.-i. Yang, S.I. Lee, M.W. Kim, Novel trisilyl amine derivative, method for preparing the same and silicon-containing thin film using the same, U.S. Patent 2016/0333030 A1, 2016.

[166] C. Cushman, N. Smith, M. Kaykhaii, N. Podraza, M. Linford, An Introduction to Modeling in Spectroscopic Ellipsometry, Focusing on Models for Transparent Materials: the Cauchy and Sellmeier Models, Vacuum Technology & Coating, 2016.

[167] C. Jeynes, J.L. Colaux, Thin film depth profiling by ion beam analysis, *Analyst*, 141 (2016) 5944-5985.

[168] M. Mayer, SIMNRA, a simulation program for the analysis of NRA, RBS and ERDA, *AIP Conf Proc*, 475 (1999) 541-544.

[169] P. Lange, W. Windbracke, Characterization of Thermal and Deposited Thin Oxide Layers by Longitudinal Optical-Transverse Optical-Excitation in Fourier-Transform IR Transmission Measurements, *Thin Solid Films*, 174 (1989) 159-164.

[170] B. Harbecke, B. Heinz, P. Grosse, Optical-Properties of Thin-Films and the Berreman Effect, *Appl Phys A: Mater Sci Process*, 38 (1985) 263-267.

[171] C. Martinet, R.A.B. Devine, Analysis of the vibrational mode spectra of amorphous SiO_2 films, *J Appl Phys*, 77 (1995) 4343-4348.

[172] N. Primeau, C. Vautey, M. Langlet, The effect of thermal annealing on aerosol-gel deposited SiO_2 films: a FTIR deconvolution study, *Thin Solid Films*, 310 (1997) 47-56.

[173] D. Rouchon, N. Rochat, F. Gustavo, A. Chabli, O. Renault, P. Besson, Study of ultrathin silicon oxide films by FTIR-ATR and ARXPS after wet chemical cleaning processes, *Surf Interface Anal*, 34 (2002) 445-450.

[174] W.C. Oliver, G.M. Pharr, An improved technique for determining hardness and elastic modulus using load and displacement sensing indentation experiments, *J Mater Res*, 7 (2011) 1564-1583.

[175] T. Young, III. An essay on the cohesion of fluids, *Philos Trans R Soc London*, 95 (1805) 65-87.

[176] R.N. Wenzel, Surface Roughness and Contact Angle, *J Phys Colloid Chem*, 53 (1949) 1466-1467.

[177] W.A. Pliskin, Comparison of properties of dielectric films deposited by various methods, *J Vac Sci Technol*, 14 (1977) 1064-1081.

[178] W.A. Pliskin, R.P. Gnall, Evidence for Oxidation Growth at the Oxide-Silicon Interface from Controlled Etch Studies, *J Electrochem Soc*, 111 (1964) 872.

[179] P. Cova, R.A. Masut, O. Grenier, S. Poulin, Effect of unintentionally introduced oxygen on the electron–cyclotron resonance chemical-vapor deposition of SiN_x films, *J Appl Phys*, 92 (2002) 129-138.

[180] V.T. Volkov, L.F. Satunkina, Influence of oxygen on the composition and some properties of the films obtained by r.f. sputtering from a Si_3N_4 target, *Thin Solid Films*, 247 (1994) 145-147.

[181]   G.A.C.M. Spierings, Wet chemical etching of silicate glasses in hydrofluoric acid based solutions, *J Mater Sci*, 28 (1993) 6261-6273.

[182]   R.B. Bird, Transport phenomena, *Appl Mech Rev*, 55 (2002) R1-R4.

[183]   H. Versteeg, W. Malalasekera, Computational fluid dynamics: the finite volume method, Harlow, England: Longman Scientific & Technical, London, England, 1995.

[184]   G.A. Chliavoras, Computational study and development of a kinetic model for the moderate temperature, atmospheric pressure chemical vapor deposition of SiO_2 films from the $TEOS/O_3/O_2$ chemical system, National Technical University of Athens, Greece, 2020.

[185]   J. Henrie, S. Kellis, S.M. Schultz, A. Hawkins, Electronic color charts for dielectric films on silicon, *Opt Express*, 12 (2004) 1464-1469.

[186]   S. Nguyen, D. Dobuzinsky, D. Harmon, R. Gleason, S. Fridmann, Reaction-Mechanisms of Plasma-Assisted and Thermal-Assisted Chemical Vapor-Deposition of Tetraethylorthosilicate Oxide-Films, *J Electrochem Soc*, 137 (1990) 2209-2215.

[187]   S.N. Taraskin, S.R. Elliott, Nature of vibrational excitations in vitreous silica, *Phys Rev B*, 56 (1997) 8605-8622.

[188]   P. Innocenzi, P. Falcaro, D. Grosso, F. Babonneau, Order-disorder transitions and evolution of silica structure in self-assembled mesostructured silica films studied through FTIR spectroscopy, *J Phys Chem B*, 107 (2003) 4711-4717.

[189]   T.M. Parrill, Transmission infrared study of acid-catalyzed sol-gel silica coatings during room ambient drying, *J Mater Res*, 7 (2011) 2230-2239.

[190]   P. Lange, Evidence for disorder-induced vibrational mode coupling in thin amorphous SiO_2 films, *J Appl Phys*, 66 (1989) 201-204.

[191]   D.W. Berreman, Infrared Absorption at Longitudinal Optic Frequency in Cubic Crystal Films, *Phys Rev*, 130 (1963) 2193-2198.

[192]   G. Rzepa, G. Pieczara, A. Gaweł, A. Tomczyk, R. Zalecki, The influence of silicate on transformation pathways of synthetic 2-line ferrihydrite, *J Therm Anal Calorim*, 125 (2016) 407-421.

[193]   M.I. Baraton, M.S. ElShall, Synthesis and characterization of nanoscale metal oxides and carbides: II. Micro-Raman and FT-IR surface studies of a silicon carbide powder, *Nanostruct Mater*, 6 (1995) 301-304.

[194]   G. Ramis, P. Quintard, M. Cauchetier, G. Busca, V. Lorenzelli, Surface-Chemistry and Structure of Ultrafine Silicon-Carbide - an FT-IR Study, *J Am Ceram Soc*, 72 (1989) 1692-1697.

[195]   F.X.L.i. Xamena, A. Zecchina, FTIR spectroscopy of carbon dioxide adsorbed on sodium- and magnesium-exchanged ETS-10 molecular sieves, *Phys Chem Chem Phys*, 4 (2002) 1978-1982.

[196]   R.W. Stevens, R.V. Siriwardane, J. Logan, In situ Fourier transform infrared (FTIR) investigation of CO_2 adsorption onto zeolite materials, *Energy Fuels*, 22 (2008) 3070-3079.

[197]   J. Gope, S. Kumar, S. Singh, C.M.S. Rauthan, P.C. Srivastava, Growth of Mixed-Phase Amorphous and Ultra Nanocrystalline Silicon Thin Films in the Low Pressure Regime by a VHF PECVD Process, *Silicon*, 4 (2012) 127-135.

[198]   A. Milella, F. Palumbo, J.L. Delattre, F. Fracassi, R. d'Agostino, Deposition and Characterization of Dielectric Thin Films from Allyltrimethylsilane Glow Discharges, *Plasma Processes Polym*, 4 (2007) 425-432.

[199]   B.C. Smith, Infrared spectral interpretation: a systematic approach, CRC press, 1998.

[200]   R.D. Aines, G.R. Rossman, Water in minerals? A peak in the infrared, *J Geophys Res: Solid Earth*, 89 (1984) 4059-4071.

[201]   S. Nakashima, S. Ohki, S. Ochiai, Infrared microspectroscopy analysis of the chemical state and spatial distribution of hydrous species in minerals, *Geochemical Journal*, 23 (1989) 57-64.

[202]   F. Massines, N. Gherardi, A. Fornelli, S. Martin, Atmospheric pressure plasma deposition of thin films by Townsend dielectric barrier discharge, *Surf Coat Technol*, 200 (2005) 1855-1861.

[203]   K.M. Davis, M. Tomozawa, An infrared spectroscopic study of water-related species in silica glasses, *J Non-Cryst Solids*, 201 (1996) 177-198.

[204] D. De Sousa Meneses, M. Eckes, L. del Campo, C.N. Santos, Y. Vaills, P. Echegut, Investigation of medium range order in silicate glasses by infrared spectroscopy, *Vib Spectrosc*, 65 (2013) 50-57.

[205] I.I. Montero, L. Galan, O. Najmi, J.M. Albella, Disorder-induced vibration-mode coupling in SiO_2 films observed under normal-incidence infrared radiation, *Phys Rev B Condens Matter*, 50 (1994) 4881-4884.

[206] I.W. Boyd, J.I.B. Wilson, A study of thin silicon dioxide films using infrared absorption techniques, *J Appl Phys*, 53 (1982) 4166-4172.

[207] F.L. Galeener, Planar Rings in Glasses, *Solid State Commun*, 44 (1982) 1037-1040.

[208] F. Ruiz, J.R. Martinez, J. Gonzalez-Hernandez, A simple model to analyze vibrationally decoupled modes on SiO_2 glasses, *J Mol Struct*, 641 (2002) 243-250.

[209] C.T. Kirk, Quantitative analysis of the effect of disorder-induced mode coupling on infrared absorption in silica, *Phys Rev B Condens Matter*, 38 (1988) 1255-1273.

[210] R. Almeida, H. Vasconcelos, L. Ilharco, Relationship between infrared absorption and porosity in silica-based sol-gel films, in: SPIE International Symposium on Optics, Imaging, and Instrumentation, Sol-Gel Optics III, 1994.

[211] J.T. Fitch, S.S. Kim, C.H. Bjorkman, G. Lucovsky, The Effect of Postdeposition Thermal-Processing on Mos Gate Oxides Formed by Remote Pecvd, *J Electron Mater*, 19 (1990) 151-158.

[212] Z. Yin, D.V. Tsu, G. Lucovsky, F.W. Smith, Annealing Study of the Infrared-Absorption in an Amorphous-Silicon Dioxide Film, *J Non-Cryst Solids*, 114 (1989) 459-461.

[213] J.T. Fitch, Effects of thermal history on stress-related properties of very thin films of thermally grown silicon dioxide, *J Vac Sci Technol B*, 7 (1989) 153-162.

[214] S. Bulou, L. Le Brizoual, P. Miska, L. de Poucques, R. Hugon, M. Belmahi, J. Bougdira, The influence of CH_4 addition on composition, structure and optical characteristics of SiCN thin films deposited in a CH_4/N_2/Ar/hexamethyldisilazane microwave plasma, *Thin Solid Films*, 520 (2011) 245-250.

[215] R.M. de Vos, W.F. Maier, H. Verweij, Hydrophobic silica membranes for gas separation, *J Membr Sci*, 158 (1999) 277-288.

[216] E. Gil, J.B. Park, J.S. Oh, G.Y. Yeom, Characteristics of SiO_x thin films deposited by atmospheric pressure chemical vapor deposition as a function of HMDS/O_2 flow rate, *Thin Solid Films*, 518 (2010) 6403-6407.

[217] N. Hirashita, S. Tokitoh, H. Uchida, Thermal-Desorption and Infrared Studies of Plasma-Enhanced Chemical Vapor-Deposited Sio Films with Tetraethylorthosilicate, *Jpn J Appl Phys, Part 1*, 32 (1993) 1787-1793.

[218] G. Lucovsky, J.T. Fitch, E. Kobeda, E.A. Irene, Local Atomic Structure of Thermally Grown SiO_2 Films, in: C.R. Helms, B.E. Deal (Eds.) The Physics and Chemistry of SiO_2 and the Si-SiO_2 Interface, Springer US, Boston, MA, 1988, pp. 139-148.

[219] P.N.K. Deenapanray, Influence of Low-Temperature Chemical Vapor Deposited SiO_2 Capping Layer Porosity on GaAs/AlGaAs Quantum Well Intermixing, *Electrochem Solid-State Lett*, 3 (1999) 196.

[220] K. Maeda, J. Sato, Very Low-Temperature Chemical Vapor-Deposition of Silicon Dioxide Films Using Ozone and Organosilane, *Denki Kagaku*, 45 (1977) 654-659.

[221] N. Suyal, T. Krajewski, M. Mennig, Sol-gel synthesis and microstructural characterization of silicon oxycarbide glass sheets with high fracture strength and high modulus, *J Sol-Gel Sci Technol*, 13 (1998) 995-999.

[222] C. Comte, J. von Stebut, Microprobe-type measurement of Young's modulus and Poisson coefficient by means of depth sensing indentation and acoustic microscopy, *Surf Coat Technol*, 154 (2002) 42-48.

[223] R.J. Brook, Concise encyclopedia of advanced ceramic materials, Elsevier, 2012.

[224] S. Choudhary, M. Singh, R.K. Kale, Surfactant-catalyzed SiO_2 thin films preparation and characterization, *J Adhes Sci Technol*, 27 (2013) 2629-2641.

References

[225] M.L. Hair, W. Hertl, Adsorption on hydroxylated silica surfaces, *J Phys Chem*, 73 (1969) 4269-4276.

[226] S. Lithotech, Synthetic Fused Silica—Optical and Technical Grades, Schott Lithotec. Available at: http://www.jmcglass.com/down/fused_silica_us.pdf. Last Accessed: January 21, 2021.

[227] R.L. DeRosa, P.A. Schader, J.E. Shelby, Hydrophilic nature of silicate glass surfaces as a function of exposure condition, *J Non-Cryst Solids*, 331 (2003) 32-40.

[228] T. Herak, T. Chau, D. Thomson, S. Mejia, D. Buchanan, K. Kao, Low-temperature deposition of silicon dioxide films from electron cyclotron resonant microwave plasmas, *J Appl Phys*, 65 (1989) 2457-2463.

[229] C. Vallée, A. Goullet, A. Granier, In situ ellipsometry and infrared analysis of PECVD SiO_2 films deposited in an O_2/TEOS helicon reactor, *J Non-Cryst Solids*, 216 (1997) 48-54.

[230] P.N. Deenapanray, H. Tan, M.I. Cohen, K. Gaff, M. Petravic, C. Jagadish, Silane Flow Rate Dependence of SiO_x Cap Layer Induced Impurity-Free Intermixing of GaAs/AlGaAs Quantum Wells, *J Electrochem Soc*, 147 (2000) 1950.

[231] S. Rojas, A. Modelli, W. Wu, A. Borghesi, B. Pivac, Properties of silicon dioxide films prepared by low-pressure chemical vapor deposition from tetraethylorthosilicate, *J Vac Sci Technol, B: Microelectron Process Phenom*, 8 (1990) 1177-1184.

[232] I. Kleps, C. Pavelescu, Etch rate behaviour of SiO_2 films chemically vapour desposited at low temperatures in $TEOS-O_2-N_2$ system, *Thin Solid Films*, 192 (1990) L9-L13.

[233] A. Mitra, J.D. Rimstidt, Solubility and dissolution rate of silica in acid fluoride solutions, *Geochim Cosmochim Acta*, 73 (2009) 7045-7059.

[234] M. Prokopowicz-Prigogine, La réactivité du verre. Le caractère autocatalytique du mecanisme de dissolution de la maille silicique du verre dans un mélange aqueux d'acides fluorhydrique et chlorhydrique, *J Chim Phys*, 85 (1988) 695-705.

[235] J.S. Judge, A study of the dissolution of SiO_2 in acidic fluoride solutions, *J Electrochem Soc*, 118 (1971) 1772.

[236] G. Spierings, J. Van Dijk, The dissolution of $Na_2O-MgO-CaO-SiO_2$ glass in aqueous HF solutions, *J Mater Sci*, 22 (1987) 1869-1874.

[237] J.K. Kang, C.B. Musgrave, The mechanism of HF/H_2O chemical etching of SiO_2, *J Chem Phys*, 116 (2002) 275-280.

[238] D.M. Knotter, Etching mechanism of vitreous silicon dioxide in HF-based solutions, *J Am Chem Soc*, 122 (2000) 4345-4351.

[239] R. Kee, G. Dixon-Lewis, J. Warnatz, M. Coltrin, J. Miller, H. Moffat, A Fortran computer code package for the evaluation of gas-phase, multicomponent transport properties, Report No. SAND86-8246B, in, Technical Report, Sandia National Laboratories, 1998.

[240] M.E. Coltrin, P. Ho, H.K. Moffat, R.J. Buss, Chemical kinetics in chemical vapor deposition: growth of silicon dioxide from tetraethoxysilane (TEOS), *Thin Solid Films*, 365 (2000) 251-263.

[241] Z. Yuan, S. Mokhtari, A. Ferdinand, J. Eakin, L. Bartholomew, Optimization of SiO_2 film conformality in $TEOS/O_3$ APCVD, *Thin Solid Films*, 290-291 (1996) 422-426.

[242] K. Nakamura, H. Nonaka, N. Kameda, T. Nishiguchi, S. Ichimura, Photochemical Reaction of Ozone and 1,1,1,3,3,3-Hexamethyldisilazane: Analysis of the Gas Reaction between Precursors in a Photochemical Vapor Deposition Process, *Jpn J Appl Phys*, 47 (2008) 7349-7355.

[243] H. Kotani, M. Matsuura, A. Fujii, H. Genjou, S. Nagao, Low-temperature APCVD oxide using TEOS-ozone chemistry for multilevel interconnections, in: International Technical Digest on Electron Devices Meeting, 1989, pp. 669-672.

[244] H. Nagasawa, Y. Yamamoto, M. Kanezashi, T. Tsuru, Atmospheric-Pressure Plasma-Enhanced Chemical Vapor Deposition of Hybrid Silica Membranes, *J Chem Eng Jpn*, 51 (2018) 732-739.

[245] F. Benitez, E. Martinez, J. Esteve, Improvement of hardness in plasma polymerized hexamethyldisiloxane coatings by silica-like surface modification, *Thin Solid Films*, 377 (2000) 109-114.

[246] P.H.T. Ngamou, J.P. Overbeek, R. Kreiter, H.M. van Veen, J.F. Vente, I.M. Wienk, P.F. Cuperus, M. Creatore, Plasma-deposited hybrid silica membranes with a controlled retention of organic bridges, *J Mater Chem A*, 1 (2013) 5567-5576.

[247] J.H. Lee, C.H. Jeong, J.T. Lim, V.A. Zavaleyev, S.J. Kyung, G.Y. Yeom, SiO_xN_y thin film deposited by plasma enhanced chemical vapor deposition at low temperature using HMDS–O_2–NH_3–Ar gas mixtures, *Surf Coat Technol*, 201 (2007) 4957-4960.

[248] Q. Chen, Y. Zhang, E. Han, Y. Ge, SiO_2-like film deposition by dielectric barrier discharge plasma gun at ambient temperature under an atmospheric pressure, *J Vac Sci Technol A*, 24 (2006) 2082-2086.

[249] K. Schmidt-Szalowski, Z. Rżanek-Boroch, J. Sentek, Z. Rymuza, Z. Kusznierewicz, M. Misiak, Thin Films Deposition from Hexamethyldisiloxane and Hexamethyldisilazane under Dielectric-Barrier Discharge (DBD) Conditions, *Plasmas Polym*, 5 (2000) 173-190.

[250] D. Trunec, Z. Navrátil, P. Stahel, L. Zají ková, V. Bur íková, J. Cech, Deposition of thin organosilicon polymer films in atmospheric pressure glow discharge, *J Phys D: Appl Phys*, 37 (2004) 2112-2120.

[251] M.S. Haque, H.A. Naseem, W.D. Brown, Characterization of High-Rate Deposited PECVD Silicon Dioxide Films for MCM Applications, *J Electrochem Soc*, 142 (1995) 3864-3869.

[252] R.N. Wenzel, Resistance of solid surfaces to wetting by water, *Ind Eng Chem*, 28 (1936) 988-994.

[253] T.-Y. Lo, Y.-C. Huang, Y.-N. Hsiao, C.-G. Chao, W.-T. Whang, Preparation of superhydrophobic polyimide films modified with organosilicasol as effective anticorrosion coatings, *Surf Coat Technol*, 258 (2014) 310-319.

[254] D. Lai, G. Kong, C. Che, Synthesis and corrosion behavior of ZnO/SiO_2 nanorod-sub microtube superhydrophobic coating on zinc substrate, *Surf Coat Technol*, 315 (2017) 509-518.

[255] Y.-S. Wei, W.-Y. Liu, H.-M. Wu, K.-S. Chen, V. Cech, Characteristics of SiO_x-containing hard film prepared by low temperature plasma enhanced chemical vapor deposition using hexamethyldisilazane or vinyltrimethylsilane and post oxygen plasma treatment, *Mater Chem Phys*, 189 (2017) 183-190.

[256] I.S. Merenkov, H. Katsui, M.N. Khomyakov, V.S. Sulyaeva, R.V. Pushkarev, R. Tu, T. Goto, M.L. Kosinova, Extraordinary synergetic effect of precursors in laser CVD deposition of SiBCN films, *J Eur Ceram Soc*, 39 (2019) 5123-5131.

[257] J. Park, J. Oh, E. Gil, G.Y. Yeom, Characteristics of SiO_x thin films deposited by atmospheric pressure chemical vapor deposition using a double-discharge system, *Mater Res Bull*, 47 (2012) 3011-3014.

[258] C. Shim, D. Jung, Relationship between C=C Bonds and Mechanical Properties of Carbon Rich Low-k Films deposited by Plasma Enhanced Chemical Vapor Deposition, *Jpn J Appl Phys*, 43 (2004) 940-944.

[259] R.Y. Honda, R.P. Mota, R.G.S. Batocki, D.C.R. Santos, T. Nicoleti, K.G. Kostov, M.E. Kayama, M.A. Algatti, N.C. Cruz, L. Ruggiero, Plasma-polymerized hexamethyldisilazane treated by nitrogen plasma immersion ion implantation technique, *J Phys*, 167 (2009) 012055.

[260] J.K. Choi, D.H. Kim, J. Lee, J.B. Yoo, Effects of process parameters on the growth of thick SiO_2 using plasma enhanced chemical vapor deposition with hexamethyldisilazane, *Surf Coat Technol*, 131 (2000) 136-140.

[261] J.W. Smith, S.M. Seutter, R.S. Iyer, Pattern-dependent microloading and step coverage of silicon nitride thin films deposited in a single-wafer thermal chemical vapor deposition chamber, *Journal of Vacuum Science & Technology B: Microelectronics and Nanometer Structures Processing, Measurement, and Phenomena*, 23 (2005) 2340-2346.

[262] P. Morin, G. Raymond, D. Benoit, P. Maury, R. Beneyton, A comparison of the mechanical stability of silicon nitride films deposited with various techniques, *Appl Surf Sci*, 260 (2012) 69-72.

[263] D.E. Bossi, J.M. Hammer, J.M. Shaw, Optical properties of silicon oxynitride dielectric waveguides, *Appl Opt*, 26 (1987) 609-611.

[264]   N.I. Fainer, M.L. Kosinova, E.A. Maximovsky, Y.M. Rumyantsev, F.A. Kuznetsov, V.G. Kesler, V.V. Kirienko, Study of the structure and phase composition of nanocrystalline silicon oxynitride films synthesized by ICP-CVD, *Nucl Instrum Methods Phys Res, Sect A*, 543 (2005) 134-138.

[265]   B.H. Weiller, Chemical Vapor Deposition of TiN from Tetrakis(dimethylamido)titanium and Ammonia: Kinetics and Mechanistic Studies of the Gas-Phase Chemistry, *J Am Chem Soc*, 118 (1996) 4975-4983.

[266]   J.-A. Jeong, S.W. Jeong, N.-J. Park, J.-W. Kang, J.-K. Kim, D.-G. Kim, H.-K. Kim, Characteristics of Transparent SiN_x Thin-Film Passivation Layer Grown by CECVD for Top-Emitting OLEDs, *J Electrochem Soc*, 154 (2007) J402.

[267]   C. Yang, J. Pham, Characteristic study of silicon nitride films deposited by LPCVD and PECVD, *Silicon*, 10 (2018) 2561-2567.

[268]   K. Yacoubi, C. Azzaro, J. Couderc, P., Low Pressure CVD of Silicon Nitride from a Silane-Ammonia Mixture : Analysis of Preliminary Experimental and Simulation Results, *J Phys IV*, 05 (1995) C5-291-C295-298.

[269]   P. Papavasileiou, Surface morphology, structure, and compositional characterization of MOCVD processed silicon oxynitride coatings for aqueous corrosion barriers, Diploma Thesis, National Technical University of Athens, Greece, 2020.

[270]   F. Ay, A. Aydinli, Comparative investigation of hydrogen bonding in silicon based PECVD grown dielectrics for optical waveguides, *Opt Mater*, 26 (2004) 33-46.

[271]   B. Hallam, B. Tjahjono, S. Wenham, Effect of PECVD silicon oxynitride film composition on the surface passivation of silicon wafers, *Sol Energy Mater Sol Cells*, 96 (2012) 173-179.

[272]   F. Giorgis, F. Giuliani, C. Pirri, E. Tresso, C. Summonte, R. Rizzoli, R. Galloni, A. Desalvo, P. Rava, Optical, structural and electrical properties of device-quality hydrogenated amorphous silicon-nitrogen films deposited by plasma-enhanced chemical vapour deposition, *Philos Mag B*, 77 (1998) 925-944.

[273]   Z. Yin, F. Smith, Optical dielectric function and infrared absorption of hydrogenated amorphous silicon nitride films: Experimental results and effective-medium-approximation analysis, *Phys Rev B*, 42 (1990) 3666.

[274]   P.J. Launer, Infrared analysis of organosilicon compounds: spectra-structure correlations, in: Silicone compounds register and review, Petrarch Systems Bristol, PA, 1987.

[275]   A. Pecora, L. Maiolo, G. Fortunato, C. Caligiore, A comparative analysis of silicon dioxide films deposited by ECR-PECVD, TEOS-PECVD and Vapox-APCVD, *J Non-Cryst Solids*, 352 (2006) 1430-1433.

[276]   M. Nakaya, S. Yasuhara, T. Maeda, A. Hotta, Impact of hot wire and material gas species on the Cat-CVD coating of gas barrier SiOC thin films onto PET bottles, *Surf Coat Technol*, 344 (2018) 21-29.

[277]   E.H. Oulachgar, C. Aktik, S. Dostie, R. Sowerby, S. Gujrathi, M. Scarlete, Chemical and Structural Characterization of SiONC Dielectric Thin Film Deposited by PSCVD, *J Electrochem Soc*, 153 (2006) F255-F259.

[278]   Z. Gan, C. Wang, Z. Chen, Material Structure and Mechanical Properties of Silicon Nitride and Silicon Oxynitride Thin Films Deposited by Plasma Enhanced Chemical Vapor Deposition, *Surfaces*, 1 (2018) 59-72.

[279]   K.J. Trevino, J.C. Shearer, P.R. McCurdy, S.E. Pease-Dodson, C.C. Okegbe, E.R. Fisher, Isoelectric points of plasma-modified and aged silicon oxynitride surfaces measured using contact angle titrations, *Surf Interface Anal*, 43 (2011) 1257-1270.

[280]   A. Arafat, K. Schroën, L.C. de Smet, E.J. Sudhölter, H. Zuilhof, Tailor-made functionalization of silicon nitride surfaces, *J Am Chem Soc*, 126 (2004) 8600-8601.

[281]   P. Saengdee, W. Chaisriratanakul, W. Bunjongpru, W. Sripumkhai, A. Srisuwan, W. Jeamsaksiri, C. Hruanun, A. Poyai, C. Promptmas, Surface modification of silicon dioxide, silicon nitride and titanium oxynitride for lactate dehydrogenase immobilization, *Biosens Bioelectron*, 67 (2015) 134-138.

[282] Z. Zhang, Z. Shao, Y. Luo, P. An, M. Zhang, C. Xu, Hydrophobic, transparent and hard silicon oxynitride coating from perhydropolysilazane, *Polym Int*, 64 (2015) 971-978.

[283] J. Hong, Y. Kim, H. Paik, K. No, J.R. Lukes, The effect of nitrogen incorporation on surface properties of silicon oxynitride films, *Phys Status Solidi RRL*, 3 (2009) 25-27.

[284] V.V. Tsukruk, V.N. Bliznyuk, Adhesive and Friction Forces between Chemically Modified Silicon and Silicon Nitride Surfaces, *Langmuir*, 14 (1998) 446-455.

[285] X. Zhang, S. Ptasinska, Growth of silicon oxynitride films by atmospheric pressure plasma jet, *J Phys D: Appl Phys*, 47 (2014) 145202.

[286] S. Leclerc, A. Lecours, M. Caron, E. Richard, G. Turcotte, J.F. Currie, Electron cyclotron resonance plasma chemical vapor deposited silicon nitride for micromechanical applications, *J Vac Sci Technol A*, 16 (1998) 881-884.

[287] J.W. Lee, K.D. Mackenzie, D. Johnson, J.N. Sasserath, S.J. Pearton, F. Ren, Low Temperature Silicon Nitride and Silicon Dioxide Film Processing by Inductively Coupled Plasma Chemical Vapor Deposition, *J Electrochem Soc*, 147 (2000) 1481.

[288] K.B. Sundaram, R.E. Sah, H. Baumann, K. Balachandran, R.M. Todi, Wet etching studies of silicon nitride thin films deposited by electron cyclotron resonance (ECR) plasma enhanced chemical vapor deposition, *Microelectron Eng*, 70 (2003) 109-114.

[289] U. Abidin, B.Y. Majlis, J. Yunas, Fabrication of pyramidal cavity structure with micron-sized tip using anisotropic KOH etching of silicon (100), *Jurnal Teknologi*, 74 (2015) 137–148.

[290] H. Gleskova, S. Wagner, V. Gašparík, P. Kováč, Low-temperature silicon nitride for thin-film electronics on polyimide foil substrates, *Appl Surf Sci*, 175 (2001) 12-16.

[291] V. Rathi, M. Gupta, O. Agnihotri, The dependence of etch rate of photo-CVD silicon nitride films on NH_4F content in buffered HF, *Microelectron J*, 26 (1995) 563-567.

[292] L. Goria-Gatti, A. Iannone, A. Tomasi, G. Poli, E. Albano, In vitro and in vivo evidence for the formation of methyl radical from procarbazine: a spin-trapping study, *Carcinogenesis*, 13 (1992) 799-805.

[293] A.J. Carmichael, K. Makino, P. Riesz, Quantitative aspects of ESR and spin trapping of hydroxyl radicals and hydrogen atoms in gamma-irradiated aqueous solutions, *Radiat Res*, 100 (1984) 222-234.

[294] H. Chandra, I.M.T. Davidson, M.C.R. Symons, Use of spin traps in the study of silyl radicals in the gas phase, *J Chem Soc, Faraday Trans 1*, 79 (1983) 2705-2711.

[295] H. Chandra, I.M. Davidson, M.C. Symons, Unstable intermediates. Part 202. The use of spin traps to study trialkylsilyl and related radicals, *J Chem Soc, Perkin Trans 2*, (1982) 1353-1356.

[296] N. Grassie, I. Macfarlane, The thermal degradation of polysiloxanes—I. Poly (dimethylsiloxane), *Eur Polym J*, 14 (1978) 875-884.

[297] J. Pola, A. Galíková, A. Galík, V. Blechta, Z. Bastl, J. Šubrt, A. Ouchi, UV Laser Photolysis of Disiloxanes for Chemical Vapor Deposition of Nano-Textured Silicones, *Chem Mater*, 14 (2002) 144-153.

[298] T. Tsiros, Kinetic model development and CFD simulation of a silicon oxynitride (SiO_xN_y) CVD process from $TDMSA/O_2$ mixtures, Diploma Thesis, National Technical University of Athens, Greece, 2020.

[299] R.G. Xu, Y. Leng, Solvation force simulations in atomic force microscopy, *J Chem Phys*, 140 (2014) 214702.

[300] D.E. Aspnes, A. Studna, Dielectric functions and optical parameters of Si, Ge, GaP, GaAs, GaSb, InP, InAs, and InSb from 1.5 to 6.0 ev, *Phys Rev B*, 27 (1983) 985.

[301] K. Luke, Y. Okawachi, M.R.E. Lamont, A.L. Gaeta, M. Lipson, Broadband mid-infrared frequency comb generation in a Si_3N_4 microresonator, *Opt Lett*, 40 (2015) 4823-4826.

[302] I.H. Malitson, Interspecimen comparison of the refractive index of fused silica, *Josa*, 55 (1965) 1205-1209.

[303] Z. Chen, K. Prasad, C.Y. Li, S.S. Su, D. Gui, P.W. Lu, X. He, S. Balakumar, Characterization and performance of dielectric diffusion barriers for Cu metallization, *Thin Solid Films*, 462-463 (2004) 223-226.

[304] S. Peter, S. Bernütz, S. Berg, F. Richter, FTIR analysis of a-SiCN:H films deposited by PECVD, *Vacuum*, 98 (2013) 81-87.

[305] G. Scardera, E. Bellet-Amalric, D. Bellet, T. Puzzer, E. Pink, G. Conibeer, Formation of a $Si–Si_3N_4$ nanocomposite from plasma enhanced chemical vapour deposition multilayer structures, *J Cryst Growth*, 310 (2008) 3685-3689.

[306] D. Yonekura, K. Fujikawa, R.-I. Murakami, Influence of film structure on gas barrier properties of SiO_xN_y films, *Surf Coat Technol*, 205 (2010) 168-173.

[307] K.M. Behrens, E.D. Klinkenberg, J. Finster, K.H. Meiwes-Broer, Geometric structure of thin SiO_xN_y films on Si(100), *Surface Science*, 402-404 (1998) 729-733.

[308] M.A. Schiavon, K.J. Ciuffi, I.V.P. Yoshida, Glasses in the SiOCN system produced by pyrolysis of polycyclic silazane/siloxane networks, *J Non-Cryst Solids*, 353 (2007) 2280-2288.

[309] H. Guo-Fu, G. Xin-Hua, Z. Xiao-Dan, S. Jian, Z. Jian-Jun, Z. Ying, Evolution of infrared spectra and optical emission spectra in hydrogenated silicon thin films prepared by VHF-PECVD, *Chin Phys B*, 20 (2011) 077802.

[310] J.D. Ouwens, R. Schropp, Hydrogen microstructure in hydrogenated amorphous silicon, *Phys Rev B*, 54 (1996) 17759.

[311] J.R. Shallenberger, D.A. Cole, S.W. Novak, Characterization of silicon oxynitride thin films by x-ray photoelectron spectroscopy, *J Vac Sci Technol A*, 17 (1999) 1086-1090.

[312] H. Huang, K.J. Winchester, A. Suvorova, B.R. Lawn, Y. Liu, X.Z. Hu, J.M. Dell, L. Faraone, Effect of deposition conditions on mechanical properties of low-temperature PECVD silicon nitride films, *Mater Sci Eng, A*, 435-436 (2006) 453-459.

[313] S. Bae, D.G. Farber, S.J. Fonash, Characteristics of low-temperature silicon nitride (SiN_x: H) using electron cyclotron resonance plasma, *Solid·State Electron*, 44 (2000) 1355-1360.

[314] K.C. Topka, G.A. Chliavoras, F. Senocq, H. Vergnes, D. Samelor, D. Sadowski, C. Vahlas, B. Caussat, Large temperature range model for the atmospheric pressure chemical vapor deposition of silicon dioxide films on thermosensitive substrates, *Chem Eng Res Des*, 161 (2020) 146-158.

[315] K.C. Topka, B. Diallo, D. Samelor, R. Laloo, D. Sadowski, C. Genevois, T. Sauvage, F. Senocq, H. Vergnes, V. Turq, N. Pellerin, B. Caussat, C. Vahlas, Tunable SiO_2 to SiO_xC_yH films by ozone assisted chemical vapor deposition from tetraethylorthosilicate and hexamethyldisilazane mixtures, *Surf Coat Technol*, 407 (2021) 126762.

[316] T. Fujimoto, K. Okuyama, S. Yamada, M. Adachi, Effect of cluster/particle deposition on atmospheric pressure chemical vapor deposition of SiO2 from four gaseous organic Si-containing precursors and ozone, *J Appl Phys*, 85 (1999) 4196-4206.

[317] W. Piyawattanametha, Y.-H. Park, A. Akujärvi, B. Guo, R. Mannila, A. Rissanen, MOEMS FPI sensors for NIR-MIR microspectrometer applications, in: MOEMS and Miniaturized Systems XV, 2016.

[318] U. Schmid, S. González-Castilla, J. Olivares, M. Clement, L. Vergara, L. Pulido, E. Iborra, J. Sangrador, Silicon oxide sacrificial layers deposited by pulsed-DC magnetron sputtering for MEMS applications, in: Smart Sensors, Actuators, and MEMS IV, 2009.

[319] SCHOTT AG, SCHOTT TopLine options for enhanced processing, SCHOTT TopLyo® - efficient lyophilization, Available at: https://www.schott.com/pharmaceutical_packaging/french/products/vials/top-line-options/schott-toplyo.html, Last Accessed: 23 January 2021.

[320] K. Lee Nam, H. Kim Young, G. Im Tae, U. Lee Dong, M. Shon, J. Moon Myung, Analysis of PVDF Coating Properties with Addition of Hydrophobically Modified Fumed Silica, *Corros Sci Technol*, 18 (2019) 232-242.

[321] S. Nistor, M. Stefan, V. Ralchenko, A. Khomich, D. Schoemaker, Nitrogen and hydrogen in thick diamond films grown by microwave plasma enhanced chemical vapor deposition at variable H_2 flow rates, *J Appl Phys*, 87 (2000) 8741-8746.

[322] F. Hirose, Y. Kinoshita, S. Shibuya, Y. Narita, Y. Takahashi, H. Miya, K. Hirahara, Y. Kimura, M. Niwano, Atomic layer deposition of SiO_2 from tris(dimethylamino)silane and ozone by using temperature-controlled water vapor treatment, *Thin Solid Films*, 519 (2010) 270-275.

[323] C. Vahlas, B. Caussat, F. Senocq, W.L. Gladfelter, L. Aloui, T. Moersch, A Delivery System for Precursor Vapors Based on Sublimation in a Fluidized Bed, *Chem Vap Deposition*, 13 (2007) 123-129.

[324] B.H. Choi, J.H. Lee, Long-term stable water vapor permeation barrier properties of SiN/SiCN/SiN nanolaminated multilayers grown by plasma-enhanced chemical vapor deposition at extremely low pressures, *Appl Phys Lett*, 105 (2014) 053302.

[325] C.-H. Huang, N.-F. Wang, Y. Tsai, C. Liu, C. Hung, M.-P. Houng, The formation of a SiO_x interfacial layer on low-k SiOCH materials fabricated in ULSI application, *Mater Chem Phys*, 110 (2008) 299-302.

[326] N.S.K. Gunda, M. Singh, L. Norman, K. Kaur, S.K. Mitra, Optimization and characterization of biomolecule immobilization on silicon substrates using (3-aminopropyl)triethoxysilane (APTES) and glutaraldehyde linker, *Appl Surf Sci*, 305 (2014) 522-530.

[327] W. Bensch, W. Bergholz, An FT-IR study of silicon dioxides for VLSI microelectronics, *Semicond Sci Technol*, 5 (1990) 421.

[328] T. Kaneko, D. Nemoto, A. Horiguchi, N. Miyakawa, FTIR analysis of a-SiC:H films grown by plasma enhanced CVD, *J Cryst Growth*, 275 (2005) e1097-e1101.

[329] Q. Su, S. King, L. Li, T. Wang, J. Gigax, L. Shao, W.A. Lanford, M. Nastasi, Microstructure-mechanical properties correlation in irradiated amorphous SiOC, *Scripta Mater*, 146 (2018) 316-320.

Auteur : Konstantina Christina TOPKA

Titre : Etude expérimentale et modélisation cinétique du procédé de dépôt chimique en phase vapeur de couches minces d'oxyde et d'oxynitrure de silicium pour des barrières de corrosion aqueuses

Directrice de thèse : Brigitte CAUSSAT | *Co-directeur :* Constantin VAHLAS

Date et lieu de la défense : Mardi 30 Mars 2021, ENSIACET, Toulouse, France

---

Le dépôt de matériaux à base de silice est largement utilisé dans de nombreux secteurs industriels, dont la microélectronique, l'emballage alimentaire, la séparation des gaz et la pharmacie. Selon l'application cible, ces matériaux doivent répondre à des besoins spécifiques en termes de propriétés mécaniques, durabilité et composition. La mise en œuvre de tels revêtements dans des applications pharmaceutiques nécessite, plus précisément, de bonnes propriétés de barrière aqueuse et anti-diffusion, ainsi qu'une résistance efficace à la corrosion. La résistance hydrolytique et la durabilité des revêtements sont directement liées au niveau de densification du réseau céramique. Dans le cas de SiO_2 amorphe, une réticulation et densification de réseau améliorée peut être induite par le remplacement partiel des anions O^{2-} par des anions N^{3-} ou C^{4-}, produisant des revêtements d'oxynitrure (SiO_xN_y) et de l'oxycarbure (SiO_xC_y) de silicium plus dense qui peuvent répondre aux exigences de performances dictées par les différentes applications pharmaceutiques. Cependant, très peu d'informations sont disponibles dans la littérature concernant le dépôt de revêtements SiO_xN_y et SiO_xC_y en fonction des contraintes spécifiques à l'application: à savoir la réalisation de films chimiquement inertes sur des substrats 3D complexes, déposés à pression atmosphérique et à température modérée (<570°C), avec des taux de dépôt élevés. Pour atteindre les objectifs ci-dessus, le dépôt de films à base de silice amorphe est entrepris via l'utilisation d'un procédé CVD thermique défini autour de nouvelles chimies réactives. Les voies chimiques réactives aident à la production de SiO_xN_y et SiO_xC_y à des températures inférieures aux températures conventionnelles et, plus important, compatibles avec les substrats thermosensibles. L'augmentation progressive des teneurs en N et C dans les dépôts est réalisée grâce à des molécules précurseurs et des compositions de gaz réactifs soigneusement sélectionnées. Des voies de dépôt innovantes, basées sur des combinaisons de précurseurs classiques contenant du silicium tels que le tétraéthylorthosilicate (TEOS) ou l'hexaméthyldisilazane (HMDS), et d'autres composés nouveaux tels que la tris(diméthylsilyl)amine (TDMSA) sont explorées. L'incorporation progressive d'azote et de carbone dans les films étant au cœur de ce travail, l'évolution qui en résulte du réseau silicaté est largement étudiée à travers des protocoles de caractérisation physico-chimique, structurale et mécanique. Une approche multidisciplinaire est adoptée, combinant la science des matériaux, la chimie analytique et l'ingénierie des procédés d'une manière qui implique le développement simultané de films barrières résistants grâce à des expériences CVD, parallèlement à l'analyse en phase gazeuse, à la simulation et au calcul numérique. Les informations expérimentales obtenues grâce à cette approche sont utilisées pour enrichir les modèles de la littérature ou définir des mécanismes de dépôt complètement nouveaux. Grâce à une représentation 3D du domaine spatial du réacteur, les modèles chimiques développés sont mis en œuvre afin de reproduire le processus de dépôt par simulation. Les calculs de mécanique des fluides numérique (MFN) sont utilisés pour comprendre les particularités de la formation du dépôt dans les espaces confinés et les pièces 3D complexes, obtenir des prédictions en termes de composition en phase gazeuse et solide, ainsi que pour étudier les potentiels et les solutions pour l'optimisation du processus de dépôt. Les corrélations établies entre les conditions de processus, la structure des films, la composition et les propriétés, ainsi que l'intégration d'une approche informatique et expérimentale couplée, sont utilisées pour arriver à des matériaux durables à base de silice avec des performances de barrière efficaces, flexibles pour une utilisation dans divers domaines d'application.

Author: Konstantina Christina TOPKA

Title: Experimental study and kinetic modelling of chemical vapor deposition process of silicon oxide and oxynitride thin films for aqueous corrosion barriers

Thesis director: Brigitte CAUSSAT | *Co-director:* Constantin VAHLAS

Date and place of defense: Tuesday 30th of March 2021, ENSIACET, Toulouse, France

---

The deposition of silica-based materials is widely used in numerous industrial sectors, including microelectronics, food packaging, gas separation and pharmaceutics. Depending on the target-application, these materials are required to fulfil specific requirements in terms of mechanical properties, durability, and composition. The implementation of such coatings in pharmaceutics applications require, more specifically, good aqueous barrier and anti-diffusion properties, as well as effective corrosion resistance. The hydrolytic resistance and the durability of the coatings is directly linked to the level of densification of the ceramic network. In the case of amorphous SiO_2, an improved network cross-linking, and by consequence densification, can be induced through the partial replacement of the O^{2-} anions by N^{3-} or C^{4-} ones, producing denser amorphous silicon oxynitride (SiO_xN_y) and silicon oxycarbide (SiO_xC_y) coatings that can meet the performance requirements dictated by the various pharmaceutical applications. However, very little information is available in the literature concerning the deposition of SiO_xN_y and SiO_xC_y coatings in accordance to the application-specific constraints: namely the production of chemically inert films on complex, 3D substrates, deposited at atmospheric pressure and at moderate temperatures (<570°C), with high deposition rates. To achieve the above goals, the deposition of amorphous silica-based films is undertaken via the utilization of a thermal CVD process defined around reactive, novel chemistries. The reactive chemical pathways aids in the production of SiO_xN_y and SiO_xC_y at temperatures lower than the conventional ones, and more importantly, compatible with thermosensitive substrates. The gradual increase in N and C contents in the deposits is carried out through carefully selected precursor molecules and reagent gas compositions. Innovative deposition routes, based on single or dual-precursor combinations of classic silicon-containing precursors such as tetraethylorthosilicate (TEOS) or hexamethyldisilazane (HMDS), and more novel compounds such as tris(dimethylsilyl)amine (TDMSA) are explored. Since the progressive incorporation of nitrogen and carbon in the films is at the core of this work, the resulting evolution of the silicate network is extensively studied through physicochemical, structural and mechanical characterization protocols. A multidisciplinary approach is embraced, combining materials science, analytical chemistry and process engineering in a way that involves the simultaneous development of resistant barrier films through CVD experiments, alongside gas phase analysis, simulation and numerical computation. The experimental information obtained through this approach is utilized in order to enrich previous literature models or define completely novel deposition mechanisms. Through 3D representation of the reactor spatial domain, the developed chemical models are implemented in order to replicate the deposition process via simulation. Computational fluid dynamics (CFD) calculations are used to understand the particularities of film formation in confined spaces and complex 3D-parts, obtain predictions in terms of gas phase and solid phase composition, as well as investigate potentials and solutions for optimization of the deposition process. The established correlations between process conditions, films structure, composition and properties, alongside the integration of a coupled computational and experimental approach, are used to arrive at durable silica-based materials with sustainable barrier performance, flexible for utilization in diverse application domains.